

**Fiber Bragg Grating Smart Sensor Network for Anomaly Detection,  
Estimation, and Isolation**

Maryam Etezadbrojerdi

A Thesis  
in  
The Department  
of  
Electrical and Computer Engineering

Presented in Partial Fulfillment of the Requirements  
for the Degree of Doctor of Philosophy at  
Concordia University  
Montreal, Quebec, Canada

April, 2012

© Maryam Etezadbrojerdi, 2012

**CONCORDIA UNIVERSITY**  
**SCHOOL OF GRADUATE STUDIES**

**This is to certify that the thesis prepared**

**By:** Maryam Etezadbrojerdi

**Entitled:** Fiber Bragg Grating Smart Sensor Network for Anomaly Detection, Estimation,  
and Isolation

and submitted in partial fulfillment of the requirements for the degree of

DOCTOR OF PHILOSOPHY (Electrical and computer Engineering)

complies with the regulations of the University and meets the accepted standards with respect to originality and quality.

Signed by the final examining committee:

Dr. A.M. Hanna

Chair

Dr. L. Chen

External Examiner

Dr. F. Haghghat

External to Program

Dr. A. Aghdam

Examiner

Dr. M.Z. Kabir

Examiner

Dr. M. Kahrizi and Dr. K. Khorasani

Thesis Supervisor

Approved by

Chair of Department or Graduate Program Director

Dean of Faculty

# **Abstract**

## **Fiber Bragg Grating Smart Sensor Network for Anomaly Detection, Estimation, and Isolation**

MaryamEtezadbrojerdi, Ph.D

Concordia University, 2012

A methodology is developed to provide a reliable and quantitative structural health monitoring information with emphasis on three properties, namely on locating the anomaly, modeling the anomaly profile, and identifying the damage inside the disturbed structures. Toward this end, a numerical method is developed to reconstruct the anomaly inside the monitored structure from the reflected spectrum of the Bragg gratings that are fabricated into the single mode (SM FBG) or high birefringence fiber (Hi-Bi FBG).

Firstly, the effects of a non-uniform distribution of the transversal load and temperature on the FBG are analyzed and the perturbed reflected spectrum is modeled by introducing the change of the refractive indices and grating period along the fiber by using the transfer matrix formulation method.

Furthermore, an inverse method based on the genetic algorithm (GA) is developed for reconstruction of non-uniform applied anomalies from the perturbed reflected spectrum. The genetic algorithm retrieves the changes in the characteristics of the sensor from the measured spectra information by encoding the refractive index or the grating period distribution along the Bragg grating into the genes. Moreover, the effects of the simultaneously applied transversal and longitudinal forces on an FBG sensor are analyzed. The study on the effects of the simultaneous

transversal and longitudinal forces on an FBG sensor would eliminate the need for the FBGs to be installed on both the orthogonal directions on top of the monitored surface. Consequently, the applied strain measurements can be achieved by parallel fibers in one direction. This will reduce the number of sensors and the complexity of the monitoring system. The perturbed reflected spectra are modeled by the transfer matrix formulation method. Furthermore, the anomaly gradients along the sensor's length are determined from the intensity spectrum of the sensor by means of the GA. Additionally, the presented functionality of the GA algorithm is tested on a multiplexed FBG sensor system and the anomaly is modeled along a series of the sensors. Consequently, both the location and the model of the anomaly distribution are obtained.

Secondly, the effects of the strain and the temperature changes on the Hi-Bi FBG are studied and the reflected intensity spectrums of the polarized modes of the sensor, which are affected by a non-uniform distribution of the temperature or the strain, are modeled theoretically. Each Bragg reflection corresponding to the principal axes of the fiber has different dependencies on temperature and strain. Using this property, the type of the anomaly can be specifically identified and specified. Furthermore, the temperature and the transversal load gradients along the sensor's length are determined from the intensity spectrum of the sensor by means of the GA. The solution of the genetic algorithm is expressed in terms of the characteristic changes of the sensor, which are correlated with a non-uniform anomaly distribution inside the monitored structure. The presented methods are verified through extensive set of numerical case studies and scenarios.

# Acknowledgments

Firstly, I would like to thank my supervisors Prof. Mojtaba Kahrizi and Prof. Kash Khorasani for their guidance, advice, and support throughout the completion of this thesis. This work would not have been possible without their invaluable technical suggestions and encouragements. They have been my most important professional role models.

I would also like to express my sincere gratitude to Professors Amir Aghdam, Fariborz Haghghat, Lawrence Chen, Zhahangir kabir, and Adel Hanna for their participation in my examination committee and for their invaluable suggestions.

Finally, I wish to express my heartfelt thanks to my husband Armin, my parents Giti and Reza, and my brother Mohammad for their inspiration and support during this thesis.

# Table of Contents

List of Figures .....	vii
List of Tables .....	xi
List of Symbols and Abbreviations .....	xii
<b>ACKNOWLEDGMENTS.....</b>	<b>V</b>
<b>CHAPTER 1 INTRODUCTION.....</b>	<b>1</b>
1.1 MOTIVATION AND APPLICATIONS .....	1
1.2 LITERATURE REVIEW .....	6
1.2.1 Single Mode FBG .....	6
1.2.2 High Birefringence Fiber Bragg Grating Sensors .....	13
1.3 PROBLEM STATEMENT .....	19
1.4 METHODOLOGY .....	20
1.5 BASIC ASSUMPTIONS.....	22
1.6 CONTRIBUTION OF THE THESIS.....	23
1.7 ORGANIZATION OF THE THESIS .....	25
<b>CHAPTER 2 FIBER BRAGG GRATING SENSOR .....</b>	<b>27</b>
2.1 INTRODUCTION TO THE FIBER BRAGG GRATING .....	27
2.1.1 Characterization of an FBG Sensor Subjected to an Axial or/and Transversal Load .....	29
2.1.2 Characterization of an FBG Sensor Subjected to the Temperature Changes .....	40
2.2 INTRODUCTION TO THE HIGH BIREFRINGENCE FIBER BRAGG GRATING SENSOR .....	41
2.2.1 High Birefringence Fibers.....	41
2.2.2 Bragg Grating Fabricated into the Hi-Bi Fiber (Hi-Bi FBG).....	44
2.3 THEORETICAL TOOLS .....	48
2.3.1 Coupled Mode Theory for Modelling the Reflected Spectrum of an FBG Sensor .....	49
2.3.2 Genetic Algorithm .....	60
<b>CHAPTER 3 ANALYSIS AND SYNTHESIS OF A NON-UNIFORM DISTRIBUTION OF STRAIN AND TEMPERATURE WITHIN AN FBG SENSOR: PROPOSED APPROACH .....</b>	<b>67</b>
3.1 SYNTHESIS OF THE STRAIN PROFILE SUBJECTED TO AN FBG SENSOR .....	69
3.1.1 Synthesis of the Transversal Load Subjected to an FBG Sensor.....	73
3.1.2 Synthesis of a Two-Dimensional Strain (Longitudinal and Transversal Loads) Applied to an FBG Sensor.....	82

3.2 SYNTHESIS OF THE TEMPERATURE DISTRIBUTION ALONG THE FBG SENSOR.....	88
3.3 RESULTS AND DISCUSSIONS .....	89
3.4 CONCLUSIONS .....	114
<b>CHAPTER 4 ANALYSIS OF A NON-UNIFORM DISTRIBUTION OF ANOMALY ALONG THE LENGTH OF A HIGH BIREFRINGENCE FIBER .....</b>	<b>116</b>
4.1 SYNTHESIS OF A NON-UNIFORM DISTRIBUTION OF STRAIN ALONG THE HI-BI FBG .....	119
4.1.1 Synthesis of a Non-Uniform Transversal Load .....	119
4.1.2 Synthesis of a Non-uniform Simultaneously Applied Longitudinal and Transversal Loads .....	129
4.2 RESULTS AND DISCUSSIONS .....	134
4.3 CONCLUSIONS .....	143
<b>CHAPTER 5 DETECTION OF A NON-UNIFORM DISTRIBUTION OF TEMPERATURE AND STRAIN .....</b>	<b>145</b>
5.1 SYNTHESIS OF TEMPERATURE CHANGES USING THE HI-BI FBG .....	147
5.2 RESPONSE OF THE PANDA FBG TO THE TEMPERATURE AND STRAIN CHANGES .....	150
5.3 DETECTION OF A NON-UNIFORM DISTRIBUTION OF TRANSVERSAL LOAD AND TEMPERATURE.....	156
5.4 RESULTS AND DISCUSSIONS .....	159
5.5 CONCLUSIONS .....	178
<b>CHAPTER 6 CONCLUSIONS AND FUTURE WORK .....</b>	<b>180</b>
6.1 CONCLUSIONS .....	180
6.2 FUTURE WORK.....	181
<b>BIBLIOGRAPHY.....</b>	<b>184</b>

## List of Figures

FIGURE 1.1 SCHEMATIC MODEL OF A) ORTHOGONAL FBG SENSOR ARRAY, AND B) SERIES OF FBG SENSORS. ....	20
FIGURE 2.1 SCHEMATIC OF A FIBER BRAGG GRATING SENSOR AND ITS REFLECTED AND TRANSMITTED SPECTRUM. ....	29
FIGURE 2.2 SCHEMATIC OF THE COORDINATE SYSTEM OF THE FBG SENSOR AND THE APPLIED FORCES WHEN IS MOUNTED A) ON TOP, OR B) INSIDE THE MONITORED STRUCTURE. ....	30
FIGURE 2.3 A) STRAIN FUNCTIONS $\varepsilon(z)$ FOR DIFFERENT LOAD CASES. B) THE SPECTRA MEASURED BY THE OPTICAL SPECTRUM ANALYZER FOR (A) 0 kN, (B) 4 kN, (C) 6 kN, (D) 8 kN, AND (E) 10kN [69]. ....	33
FIGURE 2.4 SCHEMATIC OF AN FBG SENSOR THAT IS SUBJECTED TO THE TRANSVERSAL LOAD $F$ AND THE INPUT AND THE REFLECTED SPECTRUM. ....	35
FIGURE 2.5 SCHEMATIC OF THE APPLIED TRANSVERSAL LOAD TO A DISK. ....	37
FIGURE 2.6 COMPUTED REFRACTIVE INDEX SPATIAL DISTRIBUTION IN THE CORE OF THE FBG ALONG ITS AXIS, WHEN SUBJECTED TO A CONSTANT TRANSVERSAL FORCE OF $F= 60$ N. THE SOLID DISTRIBUTION REPRESENTS THE REFRACTIVE INDEX DISTRIBUTION OF THE UNDISTURBED SENSOR. ....	38
FIGURE 2.7 A) SCHEMATIC OF THE EXPERIMENTAL SET UP FOR THE MEASUREMENT OF THE TRANSVERSAL LOAD, AND B) REFLECTED SPECTRUMS OF THE EXPERIMENTAL SETUP UNDER DIFFERENT TRANSVERSAL LOADS [71]. ....	39
FIGURE 2.8 SCHEMATIC OF THE EMBEDDED FBG SENSOR LOCATED IN THE $-45^\circ$ PLY, AND B) THE REFLECTIVITY OF THE SENSOR VERSUS THE CRACK DENSITY [99]. ....	39
FIGURE 2.9 SCHEMATIC OF DIFFERENT TYPES OF FIBER (A) PANDA, (B) BOW-TIE, (C) D CLADDING AND ELLIPTICAL CORE FIBER, (D) ELLIPTICAL CORE FIBER, (E) ELLIPTICAL CLAD FIBER, AND (F) MAIN POLARIZATION AXES CONFIGURATION [55]. ....	42
FIGURE 2.10 A) SCHEMATIC OF THE ELLIPTICAL CLAD FIBER, AND B) ITS REFLECTED SPECTRUM [54]. ....	45
FIGURE 2.11 A) SCHEMATIC OF THE BOW-TIE FIBER, AND B) TRANSVERSAL STRAIN SENSITIVITY PLOTTED AGAINST LOADING ANGLE FOR BRAGG GRATING FABRICATED IN A BOW-TIE FIBRE [55]. ....	46
FIGURE 2.12 A) SCHEMATIC OF THE ELLIPTICAL CLADDING FIBER, AND B) TRANSVERSAL STRAIN SENSITIVITY PLOTTED AGAINST ANGLE OF ROTATION FOR BRAGG GRATING FABRICATED IN AN ELLIPTICAL CLADDING FIBER [54]. $\blacktriangle$ AND $\bullet$ SYMBOLIZE THE RESPONSE OF THE SLOW AND FAST AXIS, RESPECTIVELY. ....	47
FIGURE 2.13 A) COMPARISON BETWEEN THE SENSITIVITIES OF THE BRAGG GRATINGS FABRICATED INTO THE BOW-TIE AND D-CLAD HI-BI FIBERS WHEN THE LOAD IS APPLIED ALONG THE FAST AXIS OF THE FIBER. $\blacklozenge$ :BOW-TIE SLOW AXIS; $\blacksquare$ :BOW-TIE FAST AXIS; $\blacktriangle$ :D-CLAD SLOW AXIS; $\times$ :D-CLAD FAST AXIS, AND B) TRANSVERSAL LOAD SENSITIVITIES FOR THE BOW TIE FBG WITH THE BRAGG WAVELENGTH FOR FAST AND SLOW AXIS AS $\lambda_{FAST}= 1301.114$ NM AND $\lambda_{SLOW}=1301.580$ NM , RESPECTIVELY [52]. ....	48
FIGURE 2.14 CALCULATED REFLECTED SPECTRA FOR A UNIFORM BRAGG GRATING SENSOR OF A $L=10$ -MM LONG UNIFORM GRATING (SOLID LINE) WHEN A LINEAR STRAIN OF $\varepsilon(z)=100(z/L)$ MICRO-STRAIN IS APPLIED ALONG THE LENGTH OF THE SENSOR IN Z DIRECTION (DOTTED LINE) USING THE RUNGE-KUTTA METHOD. ....	55
FIGURE 2.15 SCHEMATIC OF A SENSOR DIVIDED INTO $M$ SECTIONS WITH LENGTH $\Delta z$ . ....	56



FIGURE 2.16 SCHEMATIC OF ROULETTE WHEEL SELECTION.....	62
FIGURE 2.17 SCHEMATIC OF THE SINGLE POINT Crossover.....	64
FIGURE 2.18 SCHEMATIC OF THE TWO POINT Crossover.....	65
FIGURE 3.1 SCHEMATIC OF AN FBG SENSOR THAT IS SUBJECTED TO THE TRANSVERSAL AND LONGITUDINAL FORCES.....	70
FIGURE 3.2 SPECTRAL RESPONSE OF AN FBG SENSOR SUBJECTED TO A) SIMULTANEOUS UNIFORM TRANSVERSAL FORCE AND AXIAL CONSTANT STRAIN FIELD $E_0=200 \mu E$ , B) SIMULTANEOUS UNIFORM TRANSVERSAL FORCE AND NON-UNIFORM QUADRATIC AXIAL STRAIN FIELD OF $E(z) = E_0(5(z/L)^2 + 1) \mu E$ , AND C) SIMULTANEOUS UNIFORM LONGITUDINAL STRAIN $E_0=200 \mu E$ AND A NON- UNIFORM QUADRATIC $F(z)=F_0(1+(z/L)^2)$ N TRANSVERSAL FORCE. THE DOTTED LINE DEPICTS THE REFLECTION SPECTRUM AT STRAIN-FREE STATE.....	72
FIGURE 3.3 THE THEORETICALLY OBTAINED REFLECTED SPECTRUM OF FIG. 2.7 THAT IS OBTAINED BY THE T-MATRIX.....	75
FIGURE 3.4 SCHEMATIC OF THE DERIVATION OF THE TRANSVERSAL LOAD OF EACH SEGMENT OF THE FIBER FROM THE OBTAINED REFRACTIVE INDEX CORRESPONDING TO THE SAME SEGMENT.....	81
FIGURE 3.5 SCHEMATIC OF THE DERIVATION OF LONGITUDINAL STRAIN APPLIED TO EACH SEGMENT OF THE FIBER FROM THE OBTAINED GRATING PERIOD CORRESPONDING TO THAT SEGMENT.....	84
FIGURE 3.6 THE SCHEMATIC OF THE APPROACH FOR RECONSTRUCTING A NON-UNIFORM DISTRIBUTION OF LONGITUDINAL STRAIN AND TRANSVERSAL LOAD ALONG THE FBG SENSOR.....	86
FIGURE 3.7 FLOW CHART OF GENETIC ALGORITHM FOR RECONSTRUCTION OF THE LOAD IN TWO DIMENSIONS.....	87
FIGURE 3.8 REFLECTED SPECTRA OF THE FBG SENSOR (DOTTED LINE) AND THE DISTURBED FBG SUBJECTED TO A NON-UNIFORM DISTRIBUTION OF TRANSVERSAL LOAD (CONTINUOUS LINE).....	91
FIGURE 3.9 A) REFLECTED SPECTRUM OF THE OPTIMAL SOLUTION FROM GA. ALSO PLOTTED IS THE REFLECTED SPECTRUM FOR THE X- POLARIZATION OF THE BRAGG GRATING SENSOR SUBJECTED TO THE TRANSVERSAL LOAD, AND B) APPLIED TRANSVERSAL LOAD DISTRIBUTION AND RECONSTRUCTED LOAD PROFILE BY THE GA OPTIMAL SOLUTION.....	92
FIGURE 3.10 A) THE REFLECTED SPECTRUM OF THE OPTIMAL SOLUTION FROM GA FOR THE X-POLARIZATION OF THE BRAGG GRATING SENSOR SUBJECTED TO THE TRANSVERSAL LOAD. THE UNDISTURBED AND DISTURBED REFLECTED SPECTRUM OBTAINED BY THE GA IS ALSO PLOTTED, AND B) APPLIED TRANSVERSAL LOAD DISTRIBUTION AND RECONSTRUCTED TRANSVERSAL LOAD DISTRIBUTION BY USING THE GA.....	93
FIGURE 3.11 A) THE REFLECTED SPECTRUM THAT IS DISTURBED BY THE DISTRIBUTION OF TRANSVERSAL LOAD AND THE REFLECTED SPECTRUM THAT IS OBTAINED BY THE GA OPTIMAL SOLUTION, AND B) THE RECONSTRUCTED AND ACTUAL TRANSVERSAL LOAD DISTRIBUTION.....	94
FIGURE 3.12 REFLECTED SPECTRA OF THE THREE MULTIPLEXED SENSORS.....	96
FIGURE 3.13 A) APPLIED TRANSVERSAL FORCE DISTRIBUTION ALONG THE THREE FBG SENSORS, AND B) TRANSVERSAL FORCE OBTAINED BY THE GA.....	97
FIGURE 3.14 REFLECTED SPECTRA OF THE OPTIMAL SOLUTIONS FROM GA FOR A) THE FIRST SENSOR, AND B) THE SECOND SENSOR.....	97
FIGURE 3.15 THE REFLECTED SPECTRUM CORRESPONDING TO (E) OF FIG. 2.3 THAT IS OBTAINED BY THE T-MATRIX.....	99

FIGURE 3.16 A) COMPARISON BETWEEN THE ORIGINAL SPECTRUM AND THE ONE THAT IS OBTAINED BY THE GA, AND B) COMPARISON BETWEEN THE APPLIED LONGITUDINAL STRAIN AND THE ONE THAT IS OBTAINED BY THE GA.....99

FIGURE 3.17 A) UNDISTURBED REFLECTED SPECTRUM OF THE FBG, B) COMPARISON BETWEEN THE ORIGINAL DISTURBED SPECTRUM BY THE LONGITUDINAL STRAIN AND THE ONE THAT IS OBTAINED BY THE GA, AND C) COMPARISON BETWEEN THE APPLIED LONGITUDINAL STRAIN AND THE ONE THAT IS OBTAINED BY THE GA.....101

FIGURE 3.18 A) COMPARISON BETWEEN THE ORIGINAL DISTURBED SPECTRUM BY THE LONGITUDINAL STRAIN AND THE ONE THAT IS OBTAINED BY THE GA, B) COMPARISON BETWEEN THE APPLIED LONGITUDINAL STRAIN AND THE ONE THAT IS OBTAINED BY THE GA, AND C) COMPARISON BETWEEN THE APPLIED LONGITUDINAL STRAIN AND THE ONE THAT IS OBTAINED BY THE GA SETTING AN INITIAL CONDITION. ....102

FIGURE 3.19 A) COMPARISON BETWEEN THE ORIGINAL DISTURBED SPECTRUM BY THE LONGITUDINAL STRAIN AND THE ONE THAT IS OBTAINED BY THE GA, AND B) COMPARISON BETWEEN THE APPLIED LONGITUDINAL STRAIN AND THE ONE THAT IS OBTAINED BY THE GA. ....103

FIGURE 3.20 A) REFLECTED SPECTRUM OF A WDM FBG SENSOR NETWORK, B) REFLECTED SPECTRUM OF THE THREE SENSORS OF AND REFLECTION OF THE SAME SENSOR WHEN WDM SENSOR IS AFFECTED BY THE STRAIN IN FIG 3.21, AND C) ORIGINAL AND THE RECONSTRUCTED OF THE DISTURBED REFLECTED SPECTRUM BY THE GA . ....105

FIGURE 3.21 A) ARBITRARY STRAIN THAT IS APPLIED TO THE WDM FBG VERSUS ITS LENGTH, AND B) STRAIN OBTAINED FROM GA ALGORITHM. ....106

FIGURE 3.22 THE REFLECTED SPECTRUM OF THE OPTIMAL SOLUTION FROM THE GA (DASHED LINE) THAT IS COMPARED WITH THE ORIGINAL REFLECTED SPECTRUM (SOLID LINE). THE SENSOR IS SUBJECTED TO THE TWO-DIMENSIONAL ANOMALY OF FIGURE 3.22 (B) AND (C). THE UNDISTURBED REFLECTED SPECTRUM OF THE SENSOR IS ALSO SHOWN WITH THE DOTTED LINE IN FIGURE 3.22(A).107

FIGURE 3.23 A) THE DISTURBED (SOLID LINE) AND RECONSTRUCTED REFLECTED SPECTRA OF OPTIMAL SOLUTION FROM GA (DASHED LINE) SUBJECTED TO THE B) SINUSOIDAL LONGITUDINAL STRAIN DISTRIBUTION, AND C) SINUSOIDAL TRANSVERSAL FORCE DISTRIBUTION. THE RECONSTRUCTED PERTURBATIONS ARE ALSO SHOWN IN THE FIGURE. THE UNDISTURBED REFLECTED SPECTRUM OF THE SENSOR IS SHOWN WITH THE DOTTED LINE IN FIGURE 3.23(A).....108

FIGURE 3.24 A) THE DISTURBED (SOLID LINE) AND RECONSTRUCTED SPECTRUM FROM THE OPTIMAL SOLUTION OF GA (DASHED LINE) SUBJECTED TO A NON-UNIFORM PERTURBATION OF B) LONGITUDINAL STRAIN, AND C) TRANSVERSAL FORCE DISTRIBUTION. THE RECONSTRUCTED PERTURBATIONS ARE ALSO SHOWN IN THE FIGURE. THE UNDISTURBED REFLECTED SPECTRUM OF THE SENSOR IS SHOWN WITH THE DOTTED LINE IN FIGURE 3.24(A).....109

FIGURE 3.25 THE SHIFT OF THE BRAGG WAVELENGTH WHEN THE SENSOR IS SUBJECTED TO THE UNIFORM TEMPERATURE CHANGE OF 10°C. THE UNDISTURBED REFLECTED SPECTRUM OF THE SENSOR IS SHOWN WITH THE DOTTED LINE.....110

FIGURE 3.26 TEMPERATURE CHANGE OF  $T(z)=T_0(1+(z/L)^2)$  °C ALONG ITS LENGTH IN Z DIRECTION. ....110

FIGURE 3.27 A) SPECTRAL RESPONSE OF AN FBG SUBJECTED TO NON-UNIFORM TEMPERATURE DISTRIBUTION IN (B), AND B) COMPARISON BETWEEN THE APPLIED AND RECONSTRUCTED TEMPERATURE DISTRIBUTION. ....111

FIGURE 3.28 A) SPECTRAL RESPONSE OF AN FBG SUBJECTED TO NON-UNIFORM TEMPERATURE DISTRIBUTION IN (B), AND B) COMPARISON BETWEEN THE APPLIED AND RECONSTRUCTED TEMPERATURE DISTRIBUTION. ....112

FIGURE 3.29 A) SPECTRAL RESPONSE OF AN FBG SUBJECTED TO NON-UNIFORM TEMPERATURE DISTRIBUTION IN (B), AND B) COMPARISON BETWEEN THE APPLIED AND RECONSTRUCTED TEMPERATURE DISTRIBUTION. ....113

FIGURE 4.1 SIMULATED REFLECTED SPECTRA OF THE BRAGG GRATING FABRICATED INTO THE A) D-CLAD, B) PANDA, C) ELLIPTICAL-CORE, D) BOW-TIE, E) ELLIPTICAL-CLAD, AND F) TRUE-PHASE HIGH-BIREFRINGENCE FIBERS THAT ARE SUBJECTED TO THE DIFFERENT VALUES OF TRANSVERSAL LOADS.....123

FIGURE 4.2 THE RESPONSE OF A) BOW-TIE, AND B) D-CLAD FBG TO THE QUADRATIC  $F(z)=4(z/L)^2+F_0(N)$  DISTRIBUTION OF TRANSVERSAL LOAD ALONG THE LENGTH OF THE SENSORS. THE UNDISTURBED REFLECTED SPECTRUM OF THE SENSOR IS SHOWN WITH THE DOTTED LINE. ....124

FIGURE 4.3 THE RESPONSE OF THE BOW-TIE FBG TO THE NON UNIFORM DISTRIBUTION OF A) TRANSVERSAL LOAD  $F(z)=4((z/L)^2+1) N$ , AND B) SIMULTANEOUS DISTRIBUTIONS OF TRANSVERSAL LOAD  $F(z)=4((z/L)^2+1) N$  AND LONGITUDINAL STRAIN  $\epsilon(z) =200((z/L)^2 +1) \mu E$ . THE UNDISTURBED REFLECTED SPECTRUM OF THE SENSOR IS SHOWN WITH THE DOTTED LINE. ....130

FIGURE 4.4 THE RESPONSE OF ELLIPTICAL CLAD FBG TO THE NON UNIFORM DISTRIBUTION OF A) TRANSVERSAL LOAD  $F(z)=4((z/L)^2+1) N$ , AND B) SIMULTANEOUS DISTRIBUTIONS OF TRANSVERSAL LOAD  $F(z)=4((z/L)^2+1) N$  AND LONGITUDINAL STRAIN  $\epsilon(z) =200((z/L)^2 +1) \mu E$ . THE UNDISTURBED REFLECTED SPECTRUM OF THE SENSOR IS SHOWN WITH THE DOTTED LINE. ....131

FIGURE 4.5 A) THE REFLECTED SPECTRUM OF THE OPTIMAL SOLUTION FROM GA FOR THE SPECTRUM CORRESPONDING TO THE SLOW AXIS OF THE BOW-TIE FBG SUBJECTED TO THE TRANSVERSAL LOAD. THE UNDISTURBED AND DISTURBED REFLECTED SPECTRUM OBTAINED BY THE T-MATRIX IS ALSO PLOTTED, AND B) APPLIED AND RECONSTRUCTED TRANSVERSAL LOAD DISTRIBUTION BY USING THE GA.....136

FIGURE 4.6 A) THE REFLECTED SPECTRUM OF THE OPTIMAL SOLUTION FROM GA FOR THE SPECTRUM CORRESPONDING TO THE SLOW AXIS OF THE BOW-TIE FBG SUBJECTED TO THE TRANSVERSAL LOAD. THE UNDISTURBED AND DISTURBED REFLECTED SPECTRUM OBTAINED BY THE T-MATRIX IS ALSO PLOTTED, AND B) APPLIED AND RECONSTRUCTED TRANSVERSAL LOAD DISTRIBUTION BY USING THE GA.....137

FIGURE 4.7 A) THE REFLECTED SPECTRUM OF THE OPTIMAL SOLUTION FROM GA FOR THE SPECTRUM CORRESPONDING TO THE SLOW AXIS OF THE BOW-TIE FBG SUBJECTED TO THE TRANSVERSAL LOAD. THE UNDISTURBED AND DISTURBED REFLECTED SPECTRUM OBTAINED BY THE T-MATRIX IS ALSO PLOTTED, AND B) APPLIED AND RECONSTRUCTED TRANSVERSAL LOAD DISTRIBUTION BY USING THE GA.....138

FIGURE 4.8 A) THE ORIGINAL AND RECONSTRUCTED REFLECTED SPECTRUM OF THE BOW-TIE FBG WHEN IS SUBJECTED TO THE LONGITUDINAL STRAIN IN (B) AND TRANSVERSAL LOAD IN (C), B) COMPARISON BETWEEN THE ORIGINAL AND RECONSTRUCTED LONGITUDINAL STRAIN, AND C) COMPARISON BETWEEN THE ORIGINAL AND RECONSTRUCTED TRANSVERSAL LOAD. ....140

FIGURE 4.9 A) THE ORIGINAL AND RECONSTRUCTED REFLECTED SPECTRUM OF THE BOW-TIE FBG WHEN IS SUBJECTED TO THE LONGITUDINAL STRAIN IN (B) AND TRANSVERSAL LOAD IN (C), B) COMPARISON BETWEEN THE ORIGINAL AND RECONSTRUCTED LONGITUDINAL STRAIN, AND C) COMPARISON BETWEEN THE ORIGINAL AND RECONSTRUCTED TRANSVERSAL LOAD. ....141

FIGURE 4.10 A) THE ORIGINAL AND RECONSTRUCTED REFLECTED SPECTRUM OF THE BOW-TIE FBG WHEN IS SUBJECTED TO THE LONGITUDINAL STRAIN IN (B) AND TRANSVERSAL LOAD IN (C), B) COMPARISON BETWEEN THE ORIGINAL AND RECONSTRUCTED LONGITUDINAL STRAIN, AND C) COMPARISON BETWEEN THE ORIGINAL AND RECONSTRUCTED TRANSVERSAL LOAD. ....142

FIGURE 5.1 SCHEMATIC OF THE PANDA FBG. ....	151
FIGURE 5.2 REFLECTED SPECTRA OF THE PANDA FBG SUBJECTED TO A) DIFFERENT TEMPERATURE CHANGES, AND B) NON-UNIFORM DISTRIBUTION OF TEMPERATURE. THE UNDISTURBED REFLECTED SPECTRUM IS ALSO SHOWN BY DOTTED LINES. ....	152
FIGURE 5.3 REFLECTED SPECTRA OF THE PANDA FBG SUBJECTED TO A) DIFFERENT TRANSVERSAL LOADS, AND B) NON-UNIFORM DISTRIBUTION OF TRANSVERSAL LOAD. THE UNDISTURBED REFLECTED SPECTRUM IS ALSO SHOWN BY DOTTED LINES. ....	154
FIGURE 5.4 REFLECTED SPECTRA OF THE PANDA FBG SUBJECTED TO A) DIFFERENT LONGITUDINAL STRAINS, AND B) NON-UNIFORM DISTRIBUTION OF LONGITUDINAL STRAIN. THE UNDISTURBED REFLECTED SPECTRUM IS ALSO SHOWN BY DOTTED LINES. ....	155
FIGURE 5.5 A) THE APPLIED AND RECONSTRUCTED REFLECTED SPECTRUM OF THE BOW-TIE FBG WHEN IS SUBJECTED TO THE TEMPERATURE DISTRIBUTION THAT IS SHOWN IN (B), AND B) COMPARISON BETWEEN THE APPLIED AND RECONSTRUCTED TEMPERATURE PROFILE. ....	160
FIGURE 5.6 A) THE APPLIED AND RECONSTRUCTED REFLECTED SPECTRUM OF THE BOW-TIE FBG WHEN IS SUBJECTED TO THE TEMPERATURE DISTRIBUTION THAT IS SHOWN IN (B), AND B) COMPARISON BETWEEN THE APPLIED AND RECONSTRUCTED TEMPERATURE PROFILE. ....	161
FIGURE 5.7 A) SPECTRAL RESPONSE OF THE HI-BI FBG SUBJECTED TO NON-UNIFORM TEMPERATURE AND TRANSVERSAL LOAD DISTRIBUTION IN (B) AND (C), RESPECTIVELY, B) COMPARISON BETWEEN THE APPLIED AND RECONSTRUCTED TEMPERATURE DISTRIBUTION, AND C) COMPARISON BETWEEN THE APPLIED AND RECONSTRUCTED TRANSVERSAL LOAD. ....	163
FIGURE 5.8 A) SPECTRAL RESPONSE OF THE HI-BI FBG SUBJECTED TO NON-UNIFORM TEMPERATURE AND TRANSVERSAL LOAD DISTRIBUTION IN (B) AND (C), RESPECTIVELY, B) COMPARISON BETWEEN THE APPLIED AND RECONSTRUCTED TEMPERATURE DISTRIBUTION, AND C) COMPARISON BETWEEN THE APPLIED AND RECONSTRUCTED TRANSVERSAL LOAD. ....	165
FIGURE 5.9 A) SPECTRAL RESPONSE OF AN FBG SUBJECTED TO NON-UNIFORM TEMPERATURE AND TRANSVERSAL LOAD DISTRIBUTION IN (B) AND (C), RESPECTIVELY, B) COMPARISON BETWEEN THE APPLIED AND RECONSTRUCTED TEMPERATURE DISTRIBUTION, AND C) COMPARISON BETWEEN THE APPLIED AND RECONSTRUCTED TRANSVERSAL LOAD. ....	166
FIGURE 5.10 SCHEMATIC OF THE MULTIPLEXED SENSOR SYSTEM THAT CONSISTS OF THE TWO PARALLEL SERIES OF IDENTICAL PANDA FBG SENSORS. ....	167
FIGURE 5.11 REFLECTED SPECTRUMS OF THE UNDISTURBED FBGS (DOTTED LINE) AND THE REFLECTED SPECTRUM OF THE THREE PERTURBED SENSORS BY A SIMULTANEOUS TRANSVERSAL FORCE SHOWN IN FIGURE 5.13 AND CONSTANT TEMPERATURE CHANGE OF 100 °C. ....	169
FIGURE 5.12 ORIGINAL AND THE ONE OBTAINED FROM THE OPTIMAL SOLUTIONS FROM GA FOR A) THE FIRST SENSOR, B) THE SECOND SENSOR, AND C) THE THIRD SENSOR OF THE SERIES 1 OF THE MULTIPLEXED SENSOR. ....	170
FIGURE 5.13 A) APPLIED TRANSVERSAL FORCE DISTRIBUTION ALONG THE THREE FBG SENSORS, AND B) TRANSVERSAL FORCE OBTAINED BY THE GA. ....	171
FIGURE 5.14 REFLECTED SPECTRUMS OF THE UNDISTURBED FBGS (DOTTED LINE) AND THE REFLECTED SPECTRUM OF THE THREE PERTURBED SENSORS BY A SIMULTANEOUS LONGITUDINAL STRAIN SHOWN IN FIGURE 5.16 AND CONSTANT TEMPERATURE CHANGE OF 100 °C. ....	172

FIGURE 5.15 ORIGINAL SPECTRUM AND THE ONE OBTAINED FROM THE OPTIMAL SOLUTIONS FROM GA FOR A) THE FIRST SENSOR, B) THE SECOND SENSOR, AND C) THE THIRD SENSOR OF THE SECOND SERIES OF PANDA FBGs OF THE MULTIPLEXED SENSOR SYSTEM IN FIGURE 5.10. ....173

FIGURE 5.16 A) APPLIED LONGITUDINAL STRAIN DISTRIBUTION ALONG THE THREE FBG SENSORS, AND B) LONGITUDINAL STRAIN OBTAINED BY THE GA. ....174

FIGURE 5.17 REFLECTED SPECTRUMS OF THE UNDISTURBED FBGs (DOTTED LINE) AND THE REFLECTED SPECTRUM OF THE THREE PERTURBED SENSORS BY A NON-UNIFORM DISTRIBUTION OF TEMPERATURE ALONG A SERIES OF THE THREE IDENTICAL PANDA FBGs.....175

FIGURE 5.18 ORIGINAL SPECTRUM AND THE ONE OBTAINED FROM THE OPTIMAL SOLUTIONS FROM GA FOR A) THE FIRST SENSOR, B) THE SECOND SENSOR, AND C) THE THIRD SENSOR OF A SERIES OF PANDA FBGs OF THE MULTIPLEXED SENSOR SYSTEM IN FIGURE 5.10. ....176

FIGURE 5.19 A) APPLIED TEMPERATURE DISTRIBUTION ALONG THE THREE FBG SENSORS, AND B) TEMPERATURE DISTRIBUTION OBTAINED BY THE GA. ....177

## List of Tables

TABLE 3.1 PARAMETERS OF A 1-CM FBG SENSOR.....	90
TABLE 3.2 PARAMETERS OF THE GENETIC ALGORITHM. ....	91
TABLE 4.1 PARAMETERS OF THE HI-BI FBG.....	135
TABLE 5.1 PARAMETERS OF THE PANDA FBG. ....	162

## List of Symbols and Abbreviations

FBG	Fiber Bragg Grating
Hi-Bi	High Birefringence
T-Matrix	Transfer Matrix Formulation
GA	GeneticAlgorithme
PM	Polarization Maintaining
SM	Single Mode
SHM	Structural Health Monitoring
RMS	Root Mean Square
SVEA	Slow Varying Enevelop Approximation
SAPs	Stress Applying Parts
TDM	Time Division Multiplexing
CMT	Coupled Mode Theory
CFRP	Carbon Fiber Reinforced Plastic
FEM	Finite Element Method
PDL	Polarization Dependent Loss

# Chapter 1

## Introduction

### 1.1 Motivation and Applications

Composite materials are becoming very popular for use in various structures that need to be lightweight, yet strong in even severe loading conditions such as aircraft, automobiles, and even civil infrastructures such as pipelines and bridges. In particular, in aerospace industry, modern airliners use significant amount of composites to achieve lighter weight. For instance, about ten percent of the structural weight of the Boeing 777 is composite material. The Boeing 787 Dreamliner is the world's first major airplane that uses composite material for most of its structure. Boeing has announced that as much as 50 percent of the primary structure, including the fuselage and wings, of the 787 is made of composite materials [1]. This can contribute to the use of less fuel per passenger than the airplanes with metallic material, fewer carbon emission and quieter take offs and landings. Other example is airbus A380 that contains more than 20% composite materials. Their use can significantly reduce the weight of the vehicle structure.

The issue with composite structures is that they are susceptible to hidden damages that are not easily detectable. The hidden induced damage can greatly reduce both the strength and the stiffness of the given structure. This has spurred a broad interest in the structural health-monitoring (SHM) field with the goal of detecting the occurrence of any damage before the structures safety is compromised.



SHM refers to the process of implementing the damage detection strategy to determine the state of the monitored structure's health. The SHM process consists of three main different steps:

- Observation of the monitored structure with sensors.
- Extraction of data from the sensors with the data acquisition hardware.
- Statistical analysis of the data with the software and interpreting the results in terms of the health of the structure.

The current evolution in SHM field is mostly due to the improvement of sensor technology and the mathematical algorithms that are used to interpret the data that are obtained from the sensors. The existing popular sensors in the industry include piezoelectric, fiber-optic, strain gages, accelerometer, and ultrasonic sensors.

Each sensor has its own advantages and disadvantages and can be used depending on the applications. Most important needed characteristics for the sensors that are used in SHM can be listed as:

- The ability to embed or mount the sensors into the composite structures and metals without affecting the integrity of the monitored structure.
- Maintaining the performance of the sensor system when it is distributed over a large monitored area.
- Immunity of the sensor to any external parameter other than the one that it is sensing.

Among the sensors that are currently used in health monitoring applications, fiber optic sensors have proven to be a good candidate for health monitoring of structures in aerospace and civil industry due to their unique characteristics [2, 3]. Among the reasons, their small size, flexibility, and their low weight can be named.

In particular, optical fiber Bragg grating (FBG) sensors have been attracting the interest of health monitoring applications given their capability to measure a number of parameters such as the strain, the temperature, and the pressure, etc. In addition, due to their multiplexing capabilities, FBGs can be used for monitoring a large area using multi-point sensing arrays.

There are numerous superior qualities that make FBG sensors suitable for some specific health monitoring applications. They are immune to electromagnetic wave and even lightening interference and can be directly mounted on top or integrated inside the composite materials, which are widely used in modern structures. In addition, FBG sensors can measure high strain up to 10,000 micro-strain and can be used for highly stressed composite structures [4]. FBG sensors have high corrosion resistance and since there is no electrical power necessary in their structure, they can be positioned in high voltage and potentially explosive areas [5, 6].

The number of applications that use fiber Bragg grating (FBG) sensors for health monitoring applications is enormous. Some of the applications which necessitate the development of fiber Bragg grating sensors in aerospace are aircraft structures, spacecraft and airships in which the FBG sensors can be implemented on top or be embedded inside the composite material structure due to their size and light weight. In energy industry, the multiplexing ability and electrical and electromagnetic wave insulation characteristic of

FBGs make them a perfect candidate for health monitoring of power generators, transformers, switches, wind power stations, superconductors and nuclear fusion [7, 8]. In [9] more applications are mentioned such as railway overhead contact lines and railway pantographs where electrical insulation is very important. There has also been a significant amount of research on the application of FBG sensors in geotechnical and civil engineering, coal mining, petrol and gas exploration, rock bolts and anchors due to their multiplexing characteristics [10-13].

Recently, the use of FBG in robotic systems has also been explored [14-16]. The use of FBG as a tactile sensor has become a promising field for robotic applications where a new sensing approach is desirable for applications that require immunity to electromagnetic fields. The potential of the FBG sensors for detecting the texture and temperature can open a promising set of applications for the next generation of information collection.

Despite the peculiar advantages of FBGs, the progress in introducing and applying the FBG sensors to real life applications such as monitoring the aerospace vehicles and civil structures has been few and limited. The lack of standard system for the fiber Bragg gratings can hinder this class of sensors to compete with the standardized sensors that are available in the market with high production and low cost.

Another common issue with using FBG as a sensor is that, since both temperature and strain results in the shift in the Bragg wavelength, it is not possible to separate the effects of the temperature and strain from a single shift of the Bragg wavelength.

A different challenge emerges when the FBG sensor is used for the measurement of the strain in more than one direction. In general, in order to investigate the three

dimensional state of the strain the sensors are embedded in different directions in the composite which is proven to be complicated and impractical[10, 17].

Furthermore, there is still difficulty in the interoperation of the response of the FBG sensor when it is subjected to a non-uniform distribution of the anomaly. In general, the focus of FBG sensing is mostly on the effects of the uniform applied strains along the length of the sensor. However, when the anomaly is not distributed uniformly along the sensor, the reflected spectrum breaks up to several peaks and becomes heavily distorted. This mostly happens in real applications when the sensors are embedded inside the monitored structures [17] or as a result of residual stresses that are generated during the manufacturing process [17]. The orientation of the FBG sensor with respect to the reinforcing fibers in adjacent plies, asymmetric loading, local micro-bending, and debonding over the region of the grating can also influence the reflected spectrum of the sensor and make it distorted [19, 21]. The detection of the anomaly distribution along the sensor from its reflected spectrum can enhance the capabilities of the FBG sensors for health monitoring applications. In summary, the challenges encountered for health monitoring applications that use the FBG can be listed as:

- Lack of standards for FBG sensors.
- Cross sensitivity between the effects of the temperature and strain to the sensor.
- Difficulty in analyzing the reflected spectrum of the sensor when it is subjected to the strain along more than one axis.
- Difficulty in detection of the anomaly information from the reflected spectrum of the sensor when the spectrum is distorted and deformed due to non-uniform distribution anomaly along the fiber.

In the next section the literature review on the use of the FBG as a sensor and the above mentioned challenges are discussed.

## **1.2 Literature Review**

The published literature works have shown that the FBG is a promising sensor for temperature and strain sensing applications. In the following sections, we list and discuss the research works that have been conducted on the study of the response of the fiber Bragg grating and Bragg grating written into high birefringence fiber to the uniform and non-uniform distribution of longitudinal strain, multi-axial strain, transversal load, and temperature change. The published works on the identification of the anomaly with FBG sensors are also discussed.

### **1.2.1 Single Mode FBG**

#### **1.2.1.1 Effect of the Longitudinal Strain on an FBG Sensor**

If the strain is uniform along the gauge length of the FBG, all the grating parameters along the sensor experience the same perturbation. Due to the elongation of the sensor (which results in the change in the grating pitch), and the change in the refractive index (due to the photo-elastic effect) the Bragg wavelength gets shifted from its initial value. The wavelength shift has been used extensively in the literature as a tool for measuring the applied longitudinal strain to the monitored substrate. In 1997, Kersy *et al.* [21] and Hill and Meltz [22] have shown experimentally that, at a constant temperature, the Bragg wavelength ( $\lambda_B$ ) of 1300 nm shifts 1 nm when the sensor is subjected to the strain ( $\varepsilon$ ) of 1000 micro-strain.

In other words, the measured strain response was found to be

$$\frac{1}{\lambda_B} \frac{\delta \lambda_B}{\delta \varepsilon} = 0.781 \times 10^{-6} \mu\varepsilon^{-1} \quad (1.1)$$

In a case where the longitudinal strain is not uniform along the FBG sensor, its reflected spectrum not only gets shifted but gets distorted as well [23-27]. The information about a non-uniform strain distribution along the length of the sensor is encoded in the grating reflection intensity and phase spectrum.

LeBlanc *et al.* have obtained the strain distribution profile along the length of the sensor from the intensity of the reflected spectrum [24]. However, their technique is only valid when the strain profile is monotonic.

Volanthen *et al.* [25] have presented the first measurement of a non-monotonic arbitrary strain profile. The non-uniform strain within an FBG was detected by interrogating short sections of the fiber using low coherence reflectometry and using a wavelength tunable grating as a reference. The strain gradient was obtained against the distance measurement. The setback of this method, besides the complexity of the hardware, is the trade-off between the strain resolution and spatial resolution.

The inverse methods [26-33], as an alternative for the experimental methods, shows great potential for detecting a non-uniform strain profile with spatial resolution of 1 mm or better. The inverse approach is based on calibrating the parameters of a mathematical model to reproduce observations. Several inverse methods have been proposed in the literature for reconstructing the grating parameters of the FBG from its corresponding reflected spectrum [26-33]. A Fourier transform method for the synthesis

of the grating parameters has been developed, but it is limited to low reflectance sensors (reflectivity below 30%) and requires both the intensity and the phase spectra [26]. Feced *et al.* [27] presented a layer-peeling method which is an efficient inverse method that takes into account the multiple reflections inside the grating. An exact solution of the inverse problem can be obtained by the coupled integral equations derived in scattering theory by Gel'fand-Levitan and Marchenko (GLM). However these equations can only be solved when the reflection coefficients are written as a rational function. This limitation can be overcome by an iterative solution of the GLM equations but the mathematical complexity of the solution is high [28, 29].

All the above mentioned methods use both amplitude and phase of the spectral response to recover the grating properties. This would limit the applications of such methods because in order to obtain the phase spectrum, an interferometric detection scheme has to be used in a stable thermo-mechanical environment during the measurement. Inverse methods, such as the simulated annealing (SA) [30] and genetic algorithm (GA) [31, 32], can retrieve the grating parameters based on only the amplitude spectral. However, the simulated annealing method has the tendency to become slow when the number of parameters increases. Skaar and Risvik and Cormier *et al.* developed genetic algorithms (GA) for the solution of the Bragg grating physical parameters which can retrieve the grating parameters based on only the amplitude spectra [32, 33].

In addition to the strain, the fiber Bragg grating response is also sensitive to the temperature changes. In the following paragraphs, a literature review is given on the study of the effects of the temperature changes on an FBG.

### **1.2.1.2 Effects of the Temperature Changes on an FBG Sensor**

The thermal response of an FBG sensor arises due to the thermal expansion of the fiber and its refractive index dependence to the temperature. It has been shown that the temperature sensitivity of a bare fiber is mostly due to the thermo-optic effect [35, 37]. In silica FBGs, the change in the Bragg wavelength is mostly dominated by the refractive index change, which accounts for the 95% of the Bragg wavelength shift [36]. The effects of the grating period on the Bragg wavelength shift are almost negligible. In 1997, Rao *et al.* have demonstrated a four FBG temperature sensor system with a resolution of 0.1 °C for medical applications [38]. It is shown that a typical value for the thermal response of an FBG with Bragg wavelength of 1550 nm is 0.01 nm/ °C and at higher temperature the response becomes slightly nonlinear [38].

There are a handful of studies on the effects of a non-uniform temperature on an FBG sensor. In 2006, Chapeleau *et al.* have measured the temperature gradient along a chirped FBG sensor by combining the optical low coherence interferometry and the layer peeling algorithm. The theoretical temperature gradient measurement was compared with the one that was obtained by thermocouple and the agreement was excellent [39].

Temperature change like strain change results in the Bragg wavelength shift. Therefore, when the source of the perturbation is unknown, the wavelength shift can be due to either or both of the temperature and strain changes.

In the next section, the literature review on the investigation of the cross sensitivity between the temperature and the strain effect is presented.



### **1.2.1.3 Simultaneous Strain and Temperature Measurements with Fiber Bragg Grating**

One of the problems with using the FBG as a sensor is that the single measurement of the Bragg wavelength shift cannot help us to distinguish between the effects of the temperature and the strain. In this case, any change in the wavelength of the disturbed sensor can be due to the sum of the mechanical deformation and the temperature changes [40].

Many studies have been conducted on the discrimination of the strain and the temperature. However, most of the proposed schemes require two independent measurements with two gratings. Dual wavelength superimposed gratings [41], hybrid Bragg grating/long period grating and two spliced gratings in different doping sections are the examples of the measurement of temperature and strain with a fiber with two different gratings [42]. The most straightforward way is the use of two identical FBGs when one of them is immune to any strain change. This FBG sensor is located in the same thermal environment as the strain sensor. The strain can be obtained by subtracting the wavelength shift of the temperature sensor, which is insensitive to any strain, from the strain sensor [43].

Another method for discriminating between the strain and the temperature is the use of dual-wavelength superimposed FBG. The sensor is produced by writing two sets of grating written at the same location in the fiber. The temperature and the strain can be obtained from the two Bragg wavelength shifts and the information on the strain and the temperature sensitivities of the FBG [41, 43].

Another issue with analyzing the reflected spectrum emerges when the sensor is subjected to the strain along more than one axis. Currently, FBGs are mostly used for measuring the strain along the length of the sensor. However, in health monitoring applications, it is usually necessary to analyze the subjected perturbation for more than one axis.

Recently, in addition to characterizing the spectral response of an optical fiber Bragg grating subjected to the axial strain, theoretical and experimental studies on the effects of the transversal force on an FBG sensor have also been developed.

The literature review on the study of the effects of transversal loads on the behavior of the Bragg wavelength of the FBG sensors is presented in the next section.

#### **1.2.1.4 Effects of the Transversal Load on an FBG Sensor**

The Bragg spectrum of the sensor that is affected by the transversal load splits and alters into two distinct Bragg wavelengths [44-48]. In 1996, Wagreich *et al.*[44] studied theoretically and experimentally the effects of the diametric load (up to 90 N) on a 2.5 cm long Bragg grating that was fabricated into a single mode low birefringence fiber. The results showed that the Bragg wavelength of the disturbed sensor changes as the transversal load increases. It has also been observed that the bifurcation becomes observable for loads larger than 40 N.

Similarly, Okabe *et al.* have investigated the response of an FBG to various tensile stresses and have shown that the reflected spectrum bandwidth at half maximum is a good indicator for quantitative measurement of the transversal crack density [20].

In 2000, Gafsi and El-Sharif[45]have reported a thorough study on the birefringence effects on an FBG when the grating zone was subjected to a static

transversal load in the case of plane stress (normal stress is zero) or plane strain (longitudinal strain is zero). They have modeled the disturbed reflected spectrum using the coupled-mode theory. The results show that the wavelength variations for the slow axis (direction having a high index of refraction) are larger than for the fast axis (direction having a slow refractive index) [45].

In 2002, Guemes and Menendez [46] have experimentally shown that the transversal load on an FBG results in the split of its Bragg spectrum and the bandwidth between the two peaks provides data about the transversal load. Consequently, Caucheteur *et al.* have demonstrated the use of polarization dependent loss (PDL: The power loss in selective directions due to the spatial polarization interaction) generated by the FBGs for transversal strain measurement with small values, which is not directly possible through amplitude measurement. The transversal strain measurement in the range of 0-250 N is possible with this temperature-insensitive technique. The experimental results were confirmed by theoretical simulation results using the couple mode theory and the Jones formalism [47].

Few studies have been performed on the study of the response of an FBG to a non-uniform transversal load along its length. In 2006, Prabhugoud and Peters[48] predicted the spectral response of an embedded fiber under non-uniform field of transversal load by finite element (FE) analysis. Although the response of an FBG due to the applied load was modeled, the inverse problem of reconstructing the anomaly was not solved. In 2008, Wang *et al.* have characterized, both experimentally and theoretically, the response of an FBG sensor when it is subjected to non-uniform transversal load. Their

results showed that the transversal strain gradient along the fast axis would result in distinguishable bifurcation of spectrum for the slow axis [49].

In general, the detection of the anomaly depends on the bifurcation of the reflected spectrum due to the transversal load, which mostly becomes observable for larger loads [49]. This would put a limitation on detecting the small transversal loads with the conventional single mode FBGs.

In order to measure the transversal loads with smaller values, recent reported works have employed Bragg gratings fabricated in a high-birefringence (Hi-Bi), polarization-maintaining (PM) fiber where the initial peak separation due to the induced birefringence during the fabrication of the fiber already exists.

The performed studies on exploring the potentials of Hi-Bi FBGs for multi-axial strain measurements are discussed in the next section.

## **1.2.2 High Birefringence Fiber Bragg Grating Sensors**

Bragg gratings fabricated in high birefringence (Hi-Bi) polarization maintaining (PM) fibers (Hi-Bi FBG) have been proposed as an ideal sensor for the detection of the stress and multi-component strain in composite materials. The following sections present the literature review on the studies on the effects of the transversal load, the multi-axial load and the temperature changes on Hi-Bi FBGs.

### **1.2.2.1 Effects of the Transversal Load on the Hi-Bi FBG**

There are a number of studies on the relationship between the transversal load and the birefringence of different classes of Hi-Bi FBGs. These studies have mainly focused on the Bragg gratings fabricated into the elliptical cladding and bow-tie fibers [50-53]. In

1999, Lawrence *et al.* [54] presented a transversal sensor that is formed by writing a Bragg grating into a high birefringence, PM optical fiber consists of a circular core and inner cladding surrounded by an elliptical stress applying region. The sensor could simultaneously measure two independent components of transversal strain from the two reflected Bragg wavelengths corresponding to the two orthogonal polarization modes of the fiber. The axial strain and temperature changes in the fiber were considered as either zero or known. Their results showed that for all of the load cases that were observed, the sensor response was linear to the load unless the angle of the applied load was not aligned with the intrinsic polarization axes of the fiber. The nonlinearity was observed mostly for the higher load levels, and the nonlinearity was insignificant for the lower transversal strain levels.

In 2004, Chehura *et al.* have experimentally investigated the transversal and temperature sensitivities of fiber Bragg grating sensors that were fabricated in a range of commercially available stresses and geometrically induced PM FBGs [55]. The sensors were subjected to transversal loads at various orientations. They have shown that the transversal load sensitivity of the FBG sensor for slow axis is higher than that for the fast axis. Moreover, their results showed that PM FBGs fabricated in elliptically clad fiber have the highest transversal load sensitivity among other FBGs. This can make elliptically clad FBGs a good candidate for transversal strain measurement with high resolution.

In 2010, Botero *et al.* [56] have studied the dependency of the spectral response of an FBG written into the Panda PM fiber under a diametrical load. The results of their experimental and numerical solutions have shown that the bandwidth between the two

reflected peaks of the spectra is dependent on the magnitude and the angle of the applied force over the optical fiber.

There are a very few number of studies on the non-uniform effects of transversal strain fields on PM fiber Bragg gratings [57-60]. In these works, although the spectrum of the disturbed sensor is predicted, the inverse problem of obtaining a non-uniform distribution of the strain from the spectrum has not been solved.

In configuration that is closer to real applications it is important to determine more than one component of the strain. In the following paragraphs the literature review on measuring the multi-axial load is discussed.

#### **1.2.2.2 Effects of the Multi-Axial Load on an Hi-Bi FBG**

Hi-Bi FBGs have been proposed as an ideal sensor for the detection of the strain along the three axes of the fiber. In 2002, Udd *et al.* and Black *et al.* have used a multi-axis fiber Bragg grating sensor for the detection of axial strain, transversal strain and transversal strain gradients in composite weave structures [50, 51]. They have observed the occurrence of the strain gradients during curing although no quantitative analysis was performed. In 2003, Bosia *et al.* have demonstrated the feasibility of diametrical and multi-axial strain measurements with a Bragg grating fabricated into the bow-tie type PM fiber both experimentally and theoretically [61].

It has been shown that the multi-axial strain measurement can also be achieved by fabricating two superimposing FBGs in a high birefringence fiber. In 2004, Abe *et al.* [62] have measured the longitudinal, transversal strain and temperature simultaneously by a pair of superimposed FBGs written in a Hi-Bi fiber. In 2008, Mawatari and Nelson have described a model for prediction of the longitudinal and two orthogonal transversal

strain components from the measured reflection peak of Bragg peaks that is observed in combined loading tests. They have used a three by three matrix model for prediction of the tri-axial strain combinations from the measured wavelength shifts. Like strain, the temperature change affects the Bragg peaks of the Hi-Bi FBG. The following section explains the literature review that has been conducted on the effects of the temperature changes on the reflected spectrum of a Hi-Bi FBG.

### **1.2.2.3 Effects of the Temperature on a High Birefringence Fiber Bragg Grating Sensor**

There are few studies on the effects of temperature changes on the response of a Hi-Bi FBG. In 2004, Chehura *et al.* have characterized the response of a Hi-Bi FBG to the temperature by placing the sensor in a tube furnace, which was isolated from any applied strain [55]. Six types of Hi-Bi FBG were fabricated and tested for the measurements. The results showed that the Bragg wavelength changes corresponding to the slow and fast axes of the fibers are linear to the change of the temperature but do not have the same sensitivity to it. It was found that in contrast to the transversal strain results, the fast axis of the Hi-Bi FBG is generally more sensitive to the temperature than the slow axis.

In addition, they have shown that the stress induced FBGs have higher sensitivities to temperature than those that were fabricated geometrically. This is found to be due to the release of thermal stress that was frozen internally in the Hi-Bi fiber during its fabrication. This can add to the temperature sensitivity of the stress induced Hi-Bi fibers. Furthermore, they have shown that the FBGs that were fabricated in a Panda fiber were the most sensitive to the temperature. However, the elliptical clad fiber showed the

greatest differential temperature sensitivity between the Bragg wavelengths corresponding to the two polarization axes. Luyckx *et al.* have performed a temperature calibration for detecting the sensitivities of the fast and slow axes of a Bow-Tie FBG. The difference between the sensitivities of the fast and slow axis was detected to be  $\pm 0.4$  pm/ $^{\circ}$ C [64]. In the applications where both the strain and the temperature are applied to the FBG sensor fabricated in a single mode or Hi-Bi FBG, the identification between the two effects can be challenging. The following section lists the studies on the discrimination between the temperature and the strain when they are applied simultaneously to the FBG sensor.

#### **1.2.2.4 Discrimination between the Temperature and Strain Effects on the Hi-Bi FBG**

In 2008, Mawatari *et al.* have used a PM optical fiber with Bragg gratings created at two different wavelengths for measuring the three strain components and temperature changes simultaneously [63]. The combination of the double grating and birefringence creates four peaks that were shifted when loading is applied or temperature changes. In other words, the availability of four wavelength peaks allows the determination of four parameters, i.e. strain, temperature and two normal axes of the stress due to the loading. However, superimposing two Bragg wavelengths in a fiber increases the complication of the fabrication and computation.

Single Bragg gratings written in a Hi-Bi optical fiber were demonstrated to be a good candidate for the simultaneous measurement of temperature and strain. In 1997, Sudo *et al.* have simultaneously measured the temperature and the strain using a fiber



grating written in a Panda fiber [65]. Since each polarization axis have a different dependence on temperature and strain, the simultaneous measurement of the two anomalies was obtained from a pair of measured Bragg reflection wavelengths. The difference of sensitivities to temperature for the slow and fast axis was obtained to be 0.095 nm/C° and 0.0101 nm/C°, respectively. The strain sensitivities of the polarized axes modes were calculated with a small difference of 0.001342 (nm/μ $\epsilon$ ) and 0.001334 (nm/μ $\epsilon$ ) for the slow and fast axis, respectively.

The same idea was demonstrated in 2003 by Chen *et al.* for the simultaneous gas pressure and temperature measurement using a novel Hi-Bi fiber Bragg grating sensor [66]. Their fabricated fiber had a high birefringence of  $7.2 \times 10^{-4}$  compared to the Panda fiber which is  $4.5 \times 10^{-4}$ . Due to the large Bragg wavelength separation which is 0.77 nm for this novel sensor, this sensor can principally have a wider range for measuring the temperature and the pressure as compared to other Hi-Bi FBGs. The results showed that the fast and slow axis Bragg modes shift linearly with temperature and gas pressure change.

In 2004, Oh *et al.* demonstrated a new technique to discriminate the effect of the temperature and strain on a sensor by measuring the Bragg wavelength shift and the changes of polarization dependence loss (PDL) when the birefringence of the fibre is low in the order of  $10^{-6}$ . The problem with this method is that the measurement system setup needs to measure both the PDL and the transmission spectrum which makes the measurement setup more complicated [67].

## 1.3 Problem Statement

In health monitoring studies, realistic information about a non-uniform distribution of the anomaly is very difficult to obtain. The conventional method for obtaining the magnitude of the perturbation with FBGs, which is usually obtained by measuring the Bragg wavelength shift of the disturbed sensor, fails to detect and model the perturbation non-uniformity along the sensor. In modeling the perturbation distribution inside the monitored structures, the main challenge is to adopt a method to reconstruct the perturbation distribution from the output of the monitoring sensor. The first task of this work is focused on the detection of distribution and severity of the strain, stress and temperature changes inside the monitored structures from the output of the sensor.

For sensing applications, it is also very important to detect the anomaly in more than one direction. Fig. 1.1.a shows an “orthogonal array” of fiber Bragg gratings which is the most convincing solution for positioning and measuring the anomaly in two principal directions. According to Fig. 1.1.a, Bragg gratings are inscribed in series along the optical fibers, which are embedded longitudinally and transversally in the material. As a result, the anomaly can be positioned and monitored in two orthogonal directions by corresponding FBG sensors based on the gratings sensitivity. The model in Fig. 1.1.a can be greatly improved by detecting the two dimensional anomaly (longitudinal and transversal) with a series of sensors in one dimension. This would considerably reduce the complexity of the hardware and the measurement time.

The second task of this thesis is focused on the study of the effects of a non-uniform distribution of the simultaneously applied longitudinal and transversal loads on a single FBG.

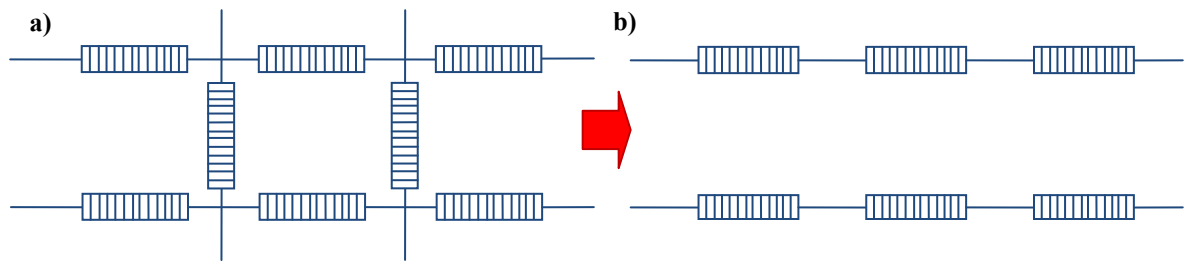


Figure 1.1 Schematic model of a) orthogonal FBG sensor array, and b) series of FBG sensors.

Another problem in using FBG as a sensor is that a single measurement of the Bragg wavelength shift cannot help us to distinguish between the effects of temperature and the strain. Thus, in recent studies, Bragg gratings fabricated into high birefringence fiber (Hi-Bi FBG) have been employed for the identification and discrimination between the temperature and the strain.

As to the third task of this thesis, the effects of the temperature and the strain to the Hi-Bi FBG are studied theoretically and the non-uniform distributions of the anomaly along the sensor are reconstructed.

## 1.4 Methodology

Realistic internal anomaly information of the composite materials is very difficult to obtain. The conventional techniques fail to detect the profile of a non-uniform anomaly inside the monitored structures. The non-uniform profile of the anomaly along the FBG sensor would result in the distortion of its reflected spectrum. There is no direct methodology to conform the distorted spectrum to the applied anomaly. Iterative methods

offer a promising alternative to correlate the perturbation within the sensor with its distorted reflected spectrum.

We have adopted an inverse approach [77] for obtaining a non-uniform distribution of anomaly from the reflected spectrum of the Bragg grating sensors. The problem of reconstruction of a non-uniform distribution of anomaly is formulated by studying the effects of the transversal load, longitudinal strain, simultaneously applied longitudinal strain and transversal load, and temperature to the sensor and modeling the reflected spectrum of the sensor theoretically.

Moreover, an inverse approach based on the genetic algorithm (GA) is proposed for reconstructing a non-uniform applied anomaly from the reflected spectrum of the sensor. The amplitude of the reflected signal (that is obtained by the T-matrix formulation in this study) is sufficient for the GA to model the distribution of the anomaly. In addition, the GA starts the search for the best answers from a large possible set of solutions, which can prevent the algorithm from converging to a local minimum. Therefore, the GA is an excellent inverse method for reconstructing the anomaly.

We will show that the algorithm can effectively model a non-uniform distribution of the longitudinal strain, transversal load, two dimensional strain, and temperature along the Bragg grating fabricated into a single mode and high birefringence fiber. The initial population used in the genetic algorithm is chosen from the grating periods or the refractive indices along the Bragg grating. The algorithm converges to the best solution when the successive iterations can no longer produce better results. The obtained information about the changes along the sensors can then be used to model the anomaly

inside the monitored structure. The proposed approach is validated by several numerical examples.

## 1.5 Basic Assumptions

The modeling and reconstructing of the anomaly involve some assumptions, which are clarified in this section.

The optical behaviour changes of the embedded sensor whenever embedded in the material are not counted in this research. Although, one must recognize that the sensor is regarded as a foreign entity to the host structure and its optical behaviour alters whenever embedded in the material.

In addition, for studying the response of the grating that is fabricated into the high birefringence fiber, the correct orientation of the fiber when being embedded in a host material is important to be known as a *priori* information. Bad orientation of the embedded fiber can lead to big errors. In this thesis, the applied transversal load to the fiber is assumed to be in parallel with the main polarization axes of the fiber.

Furthermore, the derivation of the anomaly from the reflected spectrum of the high birefringence FBG is based on the assumption that the power of reflected spectra corresponding to the polarization axes of the sensor are equal and are normalized to unity.

While it is shown subsequently that the anomaly profile can be determined analytically, the inverse problem, in general, for a highly non-uniform anomaly distribution may have more than one solution. In this case, by incorporating some *a priori* knowledge one can ensure that a unique solution is selected. For the GA algorithm, the

uniqueness can be achieved by assuming that for example the first segment has a strain value higher or equal to that of the final segment before the first iteration is performed.

## **1.6 Contribution of the Thesis**

The main contributions of this thesis are as follows:

- Analysis of the transversal strain load profile by using single mode fiber Bragg grating sensor and genetic algorithms

We studied the effects of a non-uniform distribution of the transversal load on a single mode FBG theoretically. The strain distribution sensing approach is developed to inversely trace the transversal strain distribution from the reflected spectrum of the disturbed FBG sensor.

Our proposed methodology can readily analyze the trend line of the highly nonlinear transversal strain distribution along the sensor. This would allow the use of the FBG sensor near critical areas such as bond joints for the detection of a non-uniform distribution of transversal cracks.

- Non-uniform transversal and longitudinal strain profile reconstruction by using fiber Bragg grating sensor and genetic algorithms

The reflected intensity spectrum of the FBG sensor, which is affected by an arbitrary non-uniform distribution of the simultaneously applied transversal and longitudinal forces, is modeled theoretically. The study of the effects of the two dimensional (i.e. transversal and longitudinal) forces on an FBG sensor would eliminate the need for the

FBGs to be installed on both orthogonal directions inside the monitored surface. Consequently, the applied strain measurements can be achieved by parallel fibers in one direction.

The axial strain and transversal load gradients along the sensor's length is determined from the intensity spectrum of the sensor by means of a genetic algorithm population-based optimization process. The methodology can be applied for studying the residual strains, internal strain distribution, and crack propagation inside the monitored structure by obtaining the strain/stress field in the surrounding material of the sensor.

- Analysis of the transversal load and longitudinal strain change non-uniform distribution along the FBG sensor fabricated into the high birefringence fiber

In order to measure the transversal loads with smaller values, we have developed an approach to detect the transversal load distribution from the reflected spectrum of the Bragg gratings that is fabricated into a high-birefringence (Hi-Bi), polarization-maintaining (PM) fiber. The non-uniform distributions of the longitudinal and transversal strains were inversely obtained from the polarized reflected bands corresponding to the main polarization axes of the fiber. The results demonstrate the efficiency of the approach for detection of small transversal load values with high gradients. The results demonstrate the use of the presented approach as a powerful tool in the field of force sensing.

- A developed approach based on the GA for reconstruction of a non-uniform temperature along the Hi-Bi FBG.

A theoretical study was conducted on the behaviour of the Hi-Bi FBG subjected to a non-uniform distribution of the temperature. Furthermore, the applied non-uniform temperature along the Hi-Bi FBG was reconstructed by using the genetic algorithms. The approach enhances the capability of the FBG sensor to be used as a sensor to detect anomaly distribution of closely situated points that differ considerably in temperature.

- A developed approach for the simultaneous measurement of temperature and transversal load

A novel approach for the detection of a non-uniform profile of the temperature and the transversal load when they are applied simultaneously to the Bragg grating that is inscribed in a high birefringence Panda fiber is proposed. The variation of the temperature and strain is detected inversely from the distorted reflected spectrum of the sensor.

It is shown that in addition to detecting the effects of the temperature on the spectrums of the sensor system, the longitudinal and transversal load variations can be obtained from the reflected spectrum of the series of the Panda FBGs.

## **1.7 Organization of the Thesis**

Chapter 2 reviews the Bragg grating sensor fabricated into the single mode or high birefringence fiber and the characteristics of these classes of sensors when they are subjected to the axial strain, transversal load and temperature change. Furthermore, the mathematical tools that are used in this thesis are discussed. Chapter 3 presents the



proposed approach and methodology for the detection of a non-uniform distribution of transversal load, two dimensional strain, and temperature along an FBG sensor. Chapter 4 carries out the calculation of the distribution of the anomaly for the Bragg grating fabricated in the high birefringence fiber. Chapter 5 presents the developed approach for the simultaneous measurement of the strain and the temperature. Chapter 6 gives a conclusion and discusses the potential research topics for the future work.

# Chapter 2

## Fiber Bragg Grating Sensor

This chapter first reviews the fiber Bragg grating sensor and the change in its characteristics when it is subjected to the axial strain, transversal load and temperature change. Next, the characteristics of the Bragg grating fabricated into the high birefringence fiber (Hi-Bi FBG) are reviewed and the response of the sensor to the anomaly is discussed.

Moreover, the mathematical tools for modeling the reflected spectrum of the sensor (T-Matrix) and the inverse method that is used to reconstruct the anomaly (Genetic algorithms) is discussed in details.

### 2.1 Introduction to the Fiber Bragg Grating

Fiber Bragg grating sensors are fabricated by doping a small portion of a bare fiber with Germanium to obtain photosensitive core fiber. A periodically varying refractive index is then induced into the fiber by its exposure to a fringes pattern of ultraviolet (UV) radiation. The resulting structure acts as wavelength selective reflection filter in which its peak reflectivity, known as the Bragg wavelength, is determined by [36]

$$\lambda_B = 2n_{eff}\Lambda_0 \quad (2.1)$$

where  $n_{eff}$  is the effective core refractive index and  $\Lambda_0$  is the grating period as is shown in Figure2.1.

Assuming an optical fiber along the  $z$  axis, the local mode effective index of the refraction that defines the grating is periodic and can be represented by the following periodic function.

$$n_{eff}(z) = n_{eff} + \overline{\delta n_{eff}} \{1 + \zeta \cos[(\frac{2\pi}{\Lambda_0})z + \Phi(z)]\} \quad (2.2)$$

where  $\overline{\delta n_{eff}}$  is the mean mode effective index of the refraction change,  $\zeta$  is the fringe visibility of the index change, and  $\Phi(z)$  describes the change in the grating period along the fiber. The grating period is of the order of hundreds of nanometres.

Both parameters, i.e. refractive index and the grating period, are temperature and strain dependent. Consequently, the temperature and the strain change along the sensor can modulate the reflected Bragg wavelength as given by the following expression [36]

$$\Delta\lambda_B = 2 \left( n_{eff} \frac{\partial \Lambda}{\partial \varepsilon} + \Lambda_0 \frac{\partial n_{eff}}{\partial \varepsilon} \right) \Delta\varepsilon + 2 \left( n_{eff} \frac{\partial \Lambda}{\partial T} + \Lambda_0 \frac{\partial n_{eff}}{\partial T} \right) \Delta T \quad (2.3)$$

Therefore, FBGs can be used as a temperature or strain sensor.

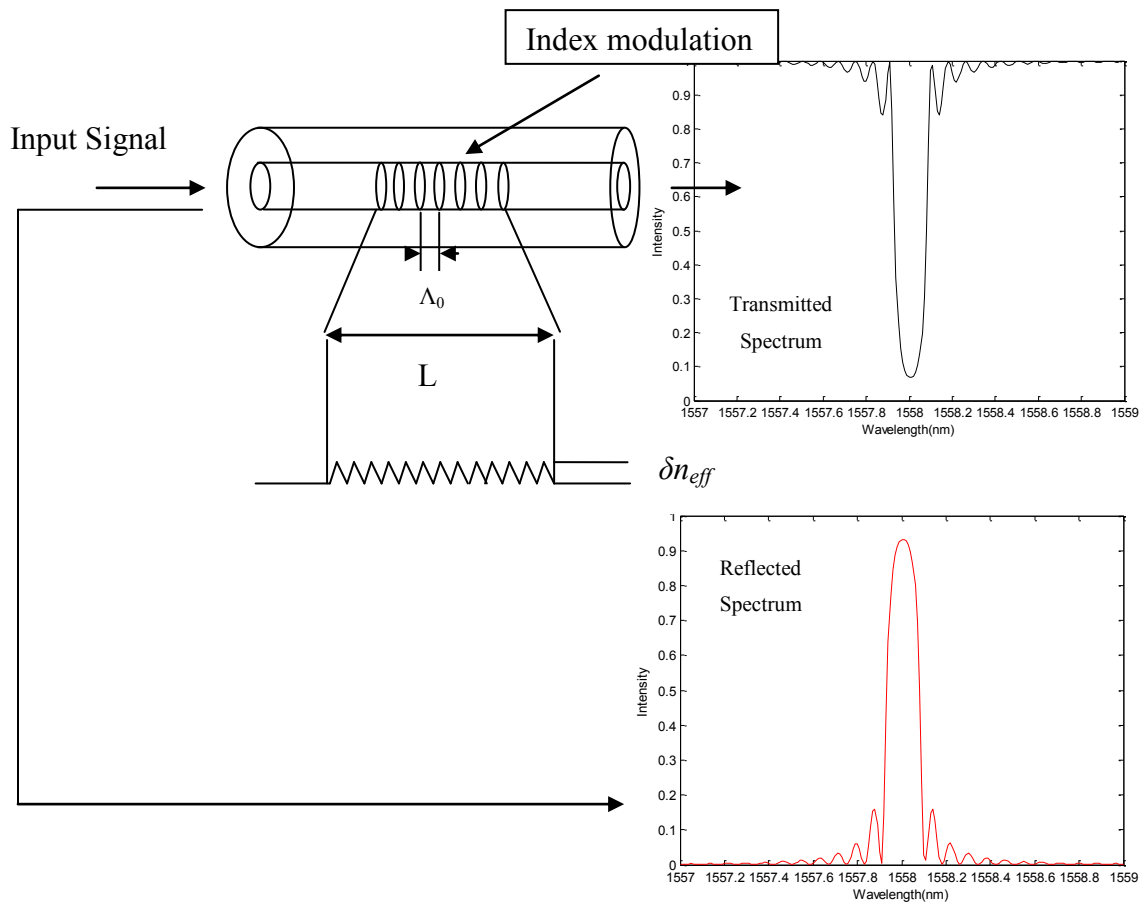


Figure 2.1 Schematic of a fiber Bragg grating sensor and its reflected and transmitted spectrum.

In the following sections 2.1.1 and 2.1.2 we discuss the characteristics changes of the FBG sensor when it is subjected to the strain and the temperature changes.

## 2.1.1 Characterization of an FBG Sensor Subjected to an Axial or/and Transversal Load

One of the main attractive applications of the FBG sensor in industry is its ability to detect and measure the subjected strain and stress to the monitored substrate.

The first part of this section discusses the change in the characteristics of the fiber when it is subjected to the uniform and non-uniform longitudinal strain along its length. Subsequent to that, the characteristic changes of the fiber when it is subjected to a uniform and non-uniform distribution of transversal load are then discussed.

Figure 2.2 shows the schematic of an FBG sensor that can be mounted on top and inside the monitored substrate in order to investigate the effects of the transversal and axial load to the structure. The coordinate system that is shown in Figure 2.2 is used as the reference throughout this section.

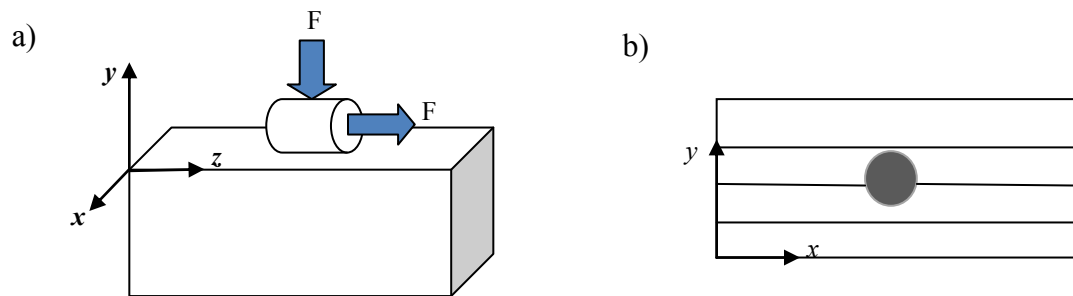


Figure 2.2 Schematic of the coordinate system of the FBG sensor and the applied forces when is mounted a) on top, or b) inside the monitored structure.

The applied strain and stress alter the refractive index and grating period of the FBG sensor and consequently would change its reflected Bragg wavelength (see equation (2.1)). The refractive index changes of an optical fiber induced by the applied strains are called photoelastic phenomena.

The refractive index changes due to the photoelastic effect for a homogenous isotropic material is presented as [68]

$$\begin{bmatrix} \Delta \left( \frac{1}{n_{eff,x}^2} \right) \\ \Delta \left( \frac{1}{n_{eff,y}^2} \right) \\ \Delta \left( \frac{1}{n_{eff,z}^2} \right) \\ \Delta \left( \frac{1}{n_{eff,xy}^2} \right) \\ \Delta \left( \frac{1}{n_{eff,yz}^2} \right) \\ \Delta \left( \frac{1}{n_{eff,zx}^2} \right) \end{bmatrix} = \begin{bmatrix} p_{11} & p_{12} & p_{12} & 0 & 0 & 0 \\ p_{12} & p_{11} & p_{12} & 0 & 0 & 0 \\ p_{12} & p_{12} & p_{11} & 0 & 0 & 0 \\ 0 & 0 & 0 & \frac{p_{11}-p_{12}}{2} & 0 & 0 \\ 0 & 0 & 0 & 0 & \frac{p_{11}-p_{12}}{2} & 0 \\ 0 & 0 & 0 & 0 & 0 & \frac{p_{11}-p_{12}}{2} \end{bmatrix} \begin{bmatrix} \varepsilon_x \\ \varepsilon_y \\ \varepsilon_z \\ \varepsilon_{xy} \\ \varepsilon_{yz} \\ \varepsilon_{zx} \end{bmatrix} \quad (2.4)$$

Where  $p_{11}$  and  $p_{12}$  are the strain-optic coefficients of the optical fiber and  $\varepsilon_x, \varepsilon_y$ , and  $\varepsilon_z$  are the strain components in three principal directions.  $\varepsilon_{xy}$ ,  $\varepsilon_{yz}$  and  $\varepsilon_{zx}$  are the shear stress components for the applied strain to the fiber.

The induced strains in the  $x$  and  $y$  directions of a homogeneous isotropic fiber that is subjected to the longitudinal strain ( $\varepsilon_z$ ) are identical and can be expressed as

$$\varepsilon_x = \varepsilon_y = -\nu \varepsilon_z \quad (2.5)$$

where  $\nu$  is the Poisson's ratio.

Therefore, as can be seen from equations (2.4) and (2.5), the longitudinal strain  $\varepsilon_z$  results in the changes in the refractive index along the fiber which can be expressed as [40]

$$\Delta n_{eff} = \Delta n_{effx} = \Delta n_{effy} = -\frac{n_{eff}^3}{2}[p_{12} - \nu(p_{11} + p_{12})]\varepsilon_z \quad (2.6)$$

In addition, the grating period of the fiber that is subjected to the longitudinal strain changes as

$$\Delta \Lambda = \varepsilon_z \Lambda_0 \quad (2.7)$$

Consequently, the shift in the Bragg wavelength at maximum reflectivity, which is linearly proportional to the uniform axial strain along the length of the fiber, can be measured directly from [36, 40]

$$\Delta \lambda_B = \lambda_B (1 - p_e) \Delta \varepsilon_z \quad (2.8)$$

where  $p_e$  is the effective strain-optic coefficient of the Bragg grating and is given by

$$p_e = \frac{n_{eff}^2}{2}[p_{12} - \nu(p_{11} + p_{12})] \quad (2.9)$$

In the case when the sensor is subjected to a non-uniform strain distribution along its length, the reflected spectrum of the FBG sensor not only gets shifted but gets distorted as well.

Figure 2.3 shows the experimentally measured reflected spectra of a 12 mm FBG sensor with the core refractive index of  $n_0=1.4516$ , main grating period of  $\Lambda_0= 529$  nm and index modulation amplitude of  $\overline{\delta n_{eff}}=10^{-4}$  that is disturbed by the longitudinal strain profiles that are shown in Figure 2.3 (a)[69]. As can be seen from the Figure 2.3, due to the longitudinal strain gradient along the sensor, in addition to the shift of the Bragg wavelength, the shape of the spectrum becomes broadens and gets distorted.

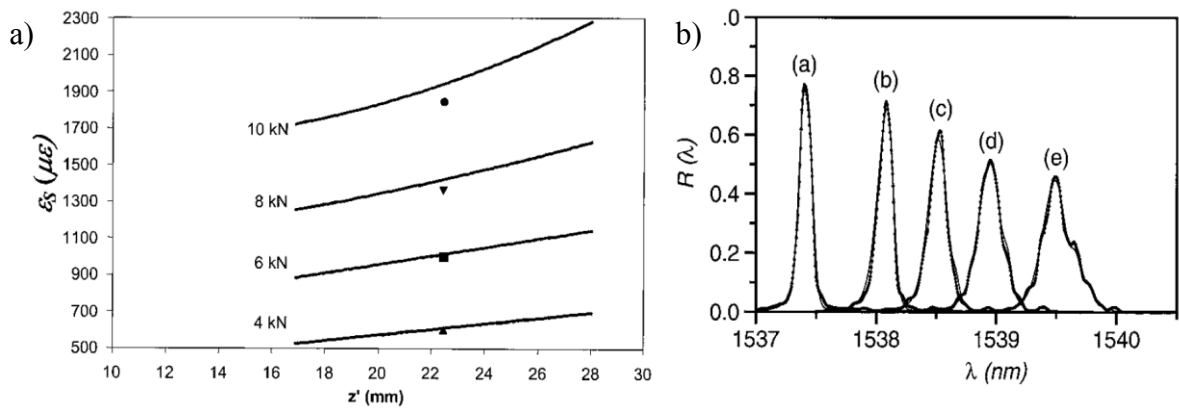


Figure 2.3 a) Strain functions  $\varepsilon(z)$  for different load cases. b) The spectra measured by the optical spectrum analyzer for (a) 0 kN, (b) 4 kN, (c) 6 kN, (d) 8 kN, and (e) 10kN [69].

As can be observed from Figure 2.3, by increasing the longitudinal strain, some peaks appear along the spectrum of the sensor and the spectrum becomes broad and the highest intensity peak becomes small.

The FBG response to the transversal force ( $F$ ) is different from that of the axial force.



The transversal load that is applied along the  $y$  axis of the fiber, as is shown in Figure 2.4, induces stresses along the main axes of the fiber which can be expressed as

$$\begin{aligned}\sigma_x &= \frac{F}{\pi R} \\ \sigma_y &= \frac{-3F}{\pi R}\end{aligned}\tag{2.10}$$

where  $t$  is the length of the fiber and  $R$  is the radius of the cross section of the fiber. The applied load induces deformation to the fiber which results in the refractive index changes and consequently birefringence in the fiber.

The created birefringence due to the transversal load results in two distinct Bragg wavelengths,  $\lambda_{Bx}$  and  $\lambda_{By}$ , corresponding to each of the principal axes ( $x$  and  $y$ ) (see Figure 2.4), which can be written in terms of the induced stresses as given by [45]

$$\begin{aligned}\lambda_{Bx} &= \lambda_B + (\Delta\lambda_B)_x = -\frac{(n_{eff})^3 \Lambda_0}{E} \{(p_{11} - 2\nu p_{12})\sigma_x + ((1 - \nu)p_{12} - \nu p_{11})(\sigma_y + \sigma_z)\} \\ &+ 2\frac{n_{eff}\Lambda_0}{E} \{\sigma_z - \nu(\sigma_x + \sigma_y)\} \\ \lambda_{By} &= \lambda_B + (\Delta\lambda_B)_y = -\frac{(n_{eff})^3 \Lambda_0}{E} \{(p_{11} - 2\nu p_{12})\sigma_y + ((1 - \nu)p_{12} - \nu p_{11})(\sigma_x + \sigma_z)\} \\ &+ 2\frac{n_{eff}\Lambda_0}{E} \{\sigma_z - \nu(\sigma_x + \sigma_y)\}\end{aligned}\tag{2.11}$$

where  $E$  and  $\nu$  are the Young's modulus and the Poisson's ratio of the fiber optic, respectively.

The two distinct Bragg wavelengths are induced by the two different effective refractive indices along the  $x$  and  $y$  axis which can be expressed as [45]

$$\begin{aligned} n_{effx} &= n_{eff} - \frac{n_{eff}^3}{2} \{p_{11}\varepsilon_x + p_{12}[\varepsilon_y + \varepsilon_z]\} \\ n_{effy} &= n_{eff} - \frac{n_{eff}^3}{2} \{p_{11}\varepsilon_y + p_{12}[\varepsilon_x + \varepsilon_z]\} \end{aligned} \quad (2.12)$$

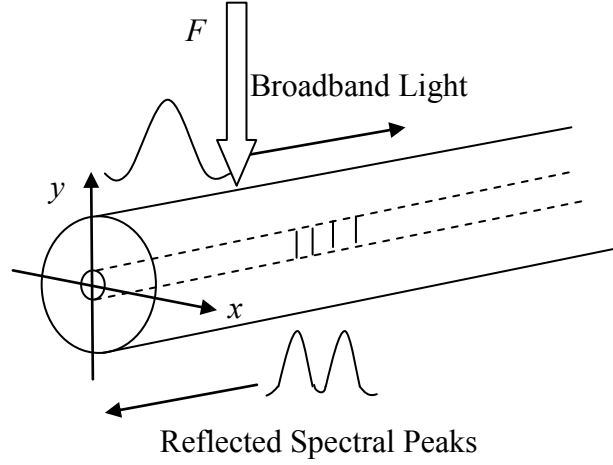


Figure 2.4 Schematic of an FBG sensor that is subjected to the transversal load  $F$  and the input and the reflected spectrum.

The stresses in equation (2.10) are obtained from the plane strain elasticity solution for a disk at the point  $x = y = 0$  which is given by [68]

$$\begin{aligned} \sigma_x &= \frac{-2F}{\pi t} \left\{ \frac{\cos\theta_1 \sin^2\theta_1}{r_1} + \frac{\cos\theta_2 \sin^2\theta_2}{r_2} - \frac{1}{d} \right\} = \frac{-2F}{\pi t} \left\{ \frac{(R-y)x^2}{r_1^4} + \frac{(R+y)x^2}{r_2^4} - \frac{1}{d} \right\} \\ \sigma_y &= \frac{-2F}{\pi t} \left\{ \frac{\cos^3\theta_1}{r_1} + \frac{\cos^3\theta_2}{r_2} - \frac{1}{d} \right\} = \frac{-2F}{\pi t} \left\{ \frac{(R-y)^3}{r_1^4} + \frac{(R+y)^3}{r_2^4} - \frac{1}{d} \right\} \end{aligned} \quad (2.13)$$

where  $t$  is the thickness of the disk,  $d$  is the diameter, and  $R$  is the radius of the disk. The parameters  $r_1$ ,  $r_2$ ,  $\theta_1$  and  $\theta_2$  are shown in Figure 2.5.

The stresses across the fiber are correlated with the strains as given by [68]

$$\begin{bmatrix} \sigma_x \\ \sigma_y \\ \sigma_z \\ \tau_{yz} \\ \tau_{zx} \\ \tau_{xy} \end{bmatrix} = \begin{bmatrix} \frac{E(1-\nu)}{(1-2\nu)(1+\nu)} & \frac{\nu E}{(1-2\nu)(1+\nu)} & \frac{\nu E}{(1-2\nu)(1+\nu)} & 0 & 0 & 0 \\ \frac{\nu E}{(1-2\nu)(1+\nu)} & \frac{E(1-\nu)}{(1-2\nu)(1+\nu)} & \frac{\nu E}{(1-2\nu)(1+\nu)} & 0 & 0 & 0 \\ \frac{\nu E}{(1-2\nu)(1+\nu)} & \frac{\nu E}{(1-2\nu)(1+\nu)} & \frac{E(1-\nu)}{(1-2\nu)(1+\nu)} & 0 & 0 & 0 \\ \frac{\nu E}{(1-2\nu)(1+\nu)} & \frac{\nu E}{(1-2\nu)(1+\nu)} & \frac{E(1-\nu)}{(1-2\nu)(1+\nu)} & 0 & 0 & 0 \\ 0 & 0 & 0 & G & 0 & 0 \\ 0 & 0 & 0 & 0 & G & 0 \\ 0 & 0 & 0 & 0 & 0 & G \end{bmatrix} \begin{bmatrix} \varepsilon_x \\ \varepsilon_y \\ \varepsilon_z \\ \gamma_{yz} \\ \gamma_{zx} \\ \gamma_{xy} \end{bmatrix} \quad (2.14)$$

where  $E$  and  $\nu$  are the Young's modulus and the Poisson's ratio of the fiber optic, respectively. The parameter  $G$  is the rigidity and can be obtained by  $G=E/2(1+\nu)$ . The parameters  $\sigma_x, \sigma_y$ , and  $\sigma_z$  are the stress components at the point  $(x,y,z)$  in the optical fiber along the  $x, y$  and  $z$  directions, respectively. Furthermore,  $\sigma_{xy}, \sigma_{yz}$  and  $\sigma_{xz}$  are the shear stress components at the point  $(x,y,z)$  in the fiber optic.

As can be noted from equation (2.12), due to the photo-elastic properties of the optical fiber's material ( $p_{11} < p_{12}$ ), for a transversal load that is applied along the  $y$  axis, the refractive index change for the  $x$ -polarization is higher than that for the  $y$ -polarization. As a result, the Bragg wavelength corresponding to the  $x$  axis has a higher sensitivity to the transversal load compare to that corresponding to  $y$ -axis ( $\Delta\lambda_{By} < \Delta\lambda_{Bx}$ ).

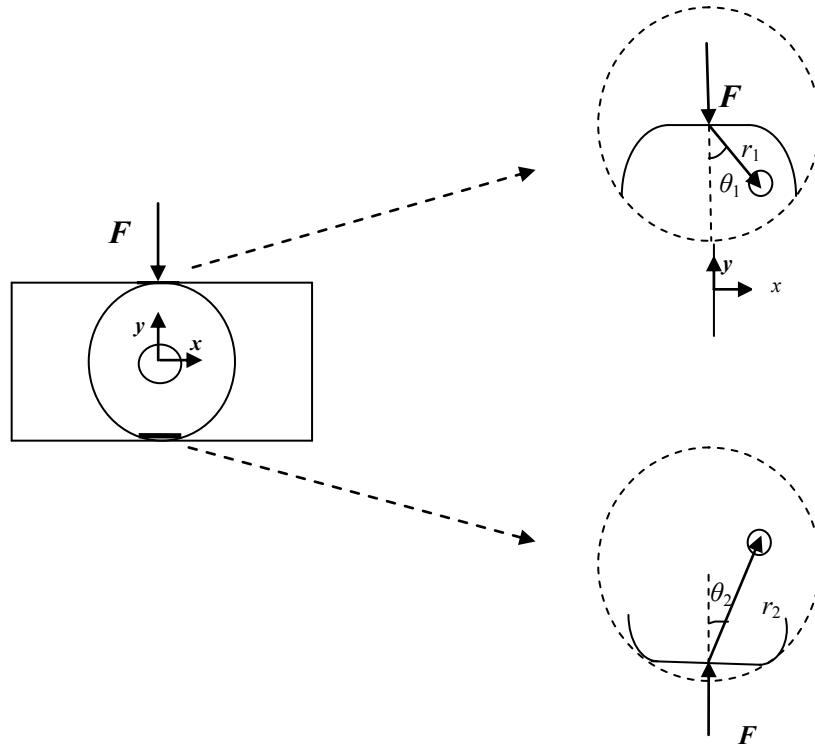


Figure 2.5 Schematic of the applied transversal load to a disk.

As an example, Figure 2.6 shows the refractive index changes for the  $x$  and  $y$  polarizations when the FBG sensor is under a 60 N uniform transversal force along the  $y$  axis.

The induced birefringence  $B$  due to the difference in refractive index changes along the main axes of the fiber can be expressed as [70]

$$B = \frac{|n_y - n_x|}{n_{eff}} \quad (2.15)$$

Where  $n_{eff}$  is the initial effective refractive index of the undisturbed optical Bragg grating fiber and  $n_x$  and  $n_y$  are the refractive indices for the  $x$  and  $y$ -polarizations axes, respectively.

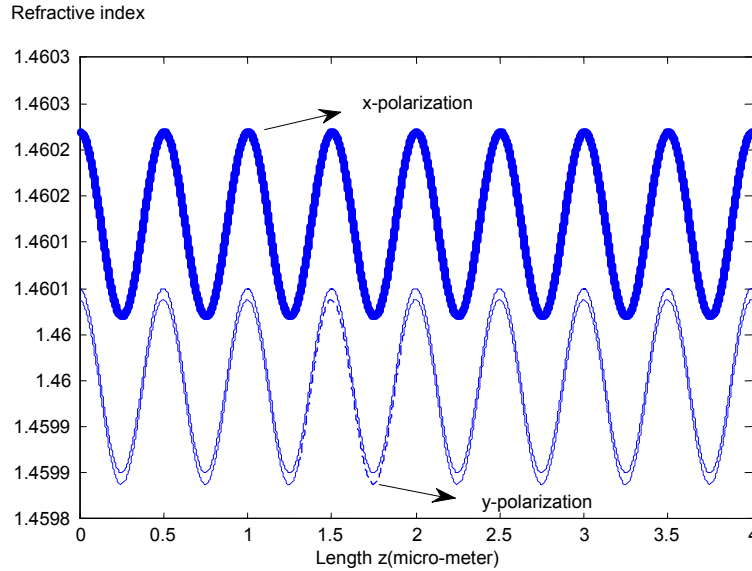


Figure 2.6 Computed refractive index spatial distribution in the core of the FBG along its axis, when subjected to a constant transversal force of  $F=60$  N. The solid distribution represents the refractive index distribution of the undisturbed sensor.

As can be observed from equations (2.10) and (2.11), from the peak separation between the Bragg wavelengths corresponding to the  $x$  and  $y$  polarization axes, the magnitude of the transversal load can be derived. In general, for conventional FBGs, the peak separation occurs when the applied load is above 40 N [54]. Therefore, the FBGs cannot be used for measuring the small loads.

Similar to the response of the sensor to a non-uniform longitudinal strain, the reflected spectrum of an FBG sensor that is subjected to a non-uniform transversal load gets distorted and comprises several peaks.

As an example, Figure 2.7 shows an experimentally obtained reflected spectrum of a 10 mm FBG sensor with the Bragg wavelength of 1555.6 nm when is subjected to different transversal loads. The results are obtained by Wang *et al.* in [71].

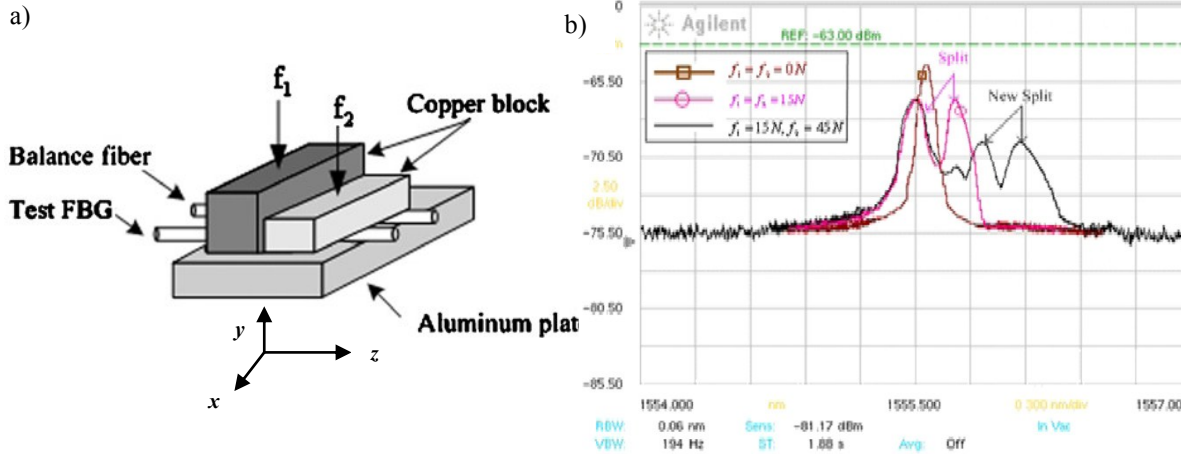


Figure 2.7a) Schematic of the experimental set up for the measurement of the transversal load, and b) reflected spectrums of the experimental setup under different transversal loads [71].

The distortion of the reflected spectrum is mostly observed when the sensor is embedded into the monitored disturbed structure. Figure 2.8 shows the reflected spectra of an FBG sensor when is embedded in to Carbon fiber reinforced plastic (CFRP) laminate for the detection of the transversal cracks in the  $90^\circ$  ply [99].

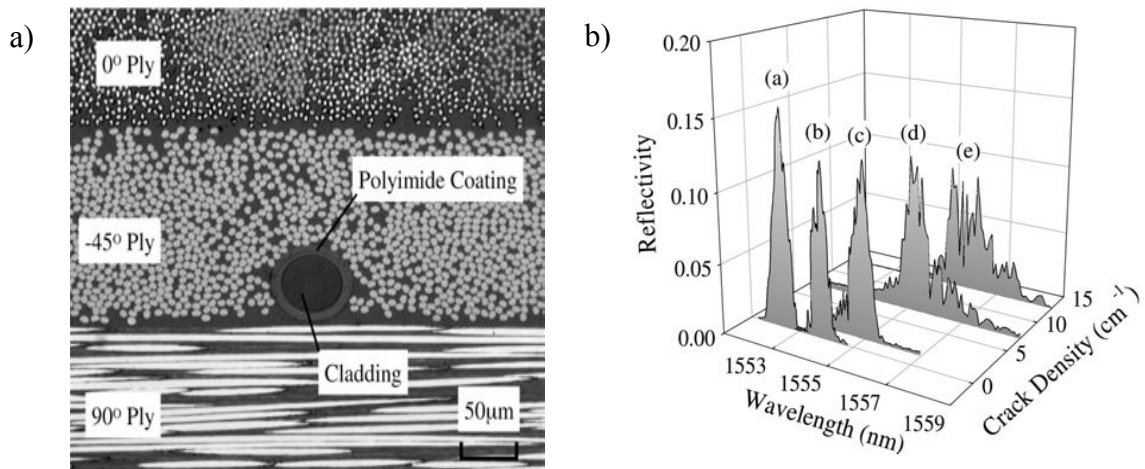


Figure 2.8 Schematic of the embedded FBG sensor located in the  $-45^\circ$  ply, and b) the reflectivity of the sensor versus the crack density [99].

It can be seen from the figure that as the crack density increases the spectrum gets more deformed and the detection of the anomaly becomes more complex.

The inverse method for the detection of the strain that result to the distortion of the reflected spectrum is explained in section 2.3.2.

In addition to measuring the strain, the FBGs have been introduced as perfect sensors for measuring the temperature changes. The effects of the temperature on an FBG sensor are discussed in the next section.

## **2.1.2 Characterization of an FBG Sensor Subjected to the Temperature Changes**

The variation in temperature affects the response of an FBG sensor through the thermal expansion or contraction of the grating period and the changes in the refractive index.

The Bragg wavelength shift due to the temperature change is given by [36]

$$\Delta\lambda_B = \lambda_B(\xi + \alpha)\Delta T \quad (2.16)$$

Where  $\xi$  and  $\alpha$  are the thermo-optic coefficient and the thermal expansion coefficient, respectively. The change in the refractive index of silica is generally ten times more than its thermal expansion coefficient [36]. As a result, the change in the Bragg wavelength is dominantly due to the change in refractive index of the fiber.

Although conventional FBGs are quite effective as the sensors for health monitoring applications, in certain areas, like measuring the small transversal loads, they cannot be used. Fiber Bragg grating fabricated in the high birefringence fiber is used to overcome the setbacks of the conventional FBGs.

In the following sections, the high birefringence fiber and Bragg grating fabricated into the high birefringence fiber are discussed in details.

## 2.2 Introduction to the High Birefringence Fiber Bragg Grating Sensor

In this section, firstly, the types and characteristics of a high birefringence fiber are explained. Then the characteristics of the Bragg grating fabricated into the high birefringence fiber (Hi-Bi FBG) are discussed and a study on the change in the reflected spectrum of the Hi-Bi FBG when it is subjected to the anomaly is presented.

### 2.2.1 High Birefringence Fibers

High birefringence (Hi-Bi) fiber can be formed by deliberately enhancing the birefringence of the fiber [70]. The permanent birefringence can be introduced to the fiber by subjecting it to the anisotropic stress (stress effect) or modifying its circular core or cladding shape (geometric effect).

The stress effects around the core are generated through the use of the stress applying parts (SAPs) which are introduced in the cladding during the fabrication of the fiber. The SAPs are created in the fiber by doping two symmetrically positioned regions of the cladding that are located on either side of the core [72, 73]. Panda, bow tie and elliptical cladding fibers are examples of stress induced birefringence fibers.

The average core birefringence across the cross section ( $A$ ) of the Hi-Bi due to stresses that are induced by the applying parts can be calculated as

$$\tilde{B} = \frac{-C \iint_{core} (\sigma_x - \sigma_y) dA}{\iint_{core} dA} \quad (2.17)$$



Where  $\sigma_x$  and  $\sigma_y$  are the stresses along the principal axes of the fiber, and  $C$  is the stress-optic coefficient of the fiber.

Geometric effects are induced by modifying the circular shape of the fiber. The modification of the circular shape of the core or cladding induces both geometrical and asymmetrical stress in the fiber. As a result, due to the sum of the geometrical and stress the birefringence appears in the fiber. Elliptical core and elliptical clad fibers are examples of the geometrically induced birefringence fibers. Different types of high birefringence fibers are shown in Figure 2.9.

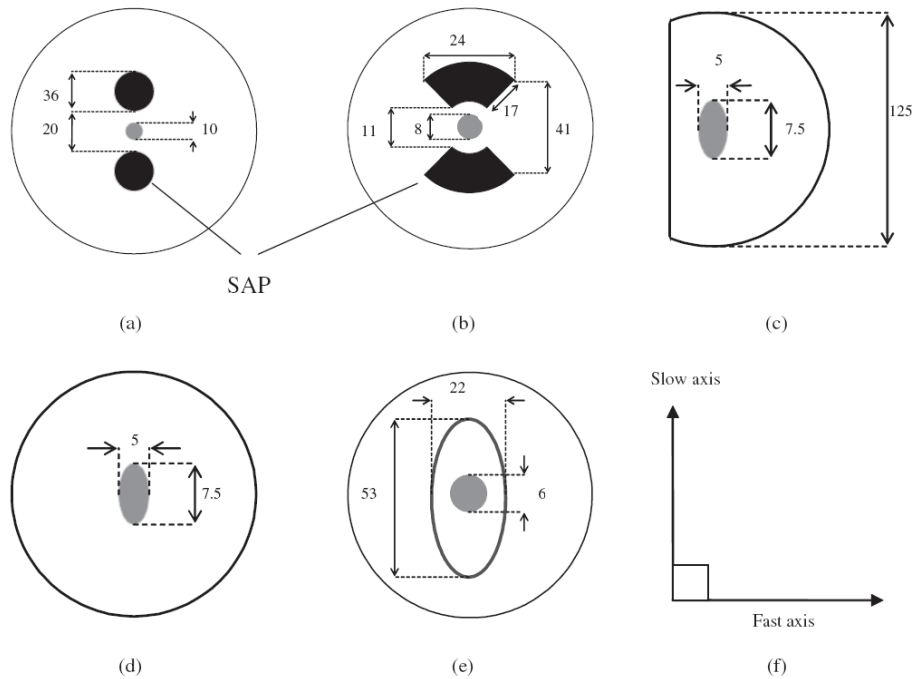


Figure 2.9 Schematic of different types of fiber (a) Panda, (b) bow-tie, (c) D cladding and elliptical core fiber, (d) elliptical core fiber, (e) elliptical clad fiber, and (f) main polarization axes configuration [55].

The propagation constants of the polarized modes of the Hi-Bi fiber are quite different from each other and therefore the coupling between the two modes is highly reduced. Consequently, the state of polarization (SOP) of the polarized modes is maintained. The polarization holding capacity of the Hi-Bi fiber can be quantified by its beat length  $L_b$ , which is defined by [70]

$$L_b = \frac{2\pi}{\beta_S - \beta_F} = \frac{\lambda}{\Delta n_{eff}} \quad (2.18)$$

Where  $\beta_S$  and  $\beta_F$  represent the propagation constants of the two orthogonally polarized modes corresponding to the slow (the polarization direction with the highest refractive index ) and fast (the polarization direction with the lowest refractive index), respectively and  $\Delta n_{eff}$  denotes the difference between the effective indices seen by the polarized modes at  $\lambda$  wavelength.

Any variation in the temperature and/or strain would alter the birefringence of the fiber and consequently would change its characteristics. The Bragg grating fabricated into the high birefringence fiber has been shown to have great potential for the sensing applications.

The next section describes the Bragg gratings fabricated into Hi-Bi fiber.

## 2.2.2 Bragg Grating Fabricated into the Hi-Bi Fiber (Hi-Bi FBG)

When the Bragg grating is fabricated into the high birefringence fiber, due to the differences in the refractive indices along the main polarization axes, its Bragg wavelength splits into two different Bragg peaks [54]

$$\begin{aligned}\lambda_{B,S} &= 2n_S\Lambda_0 \\ \lambda_{B,F} &= 2n_F\Lambda_0\end{aligned}\tag{2.19}$$

where  $\lambda_{B,S}$ ,  $\lambda_{B,F}$  represent the Bragg wavelengths for the slow and the fast axis, respectively,  $\Lambda_0$  denotes the grating period along the fiber, and  $n_x$  and  $n_y$  are the refractive indices for the  $x$  and  $y$  polarization modes.

As an example, the schematic diagram and the reflected spectrum of a Bragg grating with the Bragg wavelength centered at approximately 1545 nm that is written into a short section (5mm) of elliptical clad fiber with the birefringence of  $B=5.1\times 10^{-4}$  is shown in Figure 2.10[54].

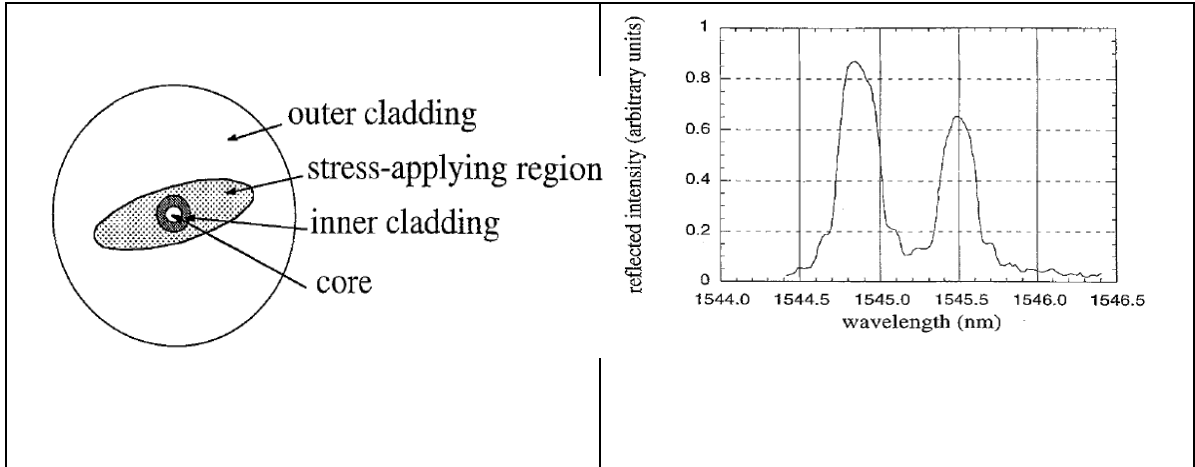


Figure 2.10a) Schematic of the elliptical clad fiber, and b) its reflected spectrum [54].

The figure clearly shows the dual peak structure of the experimentally obtained reflected spectrum of the Hi-Bi FBG sensor due to the birefringence of the fiber.

As in conventional FBGs, the subjected temperature or strain to the Hi-Bi FBG would alter its Bragg peaks. In general, the Bragg peaks corresponding to the slow and fast axes of the Hi-Bi FBG have different sensitivities to the changes in the temperature and the strain.

In the following sections, the characteristic changes of the Hi-Bi FBG when it is subjected to the strain variations are discussed.

### 2.2.2.1 Characterization of the Hi-Bi FBG Sensor Subjected to the Longitudinal or Transversal Strain Fields

The external loading subjected to the Hi-Bi FBG alters the refractive indices in the two main polarization axes

as

$$\Delta n_S = \frac{-n_S^3}{2} (p_{11} \epsilon_x + p_{12} (\epsilon_y + \epsilon_z)) \tag{2.20}$$

$$\Delta n_F = \frac{-n_F^3}{2} (p_{11} \epsilon_y + p_{12} (\epsilon_x + \epsilon_z))$$

where  $S$  and  $F$  indices refer to the slow and fast axes.

The longitudinal strain ( $\epsilon_z$ ) stretches the stress applying parts (SAPs) of the fiber in a different way than the cladding in the lateral direction (due to the difference in their Poisson's ratio). This phenomenon changes the birefringence of the fiber as [74, 75]

$$B = -(\nu_2 - \nu_1)\epsilon_z G \quad (2.21)$$

where  $\nu_1$  and  $\nu_2$  are the Poisson's ratios of the cladding and the stress applying sections, respectively, and  $G$  is the geometric factor depending on the elastic properties and the geometry of the fiber.

On the other hand, the sensor response to the transversal loads depends on many factors, including the type of the PM fiber and the loading angle relative to the polarization axes [61, 62]. Figures 2.11 and 2.12 depict the load sensitivity of the bow-tie and elliptical cladding FBG as a function of the loading angle of the Hi-Bi fibre.

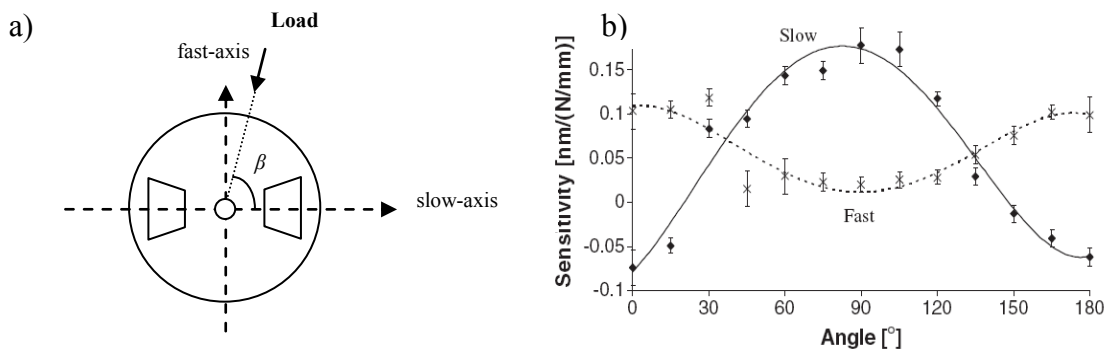


Figure 2.11 a) Schematic of the bow-tie fiber, and b) transversal strain sensitivity plotted against loading angle for Bragg grating fabricated in a bow-tie fibre [55].

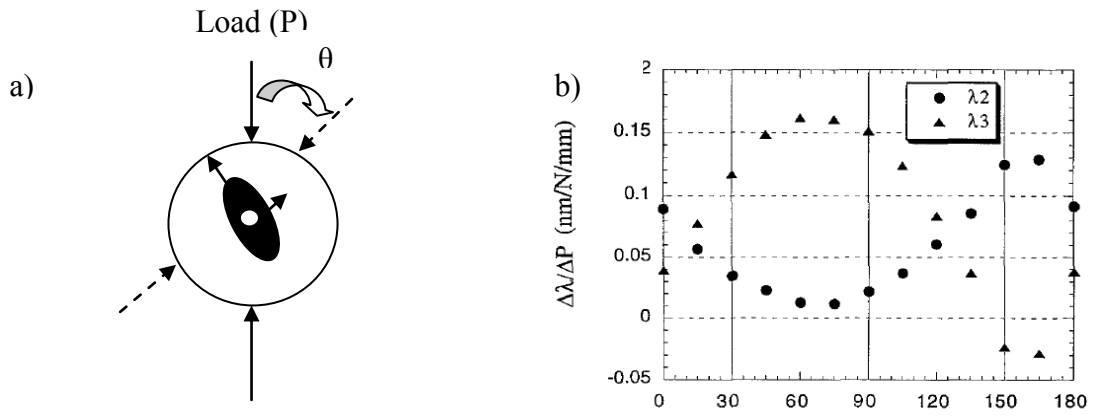


Figure 2.12 a) Schematic of the elliptical cladding fiber, and b) transversal strain sensitivity plotted against angle of rotation for Bragg grating fabricated in an elliptical cladding fiber [54].  $\blacktriangle$  and  $\bullet$  symbolize the response of the slow and fast axis, respectively.

As can be seen from the experimental results of Figures 2.11 and 2.12, for each angle of the applied transversal load, the fast and slow axes of the Hi-Bi FBG have different transversal load sensitivities. In other words, the transversal load ( $P$ ) induced shifts in the Bragg spectrums corresponding to the slow ( $\Delta\lambda_{\text{slow}}/\Delta P$ ) and fast axes ( $\Delta\lambda_{\text{fast}}/\Delta P$ ) of the sensor depend on the angle between the applied transversal load and the polarization axes of the fiber.

As can be observed from Figure 2.11 (b), the transversal load sensitivity of the Bragg spectrum corresponding to the fast axis of the bow-tie FBG reaches its minimum sensitivity when the load is applied along its axis.

Figure 2.13 shows the comparisons between the sensitivities of the slow and fast axes of the bow-tie and D-clad FBG.

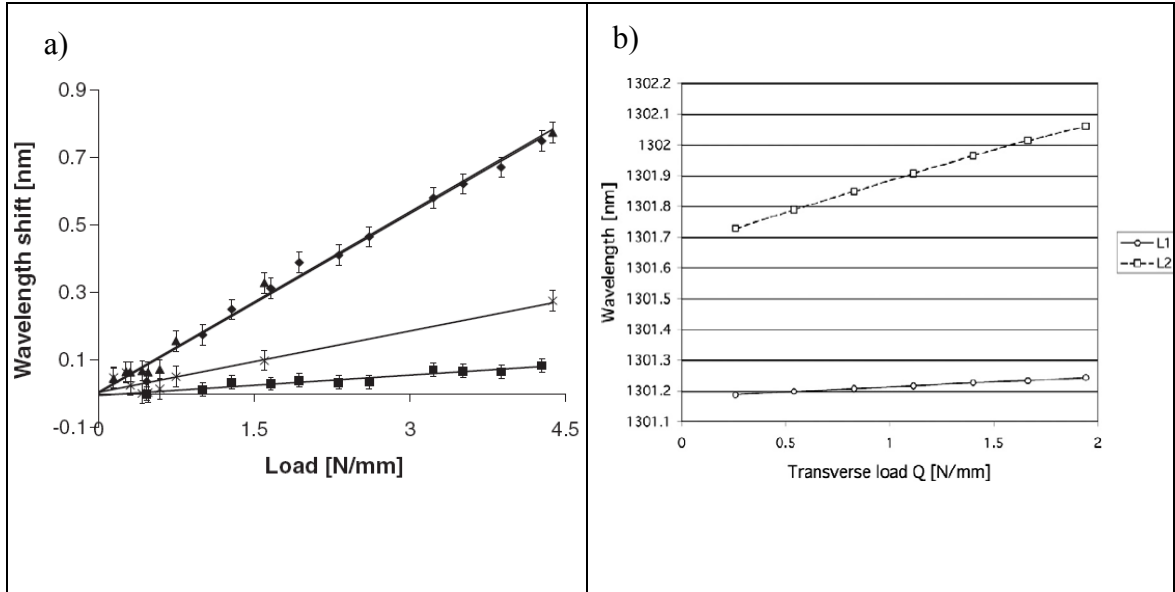


Figure 2.13 a) Comparison between the sensitivities of the Bragg gratings fabricated into the bow-tie and D-clad Hi-Bi fibers when the load is applied along the fast axis of the fiber. ♦:bow-tie slow axis; ■:bow-tie fast axis; ▲:D-clad slow axis; ×:D-clad fast axis, and b) transversal load sensitivities for the bow tie FBG with the Bragg wavelength for fast and slow axis as  $\lambda_{fast}=1301.114$  nm and  $\lambda_{slow}=1301.580$  nm ,respectively [52].

As can be observed from Figure 2.13 (a), the transversal load sensitivity of the bow-tie and D-clad FBG sensor for the slow axis is considerably higher than that for the fast axis.

The next chapter discusses the numerical methods for modeling the reflected spectrum of the Bragg grating sensor and the inverse method for reconstructing a non-uniform distribution of anomaly along the sensor's length.

## 2.3 Theoretical Tools

In this thesis, the disturbed reflected spectra of the Bragg grating fabricated into the single mode and high birefringence fiber by longitudinal strain, transversal load, and temperature are modeled by the T-matrix formulation. On the other hand, a non-uniform

distribution of the anomaly is synthesized by the proposed inverse approach which is based on the genetic algorithm (GA).

In the next section, the mathematical tools that are used in this thesis are discussed.

### 2.3.1 Coupled Mode Theory for Modelling the Reflected Spectrum of an FBG Sensor

In this section, we describe the mathematical model for deriving the reflected spectrum of an FBG sensor which is considered as the “measured” spectrum throughout this thesis.

In general, wave propagation in optical fibers can be modeled and analyzed by solving the Maxwell’s equation with the appropriate boundary conditions. In the absence of any perturbation, the propagating modes travel through the optical waveguide without any coupling among different modes and the total transversal field may be described in terms of the superposition of the  $l$  transversal guided mode amplitudes,  $A_\mu(z)$ , along with the continuum of radiation modes  $A_\rho(z)$  as[36]

$$E_t = \frac{1}{2} \sum_{\mu=1}^{\mu=l} [A_\mu(z) E_{\mu t} e^{i(\alpha t - \beta_\mu z)} + c.c.] + \sum_{\rho=0}^{\rho=\infty} A_\rho(z) E_{\rho t} e^{i(\alpha t - \beta_\rho z)} \quad (2.22)$$

Where  $\beta_\mu$  and  $\beta_\rho$  are the corresponding propagation constants of the  $\mu^{\text{th}}$  guided and  $\rho^{\text{th}}$  radiation modes, respectively,  $E_{\mu t}$  and  $E_{\rho t}$  are the radial transversal field distributions of the  $\mu^{\text{th}}$  guided and  $\rho^{\text{th}}$  radiation modes, and  $c.c.$  describes the real periodic modulation in complex notation. The fiber length is assumed to be along the  $z$  direction. In an ideal



waveguide without any perturbation the modes are normal to each other and they don't exchange energy.

The core perturbation inside the fiber, such as inscribed gratings of FBGs, leads to exchanging energy and coupling between specific propagation modes. The most common mathematical technique for modeling the wave propagation and coupling inside the FBGs is the coupled mode theory (CMT).

In order to derive the coupled-mode equation, the effects of the perturbation have to be included into the Maxwell's wave equation as

$$\nabla^2 E - \mu_0 \varepsilon_0 \frac{\partial^2 E}{\partial t^2} = \mu_0 \frac{\partial^2 P_{pert}}{\partial t^2} \quad (2.23)$$

where the perturbation is presented as a distributed polarization source  $P_{pert}(r,t)$  and accounts for the deviation of the polarization of the unperturbed medium. The dielectric constant and magnetic permeability are denoted by  $\varepsilon_0$  and  $\mu_0$ , respectively.

By ignoring couplings from guided to radiation modes, the transverse field in equation (2.22) can be expanded as

$$E_t = \frac{1}{2} \sum_{\mu} A_{\mu}^{+}(z) E_{\mu} e^{-i(\beta_{\mu} z - \alpha t)} + c.c. + \frac{1}{2} \sum_{\nu} A_{\nu}^{-}(z) E_{\nu} e^{i(\alpha t + \beta_{\nu} z)} + c.c. \quad (2.24)$$

where  $A_{\mu}^{+}(z)$  and  $A_{\nu}^{-}(z)$  are the transversal guided mode amplitudes, for the forward  $\mu$  and backward  $\nu$  modes, respectively.

By invoking the slow varying envelope approximation (SVEA), and making use of the orthogonal nature of the modes, the substitution of the transverse field of equation (2.24) into the wave equation gives

$$\left[ \frac{dA_v^-}{dz} e^{i(\beta_v z + \alpha t)} + c.c. \right] - \left[ \frac{dA_\mu^+}{dz} e^{-i(\beta_\mu z - \alpha t)} + c.c. \right] = -\frac{i}{2\omega} \frac{\partial^2}{\partial t^2} \int_{-\infty}^{+\infty} \int_{-\infty}^{+\infty} p_{grating} E_{\mu,\nu}^* dx dy \quad (2.25)$$

where  $p_{grating}$  is the perturbed polarization due to the grating.

For the fiber Bragg grating in which the dielectric constant varies periodically along the wave-propagation direction, the perturbed polarization can be related to the refractive index change as

$$p_{grating} = 2n\varepsilon_0 \left[ \overline{\Delta n} + \frac{\Delta n}{2} (e^{i[(2\pi N/\Lambda)z + \varphi(z)]} + c.c.) \right] E_{\mu,\nu} \quad (2.26)$$

where  $\overline{\Delta n}$  is the refractive index change averaged over a single period of the grating, and  $\Delta n = v\overline{\Delta n}$  is the amplitude of the ac refractive index modulation ( $v$  is the visibility of the fringes),  $\varphi(z)$  is an arbitrary spatially varying phase change,  $\Lambda$  is the period of the perturbation, and  $N$  is an integer ( $-\infty < N < +\infty$ ) that signifies its harmonic order.

By substituting the perturbation into the equation (2.25) and choosing the appropriate synchronous terms leads to the following simple coupled-mode equations from which the transfer characteristics of the Bragg grating can be calculated [36]

$$\begin{aligned}
\frac{\partial A_{\mu}^{+}}{\partial z} &= -ik_{dc}A_{\mu}^{+} - ik_{ac}^{*}A_{\nu}^{-} e^{i(\Delta\beta z - \phi(z))} \\
\frac{\partial A_{\nu}^{-}}{\partial z} &= ik_{dc}A_{\nu}^{-} + ik_{ac}A_{\mu}^{+} e^{-i(\Delta\beta z - \phi(z))}
\end{aligned}
\tag{2.27}$$

where  $k_{dc}$  and  $k_{ac}$  are the dc and ac transversal coupling coefficients between the forward and backward propagation modes, respectively and are given by

$$\begin{aligned}
k_{dc} &= n\omega\epsilon_0 \int_{-\infty}^{+\infty} \int_{-\infty}^{+\infty} \Delta n E_{\nu l} E_{\mu l}^{*} dx dy \\
k_{ac} &= n\omega\epsilon_0 \int_{-\infty}^{+\infty} \int_{-\infty}^{+\infty} \frac{\Delta n}{2} E_{\nu l} E_{\mu l}^{*} dx dy = \frac{\nu}{2} k_{dc}
\end{aligned}
\tag{2.28}$$

The parameter  $\Delta\beta$  is referred to as the phase mismatch and is given by

$$\Delta\beta = \beta_{\mu} + \beta_{\nu} - \frac{2\pi N}{\Lambda}
\tag{2.29}$$

In fiber Bragg grating sensors, the main interaction is between the mode of an amplitude  $A_{\mu}^{+}(z)$  into an identical counter-propagating mode of  $A_{\nu}^{-}(z)$  near the Bragg wavelength. The following substitutions are made for the forward and backward propagating modes, as

$$\begin{aligned}
R &= A_{\mu}^{+} e^{-\left(\frac{i}{2}\right)[\Delta\beta z - \phi(z)]} \\
S &= A_{\mu}^{-} e^{\left(\frac{i}{2}\right)[\Delta\beta z - \phi(z)]}
\end{aligned}
\tag{2.30}$$

Consequently, by differentiating equation (2.30) and substituting in equation (2.27), we have [36]

$$\begin{aligned}\frac{dR}{dz} + i\left[k_{dc} + \frac{1}{2}\left(\Delta\beta - \frac{d\phi(z)}{dz}\right)\right]R &= -ik_{ac}^*S \\ \frac{dS}{dz} - i\left[k_{dc} + \frac{1}{2}\left(\Delta\beta - \frac{d\phi(z)}{dz}\right)\right]S &= ik_{ac}R\end{aligned}\tag{2.31}$$

For a single-mode Bragg reflection grating, the coupling coefficients can be written as:

$$\begin{aligned}k_{ac} &= \frac{\pi}{\lambda} \overline{\nu \delta n_{eff}} \\ k_{dc} &= \frac{2\pi}{\lambda} \overline{\delta n_{eff}}\end{aligned}\tag{2.32}$$

By assuming the forward going wave incident for a fiber grating of Length ( $L$ ) from  $z=-\infty$ , ( $R(-L/2)=1$ ) and requiring no backward going wave for  $z \geq L/2$ , ( $S(L/2)=0$ ) the closed-form solution of the coupled first order ordinary differential equation for calculating the amplitude is

$$\rho = \frac{S(0)}{R(0)} = \frac{-k_{ac} \sinh(\alpha L)}{\delta \sinh(\alpha L) - i \alpha \cosh(\alpha L)}\tag{2.33}$$

and the power reflection coefficient  $r$  is

$$r = |\rho|^2 = \frac{|k_{ac}|^2 \sinh^2(\alpha L)}{|k_{ac}|^2 \cosh^2(\alpha L) - \delta^2}\tag{2.34}$$

where

$$\delta = k_d \pm \frac{1}{2} \left( \Delta\beta - \frac{d\phi(z)}{dz} \right) \quad (2.35)$$

and

$$\alpha = \sqrt{|k_{ac}|^2 - \delta^2} \quad (2.36)$$

It should be noted that for a grating with a constant period, the variation in the phase

$$\frac{d\phi(z)}{dz} = 0.$$

For modeling the spectrum of the disturbed FBG, equation (2.31) can be transformed into the Riccati differential equation by substituting  $\rho(z)$  with  $S(z)/R(z)$  and solving the equation numerically along the fiber when  $z$  changes from  $-L/2$  to  $L/2$ .

The boundary condition is set to  $\rho(L/2)=0$  and a fourth-order Runge-Kutta numerical integration along the length of the fiber with adaptive step size can then be used to solve the equation.

Example of the reflected spectrum of such a grating subjected to a linear strain along the FBG sensor which is obtained by using the Runge Kutta method is shown in Figure 2.14.

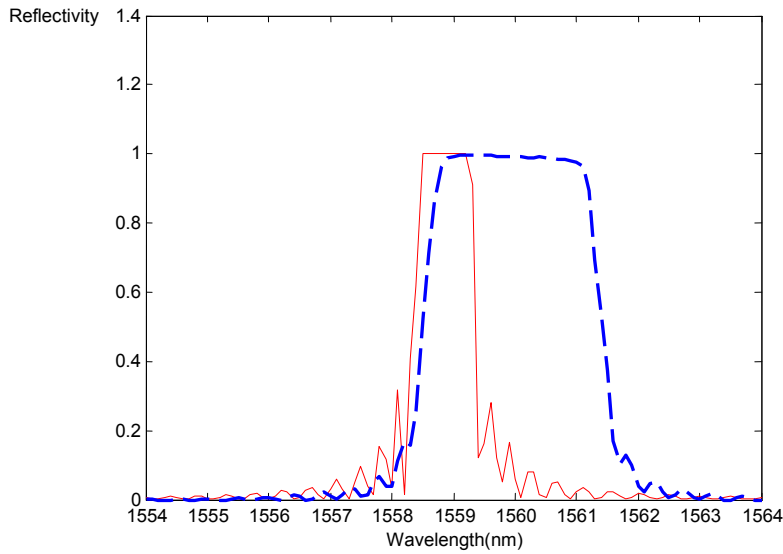


Figure 2.14 Calculated reflected spectra for a uniform Bragg grating sensor of a L=10-mm long uniform grating (solid line) when a linear strain of  $\epsilon(z)=100(z/L)$  micro-strain is applied along the length of the sensor in  $z$  direction (dashed line) using the Runge-Kutta method.

Even though this method is simple, the number of steps of the Runge-Kutta routine must be large to ensure convergence. Therefore, in some cases the algorithm might be slow.

Another well-known method for solving the coupled mode equations and obtaining the reflected spectrum of a disturbed FBG is the transfer matrix formulation (T-matrix). The T-matrix approach is used in this study to model the reflected spectrum of the sensor that is subjected to a non-uniform anomaly. This method is preferable to the direct-integration approach because it is computationally faster to implement.

In this method, as illustrated in Figure 2.15, the grating is divided into  $m$  sections and the coupled mode equations are used to calculate the output fields of a short section  $\Delta z$  in which the grating period, length, and coupling coefficients are assumed to be constant. Each section may have its different parameters.

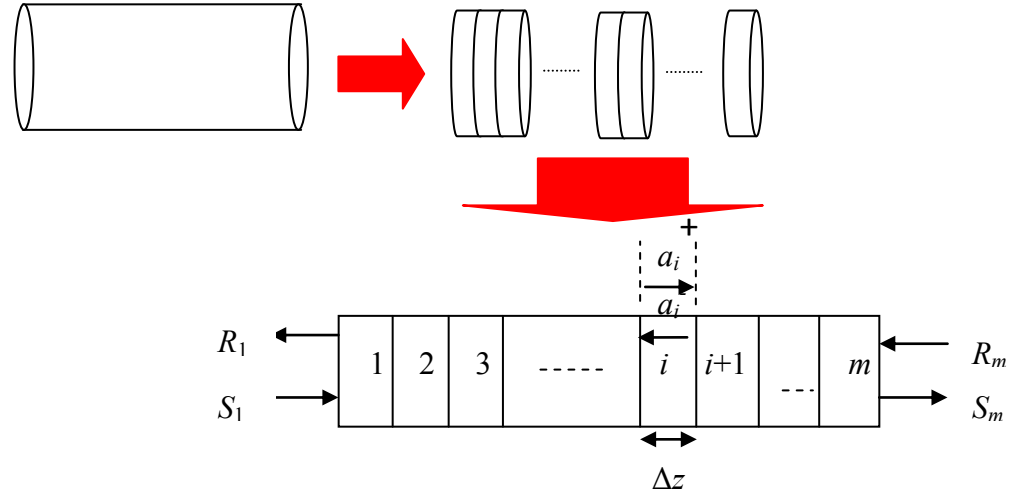


Figure 2.15 Schematic of a sensor divided into  $m$  sections with length  $\Delta z$ .

The solutions to the coupled equations for the forward  $a_i^+$  and backward  $a_i^-$  slowly varying amplitudes of the traveling waves for each  $i$  uniform segment, can be expressed in terms of a single  $2 \times 2$  matrix as [36]

$$\begin{bmatrix} a_i^+ \\ a_i^- \end{bmatrix} = T \begin{bmatrix} a_{i+1}^+ \\ a_{i+1}^- \end{bmatrix} = \begin{bmatrix} T_{11}^{(i)} & T_{12}^{(i)} \\ T_{21}^{(i)} & T_{22}^{(i)} \end{bmatrix} \begin{bmatrix} a_{i+1}^+ \\ a_{i+1}^- \end{bmatrix} \quad (2.37)$$

where the elements of the transfer matrix  $T$  for the  $i^{\text{th}}$  section are obtained from the solution to the coupled mode equations and can be written as

$$\begin{aligned} T_{11}^{(i)} = T_{22}^{(i)*} &= \cosh(\alpha \Delta z) - i \frac{\delta}{\alpha} \sinh(\alpha \Delta z) \\ T_{12}^{(i)} = T_{21}^{(i)*} &= -i \frac{k_{ac}}{\alpha} \sinh(\alpha \Delta z) \end{aligned} \quad (2.38)$$

The T-matrix of the entire grating can be obtained by multiplying the T matrices of all the segments as

$$T = T_m T_{m-1} \dots T_1 \quad (2.39)$$

Consequently the reflected wave  $R_1$  and the transmitted wave  $S_1$  (see Figure 2.15) can be expressed by means of the T as

$$\begin{bmatrix} R_1 \\ S_1 \end{bmatrix} = T \begin{bmatrix} R_m \\ S_m \end{bmatrix} \quad (2.40)$$

By imposing the nominal boundary conditions,  $S_1=1$  (normalized input field) and  $R_m=0$  (no reflected signal from the end of the grating), the reflection and the transmission coefficients are calculated for each wavelength according to the relations

$$\begin{aligned} r(\lambda) &= \frac{R_1}{S_1} = \frac{T_{12}}{T_{22}} \\ t(\lambda) &= \frac{S_m}{S_1} = \frac{1}{T_{22}} \end{aligned} \quad (2.41)$$

and consequently the reflectivity is defined as

$$R(\lambda) = |r(\lambda)|^2 \quad (2.42)$$



The T-matrix is a straightforward and fast method for simulating the reflected spectrum of the SM FBG.

In order to simulate the reflected spectrum of a Hi-Bi FBG, the two forward propagating orthogonal polarization modes and the two backward propagating modes can be represented as a column vector  $E(z)$  with four elements. The interaction among the four modes can be described by the coupled-mode theory as [72]

$$\frac{dE}{dz} = iCE \quad (2.4)$$

where the coupling matrix  $C$  can be verified for each polarization mode by assuming that there is no coupling between the polarization modes. In other words, the associated interaction matrix is assumed to be diagonal.

In most practical applications, the birefringence of the fiber is high enough to avoid the coupling between the polarization modes. As a result, we can assume that each polarized mode reflects back from separate gratings and the reflected signal is the combination of the reflected signals of the  $x$  and  $y$  modes, each one with its refractive index value associated with the principal axes of the fiber.

Referring to equation (2.2), the refractive indices for the slow and fast axes and grating period for each segment can be expressed by a  $2 \times 2$  matrix along the optical axis of the fiber as a function of the position [72]

$$\begin{aligned}
 n_{eff}(z) = & U_{dc}(z) \begin{bmatrix} n_{eff} + \Delta n_{dc}^{slow} & 0 \\ 0 & n_{eff} + \Delta n_{dc}^{fast} \end{bmatrix} U_{dc}^\dagger(z) \\
 + & U_{ac}(z) \begin{bmatrix} n_{ac}^{slow}(z) \cos\left(\frac{2\pi z}{\Lambda} + \phi^{(1)}(z)\right) & 0 \\ 0 & n_{ac}^{fast}(z) \cos\left(\frac{2\pi z}{\Lambda} + \phi^{(2)}(z)\right) \end{bmatrix} U_{ac}^\dagger(z) \quad (2.44)
 \end{aligned}$$

Where  $U_{ac}(z)$  and  $U_{dc}(z)$  relate the orientation of the coordinate system to the orientation of the  $ac$  and  $dc$  index eigen axes, respectively.

The anomaly distribution in the FBG can be obtained from its own reflected spectrum. This approach is known as an inverse approach, which is based on calibrating the parameters of a mathematical model to reproduce observations. In this thesis, a non-uniform distribution of the anomaly is reconstructed by an inverse approach based on the genetic algorithm (GA). The GA is a powerful inverse approach that only requires the amplitude spectral information of the fiber Bragg grating spectrum to reconstruct its characteristics. In addition, the GA evaluates the selection of a large possible set of solutions that can avoid the algorithm from converging to a local minimum. Therefore, GA is an excellent choice for evaluating a non-uniform distribution of anomaly along the length of the fiber.

In the next section, the genetic algorithm and its functionality for reconstruction of characteristics changes along the FBG sensor is discussed.

## 2.3.2 Genetic Algorithm

Genetic algorithm is an iterative procedure that is based on the natural evolutionary biology in which the best potential solutions will survive and create off-springs at each iteration until the entire algorithm converges to the best solution. The GA holds a strong analogy to the fundamentals of the natural evolution theory that is developed based on the principal of “survival of the fittest”, derived from what Charles Darwin has defined as the natural selection and preservation of favoured races in the struggle of life.

The genetic algorithm starts off with a population of strings (chromosomes) which represents the possible solutions (individuals) to the optimization problem. A typical population size can vary from few dozens to thousands. The space from which the possible solutions are chosen is called search space. Each chromosome consists of genes where each gene has its own position in the chromosome that is referred to as locus.

The goal of the GA is to evolve the population to the best possible solution. In general, the solutions are represented in binary as strings of zeros and ones but other forms of encodings such as a string of real numbers are also possible. Each string represents a different solution to the problem.

The population at each iteration (generation) gets evaluated and modified by going through the main genetic operators and the algorithm is repeated until a solution is found. The objective for each generation is to produce a population which is better than the previous one. The algorithm terminates when the maximum number of generations has been produced or a satisfactory fitness level has been reached.

In the following section, the main genetic operators, namely; selection, crossover, mutation and elitism are described.

## 2.3.2.1 Genetic Operators

### ➤ Selection

To perform the optimization, a fitness function is assigned for each chromosome of the population. The fitness function is defined depending on the problem and indicates how close a chromosome is to the optimal solution.

Once the fitness functions are assigned to the chromosomes, a set of solutions are selected to be mated in a given generation. The probability that each chromosome can be selected for reproduction is proportional to its fitness function.

Several selection algorithms, such as truncation selection, local selection, roulette wheel selection, tournament selection and stochastic sampling exist [77]. The two traditional selection methods which are used in this thesis are the roulette wheel selection and the tournament selection and are discussed in the following sections.

- **Roulette Wheel Selection**

The roulette wheel selection method is one of the traditional GA selection techniques and is analogous to a roulette wheel in a casino. In the roulette wheel selection (also called stochastic sampling with replacement), each individual  $i$  of the population is represented by a space proportional to its fitness  $f_i$ . The chance of a chromosome getting selected is proportional to its fitness function as [77]

$$p_i = \frac{f_i}{\sum_{j=1}^N f_j} \quad (2.45)$$

where  $N$  is the number of individuals in the population.

The individuals with higher  $p_i$  have better chances of selection for reproduction. Each individual is assigned a slice of the roulette wheel where the size of the slice is being proportional to the individual's fitness. The total expected value of the individuals in the population is calculated and then a random proportion of the sum of the fitness in the population is set as the target value.

The population is scanned through and the expected values add up until the target value is reached for each scan. The process is repeated until the desired number of individuals is obtained (mating population). It is very important for the population to not be sorted by fitness, since this would bias the selection. The procedure is analogous to the roulette wheel where their sizes of segments are proportional to the fitness of the individuals as is shown in Figure 2.16.

The wheel is then spun and the larger regions have a higher change of getting selected.

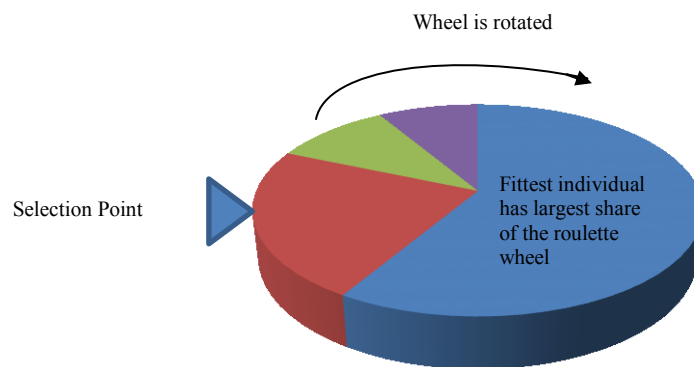


Figure 2.16 Schematic of roulette wheel selection.

- **Tournament Selection**

In the k-tournament selection,  $k$  individuals are first selected from a population and the ones with the better fitness functions are selected and are considered for reproduction. The tournament size can be adjusted in order to modify the pressure of the selection. Generally, when the tournament size is large, there is a small chance for weak individuals to be selected. The parameter for tournament size is called *Tour*. The winner of the tournament is inserted again to the mating pool. The tournament is repeated until the mating pool for generating new offspring is filled. The mating pool has a better average fitness than the population.

The new selected population goes through the next GA operator, namely; crossover as is discussed in the next section.

- **Crossover**

Crossover advances the population by recombining the individuals with better fitness to produce offsprings. It is an artificial version of biological recombination between two organisms to produce offsprings. Different forms of crossover operator can be used according to the way that the problem is encoded. Holland's traditional GA uses one point crossover. Other forms of crossover operators such as two-point and multi-point crossovers have also been successfully used in GAs. The probability that the crossover operator is applied to an individual depends on the problem and can be modified to enhance the performance of the GA.

Basically crossover operator takes two individuals according to the crossover probability (crossover for the individuals to be chosen) and cuts the chromosome strings at some randomly chosen position and then swaps the produced substrings to produce two new full length chromosomes.

Conventional crossover techniques include single point and two point crossover that are discussed in the next sections.

- **Single Point Crossover**

The single point crossover operator cuts the chosen two strings in a single random point which produces four substrings. The second parts of the strings are then swapped to produce offsprings(children). The crossover point can be chosen randomly. Figure 2.17 illustrates single point crossover operation.

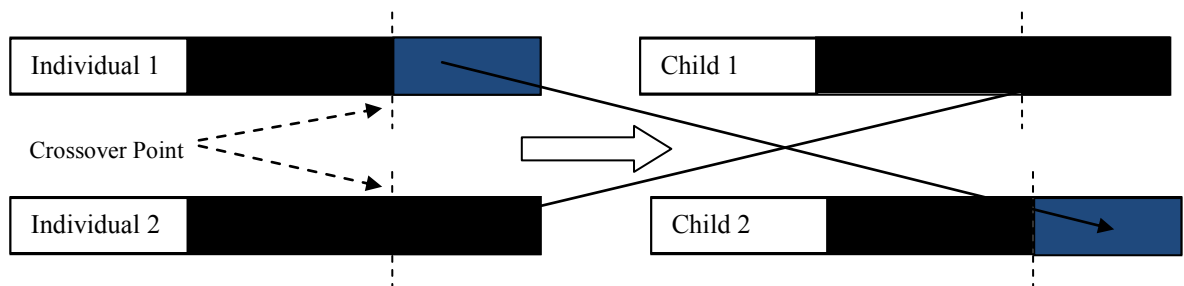


Figure 2.17 Schematic of the single point crossover.

- **Two Point Crossover**

Two point crossover is the extension of the single point crossover. The advantage of having more crossover points is that the problem space may be searched more thoroughly. In two-point crossover, two crossover points are chosen from each chromosome and the contents between these two points are swapped between the two strings. Figure 2.18 illustrates the two point crossover operation.

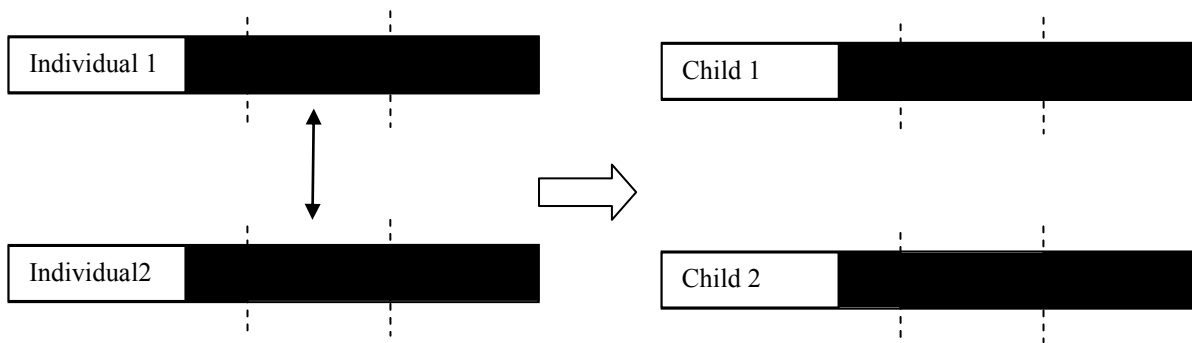


Figure 2.18 Schematic of the two point crossover.

In Figure 2.18 the dotted lines indicate the crossover points where the contents between them are exchanged between the parents to produce the children. After crossover the strings are subjected to mutation which is discussed in the next section.

➤ **Mutation**

Mutation is an operator that is used to maintain the diversity in the population and prevents the algorithm to trap to a local minimum. Mutation operator is analogous to biological mutation which introduces new structures to the population by randomly modifying some of the gens of the strings.

Mutation is applied to the population at each generation according to a user defined mutation probability which should be set to the low value in order to prevent the



search for the solution to turn into a primitive random search. There are many different forms of mutation for different types of the representation of the population.

In binary representation, mutation flips the chosen genes from 0 to 1 or vice versa. In a case where the genes are encoded as real numbers or integer encoding, uniform and non-uniform mutation operators can be used. The non-uniform mutation operator keeps the population from stagnating in the early stages of the generations and then allows the GA to fine-tune the solution in the later stages of the generations.

Finally, in order to avoid losing the chromosomes with highest fitness functions at each generation; elitism is implemented to the population at the end of each generation. The operator elitism is discussed in the next section.

#### ➤ **Elitism**

In order to prevent the loss of the fittest chromosomes during the GA generations, at the end of each generation, the best chromosomes (the ones with the lowest fitness functions) are copied to the new population. The rest of the chromosomes are chosen in a classical way.

## **2.4 Conclusions**

In this chapter, background material on the characteristics of the Bragg grating fabricated into the single mode (FBG) and high birefringence (Hi-Bi FBG) fiber were presented. Furthermore, the mathematical tools that are used in this thesis, namely, the T-matrix and the Genetic Algorithm (GA) were discussed.

## **Chapter 3**

# **Analysis and Synthesis of a Non-Uniform Distribution of Strain and Temperature within an FBG Sensor: Proposed Approach**

The first part of this chapter presents the methodology for detecting the non-uniform distribution of transversal load along the sensor. The development of the presented methodology allows the use of FBG sensor to measure both the transversal load and its non-uniform distribution along the sensor within a millimeter resolution.

In addition, the methodology for detecting a non-uniform distribution of longitudinal and transversal load when they are applied simultaneously along the sensor is presented. Structural health monitoring in general necessitates the measuring of the strain in more than one dimension. At present, FBGs are mostly employed as axial sensors. However, in practice two or more strain components exist. Embedding the FBG sensors in different directions in the monitored substrate is the most straightforward solution for detection of the strain in different directions. However, this task can prove to be excessively complicated and impractical. Therefore, it is important to assess the effects of the strain in more than one dimension on the response of the sensor.

Detection of the two dimensional strain along a series of sensors that are positioned in one dimension would eliminate the need for installing the sensors on both orthogonal

directions on top or within the monitored structure. This will reduce the number of sensors and the complexity of the monitoring system. It should be noted that in an application where the applied longitudinal and/or transversal strain along the sensor is not uniform, the spectrum becomes broader and comprises multiple peaks and the anomaly profile becomes more complicated to interpret. In the second part of this chapter, a methodology for detection of non-uniform distributions of longitudinal and transversal loads is presented.

Moreover, in this chapter, an approach for detecting a non-uniform distribution of temperature along the FBG sensor is presented. The methodology enables the sensor to detect the variation of temperature along a series of extremely closed (mm resolution) points.

For each case, the distribution of the perturbation is obtained by detecting the variation in the grating characteristics of the sensor when they stray from their initial values due to the anomaly. Therefore, the grating characteristics (the grating period and the refractive index) along the fiber are represented as the population of the genetic algorithm and the solution in which the algorithm converges to will be correlated with the distribution of the subjected anomaly. The obtained non-uniform distribution of anomaly could provide a deeper insight into the health state of the structure.

We present an approach based on the genetic algorithm, with the goal of generating the best possible reflected spectrum with the lowest fitness function with the objective reflected spectrum. From the obtained optimal spectrum, a non-uniform distribution of the strain and temperature along the length of an FBG sensor is reconstructed. Furthermore, it is shown that the approach can be extended to the

multiplexed sensor system so that the positioning and identification of the distribution of the anomaly could be performed simultaneously.

In the following sections, first we present (in Section 3.1) our methodology for reconstructing the anomaly when the sensor is subjected to the transversal load and when it is subjected to the longitudinal and transversal load simultaneously. In Section 3.2, we discuss our methodology for reconstructing the distribution of temperature along the length of the sensor. Section 3.3 presents the simulation results.

A summary of the following material has already been published in [58], [78], and [80].

## **3.1 Synthesis of the Strain Profile Subjected to an FBG Sensor**

In order to explicate our methodology for the detection of a non-uniform distribution of the strain along the FBG sensor, the theoretical study on the response of the FBG sensor when it is subjected simultaneously to the longitudinal and transversal loads is presented. Throughout this thesis the transversal load is applied along the  $y$  axis (fast axis) and the longitudinal load is applied along the optical axis of the sensor ( $z$  axis) as is shown in Figure 3.1.

As discussed in Chapter 2, the transversal load induces birefringence to the optical fiber and therefore the Bragg spectrum of the FBG sensor splits into two separate ones, each corresponds to the polarization axis. Moreover, the axial load would alter the grating period and refractive index along the fiber and would result in the shift of the reflected spectrum. Therefore, when the longitudinal strain and the transversal loads are

applied simultaneously to the sensor (as shown in Figure 3.1), the reflected spectrum of the FBG sensor not only is shifted but also gets divided into two separate peaks.

The Bragg spectrum of the disturbed FBG sensor is modeled theoretically by the T-matrix formulation method. Toward this end, the fiber is divided into  $m$  segments where the grating period and refractive index changes due to both loads for each segment along the fiber are considered constant. It should be noted, as discussed in Chapter 2, due to the applied transversal load, the effective refractive index of the sensor becomes asymmetric over the fiber cross section. The change in the refractive indices along the main polarization axes of the sensor leads to the separation of the Bragg wavelengths into two distinctive ones for the  $x$  and  $y$  polarization axes.

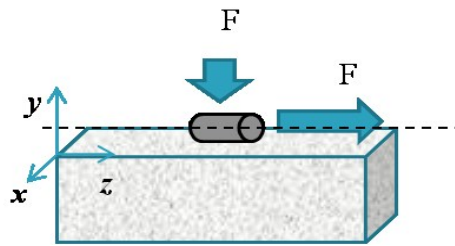


Figure 3.1 Schematic of an FBG sensor that is subjected to the transversal and longitudinal forces.

Therefore, we have modeled the Bragg wavelength corresponding to the  $x$  and  $y$  polarization separately. The overall reflected spectrum results from the combination of the two reflected spectrums.

Figure 3.2 shows the response of a  $L=1$  cm disturbed grating with initial grating period of 531.84 nm, Young's modulus  $E = 74.52$  GPa, Poisson's ratio  $\nu = 0.17$  and the strain coefficients of  $p_{11} = 0.121$  and  $p_{12} = 0.27$  to the simultaneous longitudinal and transversal loads. The FBG is divided into ten uniform sub gratings.

Figure 3.2 (a) shows the response of the sensor when in addition to a uniform longitudinal 200 micro-strain it is subjected to the different load values. As can be noted from this figure, the Bragg wavelength noticeably shifts due to the longitudinal force and then splits as one increases the transversal force. It is observed that, when the distribution of longitudinal and transversal perturbations are uniform along the sensor, the magnitudes of the axial and transversal forces can simply be obtained by detecting the shift of the Bragg wavelength and the magnitude of the separation between the two wavelengths at maximum reflectivity, respectively. In addition, it can be noted that the split point between the two polarized spectra moves forward with the increasing of the applied force. Figure 3.2(b) shows the response of the same sensor when the distribution of the longitudinal strain along its length is non-uniform and changes according to  $\varepsilon(z) = 200(5(z/L)^2 + 1) \mu\varepsilon$ . As can be observed from this figure, a non-uniform distribution of the longitudinal strain would result in the distortion of the reflected spectrum. As the transversal load increases, the effect of a non-uniform distribution of longitudinal strain on the two induced reflected Bragg peaks becomes more observable. It can be observed that a non-uniform longitudinal strain results in similar distortion of the Bragg spectrum corresponding to the slow and fast axes.

Figure 3.2(c) shows the spectrum of the same FBG when it is subjected to the uniform 200 micro-strain longitudinal strain and non-uniform transversal load distribution of  $F(z) = F_0(1 + (z/L)^2)$  N along its length. As can be observed from Figure 3.2 (c), the applied non-uniform transversal force induces distortion to the  $x$ -polarized FBG spectrum and the FBG wavelength variation for the  $y$ -polarized spectrum remains almost unchanged [45]. In general, for a sensor that is subjected to the transversal load along the

$y$  direction, as shown in Figure 3.1, due to the mechanical and photo-elastic properties of the optical fiber's material ( $p_{11} < p_{12}$ ), the reflected Bragg spectrum corresponding to the  $y$ -axis is almost insensitive to the transversal load [45-48].

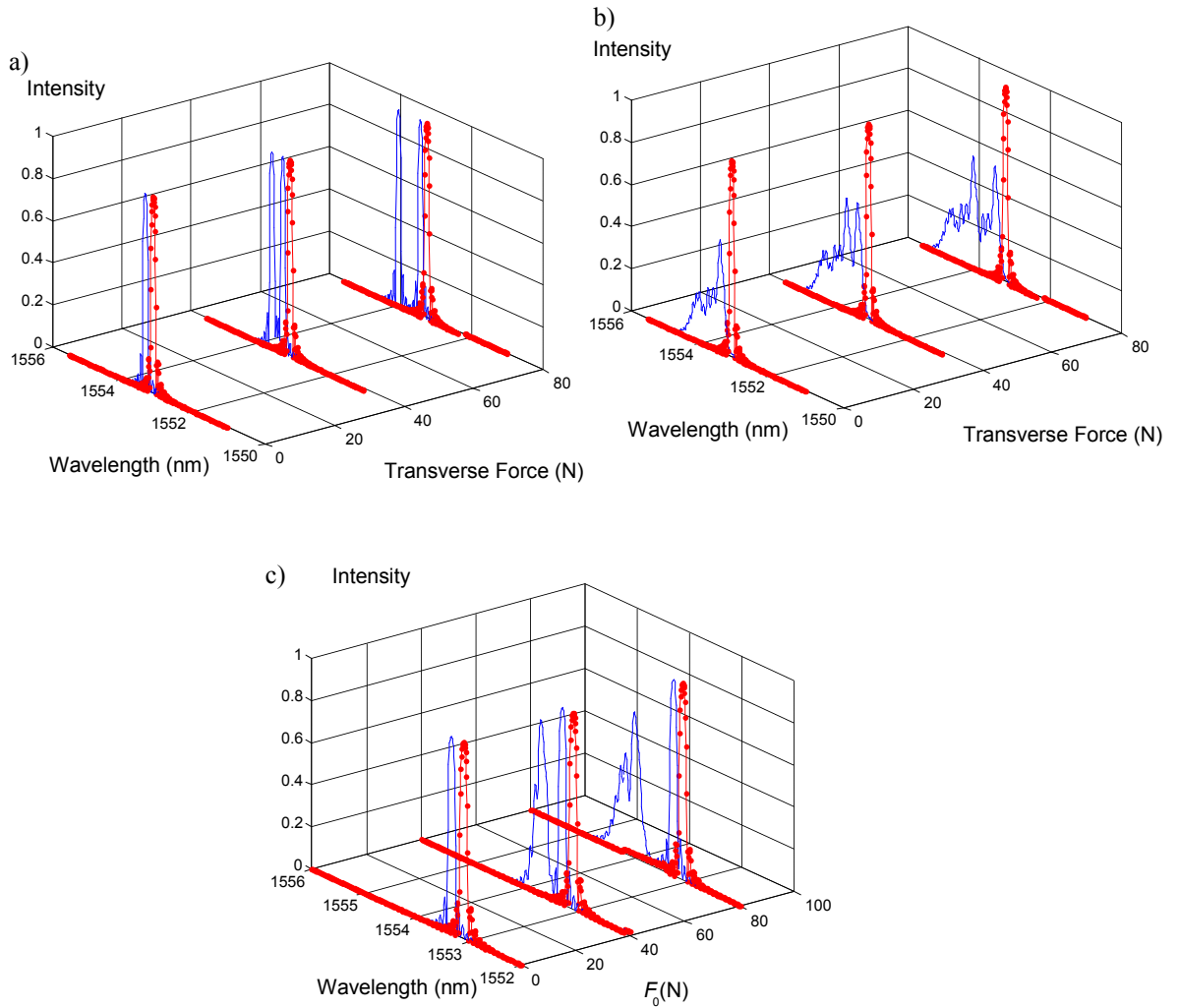


Figure 3.2 Spectral response of an FBG sensor subjected to a) simultaneous uniform transversal force and axial constant strain field  $\varepsilon_0=200 \mu\varepsilon$ , b) simultaneous uniform transversal force and non-uniform quadratic axial strain field of  $\varepsilon(z) = \varepsilon_0(5(z/L)^2 + 1) \mu\varepsilon$ , and c) simultaneous uniform longitudinal strain  $\varepsilon_0=200 \mu\varepsilon$  and a non-uniform quadratic  $F(z)=F_0(1+(z/L)^2)$  N transversal force. The “line”  $\bullet$  depicts the reflection spectrum at strain-free state.

For a case when the sensor is subjected to the simultaneous non-uniform longitudinal and non-uniform transversal forces along its length, the reflected spectrum gets more

complicated and comprises of multiple peaks. The distortion is due to the non-uniformity of the two dimensional perturbation and therefore the derivation of a non-uniform distribution of longitudinal and transversal load distribution along the sensor becomes a complex problem.

Our proposed methodology for reconstructing the strains from the distorted reflected spectrum of the FBG sensor is presented in the next sections. In Sections 3.1.1 and 3.1.2, the methodology for reconstructing the transversal load and longitudinal strain when they are applied separately to the sensor is presented. Using these approaches, in Section 3.1.3, an approach for reconstructing the strain in two dimensions is presented. The schematic of the applied forces and the coordinate axis remain unchanged throughout this thesis and is similar to the one that is shown in Figure 3.1.

### **3.1.1 Synthesis of the Transversal Load Subjected to an FBG Sensor**

In this section, the problem of reconstruction of the transversal strain profile inside the disturbed FBG is formalized. The development of the methodology will permit the use of the Bragg grating sensor for the detection of anomaly profile where strong transversal load non-uniformities exist. As can be observed from the discussion in Section 3.1, the applied transversal load induces bifurcation to the Bragg wavelength of the reflected spectrum.



The refractive indices for the two main polarization axes ( $n_{effx}$  and  $n_{effy}$ ) for the sensor that is disturbed by the transversal load are given by [45]

$$n_{effx} = n_{eff} + \Delta n_{effx} = n_{eff} - \frac{(n_{eff})^3}{2E} \left\{ (p_{11} - 2\nu p_{12})\sigma_x + ((1-\nu)p_{12} - \nu p_{11})(\sigma_y + \sigma_z) \right\} \quad (3.1)$$

$$n_{effy} = n_{eff} + \Delta n_{effy} = n_{eff} - \frac{(n_{eff})^3}{2E} \left\{ (p_{11} - 2\nu p_{12})\sigma_y + ((1-\nu)p_{12} - \nu p_{11})(\sigma_x + \sigma_z) \right\} \quad (3.2)$$

where  $E$  and  $\nu$  are the Young's modulus and Poisson's coefficient of the optical fiber, respectively. Consequently, the induced birefringence creates two distinct Bragg wavelengths corresponding to the main polarization axes of the fiber as

$$\begin{aligned} \lambda_{Bx} &= 2n_{effx}\Lambda \\ \lambda_{By} &= 2n_{effy}\Lambda \end{aligned} \quad (3.3)$$

where  $\lambda_{Bx}$  and  $\lambda_{By}$  is referred to as the reflected Bragg spectrum corresponding to the slow axis ( $x$ -axis) and fast axis ( $y$ -axis), respectively.

As a result, the information about the constant transversal force can be achieved from the separation between the two created Bragg peaks. In order to model the reflected spectrum of the sensor that is disturbed by a non-uniform transversal load, the sensor is divided into the  $m$  segments when for each segment the refractive indices corresponding to the main polarization axes of the sensor are considered constant. The reflected spectrum is modeled for the polarization modes corresponding to  $x$  and  $y$  axes separately and the total spectrum is obtained by the sum of two spectra. Figure 3.3 shows the theoretically obtained reflected spectrum of an FBG that is subjected to a non-uniform

distribution of transversal load along its length. The setup and the sensor is the same as the one in Figure 2.7.

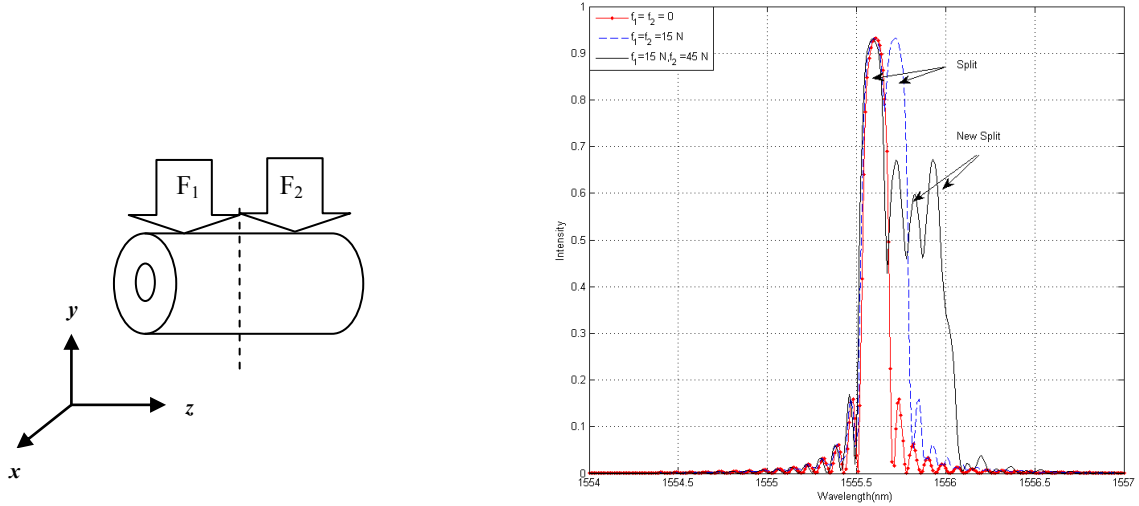


Figure 3.3 The theoretically obtained reflected spectrum of Fig. 2.7 that is obtained by the T-matrix.

It is important to note that the applied non-uniform transversal force induces distortion to the FBG spectrum. As a result, the applied force along the fiber's length can no longer be obtained directly from the magnitude of the separation between the two wavelengths at maximum reflectivity and the reconstruction of the applied force becomes an inverse problem. In general, for a sensor that is subjected to a non-uniform distribution of transversal load, the distortion of the spectrum for  $x$ -polarization (peak with larger wavelengths) is distinguishable while the reflected spectrum for  $y$ -polarization (peak with smaller wavelengths) remains almost unchanged.

Therefore, in our analysis in order to reconstruct the transversal load distribution along the sensor, the spectrum corresponding to the  $x$ -polarized axis is reconstructed by the

genetic algorithm (GA). The case of the plane strain is assumed in this section. Therefore, the grating period distribution along the sensor remains unchanged.

We start the algorithm by dividing the sensor into  $m$  segments and generating a random array of refractive indices (individual) corresponding to the  $x$ -polarized axis along the fiber as

$$n = \{n_x^1, \dots, n_x^m\} \quad (3.4)$$

where  $n_x^i$  is the refractive index corresponding to the  $x$  axis of the  $i^{\text{th}}$  segment of the sensor that is divided into  $m$  segments. The encoded genes (refractive index for each segment) are generated randomly around the initial value of the refractive index  $n_{\text{eff}}=1.46$ .

A population consist of different solutions to the refractive index distribution corresponding to the  $x$ -polarized axis in equation (3.4) in the form of  $l$  (individuals) by  $m$  (segments) matrix is then constructed which represents candidates or possible solutions to the problem as

$$\text{Population} = \text{Individuals} \left\{ \begin{array}{c} \overbrace{\left[ \begin{array}{ccc} n_{1x}^1 & \dots & n_{1x}^m \\ \vdots & & \vdots \\ n_{kx}^1 & \dots & n_{kx}^m \\ \vdots & & \vdots \\ n_{lx}^1 & \dots & n_{lx}^m \end{array} \right]}^{\text{Segments}} \end{array} \right. \quad (3.5)$$

where  $n_{kx}^i$  is the refractive index corresponding to the  $x$  axis of the  $i^{\text{th}}$  segment of the individual  $k$ .

The algorithm optimally searches for the best individual of the population that can create a reflected spectrum that has the lowest fitness function with the reflected spectrum of the sensor corresponding to the  $x$  axis (slow-axis reflected spectrum).

The fitness function  $f(k)$  for each individual  $k$  of the population is defined as the difference between the reflectivity associated with the sensor's reflected spectrum  $R_{objective}(\lambda)$  and its respective reflection constructed from the individual  $k$  of the population  $R_k(\lambda)$  when the wavelengths are discretized into the  $p$  wavelengths.

The fitness function can be expressed as

$$f(k) = \sum_{i=1}^p \left| R_{objective}(\lambda_i) - R_k(\lambda_i) \right|^2 \quad (3.6)$$

After calculating the fitness of each individual in the current generation (iteration), the individuals are assigned a relative weight. The lower the fitness function, the higher is the likelihood that an individual is going to be selected. The relative weight  $RW$  for the individual  $k$  is defined as [77]

$$RW^k = [k - (h - 1)]^a \quad (3.7)$$

where  $a$  is the weight factor  $1 \leq a \leq 1.5$  and  $h$  varies from 1 to the number of individuals when they are sorted from the minimum fitness value (best candidate solution) to the highest fitness value (worst candidate solution). Therefore, the best individual has the relative weight of  $k^a$  and the best second individual has the relative weight of  $(k-1)^a$  and

so on [84]. The probability of the selection for a given individual  $k$ ,  $PR^k$ , can be calculated according to [77]

$$PR^k = \frac{RW^k}{\frac{1}{l} \sum_{j=1}^l RW^j} \quad (3.8)$$

where  $l$  is the number of individuals.

The expected number of copies for each individual  $k$ ,  $EC^k$ , can be obtained from the probability of the selection in equation (3.8) times the number of the individuals in the population ( $l$ ) as

$$EC^k = l \frac{RW^k}{\frac{1}{l} \sum_{j=1}^l RW^j} \quad (3.9)$$

The expected number of copies for each individual in equation (3.9) is obtained by rounding its solution to the nearest integer. A new population is then formed by selecting the individuals by following the two most popular selection methods which are the tournament selection and the fitness proportionate selection (also known as the roulette wheel selection). This is done by selecting a percentage of the new population by choosing individuals (and their copies) with the lowest fitness function. The remaining population is then constructed by the tournament selection in which a group of individuals are opted for randomly from which a number of individuals with the lowest fitness functions are selected and the rests are discarded.

The number of the selected individuals with the lowest fitness function depends on the tournament size which can vary from two to the number of individuals. The procedure of the tournament selection is repeated until the new population has the same number of individuals as the initial population.

After the selection process is completed and generating a selected population, crossover operator is applied to the population. Crossover produces new individuals from the selected population in order to generate better individuals from each of the parents (selected individuals).

In this thesis, we have used the two-point crossover method, due to its reliability, which selects two points from two individuals (parents) that are selected according to the cross-over probability (the probability that the crossover operator is applied to each individual). The genes between these two points are swapped between the two individuals rendering to two new off-springs (children).

Consequently, the mutation procedure is applied to individuals of the population. Mutation occurs according to the user-defined mutation probability ( $p_m$ ). The genes of each individual  $k$  have an equal chance of being mutated according to  $p_m$ . If this probability is set too high, the selection would be primitive random. We have used a non-uniform mutation that is proposed in [73]. The maximum and the minimum values of all current members of the population are set as the lower and the upper bounds of the problem.

For each chromosome of  $n = \{n_x^1, \dots, n_x^k, \dots, n_x^m\}$ , the mutation of an element  $n_x^k$  would

result in  $n = \{n_x^1, \dots, n_x^{k'}, \dots, n_x^m\}$  where  $n_x^{k'}$  for each generation  $G$  is given by

$$n_x^{k'} = \begin{cases} n_x^k + F(\text{Max}(n_x^k) - n_x^k) & r = 0 \\ n_x^{k'} - F(n_x^{k'} - \text{Min}(n_x^{k'})) & r = 1 \end{cases} \quad (3.10)$$

where  $r$  is a random number that can be 0 or 1. The  $\text{Max}(n_x^k)$  and  $\text{Min}(n_x^{k'})$  are the Max and Min values of the chosen chromosome. The increase or decrease of the genes depends on the  $F(y)$  function that is given by [73]

$$F(y) = \left[ yr \left( 1 - \frac{G}{T} \right) \right]^B \quad (3.11)$$

where  $G$  is the number of current generation (iteration),  $T$  is the maximum number of generations (which can be set *a priori*), and  $B$  is a weighting factor ( $1 < B < 5$ ) which determines the degree of the non-uniformity. Finally, elitism detects if the lowest fitness value of the new population is higher than that of the previous one. If this is the case, the operator replaces the individual with the lowest fitness function from the previous iteration with the individual of the new generation.

The spectrum of the  $x$ -polarized modes is reconstructed in each iteration. The refractive index distribution, which is correlated to the transversal load, can be obtained from the best solution of the algorithm. The best solution for the refractive index change

of  $x$ -polarized modes is attained when the GA converges to the lowest value of the fitness.

The obtained refractive index for each segment along the fiber by the GA could be correlated with the transversal load for each segment of the sensor fiber by using equations (2.10) and (3.1) as is depicted in Figure 3.4.

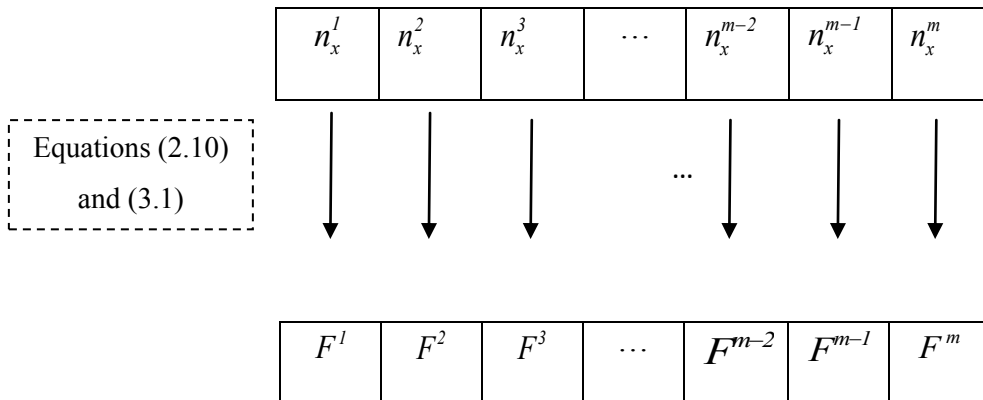


Figure 3.4 Schematic of the derivation of the transversal load of each segment of the fiber from the obtained refractive index corresponding to the same segment.

Therefore, the subjected transversal load for each segment can be obtained. In the next section, the efficiency of the GA for reconstruction of a non-uniform distribution of the longitudinal and the transversal loads that are simultaneously applied to a sensor is discussed.



### 3.1.2 Synthesis of a Two-Dimensional Strain (Longitudinal and Transversal Loads) Applied to an FBG Sensor

In this section, we present our methodology for detection of a non-uniform distribution of the longitudinal and the transversal loads along the sensor. The sensor is subjected to strains in three dimensions, i.e.,  $\varepsilon_x$ ,  $\varepsilon_y$ , and  $\varepsilon_z$ . As discussed earlier, the polarized reflected spectrum corresponding to the fast axis ( $y$ -polarized spectrum) of the FBG sensor is almost insensitive to the transversal load. Therefore, the deformation and shift of the reflected spectrum corresponding to the fast axis of the sensor that is subjected to the longitudinal and transversal loads simultaneously is dominantly due to the longitudinal strain. It can be concluded that the longitudinal strain along the fiber can be obtained by reconstructing the reflected spectrum corresponding to the fast axis of the fiber.

As discussed in Chapter 2, for a uniform grating the applied longitudinal strain induces changes in both the grating period and the refractive index. The two effects can be linearly superimposed by applying the effective strain of  $(1-p_e)\varepsilon(z)$  to the sensor [79]. Therefore, the changed grating period of each segment  $I$  due to the longitudinal strain,  $(\varepsilon_i(z))$ , along the fiber that is divided into the  $m$  segments can be estimated as [79]

$$\Lambda_i = \Lambda_0 + \Delta\Lambda_i \equiv \Lambda_0 + \Lambda_0(1-p_e)\varepsilon_i(z) \quad (3.12)$$

where

$$p_e = \frac{n_{eff}^2}{2} [p_{12} - v(p_{11} + p_{12})] \quad (3.13)$$

and  $\Lambda_0$  is the initial grating period of the undisturbed FBG sensor.

Therefore, the longitudinal strain along the sensor's fiber can be obtained by calculating the grating period of equation (3.12) in the Bragg grating for each segment  $i$  along the sensor. In order to obtain the grating period distribution, a random array ( $\Lambda_k$ ) is defined which represents a possible solution to the grating period distribution along the sensor and can be represented as [79]

$$\Lambda_k = \{\Lambda_k^1, \dots, \Lambda_k^m\} \quad (3.14)$$

where the subscript  $k$  denotes the individual number. The randomly obtained genes in equation (3.14) are represented by  $\Lambda_k^i$  and are obtained uniformly within the specified boundaries  $L$  around the initial grating period ( $\Lambda_0 = \frac{\lambda_B}{2n_{eff}}$ ) as  $\Lambda_0 - L < \Lambda_k^i < \Lambda_0 + L$ .

A population consists of  $l$  (individuals) by  $m$  (segments) is formed that represents the potential solutions to the grating period change along the fiber as

$$Population = Individual\ s \left\{ \begin{array}{c} \overbrace{\left[ \begin{array}{ccc} \Lambda_1^1 & \dots & \Lambda_1^m \\ \vdots & & \vdots \\ \Lambda_k^1 & \dots & \Lambda_k^m \\ \vdots & & \vdots \\ \Lambda_l^1 & \dots & \Lambda_l^m \end{array} \right]}^{Segments} \end{array} \right. \quad (3.15)$$

The reflected spectrum corresponding to the  $y$ -axis is then reconstructed using the individuals of population (3.15). The population goes through the process of selection, reproduction and mutation, and elitism until the GA converges to the lowest value for the fitness function. The best solution of the GA gives the grating period distribution along the sensor which is correlated to the longitudinal strain from equation (3.12). Figure 3.5 illustrates the method for obtaining the longitudinal strain along the sensor.

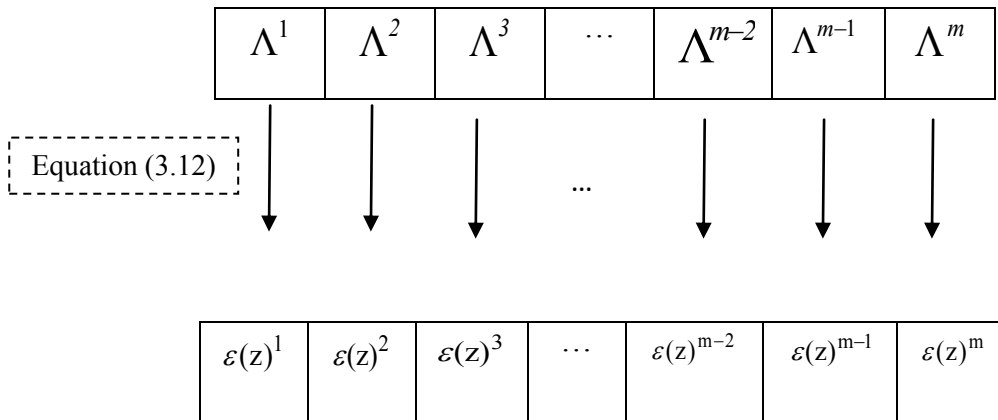


Figure 3.5 Schematic of the derivation of longitudinal strain applied to each segment of the fiber from the obtained grating period corresponding to that segment.

The superscripts in Figure 3.5 denote the number of segments along the fiber. Knowing the longitudinal strain along the sensor, the transversal load distribution can be obtained by reconstruction of the reflected spectrum corresponding to the slow axis.

In summary, the detection of the longitudinal and transversal loads from the distorted reflected spectrum of an FBG sensor that is subjected simultaneously to the longitudinal and transversal loads can be explained in two steps, namely:

**Step 1-** Since the Bragg spectrum corresponding to the fast axis ( $y$ ) of the sensor is almost insensitive to the transversal load; the longitudinal strain can be detected by the reconstruction of the fast axis reflected spectrum by the GA.

**Step 2-** The transversal load distribution along the sensor is obtained by reconstructing the reflected spectrum corresponding to the slow axis ( $x$ ) of the sensor by the grating period that was obtained in Step 1 (the grating period and the refractive index were linearly superimposed) and the best GA solution for the refractive index distribution corresponding to the slow axis.

The schematic of the GA for reconstructing the grating period and refractive index along the fiber is shown in Figures 3.6 and 3.7. Figure 3.6 graphically demonstrates the steps of the reconstruction of the longitudinal strain and the transversal loads. It should be noted that the methodology is only effective when there is a complete separation between the polarized spectra (due to the large transversal load) so that the distortion of the reflected spectrum corresponding to the fast axis can be easily detected.

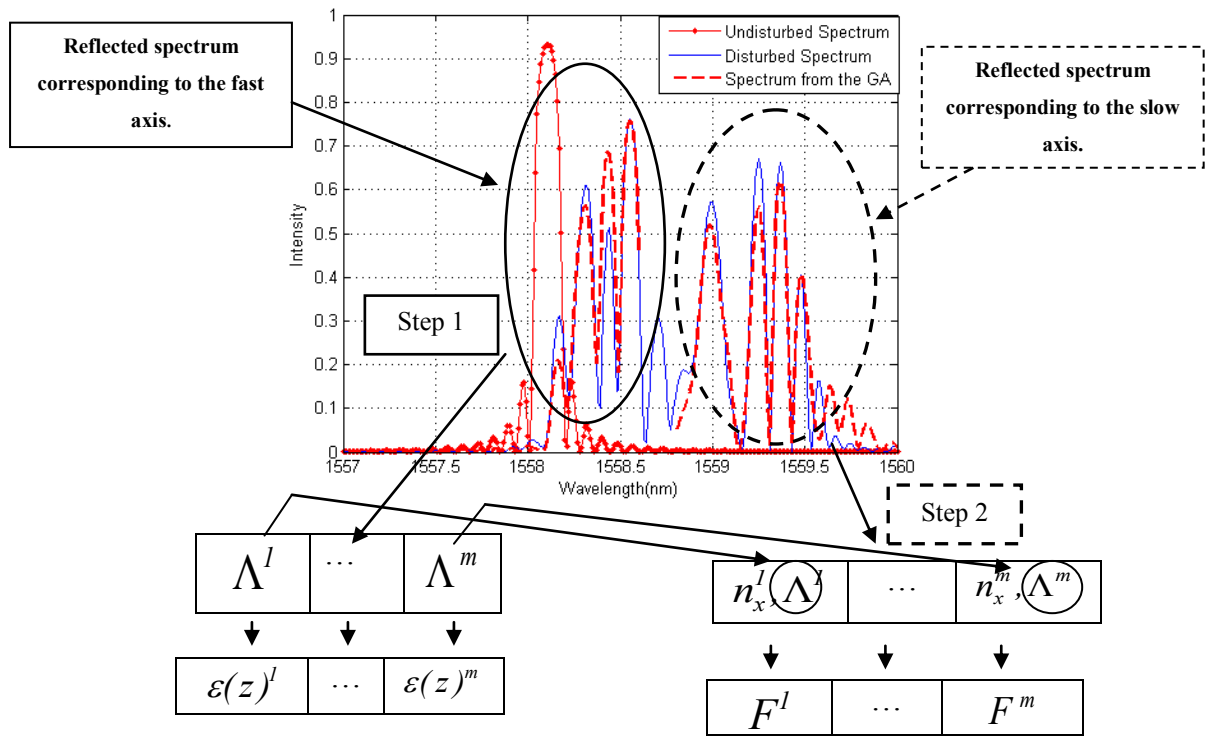


Figure 3.6 The schematic of the approach for reconstructing a non-uniform distribution of longitudinal strain and transversal load along the FBG sensor.

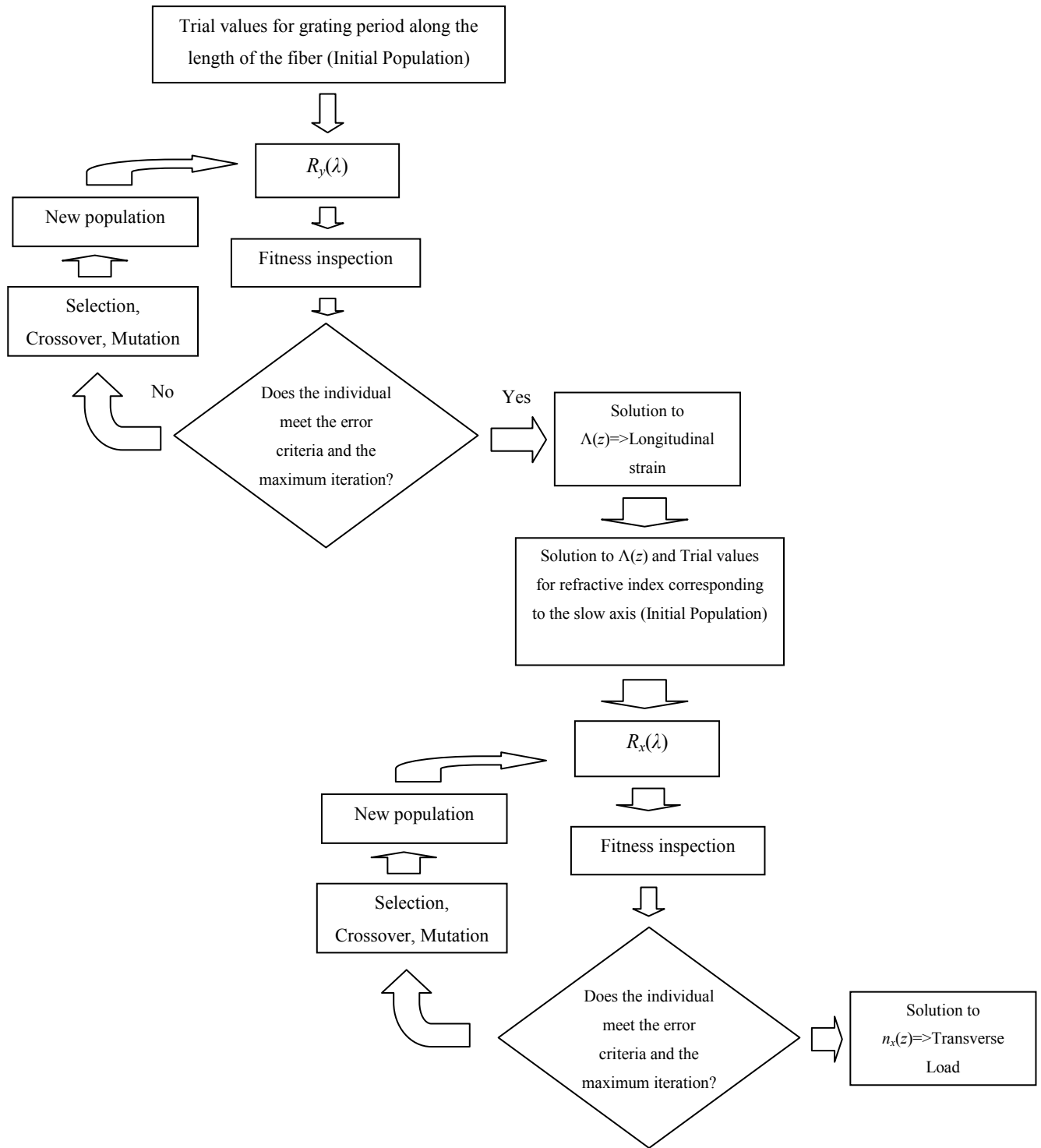


Figure 3.7 Flow chart of genetic algorithm for reconstruction of the load in two dimensions.

The procedure for our GA scheme for reconstruction of the distribution of the temperature is described in the next section.

## 3.2 Synthesis of the Temperature Distribution along the FBG Sensor

The grating period and refractive index of the fiber alter when the temperature of the fiber changes. The reflected spectrum of the FBG sensor is modeled by the T-matrix formulation. In doing so, the fiber is divided into  $m$  segments where the refractive index and the grating period of each segment  $m$  stray from their initial values  $\Lambda_0$  and  $n_{eff}$  for each segment as

$$\begin{aligned} n(m) &= n_{eff} + \Delta n(m) = n_{eff} + \xi \cdot n_{eff} \cdot T(m) \\ \Lambda(m) &= \Lambda_0 + \Delta \Lambda(m) = \Lambda_0 + \alpha \cdot \Lambda_0 \cdot T(m) \end{aligned} \tag{3.16}$$

where  $\alpha$  and  $\xi$  denote the thermal expansion and the thermo-optic coefficients, respectively. The temperature value for each segment is considered constant and is denoted by  $T(m)$ .

As discussed in Chapter 2, the distortion of the reflected spectrum that is subjected to the temperature change is mostly due to the refractive index change along the fiber. Therefore, in our approach the grating period along the fiber that is subjected to a non-uniform distribution of temperature is estimated to remain uniform and the population is defined based on the refractive index change within the specified

boundaries that are set to provide values uniformly around the initial effective refractive index of the FBG sensor,  $n_{eff}=1.46$  as

$$Population = Individuals \left\{ \begin{array}{c} \overbrace{\left[ \begin{array}{ccc} n_1^1 & \cdots & n_1^m \\ \vdots & & \vdots \\ n_k^1 & \cdots & n_k^m \\ \vdots & & \vdots \\ n_l^1 & \cdots & n_l^m \end{array} \right]}^{Segments} \end{array} \right. \quad (3.17)$$

where  $n_k^i$  denotes the refractive index corresponding to the  $i^{\text{th}}$  segment of the individual  $k$ .

For each iteration, the reflected spectrum of each individual of population given by equation (3.17) is reconstructed. The algorithm optimally searches for the best population individual that can create a reflected spectrum that has the lowest fitness function with the reflected spectrum of the FBG sensor that is subjected to the non-uniform distribution of the temperature along its length.

The population goes through the main operators of the GA until it converges to the optimal solution that gives the refractive index distribution along the sensor. The temperature change for each segment along the fiber can then be obtained from its corresponding refractive index change using equation (3.16). The proposed approach is validated by numerical examples in the next section.

### 3.3 Results and Discussions

In the first part of this section, the scenarios for reconstructing the transversal load that is applied along the FBG sensor with the characteristics given in Table 3.1 are presented.



The GA parameters are listed in Table 3.2. The case of plane strain ( $\varepsilon_z=0$ ) is assumed. The obtained fitness function for all the cases is in the order of  $10^{-1}$ .

The set separation between the two wavelengths (wavelength resolution) is 0.01 nm. As a result, for the Bragg grating fiber with the Bragg wavelength of 1558 nm, the minimum change in the transversal load that can be detected is 0.05 N. The separation of the reflected spectrum of the FBG sensor into two peaks becomes observable when the load is higher than 40 N. The effects of the non-uniform transversal force to the reflected spectrum of a 1-cm FBG sensor is modeled by using the T-matrix formulation as shown in Figure 3.8.

Table 3.1 Parameters of a 1-cm FBG sensor.

Parameters	Values
Length( $L$ )	10 mm
Mode effective index of refraction( $n_{eff}$ )	1.46
Initial period( $\Lambda_0$ )	533.5616nm
Mean index variation ( $\overline{\delta n_{eff}}$ )	$10^{-4}$
Young's modulus( $E$ )	74.52 GPa
Poisson's ratio( $\nu$ )	0.17
Strain coefficients $p_{11}, p_{12}$	0.121, 0.27
Thermal expansion coefficient( $\alpha$ )	$5.2 \times 10^{-7} \text{ } ^\circ\text{C}^{-1}$
Thermo-optic coefficient of ( $\xi$ )	$5 \times 10^{-6} \text{ } ^\circ\text{C}^{-1}$

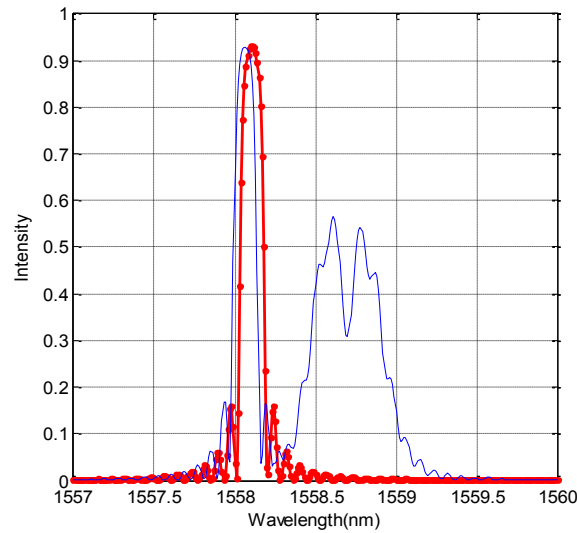


Figure 3.8 Reflected spectra of the FBG sensor ( —●— line) and the disturbed FBG subjected to a non-uniform distribution of transversal load ( — line).

The applied transversal load that is shown in Figure 3.9(b) is then detected by our proposed GA modeling approach by reconstructing the reflected spectrum as shown in Figure 3.9 (a). The parameter of the used GA is shown in Table 3.2. The genetic algorithm was iterated beyond convergence and the optimal solution has a low 0.22 fitness value (error function). Although, the difference in the reflected spectra of Figure 3.9 (a) does not seem significant, the reconstructed strain profile has about 9.23 N errors between the strain input and the GA optimal solution.

Table 3.2 Parameters of the genetic algorithm.

Parameters	Values
Segments	10
Individuals	800
Probability of crossover ( $p_c$ )	0.7
Probability of mutation ( $p_m$ )	0.01
Number of generations	60
Mutation weight factor	2
Weight factor	1.2

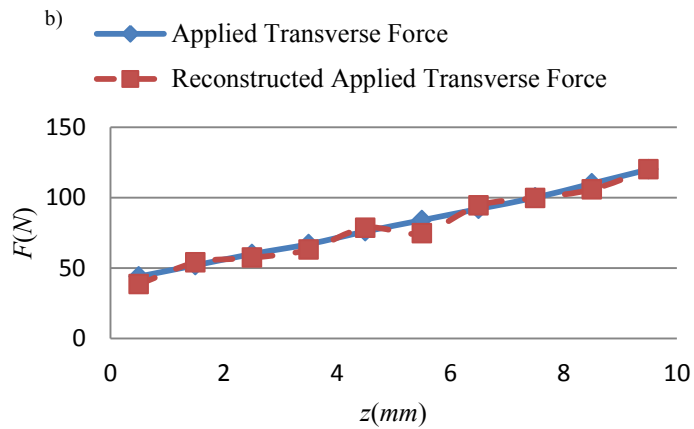
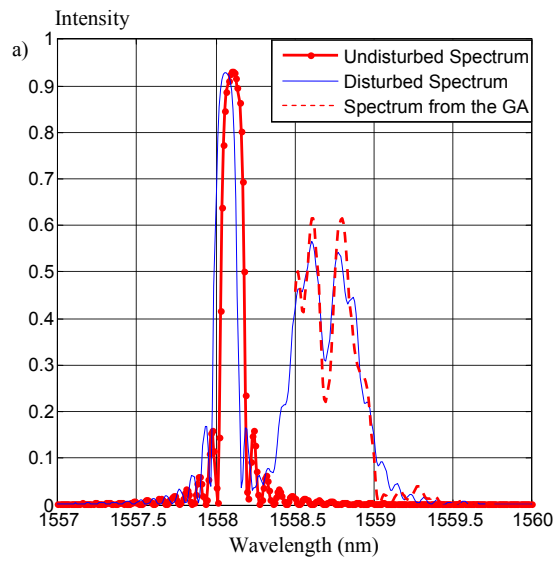


Figure 3.9a) Reflected spectrum of the optimal solution from GA. Also plotted is the reflected spectrum for the  $x$ -polarization of the Bragg grating sensor subjected to the transversal load, and b) applied transversal load distribution and reconstructed load profile by the GA optimal solution.

As the second numerical scenario, the reflected spectrum of the sensor subjected to an arbitrary transversal load distribution of Figure 3.10 (b) is shown in Figure 3.10 (a). The transversal load distribution is then obtained by reconstructing the reflected spectrum change of the FBG sensor due to the  $x$ -polarization by using the GA algorithm. A

selection of the wavelengths from 1558.5-1560 (nm) was chosen for comparison through the fitness function. The GA was iterated for 60 generations.

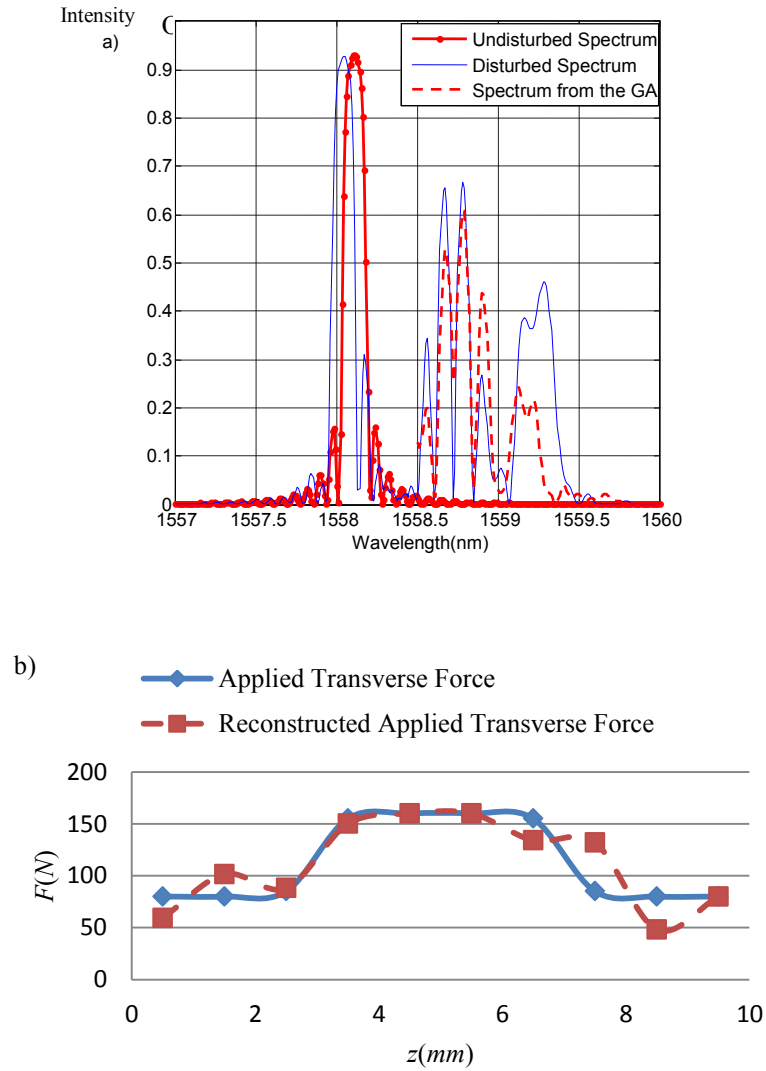


Figure 3.10 a) The Reflected spectrum of the optimal solution from GA for the  $x$ -polarization of the Bragg grating sensor subjected to the transversal load. The undisturbed and disturbed reflected spectrum obtained by the GA is also plotted, and b) applied transversal load distribution and reconstructed transversal load distribution by using the GA.

As seen in Figure 3.10 (b), although the trend-line and the estimation of the applied strain was captured, there is a maximum of 10 N error in the magnitude of the

transversal force. The genetic algorithm was iterated until it converges and the optimal solution had a 0.9 fitness value.

For the next case study, the reflected spectrum of a sensor that is disturbed by the transversal load distribution of Figure 3.11 (b) is shown in Figure 3.11(a). This was accomplished by reconstruction of the reflected spectrum change for the  $x$ -polarization.

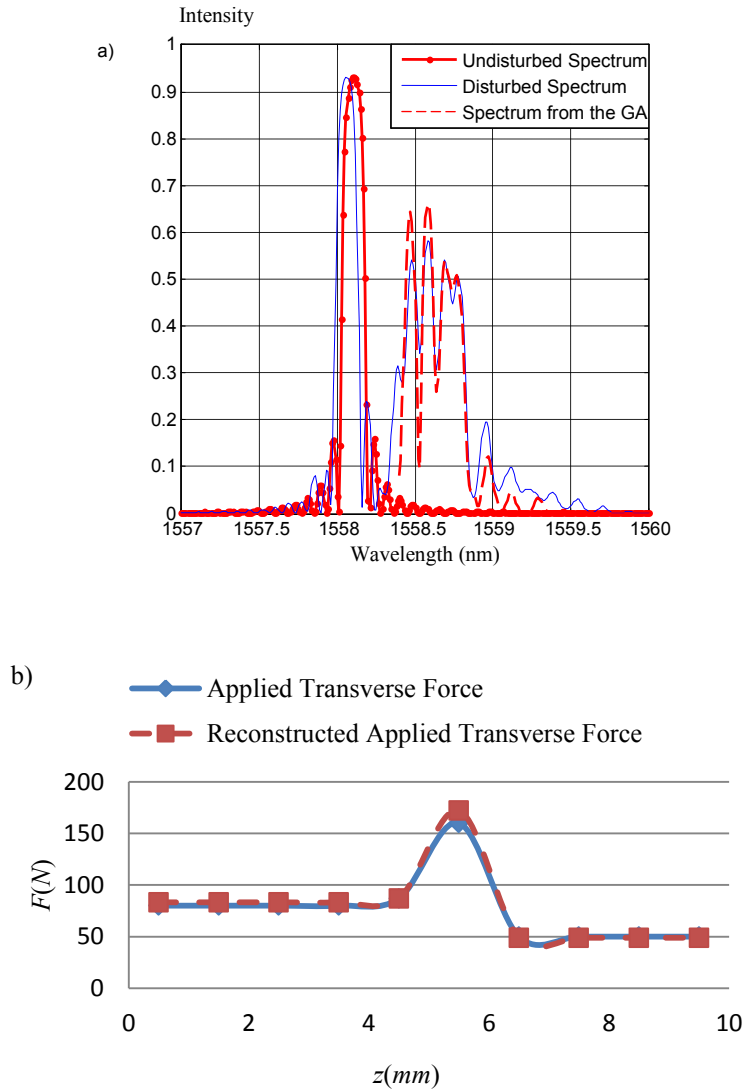


Figure 3.11 a) The reflected spectrum that is disturbed by the distribution of transversal load and the reflected spectrum that is obtained by the GA optimal solution, and b) the reconstructed and actual transversal load distribution.

The GA was calculated thorough 60 generations. The genetic algorithm was iterated until it converges and the optimal solution had a low 0.54 fitness value.

In the next scenario, the transversal load distribution along a series of identical sensors is interrogated by using the time division multiplexing (TDM) technique. A number of fiber Bragg grating sensors can be inscribed into the fiber to form a multiplexed sensor system. By using a series of the FBG sensors, the distribution of the anomaly can be detected to a larger scale problem. This would allow the FBG sensors to cover large surfaces for quasi-distributed sensing issues. In addition to detection of the transversal load distribution along an array of multiplexed FBGs, the position of the anomaly can be detected as well. This task is possible by gating the time that it takes for each reflected signal from any of the sensors to reach the detector. These reflected pulses arrive at the detector at a time determined by the distance between the interrogator and the FBG sensors.

As a numerical example, for detecting the distribution of the transversal load along the multiplexed sensor system, an optical source is assumed to be connected to a series of three identical sensors with Bragg wavelength of 1553 nm that are placed 5 mm apart from each other and are subjected to the longitudinal strain of 150, 200 and 300 micro-strain for each consecutive sensor, respectively. In addition to the longitudinal strain, the sensors are subjected to a non-uniform transversal force that is applied perpendicular to the optical axis of the sensor system. Figure 3.12 shows the shifted and the disturbed reflected spectra for the three disturbed sensors. The applied transversal force along the sensor system is shown in Figure 3.13 (a).

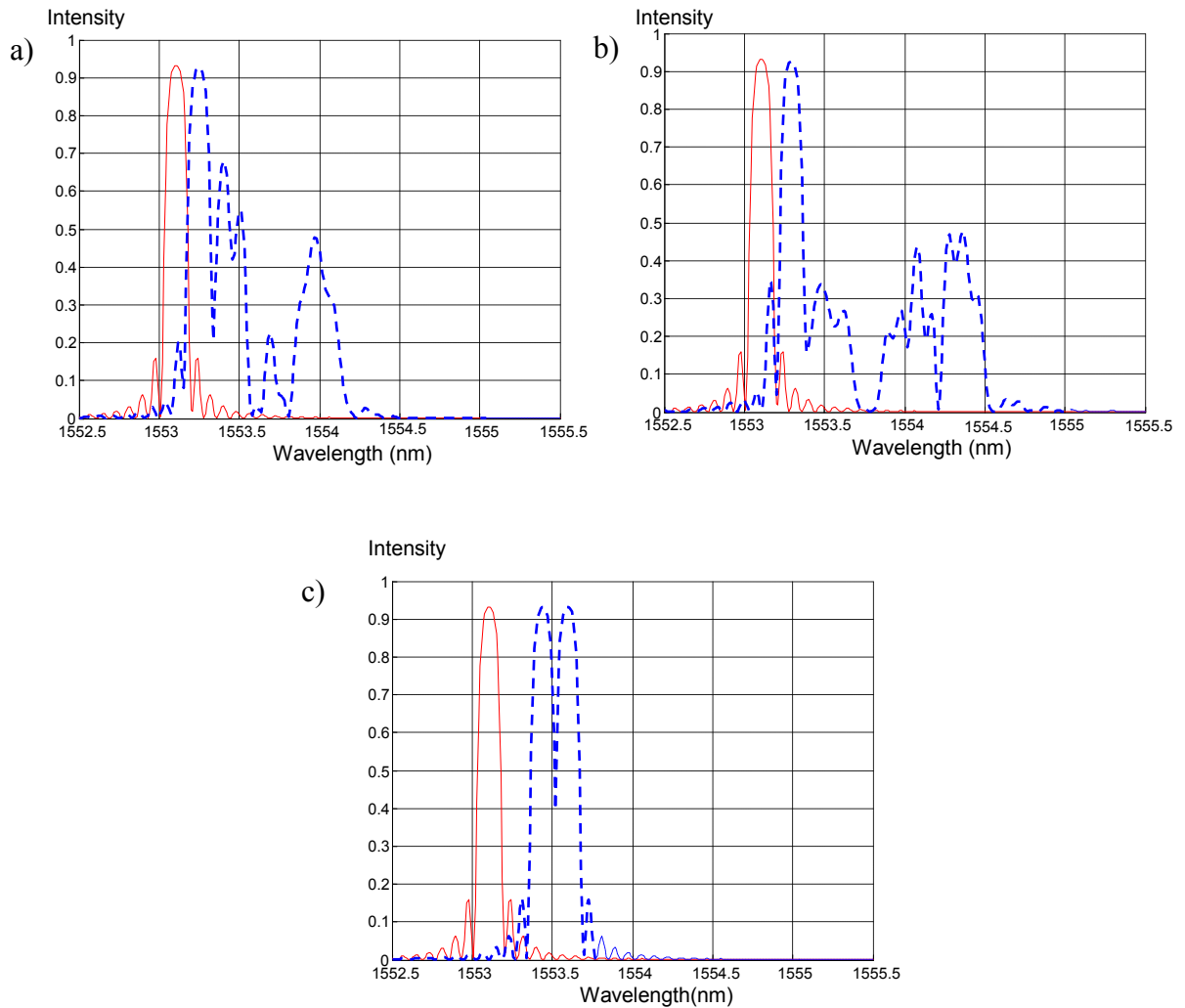


Figure 3.12 Reflected spectra of the three multiplexed disturbed sensors. The reflected spectra of the undisturbed FBGs are shown by the solid line.

As shown in Figures 3.14(a) and (b), this study performs the inverse extraction from the reflected spectrum for the  $x$ -polarized mode only since the wavelength deviation for  $y$ -polarized mode is almost insensitive to the normal transversal force. Each iteration of the algorithm improves the solution quality via the fundamental GA operators until the algorithm converges to the optimal solution. The reflected spectrum of the two

individuals with the lowest fitness value for the first and second disturbed sensors is shown in Figure 3.14 using star symbols.

The third sensor of the array is subjected to a uniform 20 N transversal force, which can be obtained directly from the separation between the two intensity peaks for the  $x$ - and  $y$ -polarized modes of the reflected spectra. The reconstructed transversal force profile along the multiplexed sensor system that is obtained through the GA is shown in Figure 3.13 (b).

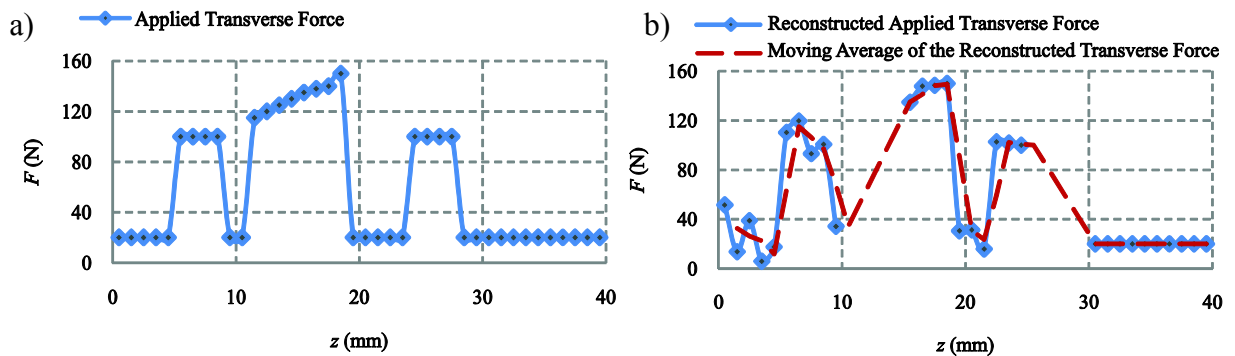


Figure 3.13a) Applied transversal force distribution along the three FBG sensors, and b) transversal force obtained by the GA.

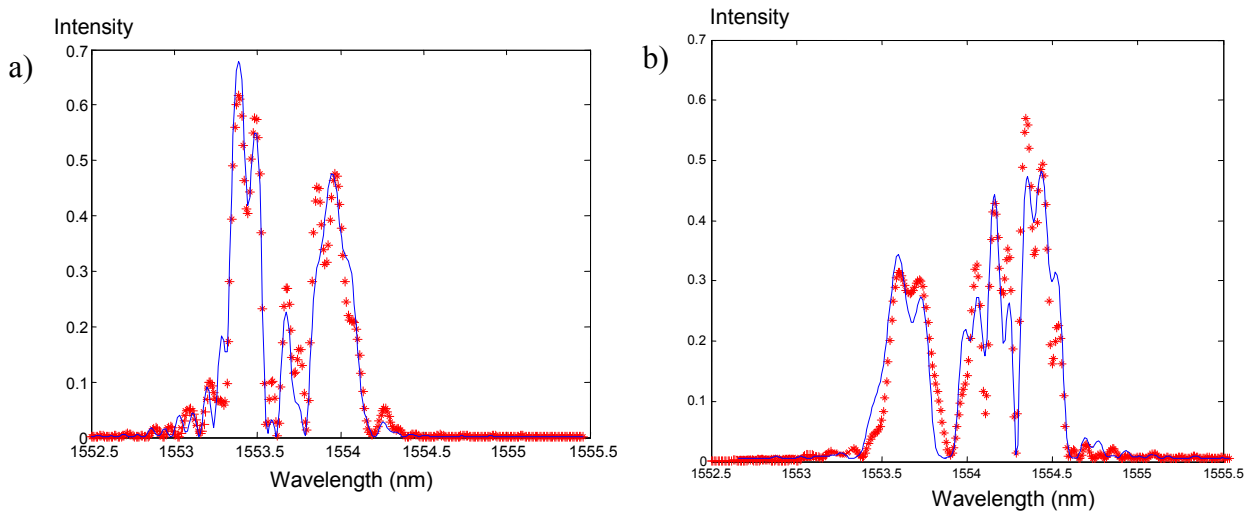


Figure 3.14 Reflected spectra corresponding to the slow axis (solid line) are reconstructed by the solution from the GA (star points) for a) the first sensor, and b) the second sensor.



The genetic algorithm was iterated until it converges and the optimal solution has a low 0.241 and 0.28 fitness values (error function) for the first and the second disturbed sensors, respectively. Although the recovered strain profile does not precisely match the applied one, the trend of the applied force is captured excellently with a minimum number of segments required for reconstruction of the reflected spectrum changes due to the transversal force.

The following numerical examples validate the technique for reconstruction of the longitudinal strain along an FBG sensor. The set separation between the two wavelengths (wavelength resolution) is 0.01 nm. Consequently, for the Bragg grating fiber with the Bragg wavelength of 1558 nm, the minimum gradient that can be detected is 8 micro-strain. The obtained fitness function for all the cases is in the order of  $10^{-1}$ .

As a first example, the longitudinal strain that results in the distortion of the reflected spectrum in Figure 3.15 is modeled by the GA. Figure 3.16 (a) shows the comparison between the original spectrum and the one that is constructed by the GA. The GA was iterated until it converges for 100 generations and the obtained optimal solution has a low 0.7017 fitness value (error function). The applied and the reconstructed longitudinal strains are also shown in Figure 3.16(b). As an example, Figure 3.15 shows the reflected spectrum of the same sensor shown in Figure 2.3 for the case of 10 kN load that is modeled theoretically by T-matrix.

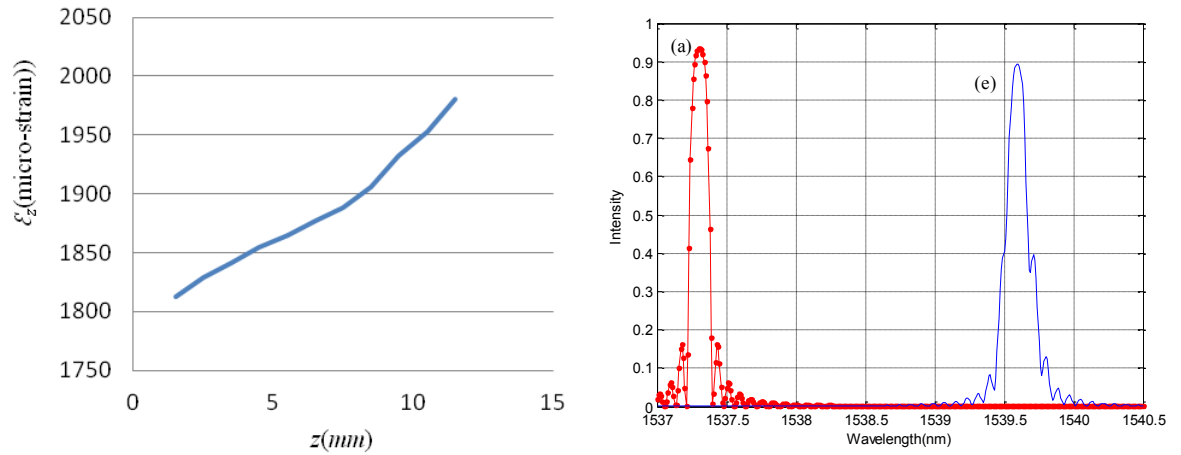


Figure 3.15 The reflected spectrum corresponding to (e) of Fig. 2.3 that is obtained by the T-matrix.

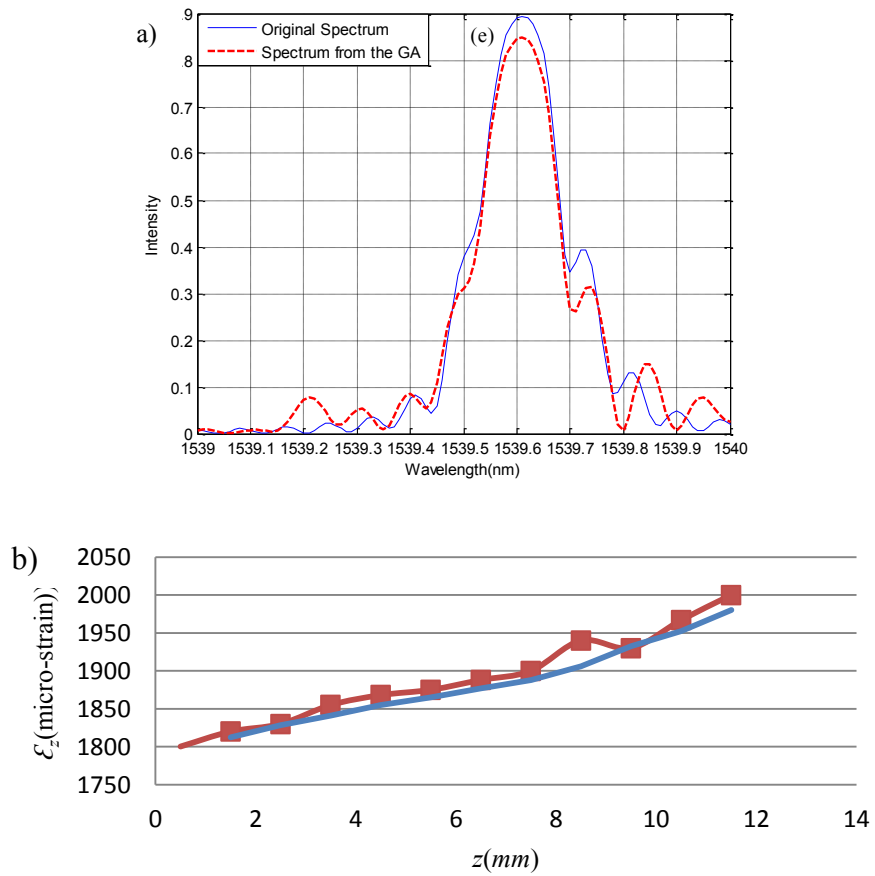


Figure 3.16 a) Comparison between the original spectrum and the one that is obtained by the GA, and b) comparison between the applied longitudinal strain and the one that is obtained by the GA.

Figures 3.17 (a) and (b) show the undisturbed and the disturbed reflected spectrum of the sensor, respectively by the longitudinal strain shown in Figure 3.17 (c). The reconstructed spectrum is also plotted in Figure 3.17 (b) which is obtained when the algorithm converges to the fitness function of 0.5532.

Figure 3.18 (a) shows the reflected spectrum of the sensor that is subjected to a non-uniform sinusoidal shaped longitudinal strain of Figure 3.18 (b). Figure 3.18 (b) also shows the longitudinal strain that was obtained by the GA. As can be observed from this figure, the reconstructed longitudinal strain profile is in the exact reverse order as the applied longitudinal strain. The reason is that the reflected spectra of the two FBG sensors that are subjected to the same strain profile in the exact reverse distribution are identical. Figure 3.18 (c) shows the longitudinal strain that was obtained by rerunning the algorithm assuming that the longitudinal strain has its Max value at  $z=0$ .

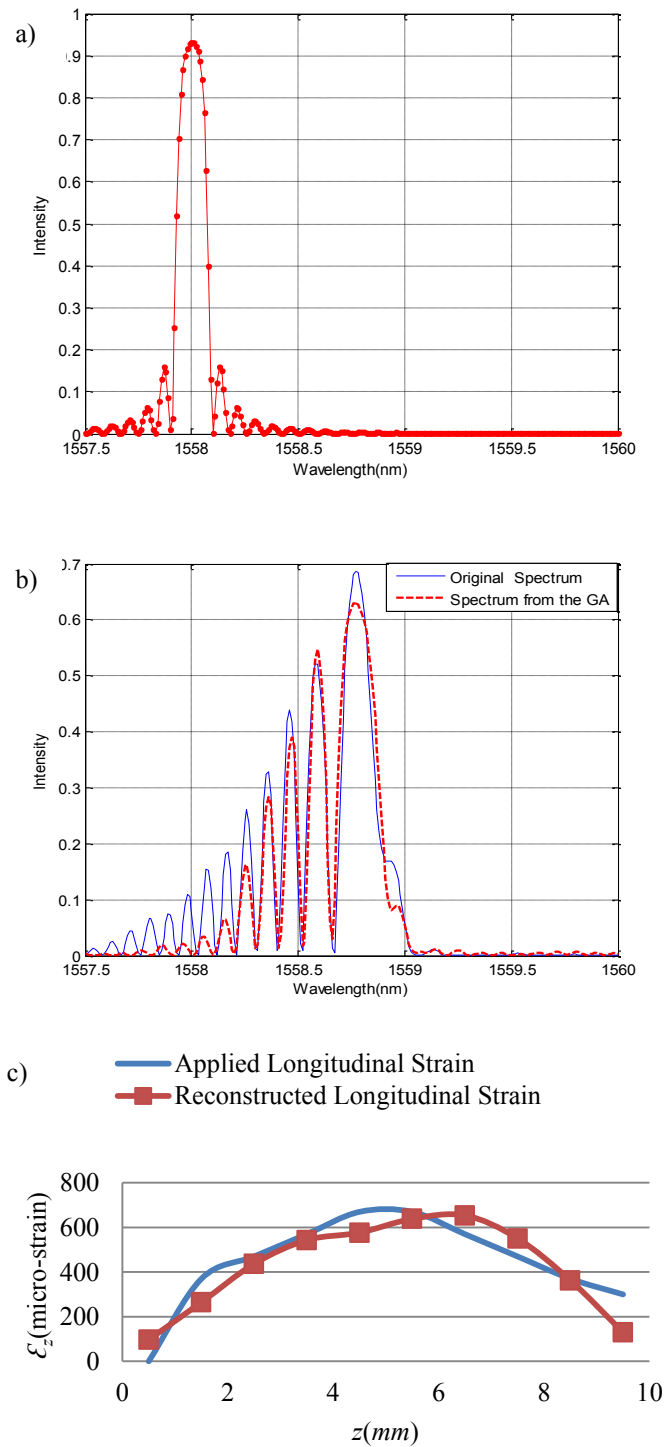


Figure 3.17a) Undisturbed reflected spectrum of the FBG, b) comparison between the original disturbed spectrum by the longitudinal strain and the one that is obtained by the GA, and c) comparison between the applied longitudinal strain and the one that is obtained by the GA.

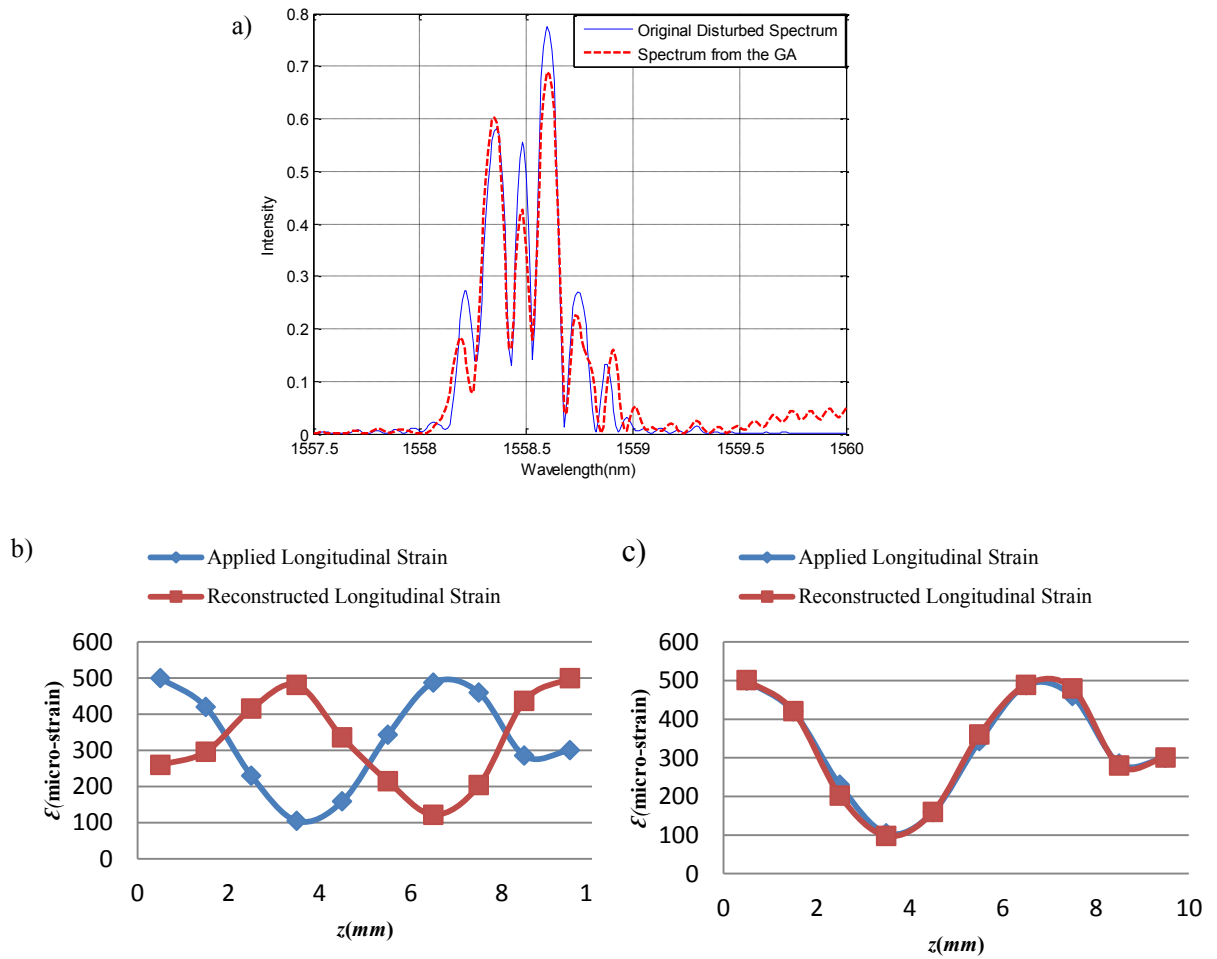


Figure 3.18a) Comparison between the original disturbed spectrum by the longitudinal strain and the one that is obtained by the GA, b) comparison between the applied longitudinal strain and the one that is obtained by the GA, and c) comparison between the applied longitudinal strain and the one that is obtained by the GA setting an initial condition.

As the last case study, Figure 3.19(a) shows the reflected spectrum of the disturbed FBG by the longitudinal strain shown in Figure 3.19(b). The obtained fitness function is 0.2 and the maximum difference between the original and reconstructed longitudinal strain is 45.32 micro-strain.

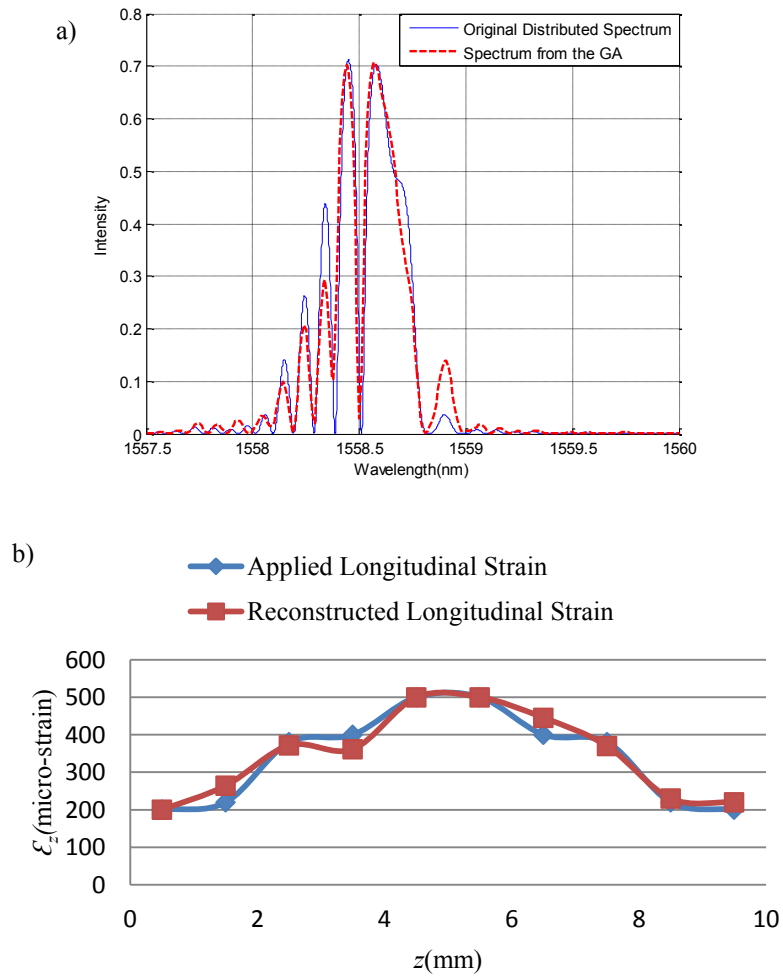


Figure 3.19a) Comparison between the original disturbed spectrum by the longitudinal strain and the one that is obtained by the GA, and b) comparison between the applied longitudinal strain and the one that is obtained by the GA.

Although the recovered anomaly profile does not precisely match the applied one, the trend of the applied perturbation is perfectly captured. For the health monitoring applications, it is very important to detect the location of an anomaly (damage) in addition to estimating the shape and the severity of the strain. Towards this end, we have reconstructed the longitudinal strain along series of multiplexed sensor system.

We have used a series of 10 sensors with different initial chirped gratings, where the first sensor has the initial grating period of 531 nm and the difference between the

two consecutive grating period is 4 nm, resulting in a wavelength division multiplexing (WDM) FBG sensor network. WDM encodes each FBG with a unique spectral slice of the available source spectrum, which defines the sensor's operating range. An immediate advantage of the wavelength discrimination between sensors is that the location of the applied strain can be realized immediately given that the fiber length is associated with different unique FBG wavelengths along the fiber.

Figure 3.20 (a) shows the reflectivity of the studied WDM FBG sensor network that is obtained by using the T-matrix method. Figure 3.20 (b) shows the perturbed reflection spectrum (dashed line) of the multiplexed sensor system when it is subjected to a non-uniform longitudinal strain shown in Figure 3.21. Figure 3.20 (c) shows the reflectivity of the sensor in the place of the damage and the strain shape that was reconstructed by using the genetic algorithm which was iterated until its convergence for 100 generations.

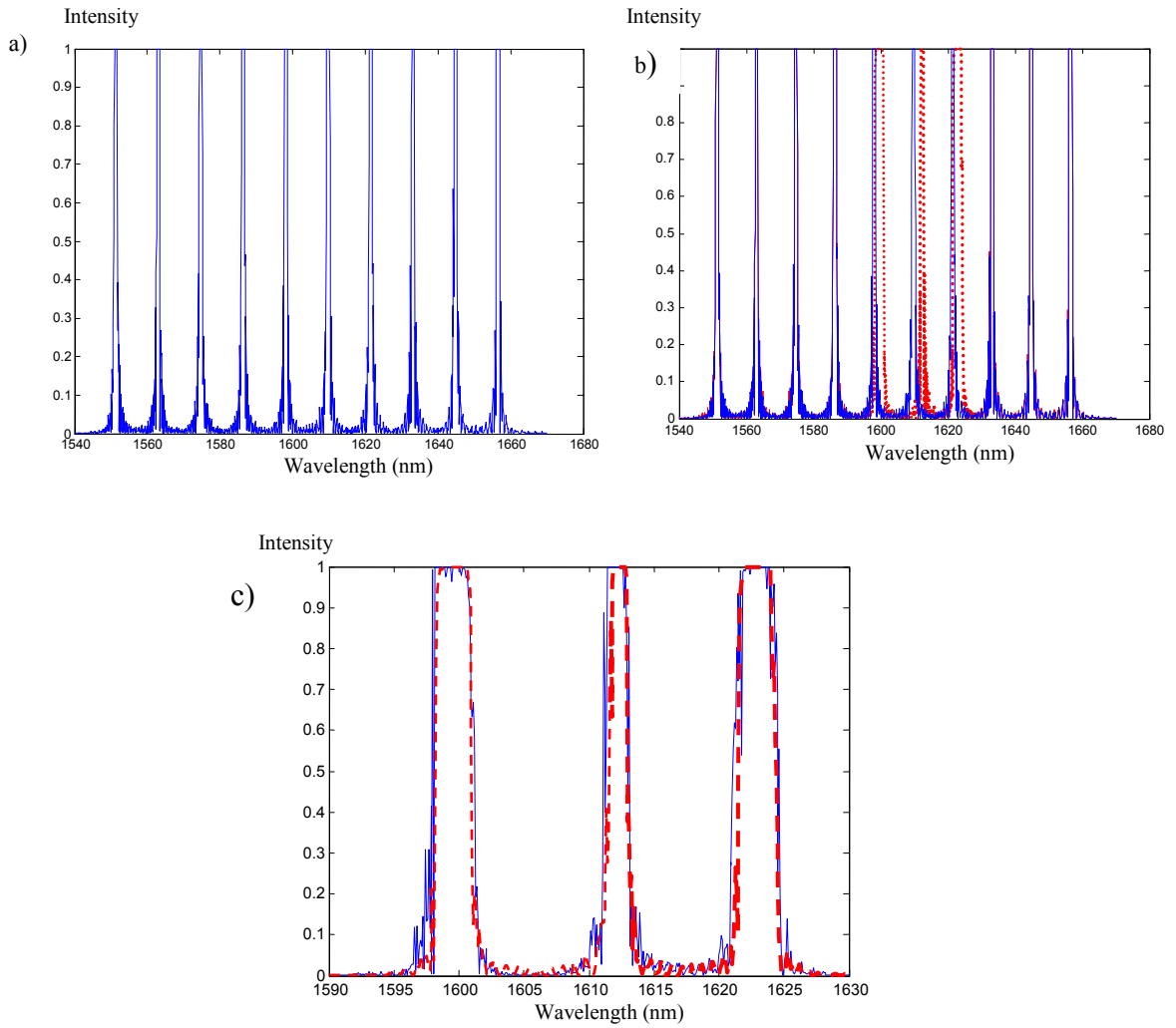


Figure 3.20a) Reflected spectrum of a WDM FBG sensor network, b) reflected spectrum of the three sensors of and reflection of the same sensor when WDM sensor is affected by the strain in Fig 3.21, and c) Original (solid line) and the reconstructed of the disturbed reflected spectrum by the GA .



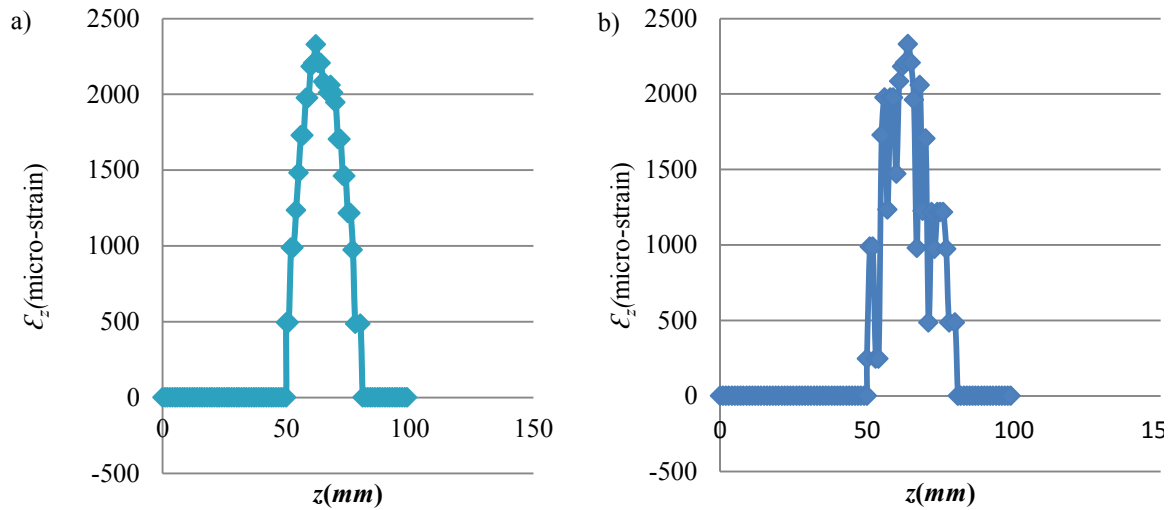


Figure 3.21a) Arbitrary strain that is applied to the WDM FBG versus its length, and b) strain obtained from GA algorithm.

As can be seen in Figure 3.21, the trend-line and estimation of the applied strain was excellently captured.

The following examples demonstrate the efficiency of our approach for modeling the distribution of the anomaly when the sensor is subjected to the longitudinal and the transversal load simultaneously. The disturbed reflected spectrum of an FBG sensor, which is subjected to the longitudinal strain and the transversal loads of Figures 3.22 (b) and (c) is shown in Figure 3.22 (a).

The reflected spectra corresponding to the  $y$  and  $x$ -polarized axes that are modeled with individuals of the GA with the lowest fitness values are also shown in Figure 3.22 (a). The fitness function values are 0.1 and 0.83 for the longitudinal and the transversal loads, respectively. The wavelengths of the  $x$ -polarized and  $y$ -polarized modes are scanned separately and as a result a gap from 1558.7 to 1558.95 is seen in the reconstructed spectrum of Figure 3.22 (a).

Figures 3.22(b) and (c) show the reconstructed longitudinal strain and the transversal loads by the GA that is obtained after 70 generations. The algorithm was iterated until its convergence. The root mean square (RMS) errors between the original anomaly and the reconstructed one for the longitudinal strain and the transversal loads are  $72.84 \mu\epsilon$  and  $21.15 N$ , respectively. As observed from Figure 3.22(a), although the calculated spectrum with the GA does not exactly match the original disturbed spectrum, the wavelengths with the local maximum intensity were captured.

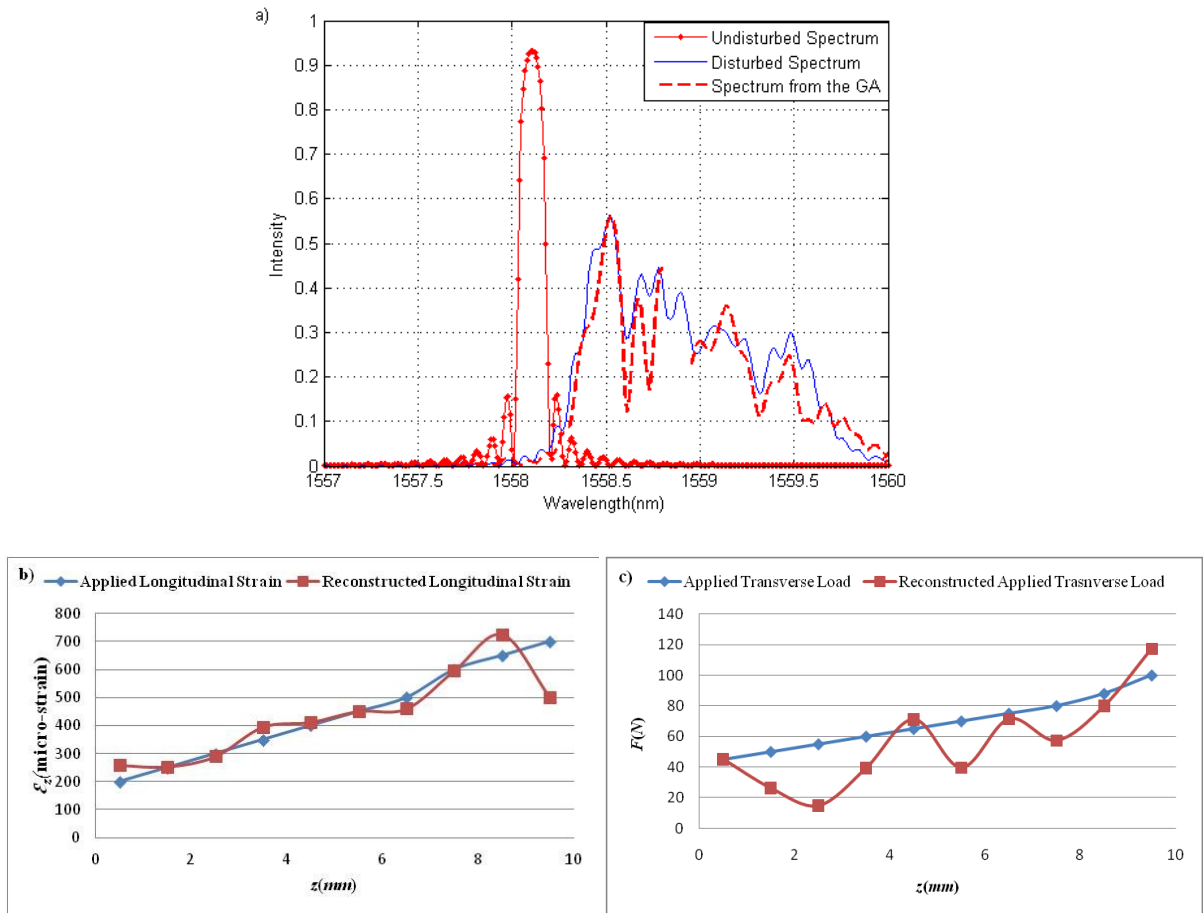


Figure 3.22 The reflected spectrum of the optimal solution from the GA (dashed line) that is compared with the original reflected spectrum (solid line). The sensor is subjected to the two-dimensional anomaly of figure 3.22 (b) and (c). The undisturbed reflected spectrum of the sensor is also shown with the dotted line in figure 3.22(a).

Figure 3.23(a) depicts the original and the reconstructed reflected spectrum of the sensor subjected to the more complicated sinusoidal strain distribution of Figures 3.23(b) and

(c). The reconstructed strain distributions are also shown in Figures 3.23(b) and (c). The RMS errors between the original longitudinal strain profile and the reconstructed one and the original transversal load profile and reconstructed one are  $67.92\mu\epsilon$  and  $17.98\text{N}$ , respectively. The genetic algorithm was iterated until its convergence for the 70 generations.

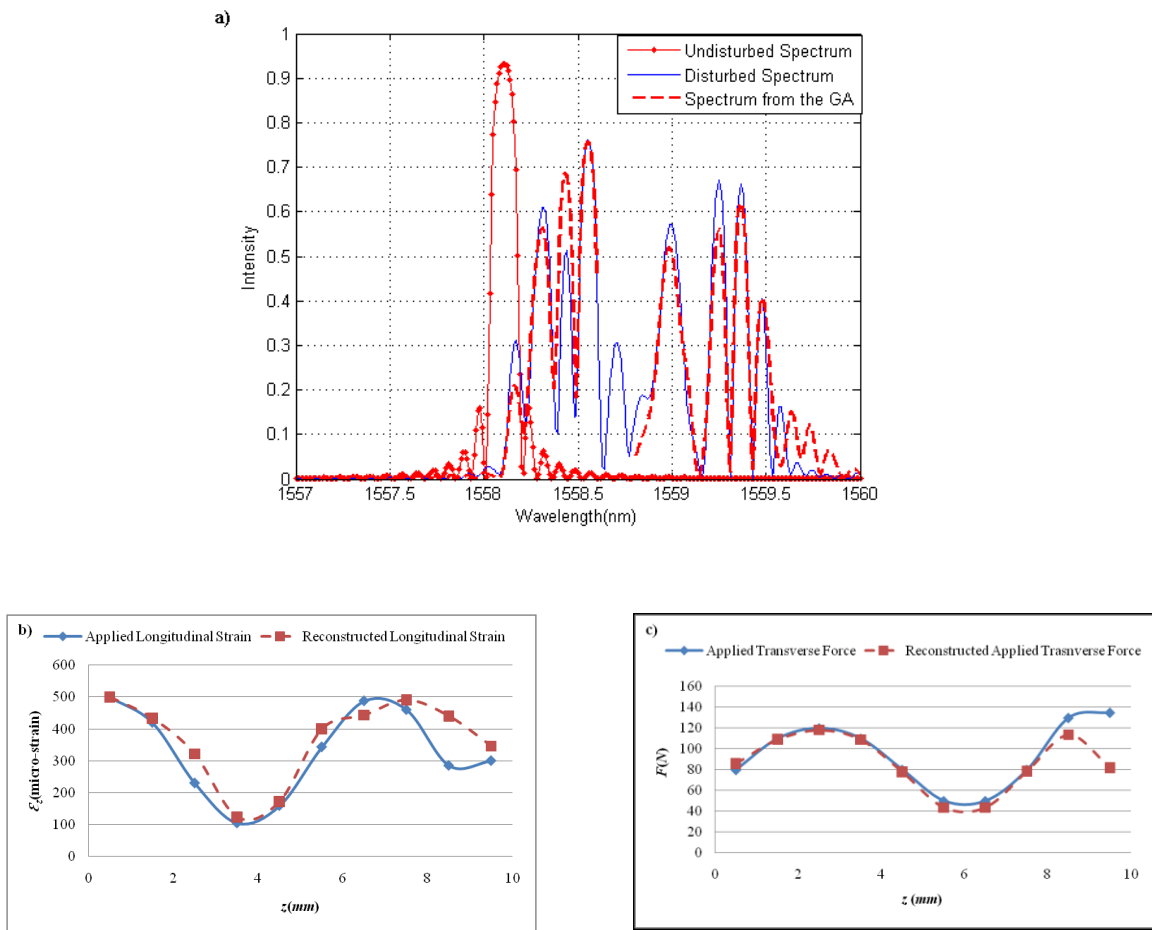


Figure 3.23a) The disturbed (solid line) and reconstructed reflected spectra of optimal solution from GA (dashed line) subjected to the b) sinusoidal longitudinal strain distribution, and c) sinusoidal transversal force distribution. The reconstructed perturbations are also shown in the figure. The undisturbed reflected spectrum of the sensor is shown with the dotted line in figure 3.23(a).

Similarly, Figure 3.24(a) depicts the reflected spectrum and the reconstructed spectrum by the GA of the sensor that is subjected to an arbitrary shaped simultaneously applied

longitudinal strain and the transversal load of Figures 3.24(b) and (c). The reconstructed longitudinal and the transversal loads profiles are also shown in Figures 3.24(b) and (c), respectively. The RMS error between the original longitudinal strain profile and the reconstructed one and the original transversal load profile and the reconstructed one have been obtained to be  $26.13 \mu\epsilon$  and  $9.08 \text{ N}$ , respectively.

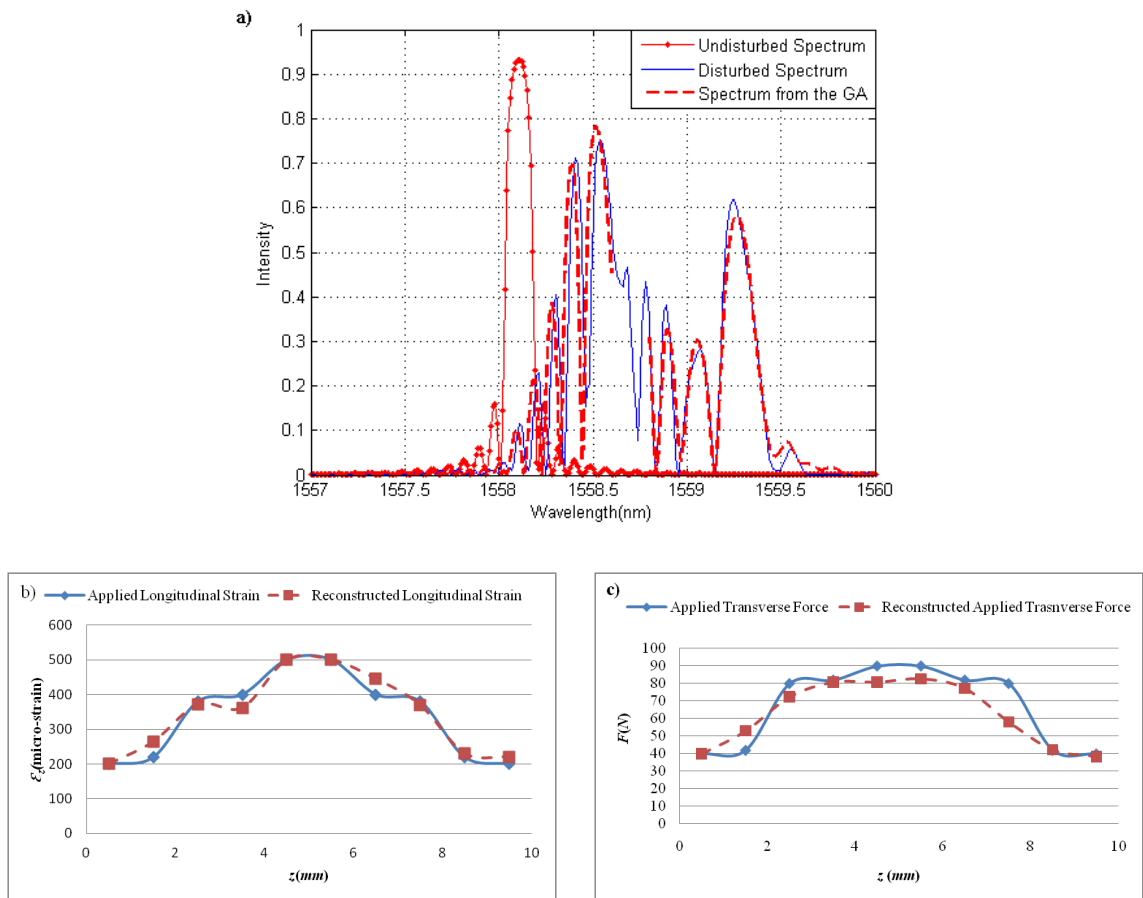


Figure 3.24a) The disturbed (solid line) and reconstructed spectrum from the optimal solution of GA (dashed line) subjected to a non-uniform perturbation of b) longitudinal strain, and c) transversal force distribution. The reconstructed perturbations are also shown in the figure. The undisturbed reflected spectrum of the sensor is shown with the dotted line in figure 3.24(a).

The following numerical examples demonstrate the approach for reconstruction of a non-uniform distribution of temperature along the FBG sensor. Figure 3.25 shows the 0.1 nm

shift of the Bragg wavelength due to the temperature change of 10 °C for a sensor with characteristics as given by Table 3.1.

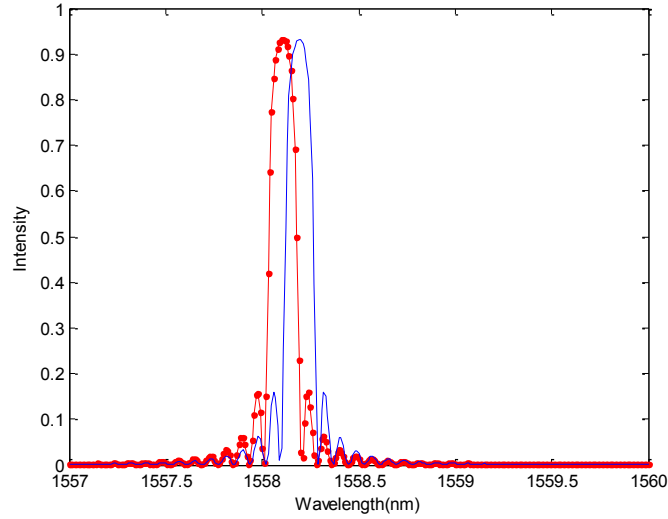


Figure 3.25 The shift of the Bragg wavelength when the sensor is subjected to the uniform temperature change of 10°C. The undisturbed reflected spectrum of the sensor is shown with the “—” line. The “—●—” line shows the spectrum after the temperature change.

Figure 3.26 shows the spectral response of the same sensor when it is subjected to different non-uniform distributions of temperature along its length.

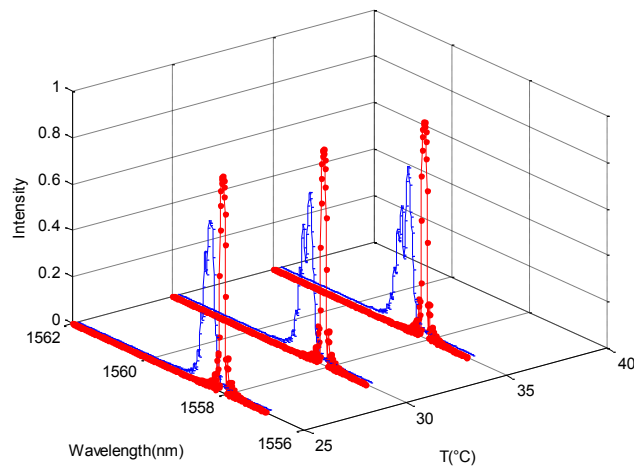


Figure 3.26 Reflected spectra of the FBG sensor subjected to the temperature change of  $T(z)=T_0(1+(z/L)^2)$  °C. The undisturbed reflected spectrum is shown with the “—●—” line.

As can be observed from Figure 3.26, for a case when the sensor is subjected to a non-uniform temperature distribution along its gauge's length, the reflected spectrum gets more complicated and comprises of multiple peaks.

Figure 3.27(a) shows the disturbed reflected spectrum of the sensor when it is subjected to a non-uniform distribution of temperature shown in Figure 3.27 (b). The disturbed reflected spectrum is reconstructed when the algorithm converges to the fitness function of 0.9.

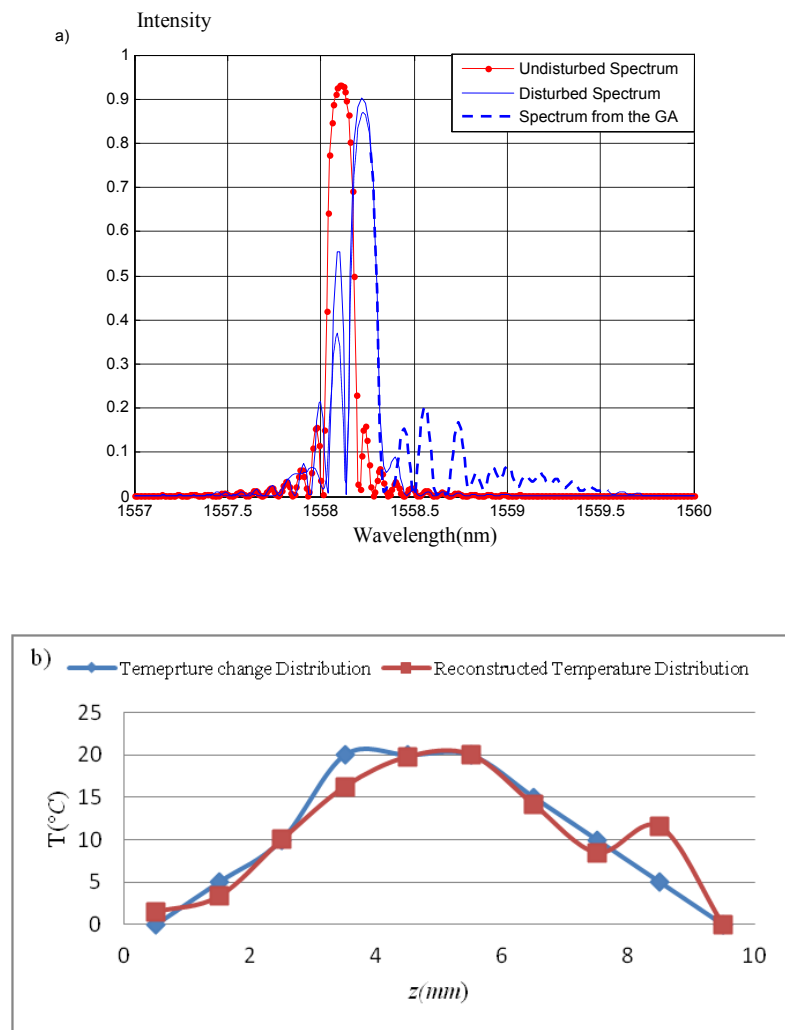


Figure 3.27a) Spectral response of an FBG subjected to non-uniform temperature distribution in (b), and b) comparison between the applied and reconstructed temperature distribution.

Figure 3.28 (a) shows the original and the reconstructed reflected spectrum of the sensor when it is subjected to the temperature distribution shown in Figure 3.28 (b). The temperature distribution is reconstructed when the algorithm reaches the fitness function of 0.52.

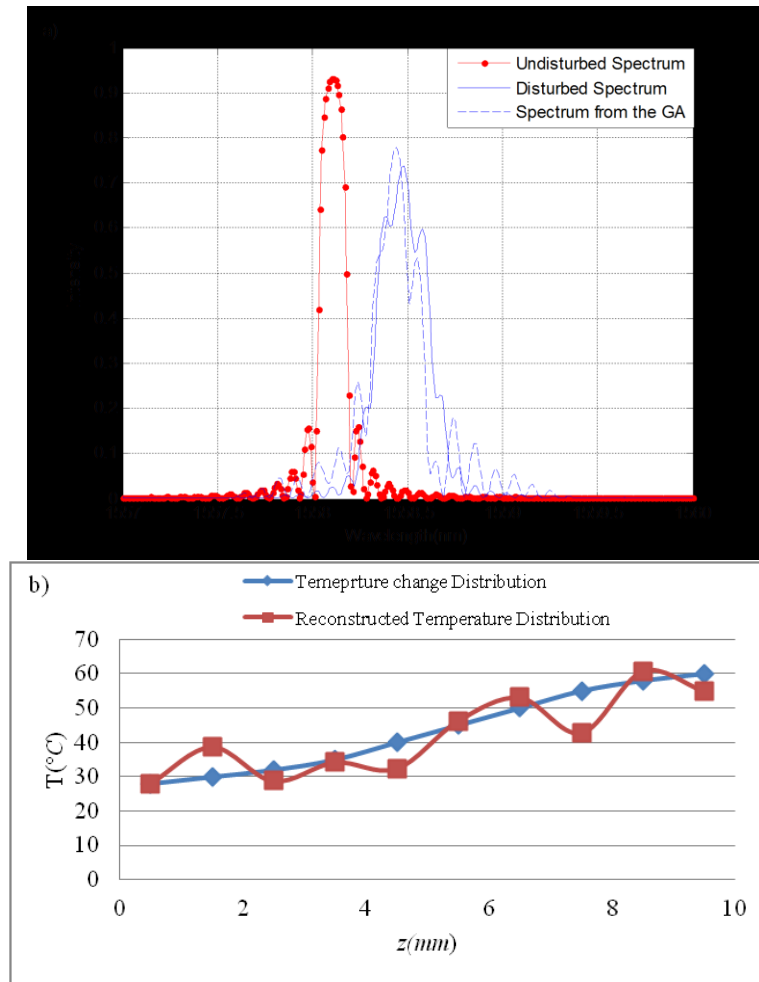


Figure 3.28a) Spectral response of an FBG subjected to non-uniform temperature distribution in (b), and b) comparison between the applied and reconstructed temperature distribution.

Figure 3.29 (a) shows the original and the reconstructed reflected spectrum of the sensor when it is subjected to the temperature change shown in Figure 3.29 (b).

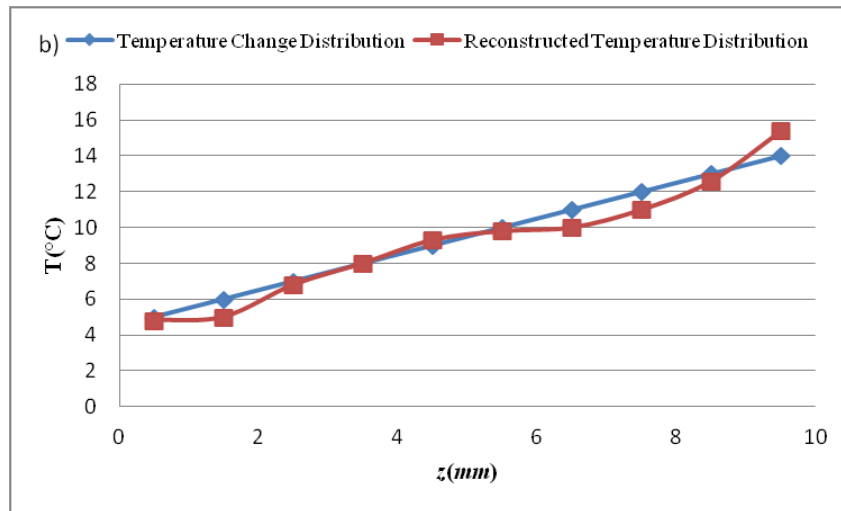
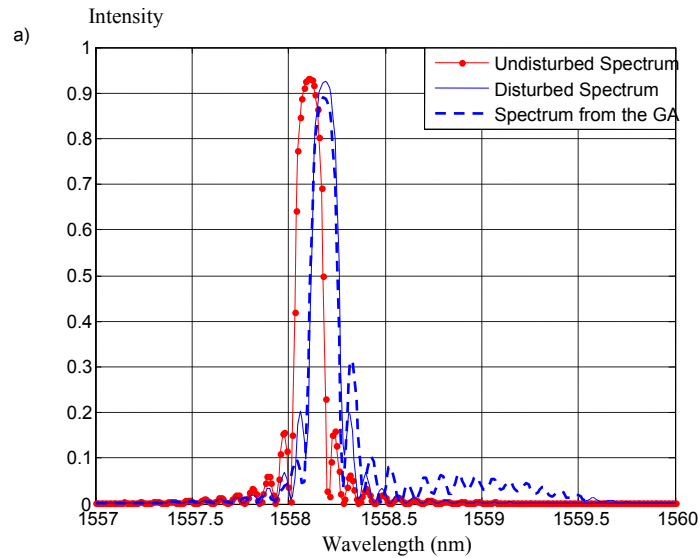


Figure 3.29a) Spectral response of an FBG subjected to non-uniform temperature distribution in (b), and b) comparison between the applied and reconstructed temperature distribution.

The reconstructed spectrum is obtained when the algorithm converges to the 0.456 fitness function. Figure 3.29 (b) also shows the reconstructed temperature distribution. As can be seen from Figure 3.29 (b) the resolution of 1 °C is detected using our proposed algorithm.



## 3.4 Conclusions

In this chapter, a theoretical approach is developed for reconstruction of a non-uniform distribution of the strain and the temperature along the principal axes of an FBG sensor and a multiplexed sensor system.

First, a theoretical analysis is presented on the effects of a non-uniform transversal load along the FBG sensor and a methodology for reconstruction of a non-uniform distribution of the transversal load along the sensor is presented. An inverse method based on the genetic algorithm is developed to detect a non-uniform distribution of the transversal load along the length of the sensor. It is shown that the distribution profile of the transversal load can be detected by reconstructing the reflected spectrum corresponding to the slow axis of the fiber. In order to detect the position of the strain in addition to its magnitude and profile, the methodology is applied to the multiplexed sensor system. It is shown that the methodology can detect the anomaly profile along a series of FBG sensors.

Furthermore, the response of the FBG sensor that is subjected to simultaneous longitudinal and the transversal loads is also investigated. It is shown that in addition to the detection of a non-uniform distribution of the transversal load from the reflected spectrum corresponding to the slow axis of the fiber, a non-uniform distribution of the longitudinal strain can be detected from the spectrum corresponding to the fast axis of the fiber.

In the second part of this chapter, the effects of a non-uniform distribution of temperature on an FBG sensor are studied. The genetic algorithm methodology based on the response of the FBG sensor to the temperature changes is developed. The profile of the

temperature change along the fiber is then shown to be detectable by reconstructing its reflected spectrum. Simulation and case studies are conducted to demonstrate and illustrate the capabilities and advantages of the proposed methodologies and techniques.

## **Chapter 4**

# **Analysis of a Non-uniform Distribution of Anomaly along the Length of a High Birefringence Fiber**

Although a conventional FBG sensor has proven to be a powerful sensor for health monitoring applications, there are still some constraints for using it in some particular applications. The two major setbacks that can be listed for using FBG sensors can be expressed as

- For conventional FBGs, the detection of the transversal load depends on the bifurcation of the reflected spectrum due to the transversal load, which mostly becomes observable for larger loads. This would put a limitation on detecting small transversal loads with a conventional single mode FBGs.
  
- In the previous chapter, a non-uniform longitudinal strain distribution was obtained from the reflected spectrum corresponding to the fast axis of the spectrum. The methodology can only be used when the bandwidth between the two peaks is large enough so that the distorted reflected spectrum corresponding to the fast axis could be easily detected.

To overcome the above mentioned setbacks and issues, the use of high birefringence FBG (Hi-Bi FBG) for detection of a non-uniform distribution of the transversal load and the load distribution in two dimensions is presented in this chapter.

The reflected spectrum of the Hi-Bi FBG, due to its initial birefringence, comprises of two separate Bragg peaks corresponding to the main polarization axes of the sensor and can be expressed as

$$\begin{aligned}\lambda_S &= 2n_S\Lambda_0 \\ \lambda_F &= 2n_F\Lambda_0\end{aligned}\tag{4.1}$$

where  $S$  and  $F$  represent the slow and the fast axis, respectively.

As a result, any small transversal load results in the shift of the two Bragg spectra, and therefore the magnitude of the transversal load can be detected. In general, the two Bragg spectrums corresponding to the main polarization axes of the Hi-Bi FBG have different sensitivities to the transversal load which depends on the type of the Hi-Bi fiber and the angle that the transversal load is applied to. Many studies have recently been performed [61-64] on exploring the potentials of Hi-Bi FBGs for multi-axial strain measurements. The focuses of these works [61, 62] are mostly on the study of the effects of the uniform applied strains along the length of the sensor.

However, when the non-uniformity exists in the distribution of the applied strains, the reflected spectrum breaks up to several peaks and becomes heavily distorted. Few studies have been performed [83, 84] on exploring the behavior of the Hi-Bi FBG when the applied strain distribution is not uniform all over the sensor. In these works, although the spectrum of the disturbed sensor is predicted, the inverse problem of obtaining a non-uniform distribution of the strain from the spectrum has not been solved and addressed.

We have developed a methodology for detecting a non-uniform distribution of an anomaly along the high-birefringence fiber. The proposed methodology enables the use of Hi-Bi FBG for detection of a non-uniform distribution of transversal loads with small values that could not otherwise be detected by conventional single mode FBGs.

In this chapter, first the detection of a non-uniform distribution of the transversal load from the reflected spectrum of the Bragg grating fabricated into the high birefringence fiber is discussed. In other words, the approach in the previous chapter is generalized to solve the problem of detection of non-uniform distribution of transversal load with small values that could not be detected with conventional FBGs. Furthermore, the methodology for detecting a non-uniform distribution of the simultaneously applied loads (in the longitudinal and the transversal directions) from the reflected spectrum of the Hi-Bi FBG is presented.

In the following sections, first (in Section 4.1) our methodology for reconstructing the transversal load and the simultaneously applied non-uniform transversal and the longitudinal strains along the sensor is presented. Section 4.2 presents the simulation results. Section 4.3 presents the conclusion remarks of this chapter. A summary of the above materials has been published in [81] and [82].

## 4.1 Synthesis of a Non-Uniform Distribution of Strain along the Hi-Bi FBG

### 4.1.1 Synthesis of a Non-Uniform Transversal Load

In this section, the methodology for detecting a non-uniform distribution of the transversal load along the Hi-Bi FBG is presented. In order to illustrate the approach, first we present a general study on the analysis of the response of the Hi-Bi FBG to a uniform transversal load.

Due to the mechanical and optical non-homogeneities in a Hi-Bi FBG, the prediction of the reflected spectrum of the sensor when it is subjected to the strain is not as straightforward as the prediction of reflected spectrum of a conventional FBG. The Bragg peak sensitivities corresponding to the slow and the fast axes for different types of Hi-Bi FBGs have been studied both experimentally and theoretically (using finite element analysis) in the literature [55, 83, 84]. The Bragg peak sensitivity ( $\frac{d\lambda_i}{dF}$ ,  $i = \text{fast, slow}$ ) is defined as the change in the center wavelength of the  $\lambda_i$  peak per change in the applied load. Previous studies have demonstrated that the Bragg wavelengths alter linearly with transversal load when the load is applied along the fast axis of the sensor [55, 85, 86]. In addition, the Bragg peaks have their maximum sensitivity to the transversal load when the applied load is aligned with the fast polarization axis. Therefore, in this thesis the sensors are assumed to be embedded in a way that the applied transversal loads are along the fast axis of the fiber.

Although in practice, this assumption would lead to a demand of extra accuracy in the embedment of the sensors in monitored structures, it would considerably decrease the complexity of the analysis of the reflected spectrum of the sensor.

Figure 4.1 shows an analysis of the responses of six different types of Hi-Bi FBGs to the uniform transversal load where the sensor has initial grating period of 533.56 nm, Young's modulus  $E_{core}=E_{clad}=70\text{GPa}$ ,  $E_{SAP}=51\text{ GPa}$ , Poisson's ratio  $\nu_{core}=\nu_{clad}=0.19$ ,  $\nu_{SAP}=0.21$  and the strain coefficients of  $p_{11}=0.113$  and  $p_{12}=0.252$ , to the transversal load. The force is applied parallel to the fast axis of the fiber. The Hi-Bi FBGs are formed by fabricating the Bragg grating into the six types of 1 cm high birefringence fibers with different birefringence ( $B$ ), namely, D-clad ( $B=5.6\times 10^{-4}$ ), Panda ( $B=3.2\times 10^{-4}$ ), elliptical core ( $B=4.8\times 10^{-4}$ ), bow-tie ( $B=3.3\times 10^{-4}$ ), elliptical-clad ( $B=5.1\times 10^{-4}$ ), and true-phase ( $B=5.3\times 10^{-4}$ ). The sensor's parameters chosen here are similar to the typical parameters in the literature given for the high birefringence fibers [45, 52, 79] and are used throughout this chapter.

The reflected spectra of the Hi-Bi FBG sensors were modeled from the superposition of the two spectra corresponding to the slow and the fast axes of the sensors by the T-matrix method using the transversal load sensitivities of the Bragg spectra corresponding to the polarization axes of the fiber that is obtained from the data that is available in the literature [45, 52, 79]. Obviously varying the properties of the high birefringence fibers would affect the sensitivities of the Hi-Bi FBGs, however the performance of the Hi-Bi FBGs remain the same. The derivation of the sensitivities of the Hi-Bi FBGs is usually obtained by using the FEM which is not within the scope of this thesis.

The reflected spectra were modeled by dividing the sensor into 10 segments where the transfer matrix elements for each segment was obtained separately for the slow and the fast axes from the following terms

$$\begin{aligned} T_{11}^{(i)} = T_{22}^{(i)*} = \cosh(\alpha_{S(F)} \delta_{S(F)} \Delta z) - i \frac{\delta_{S(F)}}{\alpha_{S(F)}} \sinh(\alpha_{S(F)} \delta_{S(F)} \Delta z) \\ T_{12}^{(i)} = T_{21}^{(i)*} = -i \frac{k_{ac}}{\alpha_{S(F)}} \sinh(\alpha_{S(F)} \delta_{S(F)} \Delta z) \end{aligned} \quad (4.2)$$

Therefore, the reflection coefficients corresponding to each polarization axis can be calculated for each wavelength according to

$$r_{S(F)}(\lambda) = -\frac{T_{12}^{S(F)}}{T_{22}^{S(F)}} \quad (4.3)$$

Consequently, the reflectivity of the disturbed sensor can be obtained by summing the two spectrums corresponding to the slow and the fast polarized spectra as

$$R(\lambda) = R_S(\lambda) + R_F(\lambda) \quad (4.4)$$

where

$$R_{S(F)}(\lambda) = |r_{S(F)}(\lambda)|^2 \quad (4.5)$$

The indices  $S$  and  $F$  denote the slow and the fast axes, respectively.

As can be observed from Figure4.1, the Bragg spectrum corresponding to the fast axis of the sensor has a considerably lower sensitivity to the transversal load than the slow axis.



In other words, the induced Bragg shift corresponding to the fast axis (peak with smaller wavelength) is smaller compared to the induced Bragg shift corresponding to the slow axis (peak with larger wavelength).

Figure 4.1 depicts the response of the sensor to a uniform transversal load. However, when the non-uniformity exists in the distribution of the applied strains, the reflected spectrum breaks up to several peaks and becomes heavily distorted. Therefore, the detection of the anomaly from the reflected spectrum of the sensor becomes a complex problem.

As an example, Figure 4.2 shows the response of the Hi-Bi FBG when it is subjected to a non-uniform distribution of transversal load. Figures 4.2 (a) and (b) correspond to the response of a Bragg grating with the initial period of 530.47 nm that is fabricated into a 1-cm bow-tie ( $B=3.3 \times 10^{-4}$ ) and D-clad ( $B=5.6 \times 10^{-4}$ ) high birefringence fibers, respectively. The characteristics of the fiber remain similar to those that were selected for Figure 4.1. The sensors are subjected to a non-uniform transversal load distribution of  $F(z)=4(z/L)^2+F_0$  along their length. The spectrum is simulated by using the linear sensitivities of  $(\frac{d\lambda_S}{dF})=0.12$  (nm/ (N/mm)) and  $(\frac{d\lambda_F}{dF})=0.01$  (nm/ (N/mm)) for the slow and the fast axes of the bow-tie FBG, and  $(\frac{d\lambda_S}{dF})=0.18$  (nm/ (N/mm)) and  $(\frac{d\lambda_F}{dF})=0.061$  (nm/ (N/mm)) for the slow and the fast axes of the D-clad FBG [55, 83, 84].

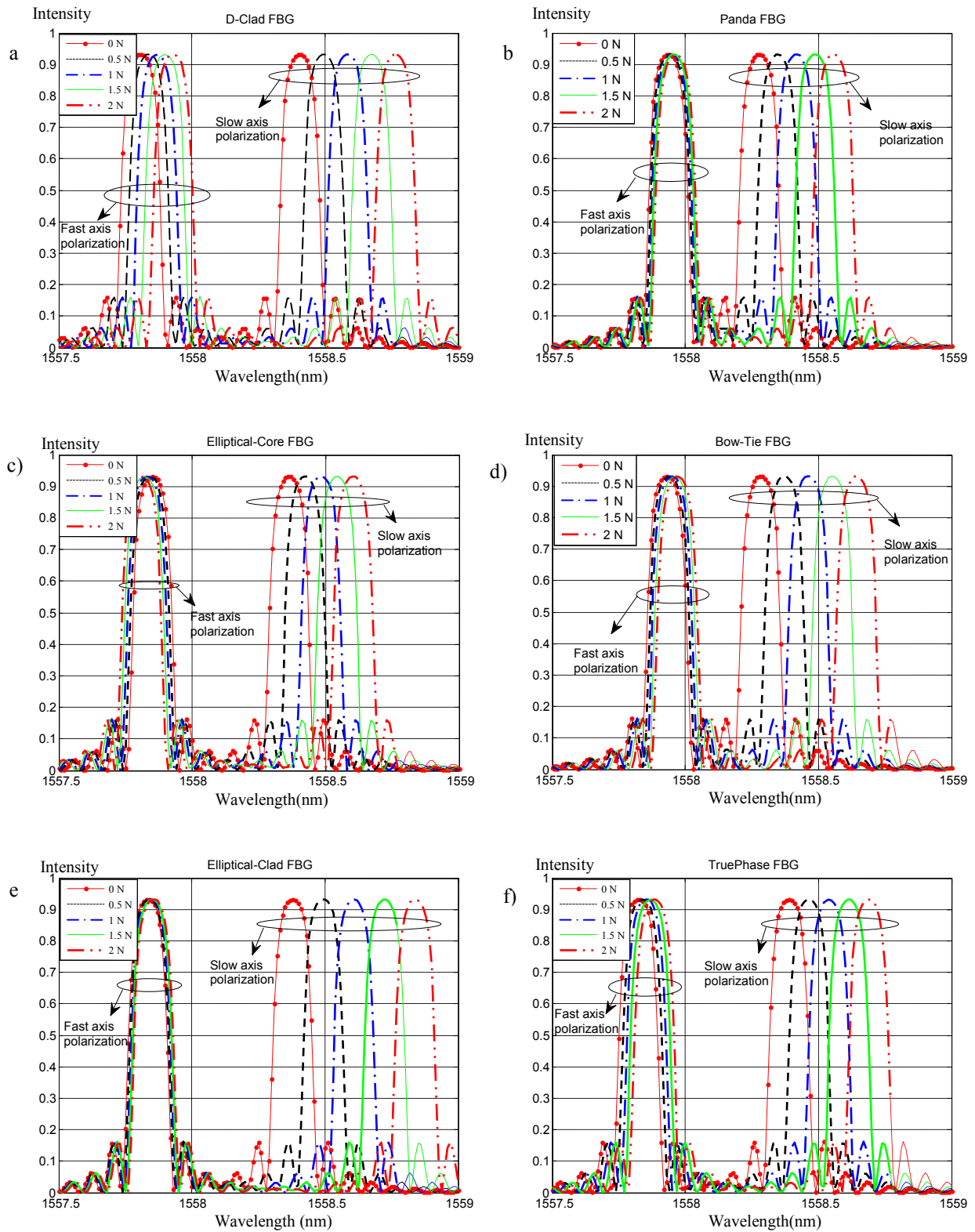


Figure 4.1 Simulated reflected spectra of the disturbed Bragg grating fabricated into the a) D-clad, b) Panda, c) Elliptical-Core, d) Bow-tie, e) Elliptical-clad, and f) True-phase high-birefringence fibers that are subjected to the different values of transversal loads.

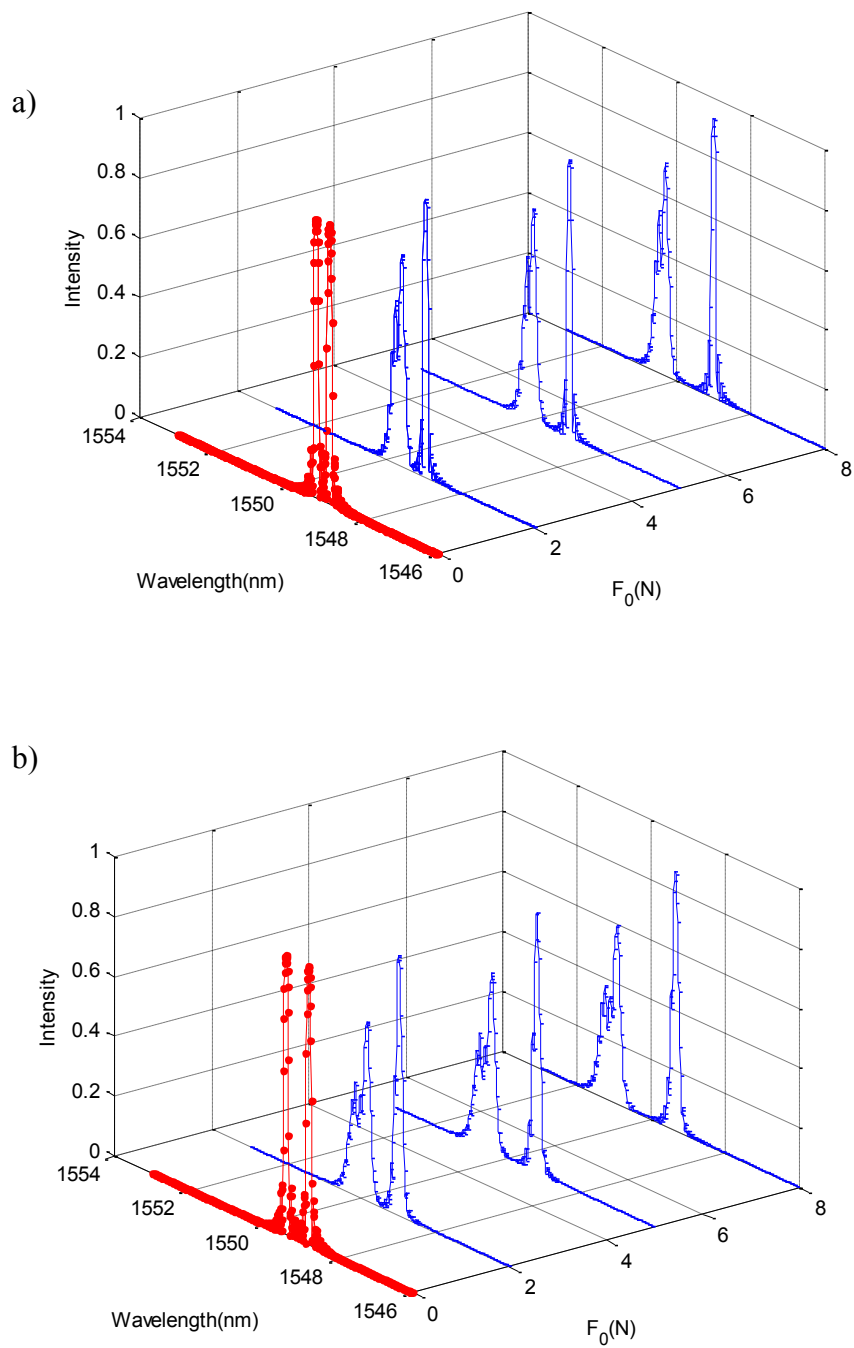


Figure 4.2 The response of a) bow-tie, and b) D-clad FBG to the quadratic  $F(z)=4(z/L)^2+F_0(N)$  distribution of transversal load along the length of the sensors. The undisturbed reflected spectrum of the sensor is shown with the “● line”.

As can be noted from Figure 4.2, the non-uniform transversal load distribution along the sensor results in the distortion of the Hi-Bi FBG reflected spectrum. We have developed an approach for detecting the distribution of a non-uniform transversal load along the Hi-Bi FBG. The methodology enables the detection of the distribution of the transversal load with small values along the sensor which was not previously possible with conventional FBGs.

The developed GA is used to detect a non-uniform distribution of the transversal load along the sensor. The best solutions of the GA provide the refractive index distributions corresponding to the slow and the fast axes along the Hi-Bi FBG. The case of a plane strain ( $\varepsilon_z=0$ ) is considered for all the cases considered in this section. Therefore the grating period of the sensor that is subjected to the transversal load is considered to remain constant.

As a first step, two populations are constructed that represent the possible solutions for the refractive index distributions corresponding to the slow and the fast axes of the sensor. The populations are represented by two  $l \times m$  matrices as

$$Population = \begin{bmatrix} n_{1_s}^1 & \cdots & n_{1_s}^m \\ \vdots & & \vdots \\ n_{k_s}^1 & \cdots & n_{k_s}^m \\ \vdots & & \vdots \\ n_{l_s}^1 & \cdots & n_{l_s}^m \end{bmatrix}, \begin{bmatrix} n_{1_f}^1 & \cdots & n_{1_f}^m \\ \vdots & & \vdots \\ n_{k_f}^1 & \cdots & n_{k_f}^m \\ \vdots & & \vdots \\ n_{l_f}^1 & \cdots & n_{l_f}^m \end{bmatrix} \quad (4.6)$$

where  $m$  is the number of sub-gratings that the fiber is divided into,  $l$  represents the number of individuals in the population, and  $n_{k_s}^i$  and  $n_{k_f}^i$  denote the refractive indices

corresponding to the slow and the fast axes of the  $i^{\text{th}}$  segment of the individual  $k$ , respectively.

The genes of the populations corresponding to the slow and the fast axes are obtained uniformly within the specified boundaries of the problem (L) around the initial effective refractive index values for the slow ( $n_{eff,S}$ ) and the fast ( $n_{eff,F}$ ) axes, respectively as

$$n_{eff,S} - L < n_{k_s}^i < n_{eff,S} + L \quad (4.7)$$

and

$$n_{eff,F} - L < n_{k_f}^i < n_{eff,F} + L \quad (4.8)$$

where  $n_{eff,S}$  and  $n_{eff,F}$  can be estimated as

$$\begin{aligned} n_{eff,S} &= n_{eff} + \frac{B}{2} \\ n_{eff,F} &= n_{eff} - \frac{B}{2} \end{aligned} \quad (4.9)$$

where  $n_{eff}$  is the initial refractive index of the FBG and  $B$  is the birefringence of the Hi-Bi Fiber.

The algorithm optimally searches for the best solutions (individuals) from the two populations that can regenerate the objective distorted reflected spectrum ( $R_{objective}$ ) of the Hi-Bi FBG. The distorted reflected spectrum of the Hi-Bi FBG is regenerated by the superposition of the reflected spectra corresponding to the slow ( $R_{k,s}$ ) and the fast ( $R_{k,f}$ ) axes that are constructed from the  $k$  individual of the two populations as given in equation (4.6). In other words, the genetic algorithm optimally searches for the individual

$k$  of the two populations that can create a reflected spectrum that has the lowest fitness function with the original reflected spectrum of the Hi-Bi FBG.

The fitness function  $f(k)$  for each individual  $k$  of the two populations can be expressed as

$$f(k) = \sum_{i=1}^p \left| R_{objective}(\lambda_i) - R_k(\lambda_i) \right|^2 \quad (4.10)$$

where the wavelengths are discretized into the  $p$  wavelengths, and  $R_k(\lambda)$  denotes the reconstructed reflected spectrum of the sensor from the individual  $k$  of the two populations that is obtained from

$$R_k(\lambda) = R_{k,S}(\lambda) + R_{k,F}(\lambda) \quad (4.11)$$

After calculating the fitness of each individual in the current generation (iteration), the individuals are assigned a relative weight from which the new population is reconstructed. The populations iteratively go through the four main GA operators, namely; selection, crossover, mutation, and elitism until it converges to best solution of the refractive index individuals corresponding to the slow and the fast axes of the sensor.

The best solution of the GA provides the refractive index for each segment (gene)  $i$  corresponding to the slow and the fast axes of the fiber as

$$n_{eff,S(F)}(i) = n_{eff} + \Delta n_{eff,S(F)}(i) \quad (4.12)$$

where the refractive index change for each segment,  $\Delta n_{eff,S(F)}(i)$ , can be correlated to the transversal load change  $\Delta F(i)$  through

$$\Delta n_{eff,S(F)}(i) = \frac{dn_{eff,S(F)}}{dF} \Delta F(i) \quad (4.13)$$

where  $\frac{dn_{eff,S(F)}}{dF}$  is the rate at which the refractive index corresponding to the slow and the fast axes change with respect to the changes in the applied load  $F$  and is correlated to the Bragg peaks sensitivities through

$$\begin{aligned} \frac{d\lambda_S}{dF} &= 2 \frac{d}{dF} (n_{eff,S} \Lambda) = 2 \frac{dn_{eff,S}}{dF} \Lambda + 2 \frac{d\Lambda}{dF} n_{eff,S} \\ \frac{d\lambda_F}{dF} &= 2 \frac{d}{dF} (n_{eff,F} \Lambda) = 2 \frac{dn_{eff,F}}{dF} \Lambda + 2 \frac{d\Lambda}{dF} n_{eff,F} \end{aligned} \quad (4.14)$$

The linear sensitivities of the slow and the fast axes reflected Bragg spectrums to the transversal load are assumed to be known *a priori*. By assuming the plane strain ( $\varepsilon_z=0$ ) case,  $\frac{d\Lambda}{dF}$  can be set to zero. Therefore, by using equation (4.14) and the solution of the refractive index distribution by the GA, the transversal load change along the fiber can be obtained from equation (4.13).

## 4.1.2 Synthesis of a Non-uniform Simultaneously Applied Longitudinal and Transversal Loads

As can be noted from Figure 4.1, some types of Hi-Bi FBGs such as the elliptical clad and the bow-tie FBGs have very small fast axis transversal load sensitivities when the load is parallel to the fast axis of the sensor. Therefore, ideally for such a sensor that is subjected simultaneously to the longitudinal and the transversal loads, a non-uniform distribution of the longitudinal strain is the dominant source of distortion on the reflected spectrum corresponding to the fast axis of the sensor. As a result, among all types of the Hi-Bi FBG sensors, the sensors with the lowest transversal load sensitivities for the fast axis such as the elliptical clad FBG and the bow-tie FBG are good candidates for the detection of a non-uniformity of the longitudinal strain when the sensor is subjected to the longitudinal and the transversal loads simultaneously. In this section, we present a methodology for detection of a non-uniform anomaly from the reflected spectrum of such sensors.

Toward this end, firstly we study the behavior of the Bragg peaks of the bow-tie and the elliptical clad FBGs when they are subjected to the transversal and the longitudinal loads simultaneously. Figure 4.3 (a) illustrates the response of the bow-tie FBG when the sensor is subjected to a non-uniform distribution of the transversal load along its length that is defined by  $F(z)=4((z/L)^2+1)N$ . Figure 4.3 (b) shows the reflected spectrum of the sensor when it is subjected to a non-uniform distribution of both transversal and longitudinal loads. The simultaneously applied transversal and longitudinal load distributions are given by  $F(z)=4((z/L)^2+1)N$  and  $\varepsilon(z)=200((z/L)^2+1)$



$\mu\epsilon$ , respectively. The transversal load is aligned with the fast axis of the sensor. Similarly, figure 4.4 shows the response of the elliptical FBG to the same perturbations.

As can be noted from the above figures, the distortion of the Bragg spectrum corresponding to the fast axis of the bow-tie and elliptical FBGs, when they are disturbed by the longitudinal and transversal loads simultaneously, is dominantly due to the longitudinal strain. Therefore the non-uniform distribution of the longitudinal strain can be detected by reconstructing the disturbed reflected spectrum corresponding to the fast axis. It is important to point out that since the Poisson's ratios of the SAPs and the cladding of the Hi-Bi FBGs are generally very close, the birefringence created by the stretching of the fiber can be neglected. Subsequent to detecting the longitudinal strain and the grating period change along the fiber, the reflected spectrum corresponding to the slow axis can be reconstructed.

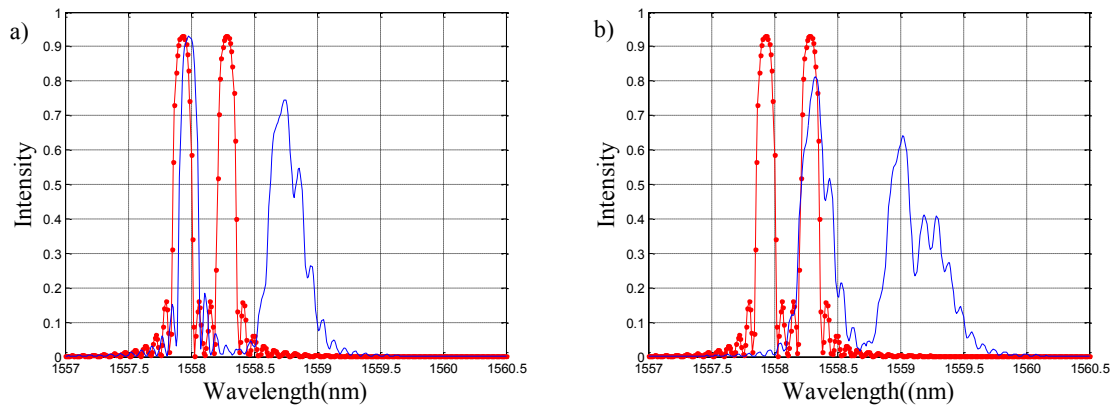


Figure 4.3 The response of the bow-tie FBG to the non uniform distribution of a) transversal load  $F(z)=4((z/L)^2+1)N$ , and b) simultaneous distributions of transversal load  $F(z)=4((z/L)^2+1)N$  and longitudinal strain  $\epsilon(z)=200((z/L)^2+1)\mu\epsilon$ . The undisturbed reflected spectrum of the sensor is shown with the “●-line”.

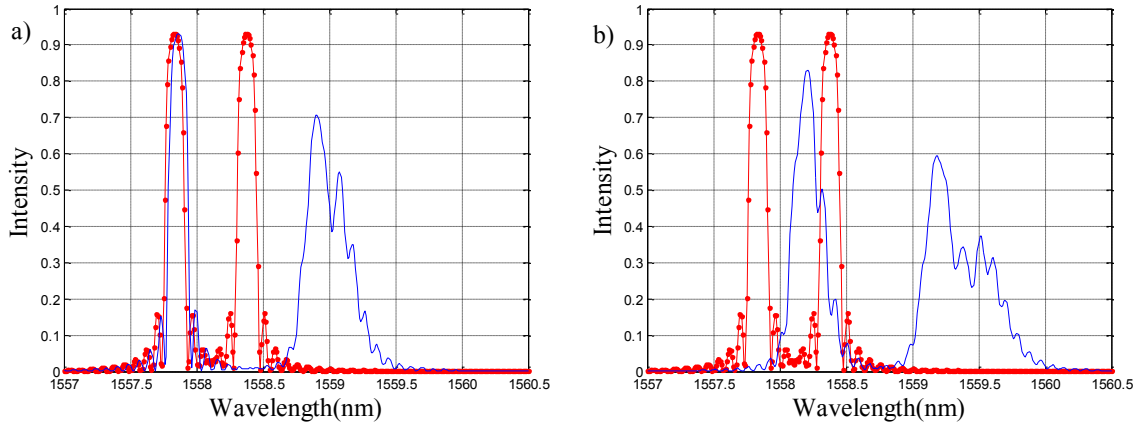


Figure 4.4 The response of elliptical clad FBG to the non uniform distribution of a) transversal load  $F(z)=4((z/L)^2+1) N$ , and b) simultaneous distributions of transversal load  $F(z)=4((z/L)^2+1) N$  and longitudinal strain  $\varepsilon(z)=200((z/L)^2+1) \mu\varepsilon$ . The undisturbed reflected spectrum of the sensor is shown with the “●-line”.

The detection of the transversal load and the longitudinal strain distributions is performed through the following steps

- I. Detection of the distribution of anon-uniform longitudinal strain from the reflected spectrum of the Hi-Bi FBG corresponding to its fast axis

The longitudinal strain is obtained by reconstruction of the spectrum corresponding to the fast axis of the Hi-Bi FBG by the GA. The methodology is the same as the one that was used for the conventional FBG as given in Chapter 3. Referring to the equation (3.12), the strain-optic effect and the grating period change are linearly superimposed by applying the effective strain of  $(1-p_e)\varepsilon(z)$  to the sensor.

Therefore, the changed grating period of each segment  $i$  due to the longitudinal strain  $\varepsilon_z$  (i) along the fiber that is divided into  $m$  segments can be estimated as

$$\Lambda(m) = \Lambda_0 + \Delta \Lambda(m) \equiv \Lambda_0 + \Lambda_0(1 - p_e)\varepsilon_z(m) \quad (4.15)$$

where  $\Lambda_0$  is the initial grating period of the undisturbed FBG sensor and the effective strain-optic coefficient is

$$p_e = \frac{n_{eff}^2}{2} [p_{12} - \nu(p_{11} + p_{12})] \quad (4.16)$$

A population consists of  $l$  (individuals) by  $m$  (segments) is formed that represents the potential solutions to the grating period change along the fiber as

$$Population \neq Individuals \left[ \begin{array}{c} \overbrace{\Lambda_1^1 \quad \dots \quad \Lambda_1^m}^{Segments} \\ \vdots \\ \Lambda_k^1 \quad \dots \quad \Lambda_k^m \\ \vdots \\ \Lambda_l^1 \quad \dots \quad \Lambda_l^m \end{array} \right] \quad (4.17)$$

The population is set to provide values uniformly around the initial grating period of the Hi-Bi FBG ( $\Lambda_0$ ). The randomly obtained genes are represented by  $\Lambda_k^i$  and are obtained uniformly within the specified boundaries  $L$  around the initial grating period ( $\Lambda_0$ ) as  $\Lambda_0 - L < \Lambda_k^i < \Lambda_0 + L$ .

The reflected spectrum corresponding to the fast axis of the Hi-Bi FBG is reconstructed by the individuals of the population as given by equation (4.17). The population goes

through the process of selection, reproduction and mutation until the GA converges to the lowest value for the fitness function. The optimum solution to the algorithm represents the grating period for each segment as given in equation (4.15) from which the longitudinal strain can be obtained.

## II. Detection of anon-uniform distribution of the transversal load from the reflected spectrum of the Hi-Bi FBG corresponding to its slow axis

In our analysis in order to reconstruct the transversal load distribution along the sensor, the spectrum corresponding to the slow axis is reconstructed by the GA.

The encoded genes (refractive index for each segment) are generated randomly around the initial value of the refractive index  $n_{eff,S}=n_{eff}+B/2$  where  $B$  is the birefringence of the fiber. A population in the form of  $l$  (individuals) by  $m$  (segments) matrix is then constructed which represents candidates or possible solutions to the problem as

$$Population = Individuals \left\{ \begin{array}{c} \overbrace{\left[ \begin{array}{ccc} n_{lS}^1 & \dots & n_{lS}^m \\ \vdots & & \vdots \\ n_{kS}^1 & \dots & n_{kS}^m \\ \vdots & & \vdots \\ n_{lS}^1 & \dots & n_{lS}^m \end{array} \right]}^{Segments} \end{array} \right. \quad (4.18)$$

where  $n_{kS}^i$  is the refractive index corresponding to the  $x$ (slow) axis of the  $i^{\text{th}}$  segment of the individual  $k$ . Subscript  $S$  refers to the slow axis.

The slow axis reflected spectrum is reconstructed by using the grating period distribution that was obtained in Step 1 and the individuals of the population as given in equation (4.18). The algorithm optimally searches for the best individual of the population that can create a reflected spectrum that has the lowest fitness function with the reflected spectrum of the sensor corresponding to the slow axis. The obtained refractive index distribution corresponding to the slow axis of the Hi-Bi FBG sensor can be correlated to the transversal load distribution by using equation (4.13).

## 4.2 Results and Discussions

In this section, a non-uniform distribution of the transversal load is obtained from the reflected spectrum of the Bragg grating fabricated into the bow-tie high birefringence fiber with the characteristics as given in Table 4.1. The obtained fitness function for all the cases is in the order of  $10^{-1}$ .

The reflected spectrum corresponding to the slow axis of the sensor is reconstructed by the GA with the wavelength resolution of 0.01 nm.

In this section, the effects of the distribution of a non-uniform anomaly are detected from the reflected spectrum of a 1 cm Hi-Bi FBG with the characteristics as given in Table 4.1. The GA approach is developed to detect the transversal load and the simultaneously applied longitudinal and the transversal loads from the Bragg reflected spectra corresponding to the main polarization axes of the Hi-Bi FBG.

The following examples demonstrate the efficiency of the methodology for detection of a non-uniform distribution of the transversal load along 1-cm bow-tie FBG sensor. The case of plane strain ( $\varepsilon_z=0$ ) is assumed for all the presented examples.

Table 4.1 Parameters of the Hi-Bi FBG.

Parameter	Value
Length ( $L$ )	10 mm
Birefringence ( $B$ )	$3.3 \times 10^{-4}$
Slow axis sensitivity to the transversal load (nm/(N/mm))	0.18 (nm/(N/mm))
Fast axis sensitivity to the transversal load (nm/(N/mm))	0.02 (nm/(N/mm))
Strain coefficients $p_{11}, p_{12}$	0.113, 0.252
Young's modulus ( $E_{core} = E_{clad}$ )	70 GPa
$E_{SAP}$	51 GPa
Thermal expansion coefficient ( $\alpha_{core} = \alpha_{clad}$ )	$0.550 \times 10^{-6} \text{ } ^\circ\text{C}^{-1}$
$\alpha_{SAP}$	$1.554 \times 10^{-6} \text{ } ^\circ\text{C}^{-1}$
Poisson's ratio ( $\nu_{core} = \nu_{clad} = \nu_{SAP}$ )	0.19
Initial period ( $\Lambda_0$ )	533.5616 nm

The first simulation case reconstructs the transversal load distribution that is shown in Figure 4.5 (b). The reflected spectrum of the sensor subjected to the transversal load distribution of Figure 4.5 (b) is shown in Figure 4.5 (a). The reconstructed spectrum corresponding to the slow axis is also shown in Figure 4.5 (a). A selection of the wavelengths from 1558.5-1560 (nm) was chosen for comparison through the fitness function. The GA was calculated through 60 generations when it converges to the 0.2853 fitness function. The maximum difference between the reconstructed and the applied transversal load is 1.37 N.

For the second example, Figure 4.6 (a) shows the reflected spectrum of the bow-tie FBG when it is subjected to the transversal load distribution shown in Figure 4.6 (b). The spectrum corresponding to the slow axis of the sensor is reconstructed by the GA as is also shown in Figure 4.6(a). Consequently, the distribution of the transversal load is reconstructed and is compared with the original one as shown in Figure 4.6 (b). The algorithm has converged to the 0.54 fitness function after 70 generations. The maximum difference between the reconstructed and the applied transversal load is 0.82 N.

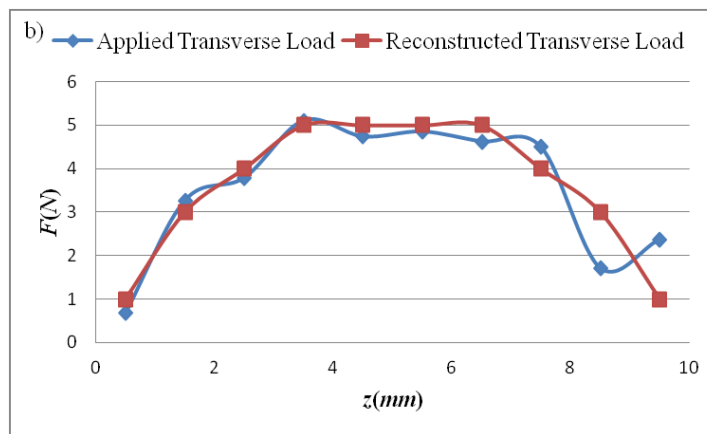
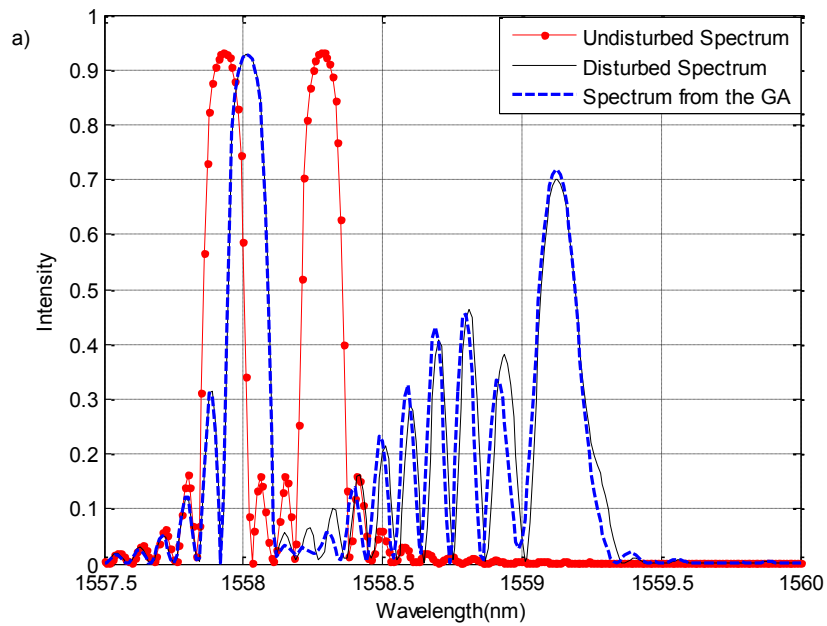


Figure 4.5a) The reflected spectrum of the optimal solution from GA for the spectrum corresponding to the slow axis of the bow-tie FBG subjected to the transversal load. The undisturbed and disturbed reflected spectrum obtained by the T-matrix is also plotted, and b) applied and reconstructed transversal load distribution by using the GA.

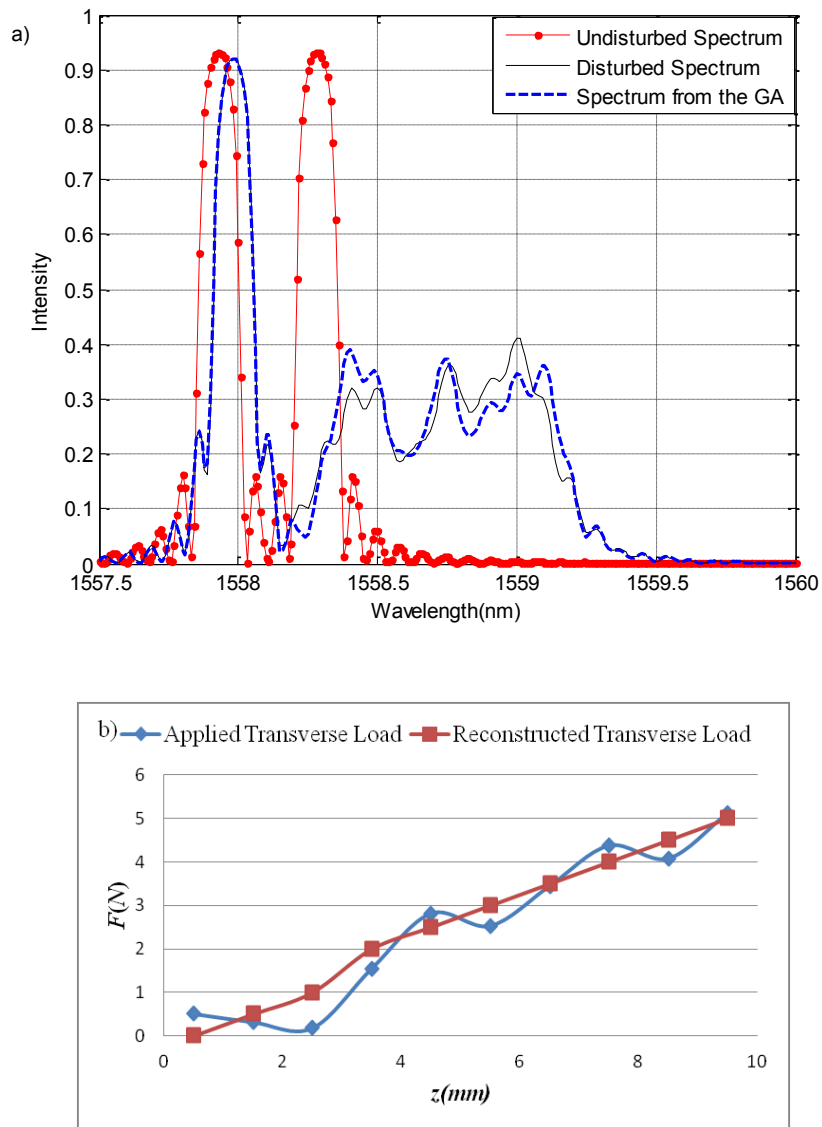


Figure 4.6 a) The reflected spectrum of the optimal solution from GA for the spectrum corresponding to the slow axis of the bow-tie FBG subjected to the transversal load. The undisturbed and disturbed reflected spectrum obtained by the T-matrix is also plotted, and b) applied and reconstructed transversal load distribution by using the GA.

Figure 4.7 shows the reflected spectrum of the same sensor when it is subjected to the more complicated sinusoidal shape transversal load. The algorithm converges to the fitness function of 1.9267, which is substantially higher than the previous cases. This can



be due to the larger selection of wavelengths that had to be scanned for the  $x$ -polarized modes (approximately 3 nm). Figure 4.7 (b) shows the applied and the reconstructed transversal load that was obtained after 60 generations. The maximum difference between the reconstructed and the applied transversal load is 5 N.

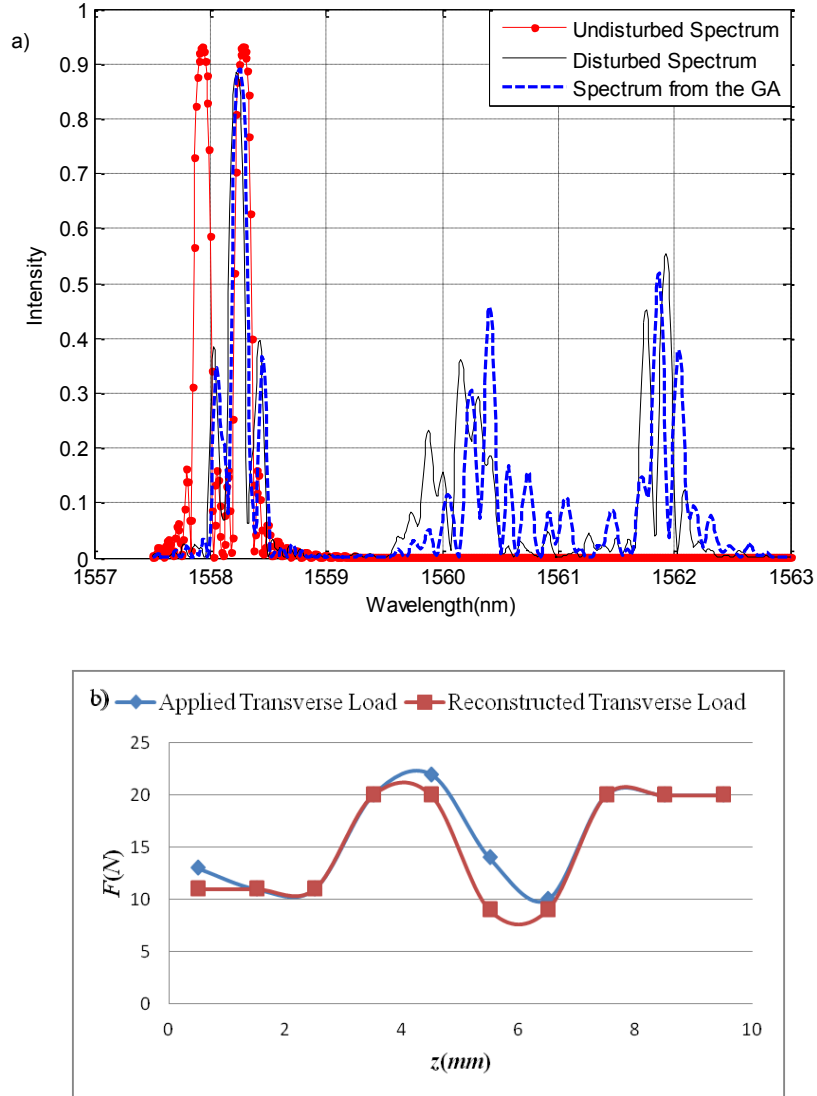


Figure 4.7 a) The reflected spectrum of the optimal solution from GA for the spectrum corresponding to the slow axis of the bow-tie FBG subjected to the transversal load. The undisturbed and disturbed reflected spectrum obtained by the T-matrix is also plotted, and b) applied and reconstructed transversal load distribution by using the GA.

The approach can effectively detect the magnitude and distribution profile of the applied non-uniform transversal load. In the following examples the effects of the simultaneously applied non-uniform longitudinal and transversal loads is studied.

Figure 4.8(a) shows the reflected spectrum of the Hi-Bi FBG when it is subjected to the simultaneous longitudinal strain and the transversal loads of Figures 4.8(b) and (c). Figures 4.8(b) and (c) show the results of the anomaly distribution reconstruction with the spatial resolution of 1 mm which is compared with the original one. The maximum difference between the original anomaly and the reconstructed one for the longitudinal strain and the transversal loads are  $10\mu\varepsilon$  and 2.32 N, respectively.

Figure 4.9 shows the reflected spectrum of the same sensor when is subjected to the longitudinal stain and the transversal loads shown in Figures 4.9 (b) and (c). The reconstructed reflected spectrum of the sensor is also shown in Figure 4.9 (a). The maximum difference between the original anomaly and the reconstructed one for the longitudinal strain and the transversal loads are  $20\mu\varepsilon$  and 4.8 N, respectively.

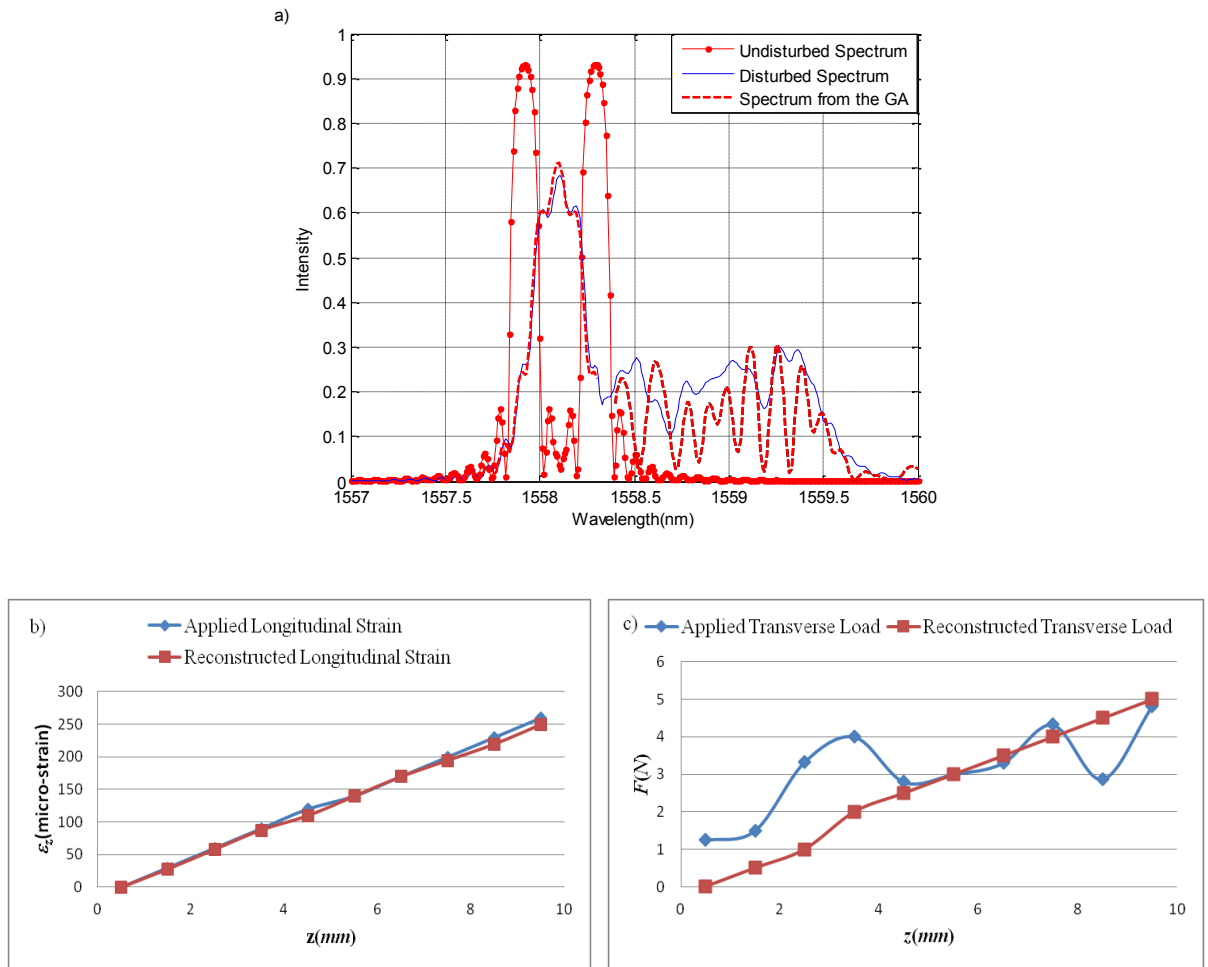


Figure 4.8 a) The original and reconstructed reflected spectrum of the bow-tie FBG when is subjected to the longitudinal strain in (b) and transversal load in (c), b) comparison between the original and reconstructed longitudinal strain, and c) comparison between the original and reconstructed transversal load.

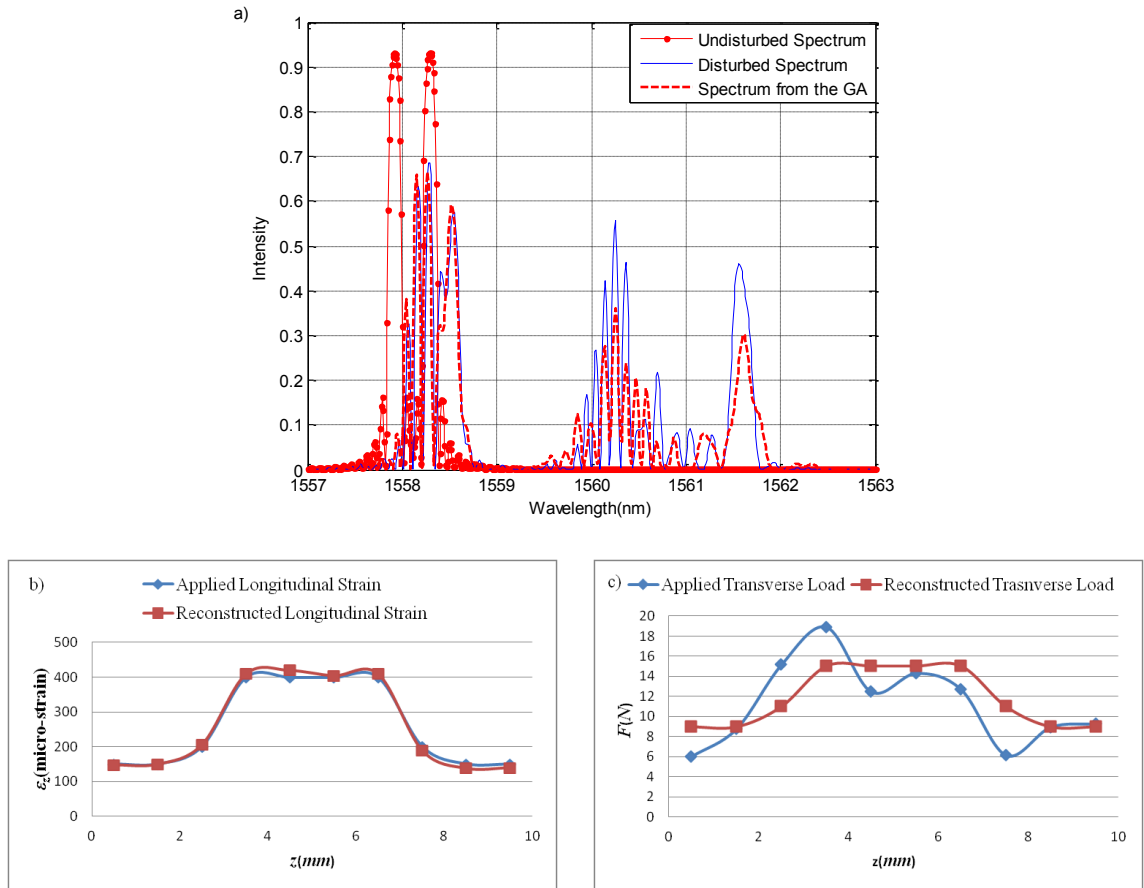


Figure 4.9a) The original and reconstructed reflected spectrum of the bow-tie FBG when is subjected to the longitudinal strain in (b) and transversal load in (c), b) comparison between the original and reconstructed longitudinal strain, and c) comparison between the original and reconstructed transversal load.

The last example shows the reflected spectrum of the sensor that is subjected to the sinusoidal shaped longitudinal and the transversal load shown in Figures 4.10 (b) and (c).

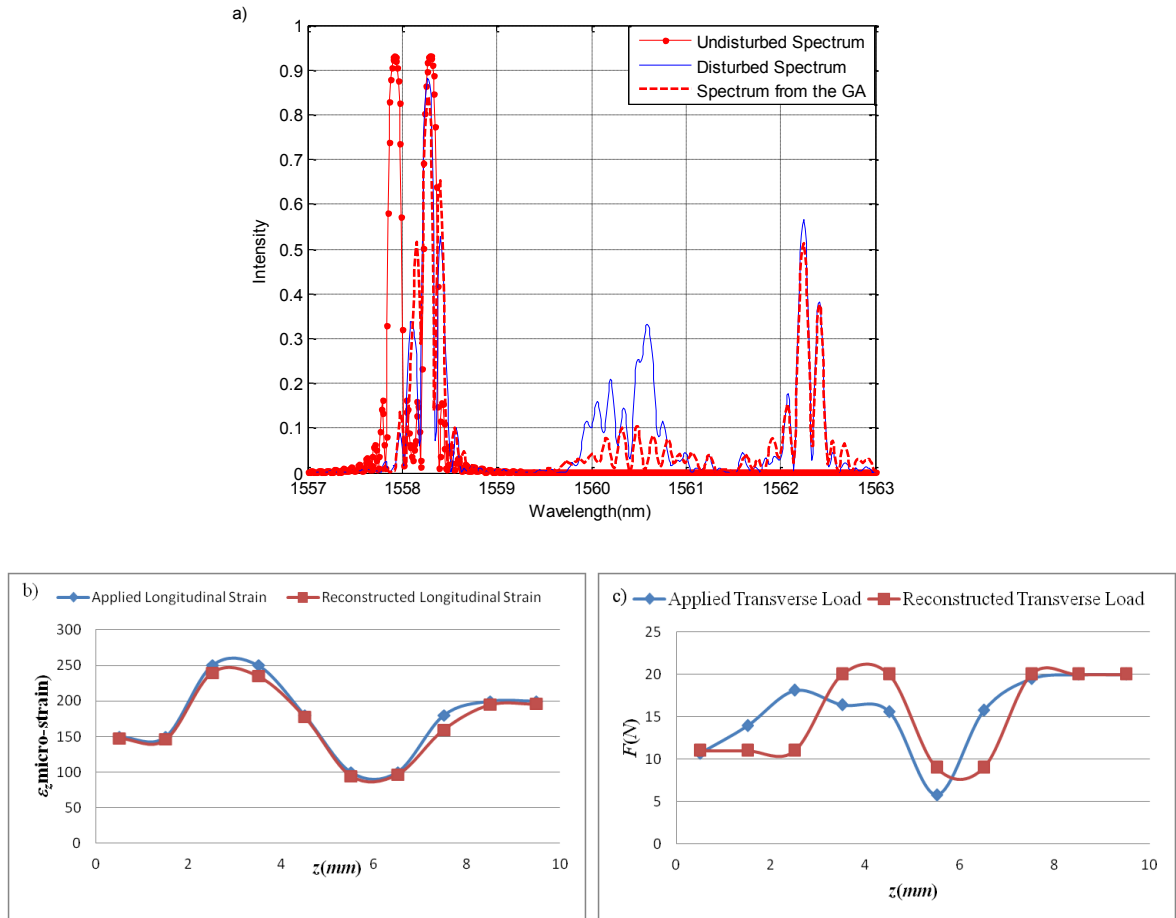


Figure 4.10 a) The original and reconstructed reflected spectrum of the bow-tie FBG when is subjected to the longitudinal strain in (b) and transversal load in (c), b) comparison between the original and reconstructed longitudinal strain, and c) comparison between the original and reconstructed transversal load.

The reconstructed reflected spectrum of the sensor is also shown in Figure 4.10 (a). The maximum difference between the original anomaly and the reconstructed one for the longitudinal strain and the transversal loads are  $20 \mu\epsilon$  and  $19.49\text{N}$ , respectively.

The genetic algorithm was iterated until its convergence for all the cases. Although the recovered non-uniform perturbation profile does not precisely match the applied one, the trend of the applied force is captured excellently. The above examples

demonstrate the efficiency of the approach based on the GA for reconstruction of a non-uniform distribution of the temperature along the bow-tie FBG.

## **4.3 Conclusions**

The problem of detection of a non-uniform transversal load profile, when the value of the transversal load is small (approximately less than 40 N), was addressed by using the Hi-Bi FBG sensor and our proposed inverse approach. The effects of a non-uniform distribution of the transversal load on the Bragg spectrums corresponding to the slow and the fast axes of the Hi-Bi were studied. The disturbed Bragg spectrum of the sensor was reconstructed by the use of genetic algorithms. The spectrum was reconstructed by defining two populations corresponding to the slow and the fast axes of the reflected spectra. A non-uniform distribution transversal load along the sensor was obtained when the algorithm converges to the best solution for the refractive index distributions corresponding to the slow and the fast axes of the sensor.

Furthermore, the use of Hi-Bi FBG for the detection of a non-uniform distribution of longitudinal and the transversal loads when they are applied simultaneously to the monitored structure was developed and presented. Each Bragg reflection corresponding to the principal axes of the fiber has different dependencies on the longitudinal and the transversal loads. It was shown that the longitudinal and the transversal loads distribution along the sensor can be obtained from the polarized modes corresponding to the main polarization axes of the fiber. An inverse approach based on genetic algorithms was developed and performed to reconstruct the disturbed reflected spectra corresponding to the sensor's polarization axes. A comparative study between the applied and the

reconstructed profile reveals that the approach can detect the trend line of the longitudinal and the transversal load profiles excellently. The methodology is particularly well suited for the detection of high strain gradients that emerge from the effects of the residual strains and crack propagation.

## Chapter 5

# Detection of a Non-uniform Distribution of Temperature and Strain

The Bragg wavelength of an FBG sensor is shifted when the sensor is exposed to both strain and temperature changes. Since the FBG has one Bragg wavelength, it is not possible to discriminate the contribution of the temperature and strain changes on the wavelength shift. The shift in the Bragg wavelength of an FBG sensor can be expressed as

$$\Delta\lambda_B = \lambda_B(K_T\Delta T + K_\varepsilon\Delta\varepsilon) \quad (5.1)$$

where  $K_T$  and  $K_\varepsilon$  denote the temperature and the strain sensitivities of the Bragg wavelength.

Using an Hi-Bi FBG sensor with two Bragg wavelengths, the temperature and the strain effects can be discriminated. The two resonant wavelengths corresponding to the fast and the slow axes of the Hi-Bi FBG show different sensitivities to the temperature and the strain. Furthermore, the shifts of the two Bragg wavelengths are given by [93-96]

$$\begin{bmatrix} \Delta\lambda_s \\ \Delta\lambda_f \end{bmatrix} = \begin{bmatrix} K_{ST} & K_{S\varepsilon} \\ K_{fT} & K_{f\varepsilon} \end{bmatrix} \begin{bmatrix} \Delta T \\ \Delta\varepsilon \end{bmatrix} = \mathbf{K} \begin{bmatrix} \Delta T \\ \Delta\varepsilon \end{bmatrix} \quad (5.2)$$



where  $K_{iT}, K_{i\varepsilon}$  ( $i=S, f$ ) denote the temperature and the strain sensitivities of the slow ( $i=S$ ) and the fast axes ( $i=f$ ). The matrix  $\mathbf{K}$  represents the sensitivity matrix.

Consequently, by taking the inverse of  $\mathbf{K}$ , the temperature and the strain changes can be detected and determined from

$$\begin{bmatrix} \Delta T \\ \Delta \varepsilon \end{bmatrix} = \mathbf{K}^{-1} \begin{bmatrix} \Delta \lambda_s \\ \Delta \lambda_f \end{bmatrix} \quad (5.3)$$

Each Bragg wavelength has different sensitivities to the temperature and the strain. Using this property, the type of an anomaly can be identified. In the studies that have recently been performed [95-97] on exploring the potentials of Hi-Bi FBGs for simultaneous measurement of the temperature and the strain, the distribution of the anomaly along the fiber is considered to be uniform. However, this is not always the case and the non-uniformity along the sensor can result in the distortion of the sensor's reflected spectrum.

In this chapter, we present the use of Hi-Bi FBG for detection of temperature and the simultaneously applied temperature and the strain when the distribution of anomaly is not uniform along the sensor.

Towards this end, the effects of a non-uniform temperature along the Hi-Bi FBG sensor are studied. In general, the reflected spectra corresponding to the slow and the fast axes of the sensor have different sensitivities to the temperature changes.

It has been shown that the polarized spectra of the Panda FBG have higher sensitivities to the temperature among the Hi-Bi FBGs [55, 91, 96]. As a result, the different sensitivities of the reflected spectra corresponding to the slow and the fast axes of the Panda FBG is utilized to discriminate between the temperature and the strain when the perturbation is non-uniform along the sensor. Towards this end, we follow the

developed approach in Chapter4 for reconstructing a non-uniform distribution of load along the Hi-Bi FBG. In other words, the previous approach is modified and some constraints are added in order to provide a solution for the sensor that is simultaneously subjected to the temperature and strain.

Section 5.1 presents our developed approach for detection of a non-uniform temperature along the length of the Hi-Bi FBG sensor. Section 5.2 presents an analysis on the response of the Panda FBG to the temperature, strain, and the transversal load. In Section 5.3, the approach for the detection of a non-uniform distribution of simultaneously applied temperature and the transversal load distribution is discussed. The approach is validated by the numerical results in Section 5.4.

## **5.1 Synthesis of Temperature Changes using the Hi-Bi FBG**

In this section, the methodology for reconstructing a non-uniform distribution of the temperature along the length of the Hi-Bi FBG sensor is presented.

The Bragg spectrum of the Hi-Bi FBG consists of two Bragg spectra that respond differently to temperature. The shift of the Bragg wavelengths are due to the temperature induced changes in the birefringence and the grating periods of the fiber.

As in conventional FBGs, the subjected non-uniform distribution of temperature along the length of the Hi-Bi FBG distorts the reflected spectrum of the sensor. In the case of Hi-Bi FBG, the deformation of the reflected spectra corresponding to the slow and the fast axes of the sensor result in distortion of the reflected spectrum. Therefore, two initial populations (instead of one) corresponding to the slow and fast axes are defined to

reconstruct the Hi-Bi FBG spectrum that is disturbed by a non-uniform distribution of the temperature along its length.

The disturbed reflected spectrum of the sensor is reconstructed with two populations corresponding to the refractive index changes related to the slow and the fast axes of the sensor. The genetic algorithm iteratively searches for the best individuals of the two populations that can regenerate the original reflected spectrum of the disturbed Hi-Bi FBG with minimum fitness function. As discussed in Chapter 2, the temperature induced distortion of the reflected spectrum of the Bragg grating is mostly due to the refractive index change along the fiber. Therefore, the grating period along the fiber that is subjected to a non-uniform distribution of temperature is estimated to remain constant and the population is defined based on the refractive index changes due to the temperature changes corresponding to the slow and the fast axes.

The two populations of the refractive indices corresponding to the slow and the fast axes are constructed with the genes values that are formed around the initial effective refractive index values for slow ( $n_{eff,S} \approx n_{eff} + B/2$ ) and fast ( $n_{eff,F} \approx n_{eff} - B/2$ ) axis within the specified boundaries of the problem, respectively. The parameter  $B$  denotes the birefringence of the fiber.

The populations iteratively go through the four main GA operators, namely; selection, crossover, mutation, and elitism until it converges to the best solution of the refractive index individuals corresponding to the slow and the fast axes of the sensor. The best solution generates the spectrum that has the lowest possible minimum fitness function with the original spectrum.

The obtained refractive index change,  $\Delta n_{eff,S(F)}(i)$ , corresponding to the slow and the fast axes of the fiber for each segment  $i$  along the sensor which is obtained by the GA, is related to the temperature change by

$$\Delta n_{eff,S(F)}(i) = \frac{dn_{eff,S(F)}}{dT} \Delta T(i) \quad (5.4)$$

where  $\frac{dn_{eff,S(F)}}{dT}$ , the refractive index sensitivity, is the rate at which the refractive index corresponding to the slow and the fast axes changes with respect to the change of the applied temperature (T). The refractive index sensitivity can be related to the Bragg peaks sensitivities through

$$\begin{aligned} \frac{d\lambda_S}{dT} &= 2 \frac{d}{dT} (n_{eff,S} \Lambda) = 2 \frac{dn_{eff,S}}{dT} \Lambda + 2 \frac{d\Lambda}{dT} n_{eff,S} \\ \frac{d\lambda_F}{dT} &= 2 \frac{d}{dT} (n_{eff,F} \Lambda) = 2 \frac{dn_{eff,F}}{dT} \Lambda + 2 \frac{d\Lambda}{dT} n_{eff,F} \end{aligned} \quad (5.5)$$

where  $(\frac{d\lambda_S}{dT})$  and  $(\frac{d\lambda_F}{dT})$  are the sensitivities of the main polarization axes to the temperature changes which are assumed to be known *a priori* to perform the GA and are assumed to be constant [55, 96,97]. The change in the grating period of the FBG due to temperature is considerably lower than the change in the refractive indices and therefore can be neglected ( $\frac{d\Lambda}{dT} \cong 0$ ).

A study on the response of Panda FBG to the strain and temperature is discussed in the next section.

## 5.2 Response of the Panda FBG to the Temperature and Strain Changes

In this section, we study the response of the Panda FBG to the temperature, strain, and transversal loads. Figure 5.1 shows the general structure of a Panda FBG.

In order to observe the effects of the temperature, transversal load, and the longitudinal strain on the reflected spectrum, we consider a Bragg grating with an initial period of 533.56 nm, fabricated in a Panda fiber with an initial birefringence of  $B=3.2 \times 10^{-4}$ , Young's modulus  $E_{core}=E_{clad}=70\text{GPa}$ ,  $E_{SAP}=51\text{ GPa}$ , Poisson's ratio  $\nu_{core}=\nu_{clad}=0.19$ ,  $\nu_{SAP}=0.21$  and the strain coefficients of  $p_{11}=0.113$  and  $p_{12}=0.252$ , thermal expansion coefficients for the core and the cladding of  $\alpha_{core}=\alpha_{cladding}=0.550 \times 10^{-6} \text{ } ^\circ\text{C}^{-1}$ , and the boron-doped SAPs thermal expansion coefficient of  $\alpha_{SAP}=3 \times 10^{-6} \text{ } ^\circ\text{C}^{-1}$ . These fiber characteristics remain unchanged for all the results shown in this section.

The reflected spectra of the Hi-Bi FBG sensor were modeled from the superposition of the two spectra corresponding to the slow and the fast axes of the Panda FBG using the temperature, transversal load, and longitudinal strain sensitivities of the Bragg spectra corresponding to the polarization axes of the fiber that is obtained from the data available in the literature [97, 98].

The effects of the temperature changes to the Panda FBG are shown in Figure 5.2 (a). As can be observed from Figure 5.2 (a) the reflected spectra corresponding to the fast and the slow axes of the sensor have different sensitivities to the temperature. In addition,

it can be noted that the spectrum corresponding to the fast axis of the sensor is more sensitive to the temperature change than the slow axis. The difference is due to the different thermal expansions of the cladding and the stress applying parts.

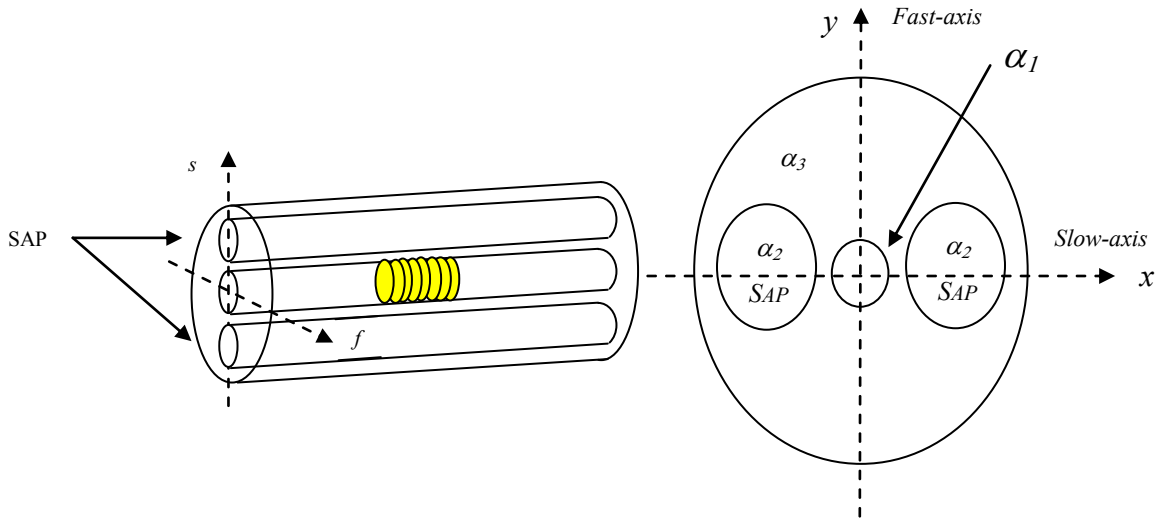


Figure 5.1 Schematic of the Panda FBG.

Figure 5.2 (a) clearly shows that as the temperature increases, the distance between the peaks corresponding to the slow and the fast axes of the sensor decreases. It can be concluded that, just by observing the behavior of the Panda FBG, the source of the perturbation (which is the temperature) can be detected.

Figure 5.2 (b) shows the reflected spectrum of the sensor when it is subjected to a non-uniform distribution of temperature along its length. This figure shows that reflected spectrum corresponding to the Hi-Bi FBG gets distorted due to a non-uniform distribution of temperature along its length.

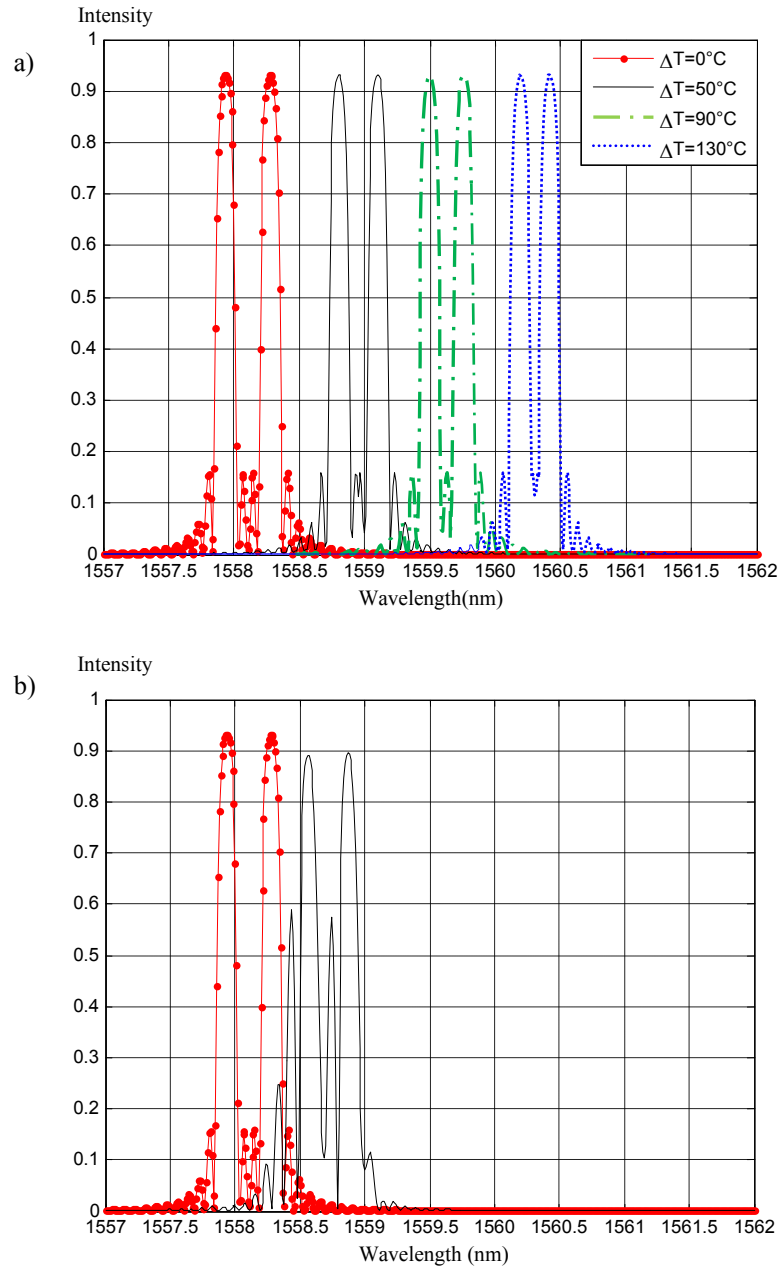



Figure 5.2 Reflected spectra of the Panda FBG subjected to a) different temperature changes, and b) non-uniform distribution of temperature. The undisturbed reflected spectrum is also shown by “ne”.

The response of the Panda FBG to the applied transversal load is different from its response to the temperature. As discussed in Chapter 2, the response of the Hi-Bi FBG depends on the loading angle relative to the polarization axes of the fiber. Figure 5.3 shows the reflected spectrum of the sensor when it is subjected to different values of the

transversal loads that is applied parallel to the fast axis of the sensor. The distance between the Bragg peaks of the sensor that is subjected to temperature decreases whereas it increases when the sensor is subjected to the transversal load.

In other words, in contrast to the temperature results, the load sensitivity of the fast axis is lower compared to the load sensitivity of the slow axis.

Figure 5.4 shows the reflected responses of the sensor subjected to different longitudinal strains. As can be observed from this figure, since the Poisson's ratio of the cladding and the SAPs are very close, the sensitivities of the fast and the slow axes to the longitudinal strain are almost identical (in the order of  $10^{-2}$  picometer/micro-strain).

It can be concluded that since in general, the slow and the fast axes of the Hi-Bi FBG have different sensitivities to the temperature and strain, by observing the spectral behavior due to the anomaly, the type of anomaly can be identified, i.e., in determining if it is either due to the temperature or the strain changes. Consequently, the temperature or the strain changes along the fiber can be obtained from the shifted Bragg wavelengths.



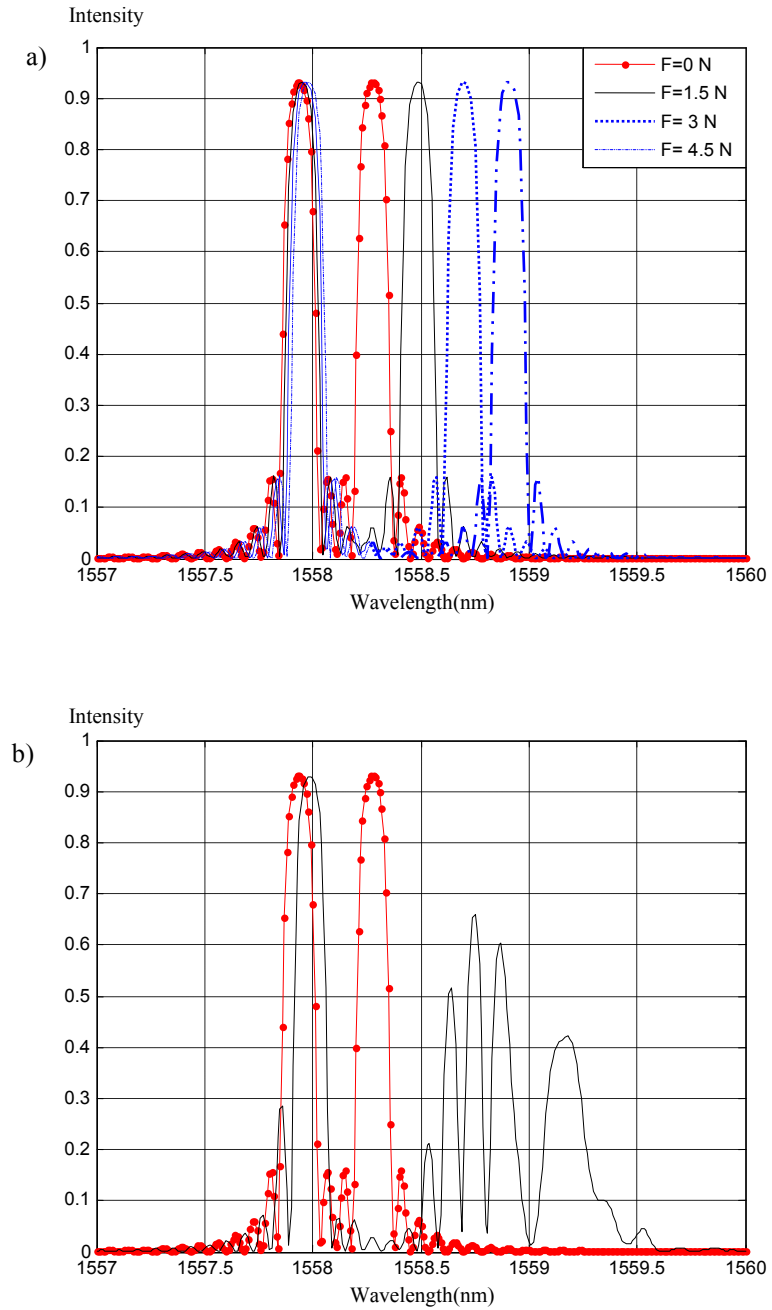


Figure 5.3 Reflected spectra of the Panda FBG subjected to a) different transversal loads, and b) non-uniform distribution of transversal load. The undisturbed reflected spectrum is also shown by “●-line”.

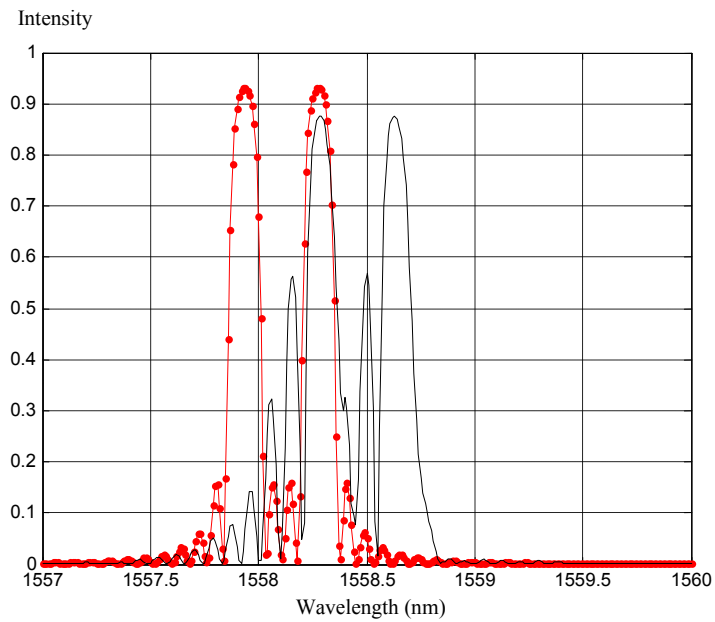
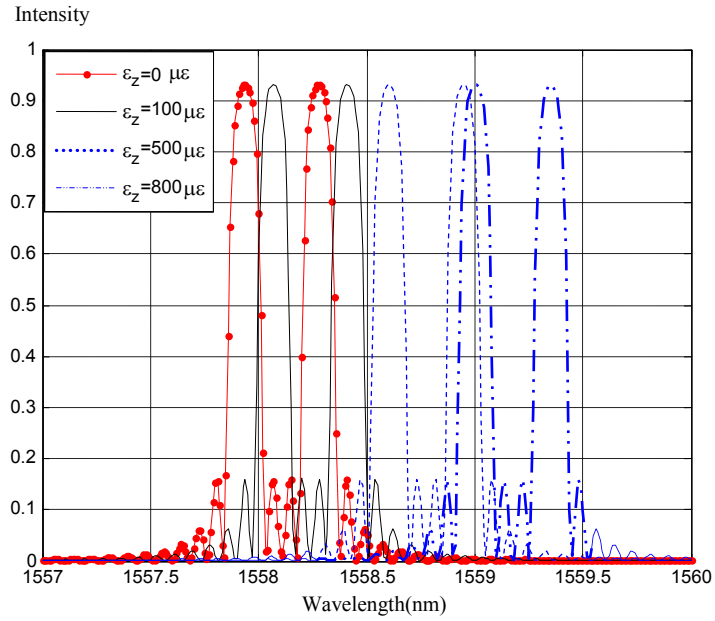


Figure 5.4 Reflected spectra of the Panda FBG subjected to a) different longitudinal strains, and b) non-uniform distribution of longitudinal strain. The undisturbed reflected spectrum is also shown by “● line”.

In a case where the distribution of the strain or temperature is not uniform across the fiber, the Bragg peaks are both shifted and distorted. Therefore, the anomaly cannot be obtained directly from the magnitude of the shift of the two Bragg wavelengths and the

reconstruction of the applied force becomes an inverse problem. The methodology for the simultaneous detection of temperature and the transversal load is presented in the next section.

## **5.3 Detection of a Non-uniform Distribution of Transversal Load and Temperature**

The goal of this chapter is to develop a solution to reconstruct the distribution of the simultaneously applied temperature and transversal loads along the Panda FBG sensor. The methodology takes advantage of different sensitivities of the slow and the fast axes to the temperature and strain changes to reconstruct the anomaly distribution along the fiber. Since the fast axis spectrum of the Panda FBG is almost insensitive to the transversal load variation (when the applied load is parallel to its fast axis), the information about the temperature variations along the sensor can be obtained by reconstructing the fast axis reflected spectrum. The following assumptions are made for the formulation of the algorithm and problem:

- For reconstructing the reflected spectrum of the Hi-Bi FBG by using the GA, only the variations in the refractive index distribution along the fiber are considered. In other words, the effects of the gating period change due to the variation of the temperature are neglected. The assumption is valid based on the high value of the thermo-optic coefficients of the sensor when compared to its thermal expansion coefficient.

- The distortion of the reflected spectrum corresponding to the fast axis of the sensor that is subjected to the temperature and the transversal load simultaneously is only considered to be due to the temperature changes. In other words, the small sensitivity of the fast axis polarized spectrum to the transversal load that is applied parallel to the fast axis of the sensor is neglected. This assumption is valid based on the low sensitivity of reflected spectrum corresponding to the fast axis of the Panda FBG to the transversal load with small values when it is applied along the fast axis.
- The sensitivities of the fast and the slow axis of the sensor to the temperature and the transversal load are considered to be known *a priori* for performing the GA algorithm. The sensitivities can be obtained either experimentally or by a FEM formulation.

As illustrated in the previous section, the reflected spectrum corresponding to the fast axis of the Panda FBG is almost insensitive to the transversal load. Therefore, in order to obtain the temperature distribution along the sensor, we have constructed a non-uniform distribution of the temperature by reconstructing the fast axis reflected spectrum. The temperature distribution is obtained following the methodology that was explained in Section 5.1.

On the other hand, the distortion of the reflected spectrum corresponding to the slow axis is due to the variation of both the temperature and the transversal load along the

sensor. Consequently, the distortion of the slow axis reflected spectrum is the result of the refractive index variation along the fiber,  $n_{eff,S,\Delta T,\Delta F}$ , due to both temperature and transversal loads which for each segment  $i$  along the fiber can be presented as

$$n_{eff,S,\Delta T,\Delta F}(i) = n_{eff,S}(i) + \Delta n_{eff,S,\Delta T}(i) + \Delta n_{eff,S,\Delta F}(i) \quad (5.6)$$

where  $n_{eff,S}$  denote the refractive index corresponding to the slow axis.

The refractive index change profile along the fiber, due to the transversal load ( $n_{eff,S,\Delta F}$ ), can then be obtained by reconstructing the reflected spectrum corresponding to the slow axis of the fiber. This is accomplished by generating a population that consists of possible solutions to  $n_{eff,S,\Delta T,\Delta F}$ . The best solution to the GA gives the refractive index changes along the fiber due to the temperature and the load changes as given in equation (5.6).

Subsequently, the refractive index changes due to the transversal load change  $\Delta n_{eff,S,\Delta F}$  can be obtained by subtracting the genes of the best solution to the algorithm from  $\Delta n_{eff,S,\Delta T}$  that was obtained by reconstructing the spectrum corresponding to the fast axis. The solution to the  $\Delta n_{eff,S,\Delta F}$  is correlated to the transversal load distribution along the sensor.

In the next section, our proposed methodology is verified by numerical simulations and results.

## 5.4 Results and Discussions

As in the conventional FBG, a non-uniform temperature along the length of the Hi-Bi FBG results in the distortion of its reflected spectrum. Our developed GA can reconstruct a non-uniform distribution of the temperature along the length of the sensor. As shown in Chapter 2, the fast axis of the bow-tie Hi-Bi FBG is generally more sensitive to temperature than the slow axis. Figure 5.5(a) shows the distorted reflected spectrum of the Hi-Bi FBG when it is subjected to the temperature changes as shown in Figure 5.5 (b). Similarly, Figure 5.6(a) shows the reflected and the reconstructed reflected spectrum of the same sensor when it is subjected to a non-uniform distribution of temperature in Figure 5.6 (b) along its length. The algorithm was iterated until convergence and the obtained fitness function is 0.2093. Although the recovered anomaly profile does not precisely match the applied one, the trend of the applied temperature change is perfectly captured.

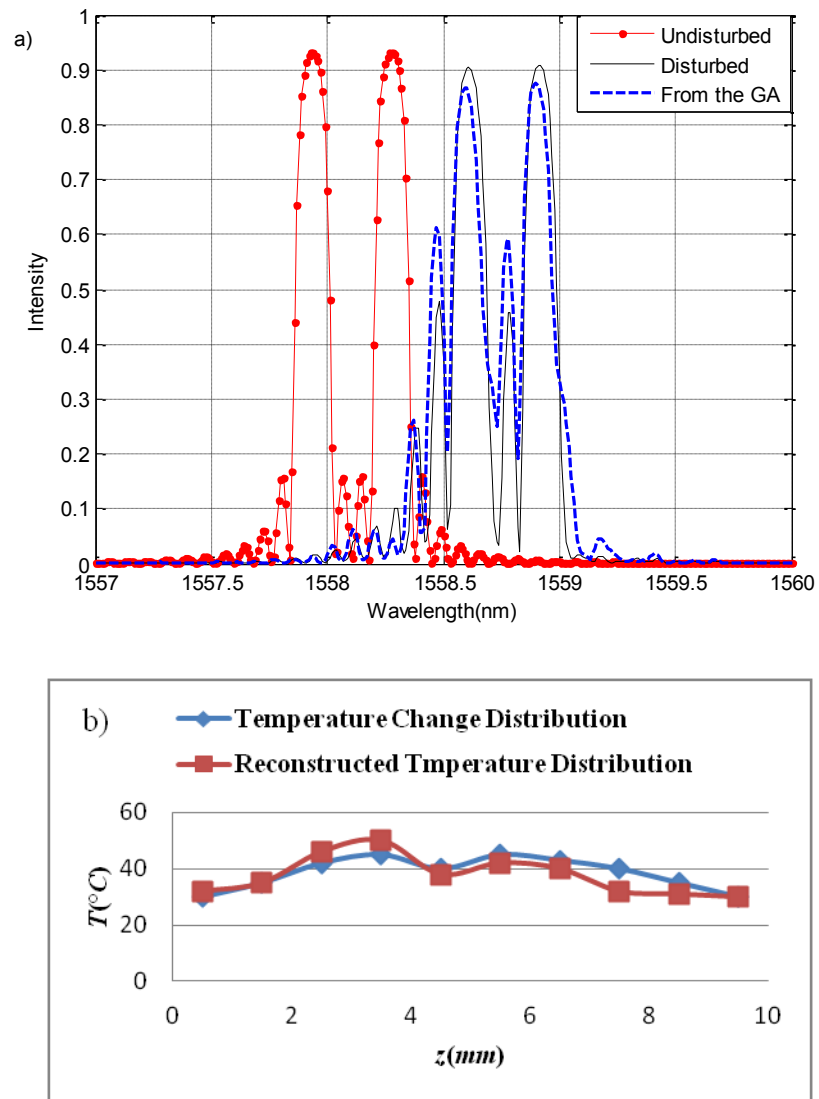


Figure 5.5 a) The applied and reconstructed reflected spectrum of the bow-tie FBG when is subjected to the temperature distribution that is shown in (b), and b) comparison between the applied and reconstructed temperature profile.

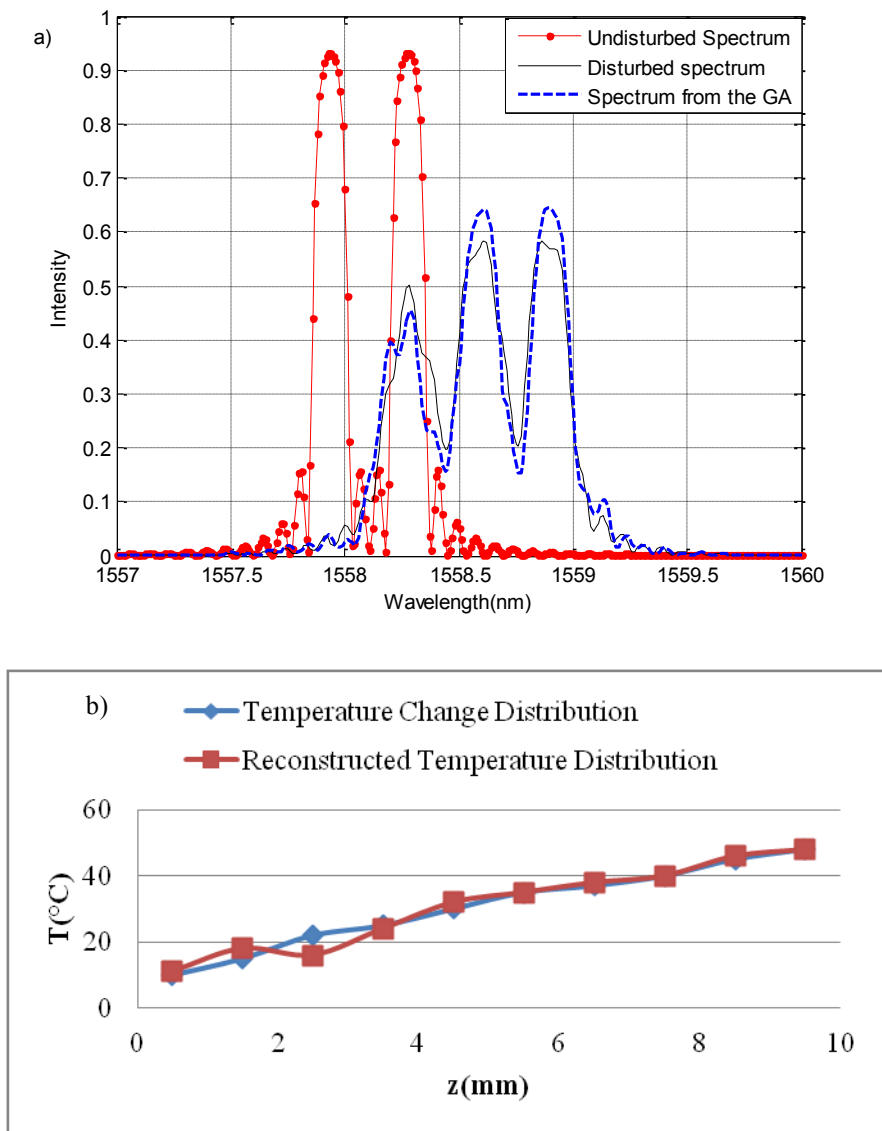


Figure 5.6 a) The applied and reconstructed reflected spectrum of the bow-tie FBG when is subjected to the temperature distribution that is shown in (b), and b) comparison between the applied and reconstructed temperature profile.

The following simulation results verify the efficiency of the approach for detecting a non-uniform distribution of the temperature and the transversal load along the Panda FBG sensor. The characteristics of the Panda FBG are shown in Table 5.1. The first simulated case is shown in Figure 5.7. Figure 5.7 (a) illustrates the response of the



Panda FBG when it is subjected to the simultaneous distribution of the temperature and the transversal loads as shown in Figures 5.7 (b) and (c) along its length.

Table 5.1 Parameters of the Panda FBG.

Parameter	Value
Length ( $L$ )	10 mm
Birefringence ( $B$ )	$3.2 \times 10^{-4}$
Slow axis transversal load sensitivity	0.14 (nm/(N/mm))
Fast axis transversal load sensitivity	0 (nm/(N/mm))
Strain coefficients $p_{11}, p_{12}$	0.121, 0.27
Young's modulus ( $E_{core} = E_{clad}$ )	74.52 GPa
$E_{SAP}$	51 GPa
Thermal expansion coefficient ( $\alpha_{core} = \alpha_{clad}$ )	$0.550 \times 10^{-6} \text{ } ^\circ\text{C}^{-1}$
$\alpha_{SAP}$	$1.554 \times 10^{-6} \text{ } ^\circ\text{C}^{-1}$
Poisson's ratio ( $\nu_{core} = \nu_{clad} = \nu_{SAP}$ )	0.19
Initial period ( $\Lambda_0$ )	533.5616 nm
Fast axis temperature sensitivity	16.5 (pm / $^\circ\text{C}$ )
Slow axis temperature sensitivity	15.6 (pm / $^\circ\text{C}$ )

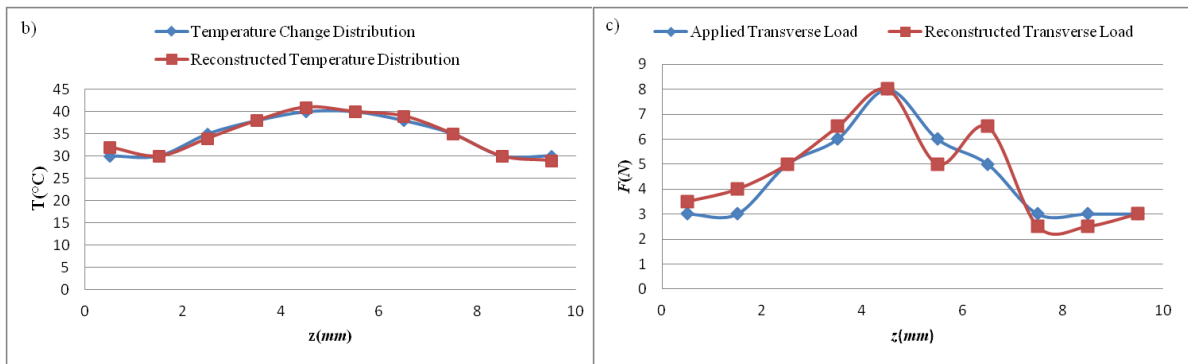
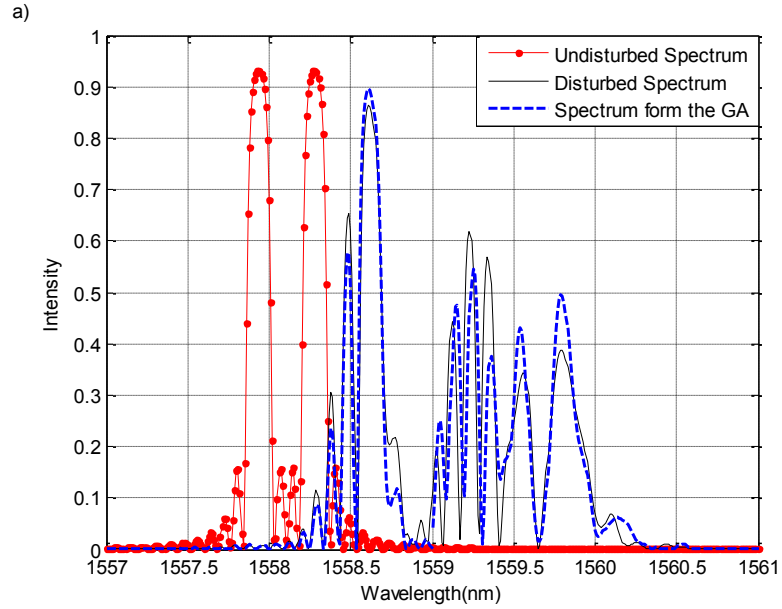


Figure 5.7a) Spectral response of the Hi-Bi FBG subjected to non-uniform temperature and transversal load distribution in (b) and (c), respectively, b) comparison between the applied and reconstructed temperature distribution, and c) comparison between the applied and reconstructed transversal load.

The reconstructed reflected spectra corresponding to the slow and the fast axis of the sensor is also shown in Figure 5.7 (a). Figures 5.7 (b) and (c) show the reconstructed distribution of the temperature change and the transversal loads along the sensor. The obtained fitness functions were in the order of  $10^{-1}$ . The maximum difference between the original anomaly and the reconstructed one for the temperature and the transversal loads are 2.1 °C and 1.32 N, respectively.

Figure 5.8 shows the distorted reflected spectrum of the sensor when it is subjected to the temperature and the transversal load variation of Figures 5.8 (b) and (c). Although the distorted reflected spectra corresponding to the slow and the fast axes of the sensor are not as obvious as in the previous example, the spectrum reconstructed with lower wavelengths from 1557 nm to 1558.7 nm is assumed to be the distorted reflected spectrum corresponding to the fast axis of the sensor from which the temperature distribution is obtained from. The reconstructed temperature distribution is shown in Figure 5.8 (b). The spectrum is reconstructed after 80 generations and the maximum difference between the original and the reconstructed temperature is 3.8 °C.

Consequently, the transversal load distribution is obtained through reconstructing the reflected spectrum corresponding to the slow axis of the sensor. The reconstructed transversal load is shown in Figure 5.8 (c). The spectrum is reconstructed after 80 generations and the maximum difference between the original and the reconstructed transversal load is 1.6 N.

Similarly, Figure 5.9 shows the disturbed reflected spectrum of the sensor when is subjected to the temperature and the transversal loads variations of Figures 5.9(b) and (c). The temperature distribution along the sensor is obtained by reconstruction of the reflected spectrum corresponding to the fast axis of the sensor as shown in Figure 5.9 (a). The reconstructed temperature distribution is shown in Figure 5.9 (b). Similarly, the reconstructed reflected spectrum corresponding to the slow axis of the sensor is reconstructed by the GA as is shown in Figure 5.9(a). The algorithm for the reconstruction of the polarized reflected spectra corresponding to the fast and the slow

axis was iterated for 80 generations and the obtained fitness functions were in the order of  $10^{-1}$ .

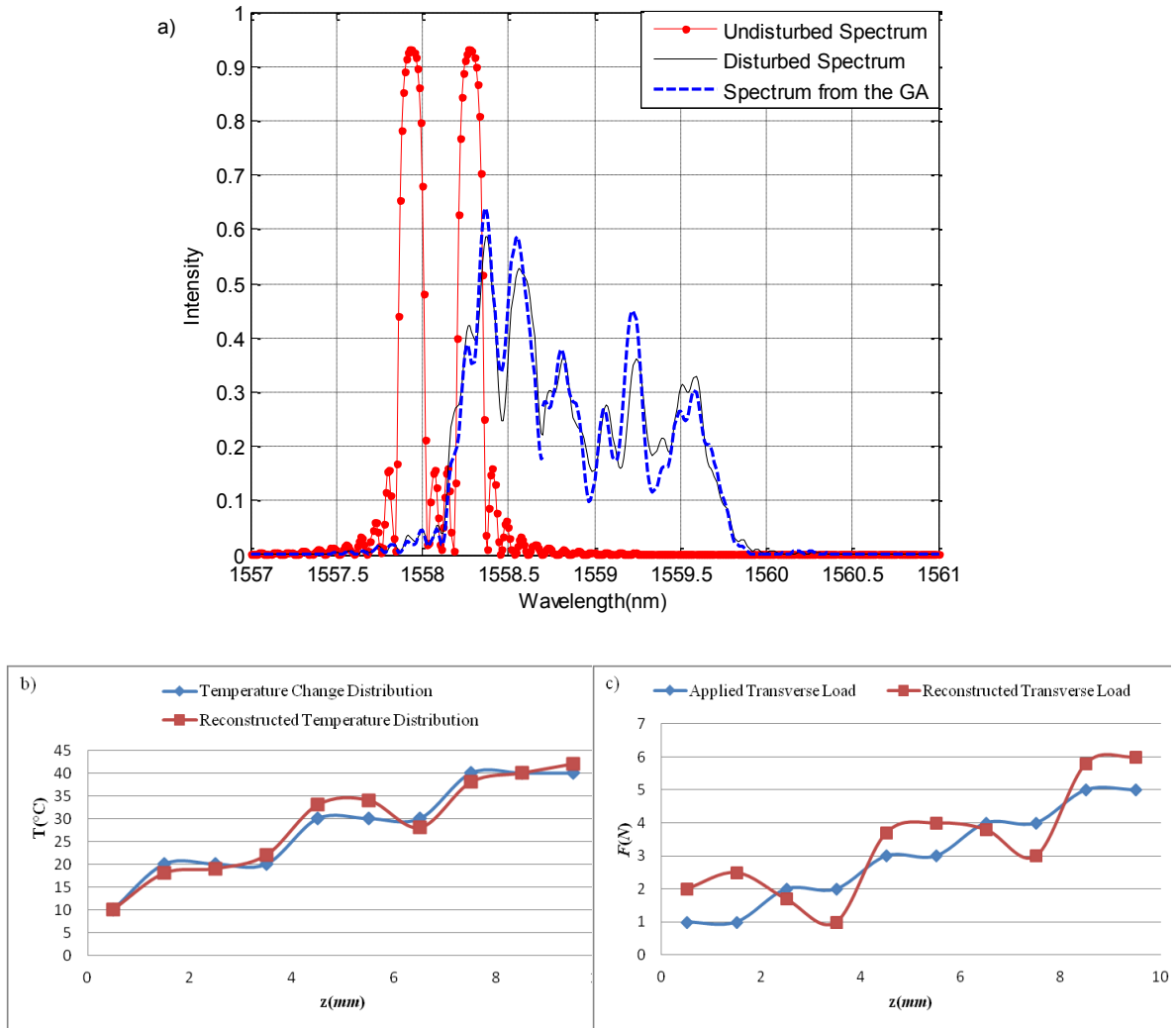


Figure 5.8a) Spectral response of the Hi-Bi FBG subjected to non-uniform temperature and transversal load distribution in (b) and (c), respectively, b) comparison between the applied and reconstructed temperature distribution, and c) comparison between the applied and reconstructed transversal load.

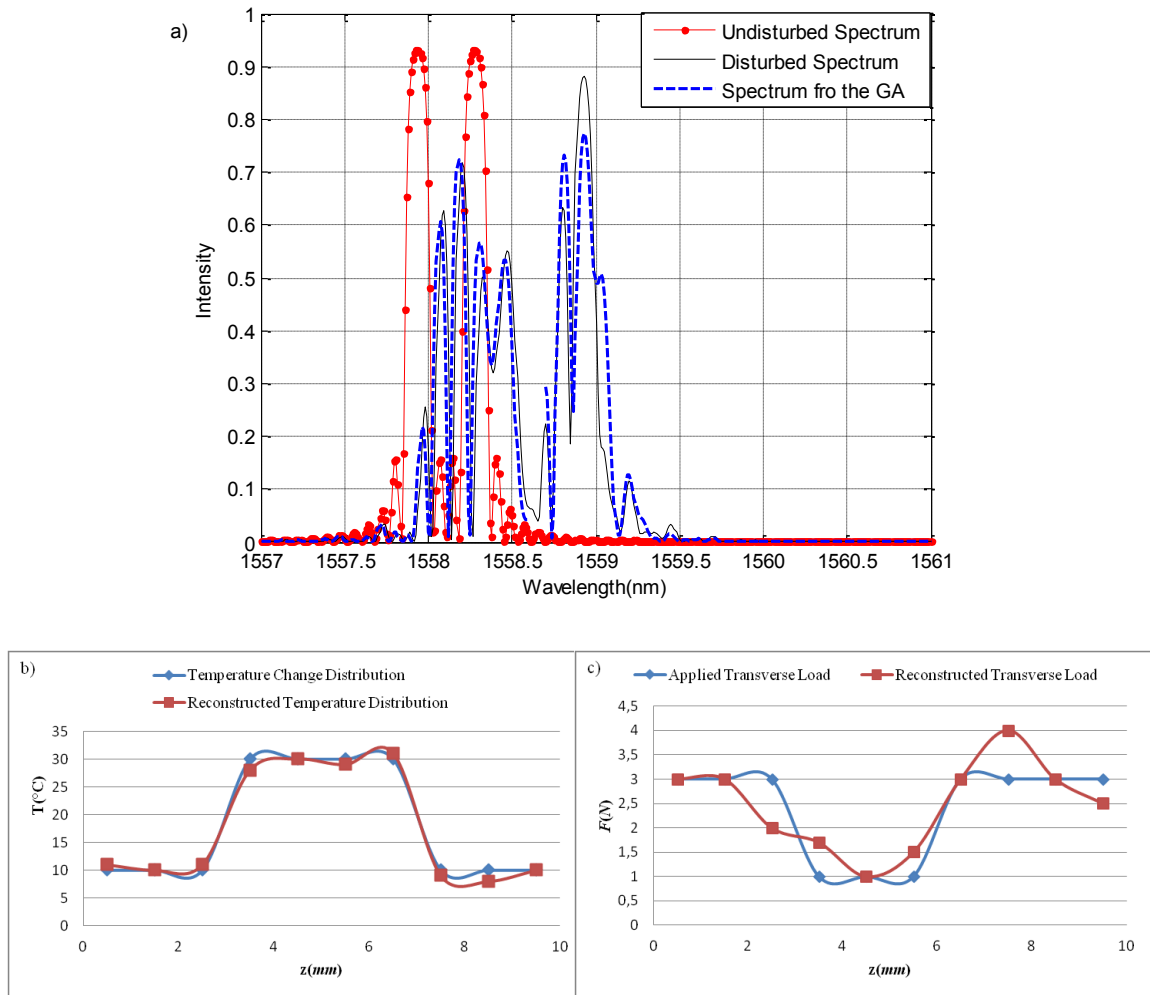


Figure 5.9a) Spectral response of an FBG subjected to non-uniform temperature and transversal load distribution in (b) and (c), respectively, b) comparison between the applied and reconstructed temperature distribution, and c) comparison between the applied and reconstructed transversal load.

The reconstructed transversal load is shown in Figure 5.9 (c). The maximum difference between the original anomaly and the reconstructed one for the temperature and the transversal loads are 1.8 °C and 1.2 N, respectively.

The presented functionality of the GA algorithm is tested on a multiplexed sensor system as shown in Figure 5.10. An optical source is assumed to be connected to a spatial multiplexed sensor system comprising of N identical Panda FBGs with the same

characteristics as mentioned in Table 5.1. The distance between the two consecutive FBGs is assumed to be 5 mm.

The sensor system is subjected to the temperature changes of 100 °C. In addition to the temperature change, three sensors in the middle of the first and the second series of sensors are subjected to a non-uniform transversal force and longitudinal strain, respectively. The applied transversal force along the three sensors of the first series of the sensors is shown in Figure 5.13 (a). Figure 5.11 shows the shifted and disturbed reflected spectra of the three disturbed sensors of the first series.

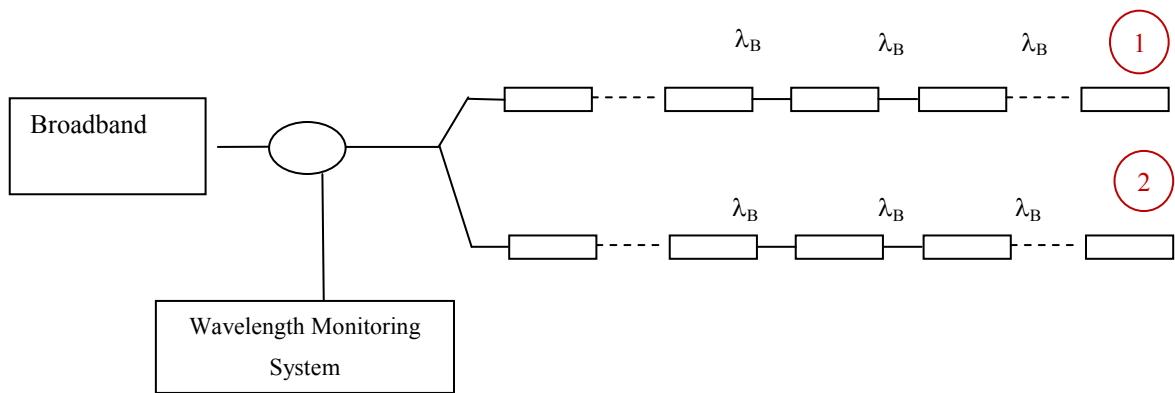


Figure 5.10 Schematic of the multiplexed sensor system that consists of the two parallel series of identical Panda FBG sensors.

As can be noted from Figure 5.11, the polarized reflected spectra corresponding to the main polarization axes of the fiber are shifted towards higher wavelengths due to the increase of the temperature. In addition, the spectra become distorted due to a non-uniform distribution of the transversal load. It can be observed from this figure that the distortion of the reflected spectrum corresponding to the slow axis of the sensor is quite noticeable while the reflected spectrum corresponding to the fast axis of the sensor

remains almost unchanged. The variation of the transversal load along the sensor can be obtained by reconstruction of the reflected spectra of the sensor corresponding to the slow axis of the sensor. The reconstructed polarized spectra corresponding to the slow polarized axes of the three consecutive sensors are shown in Figure 5.12.

The number of divided segments for the reconstruction of the spectrum is 10. The genetic algorithm was iterated until convergence and the optimal solutions have a low 0.261, 0.15 and 0.29 fitness values (error function) for the first, second and third disturbed sensors, respectively. The reconstructed transversal force profile of Figure 5.13(a) along the multiplexed sensor system that is obtained via the GA is shown in Figure 5.13 (b).

Although, the recovered strain profile does not precisely match the applied one, the trend of the applied force is captured excellently with a minimum number of segments required for reconstruction of the reflected spectrum changes due to the transversal force.

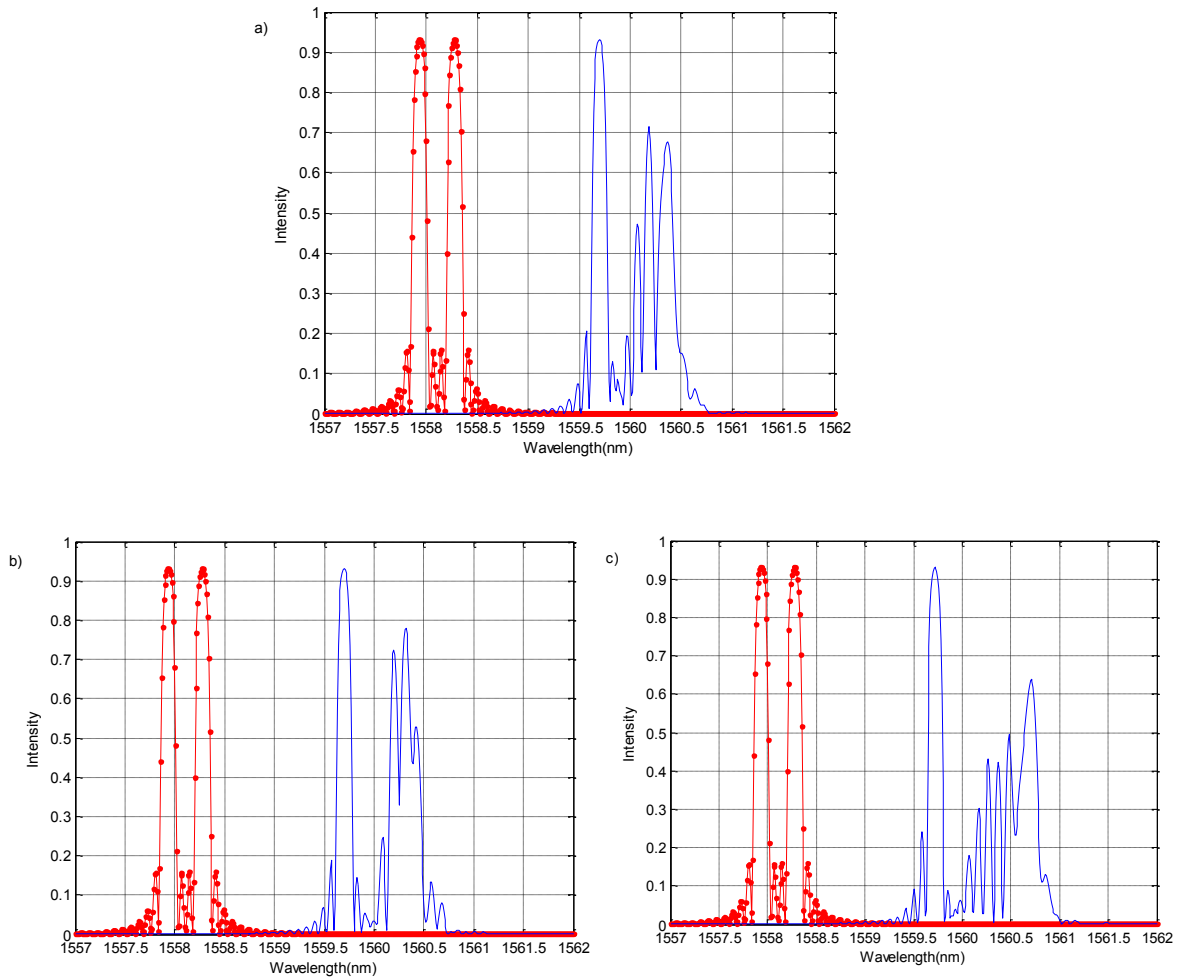


Figure 5.11 Reflected spectra of the undisturbed FBGs ( ● line) and the reflected spectra of the three perturbed sensors by a simultaneous transversal force shown in figure 5.13 and constant temperature change of 100 °C ( —line).



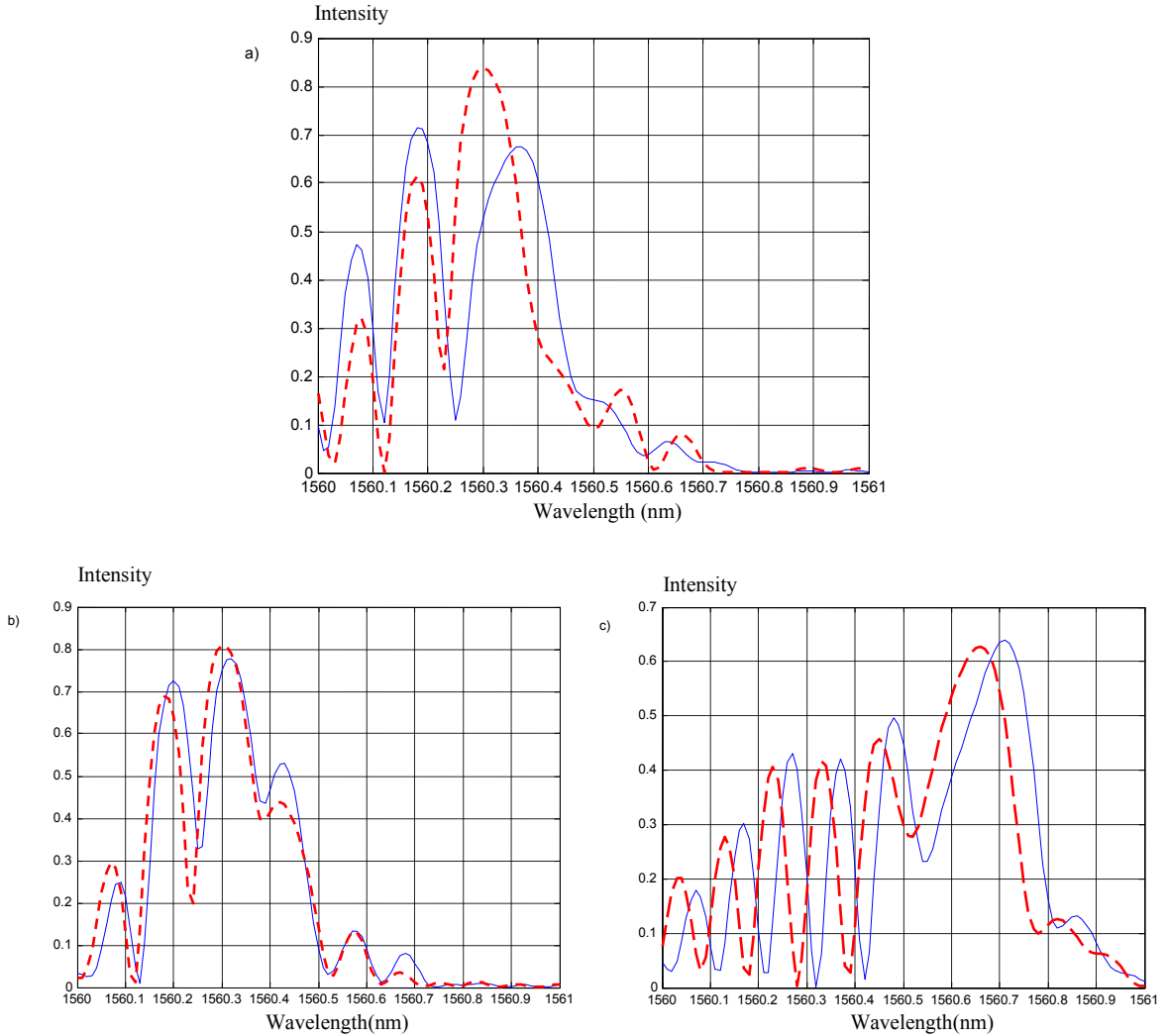


Figure 5.12 Original (solid line) and the one obtained from the optimal solutions from GA (dashed line) spectra for a) the first sensor, b) the second sensor, and c) the third sensor of the series 1 of the multiplexed sensor.

In Figure 5.13(b), the reconstructed transversal loads for the consecutive sensors are shown and then a moving average is applied to the reconstructed transversal load profiles to predict the variation profile of the transversal load along the length of the fiber sensors. The second series in Figure 5.10 is subjected to the temperature changes of  $100^{\circ}\text{C}$  and the longitudinal strain of Figure 5.16 (a).

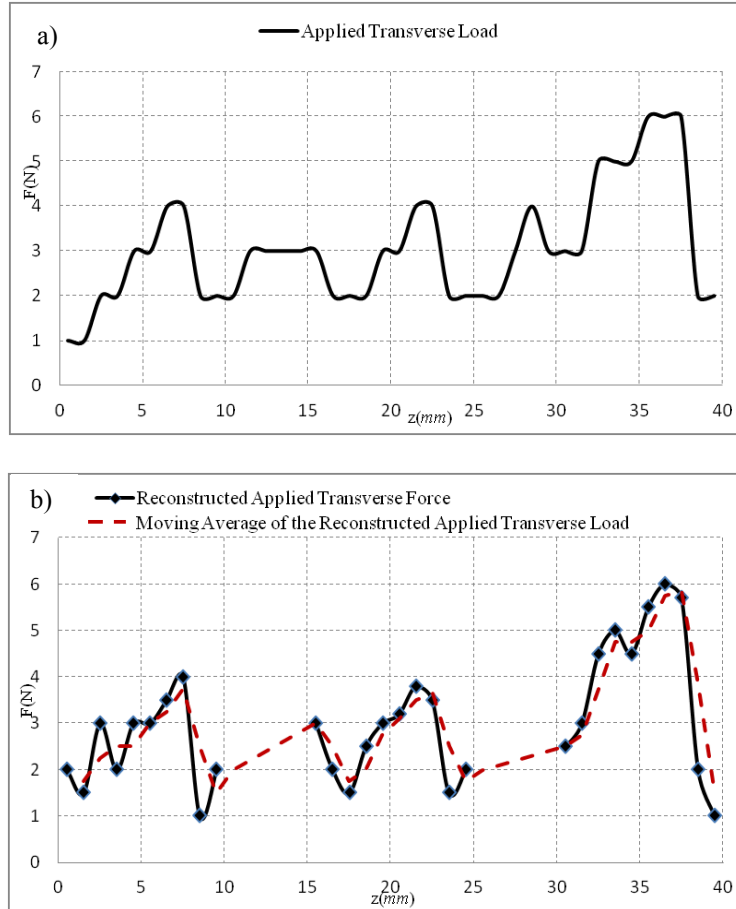


Figure 5.13a) Applied transversal force distribution along the three FBG sensors, and b) transversal force obtained by the GA.

Similar to the previous case, as can be noted from Figure 5.14, the polarized reflected spectra corresponding to the main polarization axes of the fiber are shifted towards higher wavelengths due to the increase of the temperature. In addition, both reflected spectra corresponding to the slow and the fast polarization axes of the sensor are distorted. The variations of the longitudinal strain along the sensor system can be obtained by reconstruction of the reflected spectra of the sensor. The reconstructed spectra of the three consecutive sensors are shown in Figure 5.15.

The number of divided segments for the reconstruction of the spectrum is 10. The genetic algorithm was iterated until convergence and the optimal solutions have a low 0.11, 0.09, and 0.1 fitness values (error function) for the first, second and third disturbed sensors, respectively.

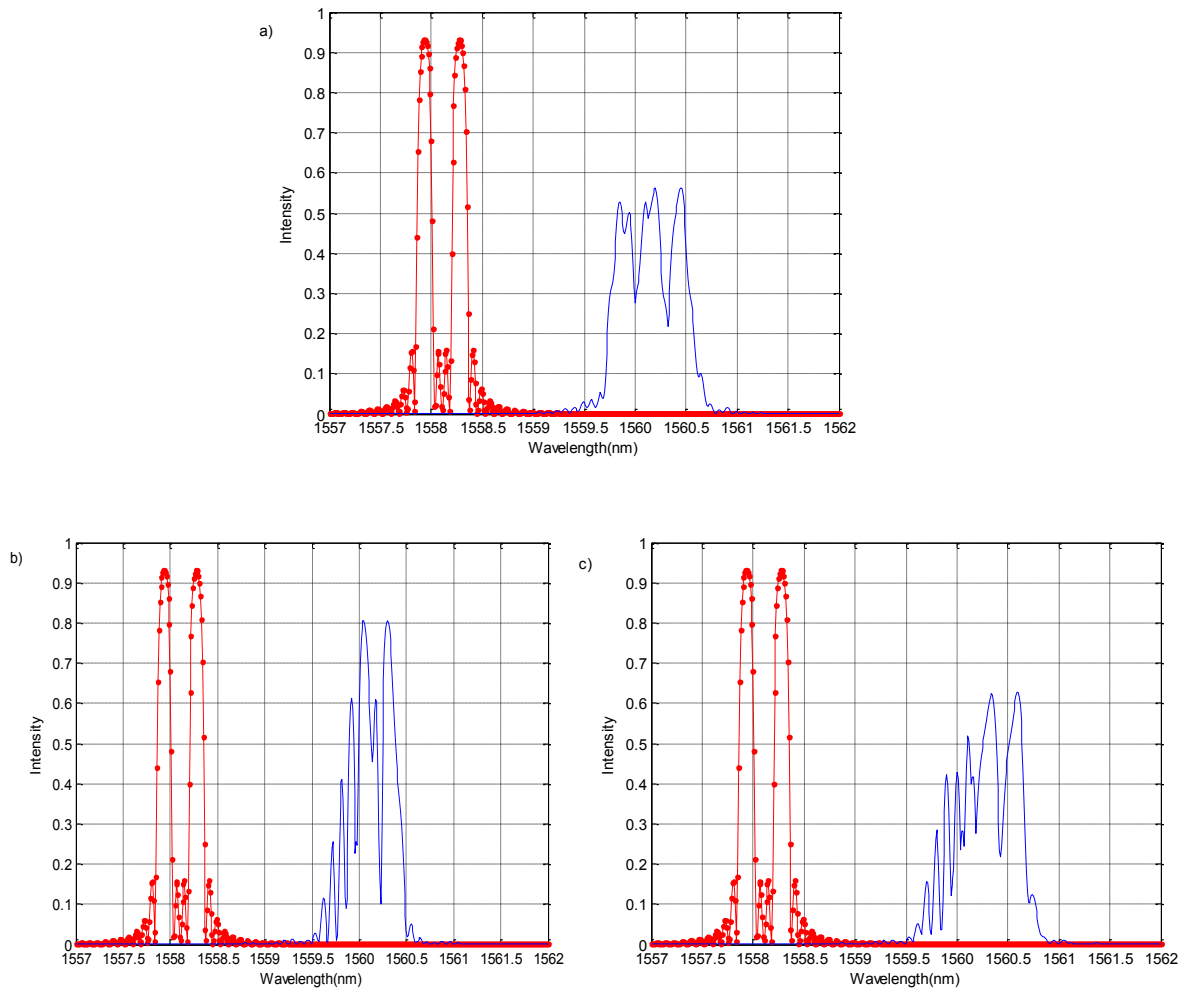


Figure 5.14 Reflected spectra of the undisturbed FBGs ( ● line) and the reflected spectra of the three perturbed sensors by a simultaneous longitudinal strain shown in figure 5.16 and constant temperature change of 100 °C ( —line).

Consequently, Figure 5.16 (b) shows the reconstructed longitudinal strain for the consecutive sensors of the second series of the sensor system. A moving average is

applied to the reconstructed longitudinal strain profiles to predict the variation profile of the strain along the length of the fiber sensors.

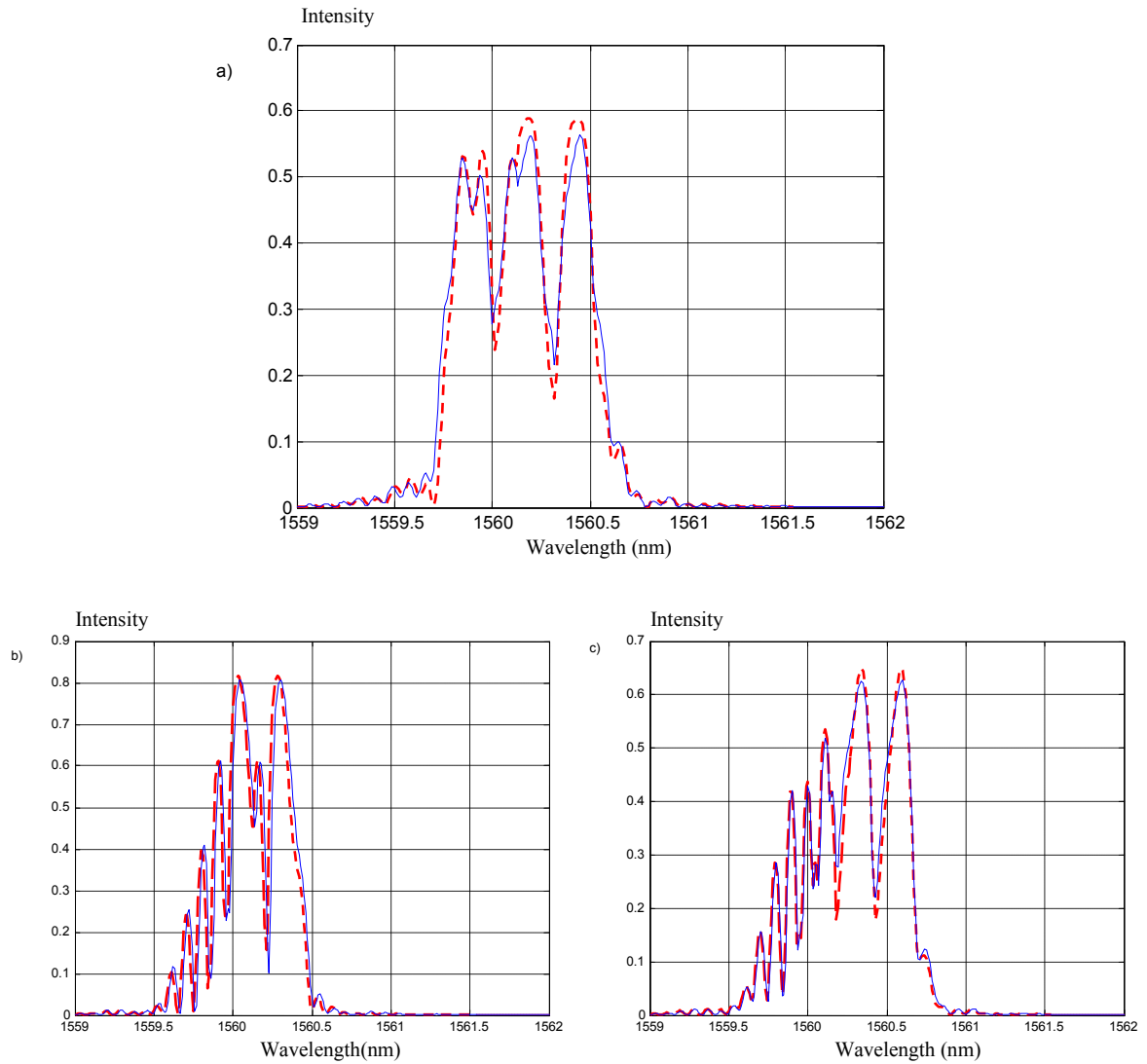


Figure 5.15 Original spectrum (solid line) and the one obtained from the optimal solutions from GA (dashed line) for a) the first sensor, b) the second sensor, and c) the third sensor of the second series of Panda FBGs of the multiplexed sensor system in figure 5.10.

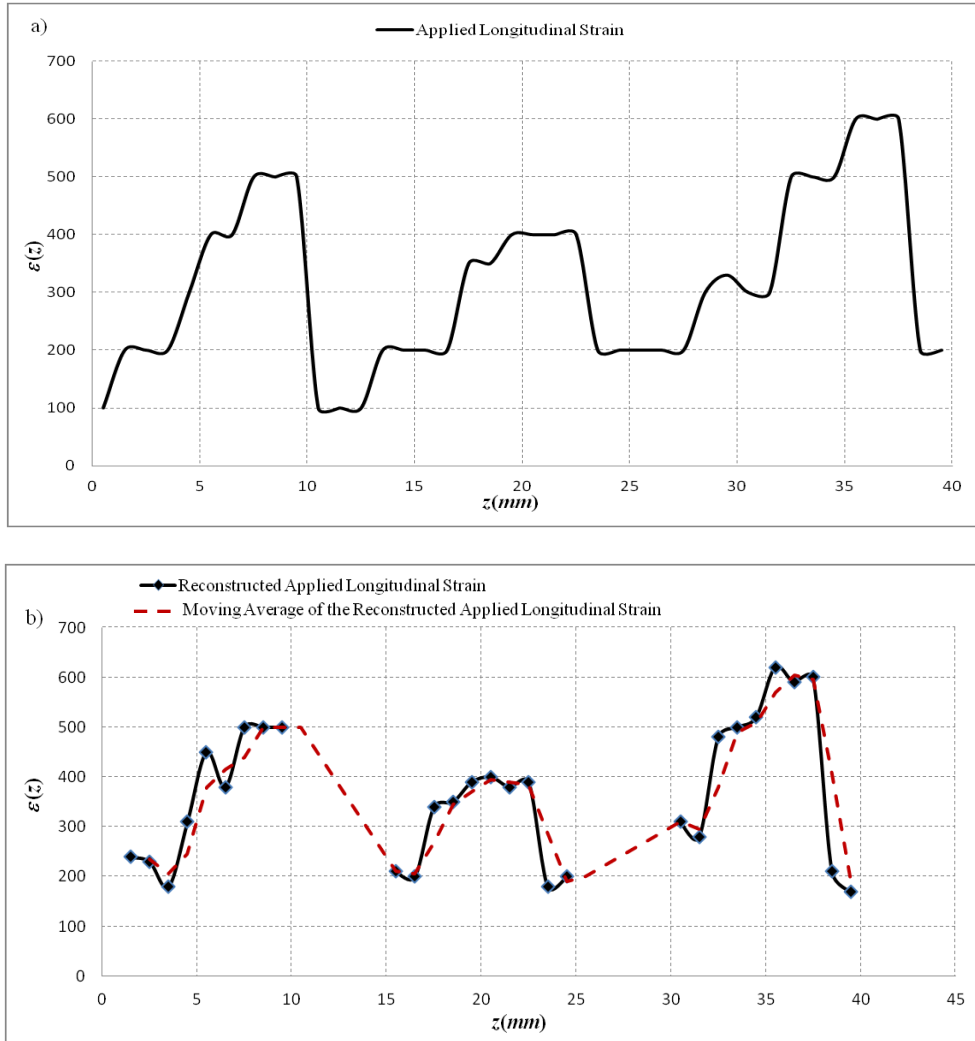


Figure 5.16 a) Applied longitudinal strain distribution along the three FBG sensors, and b) longitudinal strain obtained by the GA.

As in the last example, the efficiency of the algorithm is validated by reconstructing the temperature changes along a series of the same three Panda FBGs of the previous example that are subjected to the temperature distribution of Figure 5.19 (a). Figure 5.17 shows the disturbed reflected spectrum of the sensor by a non-uniform distribution of the temperature along the length of the sensors. The temperature profile is

recreated by reconstructing the reflected spectrum of the disturbed spectra. Figure 5.18 shows the reconstructed reflected spectra by using the GA.

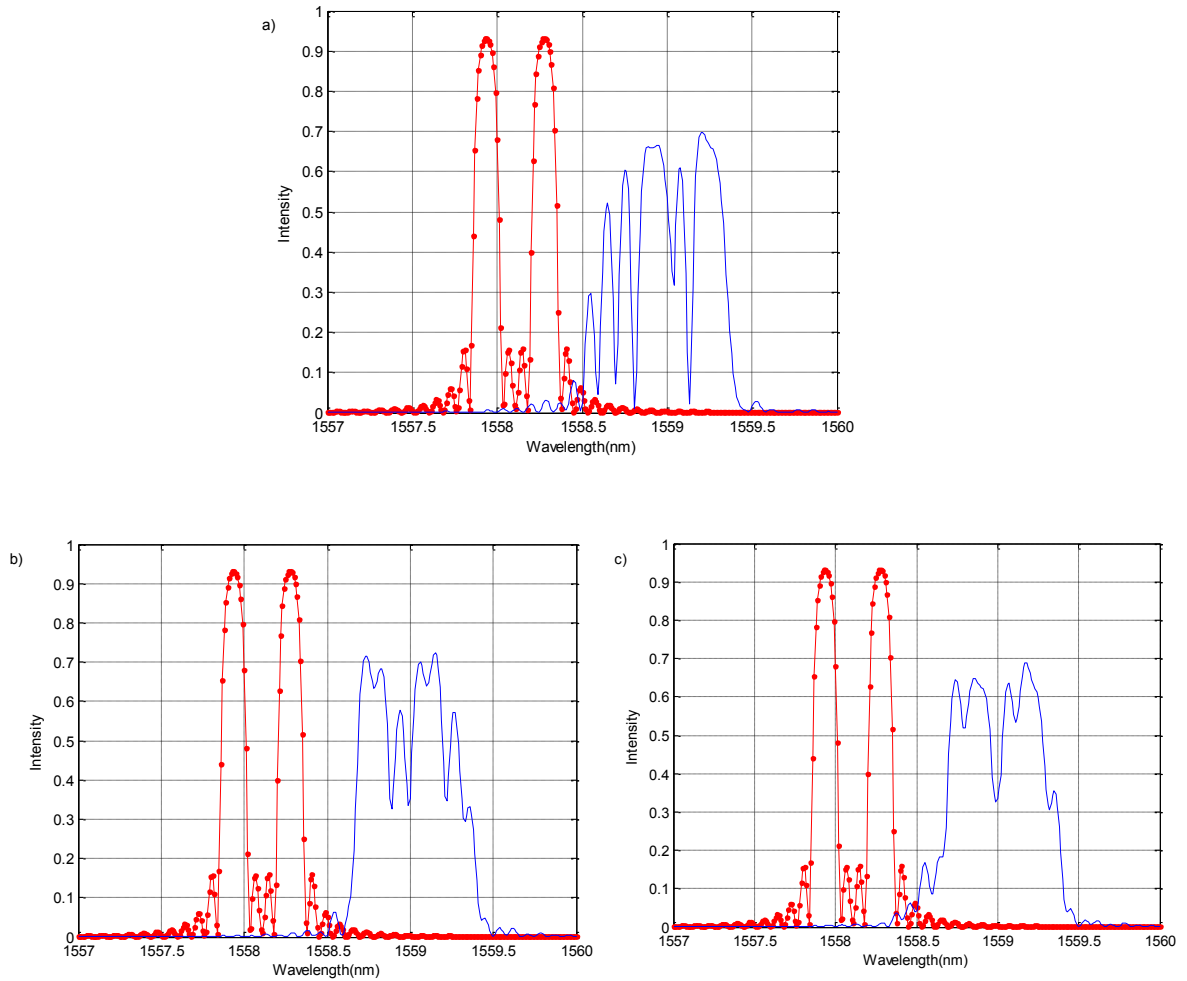


Figure 5.17 Reflected spectra of the undisturbed FBGs ( ● line) and the reflected spectra of the three perturbed sensors by a non-uniform distribution of temperature along a series of the three identical Panda FBGs( — line).

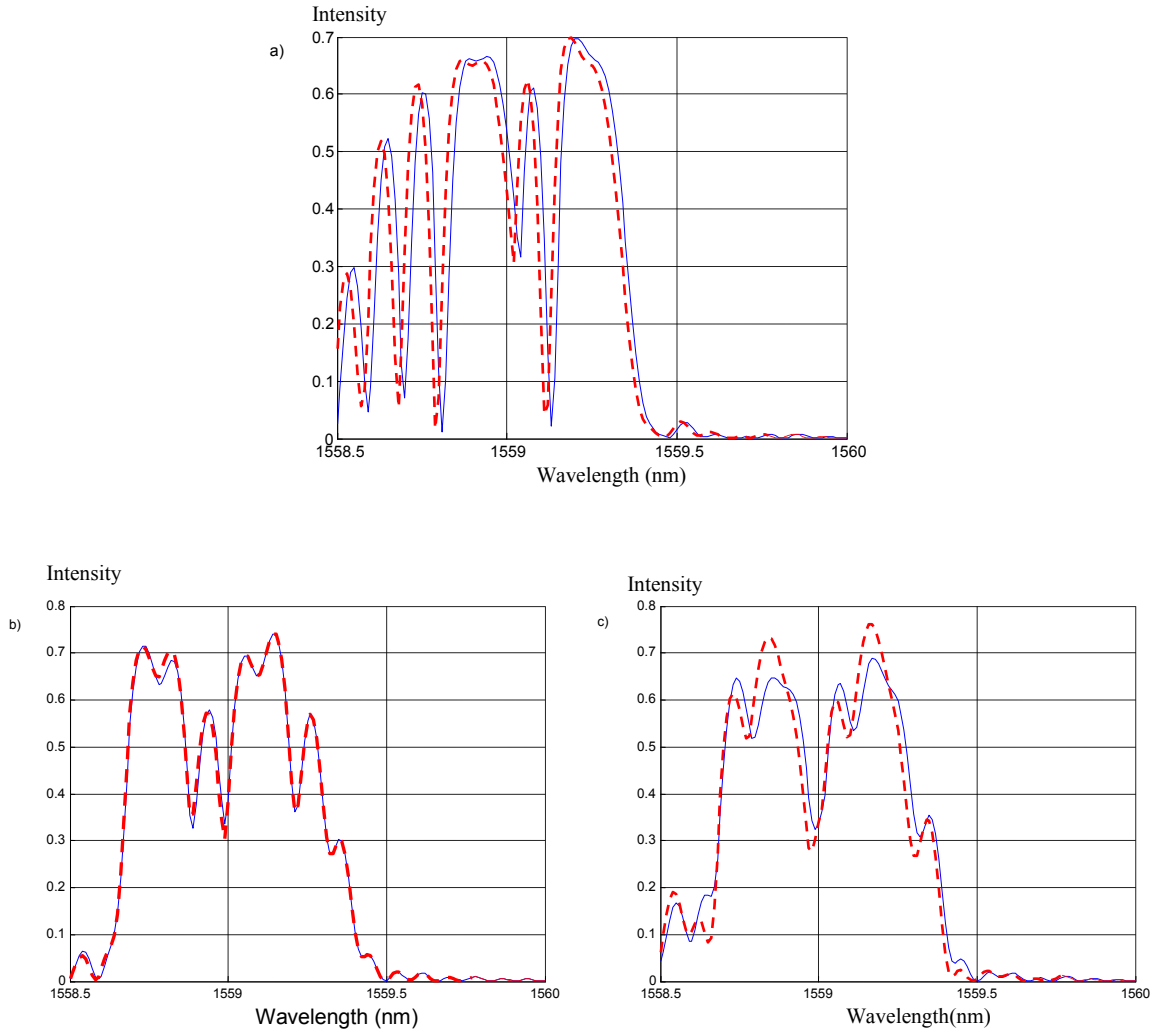


Figure 5.18 Original spectrum (solid line) and the one obtained from the optimal solutions (dashed line) from GA for a) the first sensor, b) the second sensor, and c) the third sensor of a series of Panda FBGs of the multiplexed sensor system in figure 5.10.

Consequently, the temperature distributions along the series of sensors are reconstructed. Figure 5.19 shows the original and the reconstructed temperature distribution along the series of Panda FBGs.

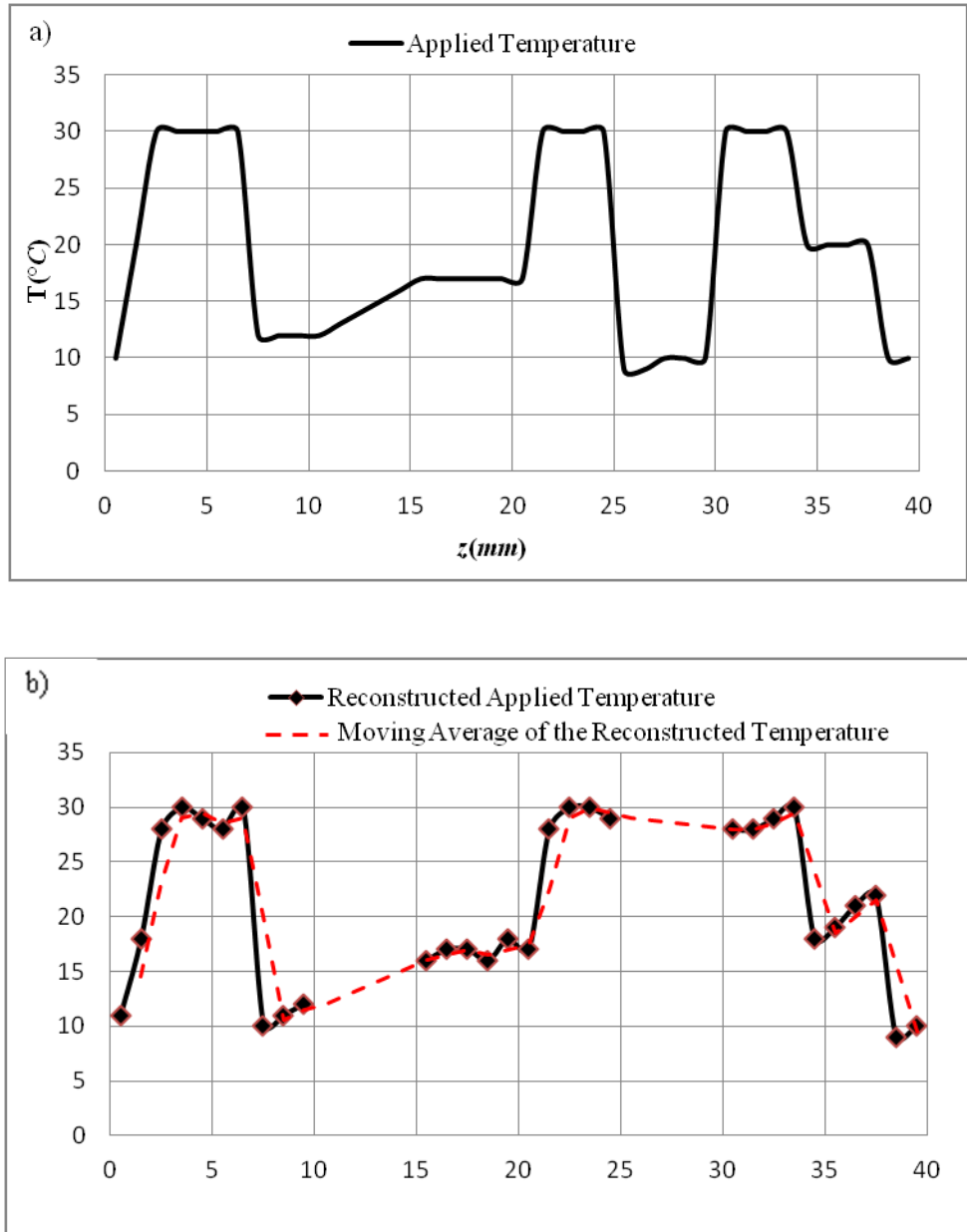


Figure 5.19a) Applied temperature distribution along the three FBG sensors, and b) temperature distribution obtained by the GA.



## 5.5 Conclusions

In this chapter a novel methodology for detecting the temperature distribution in monitored structures by using the fiber Bragg grating sensor that is fabricated into a high birefringence fiber was presented. The strain and the temperature changes effects on the embedded Hi-Bi FBG sensors were separately modeled by introducing the change of the refractive indices and the grating period along the fiber to the transfer matrix formulation method. Each Bragg reflection corresponding to the principal axes of the fiber has different dependencies on the temperature and the strain. Using this property, the temperature and the strain dependency is decoupled. Furthermore, the use of the genetic algorithms for reconstruction of a non-uniform applied temperature from the reflected spectrum is presented.

Moreover, the response of a sensor to the temperature, longitudinal strain, and transversal loads was studied and a novel approach for detection of a non-uniform profile of the temperature and the transversal loads when they are applied simultaneously to the sensor is proposed and developed. The variations of the temperature and the strain were detected inversely from the distorted reflected spectrum of the sensor. It is shown that, since the fast axis of the sensor is almost insensitive to the transversal load, the temperature variations can be detected from the spectrum corresponding to the fast axis. This was accomplished by introducing a population of the refractive index corresponding to the fast axis of the sensor. The temperature distribution was detected from the best solution of the GA for the refractive index distribution corresponding to the fast axis of the sensor. Furthermore, the load profile was obtained by reconstructing the polarized reflected spectrum of the sensor corresponding to the slow axis of the fiber.

The methodology was applied to a multiplexed sensor system when it is subjected to a uniform temperature change and non-uniform transversal load and longitudinal strain along each series of the sensor system. It is shown that in addition to detecting the effects of the temperature on the spectra of the sensor system, the longitudinal and the transversal loads variations can be obtained from the reflected spectrum of the series of Hi-Bi FBGs.

# Chapter 6

## Conclusions and Future Work

### 6.1 Conclusions

A methodology for detecting the damage profile, based on the reconstruction of the reflected spectrum of the Bragg grating fabricated into the single mode or high birefringence fiber was presented. The key step was to obtain an accurate trend line of the perturbation from the reflected spectrum of the sensors.

The reflected spectrum of the FBG sensor is sensitive to the anomalies. The effects of non-uniform distributions of the longitudinal strain, transversal load, temperature, and simultaneous longitudinal and transversal load to the reflected spectrum of the FBG and Hi-Bi FBG was studied and the disturbed reflected spectrums were modeled theoretically.

The distribution of the anomaly was obtained inversely by reconstructing the disturbed reflected spectrum of the sensor that was obtained theoretically. The possible solutions were expressed in terms of the grating period and refractive index along the fiber. The best solution was obtained when the algorithm convergences to the vector that creates the reflected spectrum that has the lowest fitness function (error) with the original spectrum. The obtained grating period and refractive index distribution along the fiber was correlated with the anomaly distribution along the fiber. The obtained perturbation

profile in millimeter level could describe the failure mechanism of the monitored structure at the macro level.

The methodology can be applied for studying the residual strains, internal strain distribution, and crack propagation by obtaining the strain/stress field in the surrounding material of the sensor even in cases of high strain gradients such as disbond in the bonded joints and delimitations in the monitored structures.

## **6.2 Future Work**

The future direction of the research can be outlined as follow:

- In this thesis, the study of a non-uniform anomaly along the high birefringence fiber is based on the assumption that the sensors are embedded in a way that the transversal loads are applied along the fast axis of the fiber. The response of the high birefringence FBG to the transversal loads varies with the loading angle relative to the polarization axes. Another area of future research is to obtain a non-uniform distribution of strains when the transversal load is applied in a direction that has an arbitrary angle with the polarization axes.
- Among the type of Hi-Bi FBGs, in this thesis, the Hi-Bi FBG sensors with a small transversal load sensitivity for the fast axis are chosen for the two-dimensional detection of the load. A solution that can retrieve the anomaly profile from the

reflected spectrum of any type of Hi-Bi FBG sensor is an important extension of this work.

- The reflected spectrum of the FBG sensor when it is subjected to the simultaneous non-uniform distribution of temperature, longitudinal strain, and transversal load is highly distorted. A problem of interest is to find the profile of each anomaly from the highly distorted reflected spectrum of the sensor.
- An area for further research is to enhance the performance of the genetic algorithm in terms of speed and accuracy, for example, this can be done by proposing a new operator or by modifying the existing operators.
- It is important to recognize that the sensor is regarded as a foreign entity to the host structure and the optical behaviour of the fiber alters whenever embedded in the material. Therefore, a problem of interest is to study the change in optical behaviour of the sensor whenever it is embedded in the monitored structure before applying the inverse method.
- Verification of the proposed approach through experimental results.
- This work is a first step for further development of the technique to apply on extended structures (for practical applications).

- Generalization of the approach to the cases when the fiber is curved. The detection of the characteristics of the fiber from its reflected spectrum when the sensor is bended can extend the use of the FBG sensors for the curvature measurement.
- Exploring other optimization methods in order to minimize the computational time for obtaining the anomaly profile (ideally close to real time) can be an important future development of this work.

Any of the above mentioned discussions can be investigated in detail as a challenging research topic which can significantly improve the current results on the use of FBG sensors for the detection of the anomaly and its non-uniform distribution within the monitored structure.

# Bibliography

- [1] www.boeing.com, September 2011.
- [2] K. Shivakumar, "Failure Mechanics of a Composite Laminate Embedded with a Fiber Optic Sensor," *J. Compos. Mater*, vol. 39, 777-98, 2005.
- [3] J. Silva, T. Devezas, A. Silva and J. Ferreira, "Mechanical Characterization of Composites with Embedded Optical Fibers," *J. Compos. Mater*, vol.39.1261-81, 2005.
- [4] J. Botsis, L. Humbert, F. Colpo, and P. Giaccari, "Embedded fiber Bragg grating sensor for internal strain measurements in polymeric materials," *Opt. Laser Eng*, vol. 43, 491-510, 2005.
- [5] W. Stephen, P. Ralph, P. Tatam, R. Stephen, R. Fuller, and Colin Crompton, "Monitoring transient strains on a gun barrel using fibre Bragg-grating sensors," *Meas. Sci. Technol*, vol. 10, 1999.
- [6] T. liu, C. Wang, Y. Wei, Y. Zhao and D. Huo, "Fiber optic sensors for mine hazard detection", *journal of physics: Conference series*, vol. 178, 2009.
- [7] M. Willsch, P. Krammer, N. M. Theune, and W. Ecke, "Highly sensitive micro mechanical fiber Bragg grating acceleration sensor combined with a new multiplexable interrogation principle," *Proc. SPIE*, 46-53, 2000.
- [8] K. Schroeder, "A fibre Bragg grating sensor system monitors operational load in a wind turbine rotor blade," *Meas. Sci. Technol*, vol.17, 1167-72, 2006.

- [9] H.Y. Tam, S.Y. Liu, B.O. Guan, W. H. Chung, T.H.T. Chan, and L.K. Cheng, "Fiber Bragg grating sensors for structural and railway applications," *In Proceedings of Photonics Asia*, 2004.
- [10] G. Zhou and L.M. Sim, "Damage detection and assessment in fibre-reinforced composite structures with embedded fibre optic sensors-review," *Smart Mater. Struct*, vol. 11, 925-39, 2002.
- [11] Y. Zhang, S. Li, z. Yin, B. Chen, and H. Liang Cui, "Fiber-Bragg-grating-based seismic geophone for oil/gas prospecting," *Opt. Eng*, vol. 45, 2006.
- [12] J. Hao, J. Leng, and W .Wei, "Non-destructive evaluation of composite pressure vessel by using FBG sensors," *Chin. J. of Aeronaut*, vol. 20, 2007.
- [13] P. M. Nellen, P. Mauron, A. Frank, U. Sennhauser, K. Bohnert, P. Pequignot, P. Bodor, and H. Brandle, "Reliability of fiber Bragg grating based sensors for downhole applications," *Sens. Actuators A*, vol. 103, 2003
- [14] J. Heo, J. Chung, and J. Lee, "Tactile sensor arrays using fiber Bragg grating sensors," *Sens. Actuators, A*, vol. 126, 312-327, 2006.
- [15] Y. Park, K. Chau, R. J. Black, M.R. Cutkosky, "Exoskeleton Force-Sensing End-Effectors with Embedded Optical Fiber-Bragg-Grating Sensors," *IEEE Trans. Rob*, vol. 25, 1319-31, 2009.
- [16] Y. Lin, J. Chen, K. Chang, J. Chem, J. Lai, "Real-time monitoring of local scour using fiber Bragg grating sensors," *Smart Mater. Struct*, vol. 14, 2005.
- [17] P. Childs, A. Wong, W. Terry, and G. Peng, "Measurement of crack formation in concrete using embedded optical fibre sensors and differential strain analysis," *Meas. Sci. Technol*, vol. 19, 2008.



- [18] Y. Okabe, Sh. Yashiro, R. Tsuji, T. Mizutani, and N. Takeda, "Effect of thermal residual stress on the reflection spectrum from fiber Bragg grating sensors embedded in CFRP laminates," *Comp. Part A*, vol. 33, 991-99, 2002.
- [19] k. S. C. Kuang, R. Kenny, M.P. Whelan, W.J. Cantwell, and P.R. Chalker, "Embedded fiber Bragg grating sensors in advanced composite materials," *Compos. Sci. Technol*, vol. 61, 1379-87, 2001.
- [20] Y. Okabe, Sh. Yashiro, T. Kosaka, and N. Takeda, "Detection of transversal cracks in CFRP composites using embedded fiber Bragg grating sensors," *Smart Mater. Struct*, vol. 9, 832-38, 2000.
- [21] A.D. Kersey, M.A. Davis, H.J. Patrick, M. LeBlanc, K.P. Koo, C.G. Askins, M.A. Putnam, and E.J. Friebele, "Fiber Grating Sensor," *J. Lightwave Technol*, vol. 15, 1442-63, 1997.
- [22] K.O. Hill and G. Meltz, "Fiber Bragg Grating Technology Fundamentals and Overview," *J. Lightwave Technol*, vol. 15, 1263-76, 1997.
- [23] S. Huang, M. Ohn, M. LeBlanc, and R.M. Measures, "Continuous arbitrary strain profile measurements with fiber Bragg gratings," *Smart Mater. Struct*, vol. 7, 248-56, 1998.
- [24] M. LeBlanc, S. Huang, M. Ohn, R. M. Measures, A. Guemes, and A. Othonos, "Distributed strain measurement based on a fiber Bragg grating and its reflection spectrum analysis," *Opt. Lett*, vol. 21, 1405-7, 1996.
- [25] M. Volanthen, H. Geuger, M.J. Cole, and J.P. Dakin, "Measurement of arbitrary strain profiles within fiber gratings," *Electron. Lett*, vol. 32, 1028-29, 1996.

- [26] M. Ohn, S.Y. Huang, R.M. Measures, and J. Chwang, "Arbitrary strain profile measurement within fibre gratings using interferometric Fourier transform technique," *Electron. Lett*, vol. 33, 1997.
- [27] R. Feced, M. N. Zervas, and M. A. Muriel, "An efficient inverse scattering of a multichannel fiber Bragg grating based on a layer-peeling method", *IEEE J. Quantum Electron*, vol. 35, 1999.
- [28] O.V. Belai, E.V. Podivilov, O.Y. Schwarz, and D.A. Shapiro, "Finite Bragg grating synthesis by numerical solution of Hermitian Gel'fand–Levitan–Marchenko equations," *J. Opt. Soc*, vol. 23, 2040-45, 2006.
- [29] E.Peral, J.Capmany, and J.Marti, "Iterative solution to the Gel'fan-Levitan-Marchenko coupled equations," *IEEE J. Quantum Electron*, vol. 32, 2078–84, 1996.
- [30] C. Z. Shi, N. Zeng, N. M. Zhang, Y. B. Liao, and S. R. Lai, "Adaptive simulated annealing algorithm for the fiber Bragg grating distributed strain sensing," *Opt. Commun*, 226,167–73, 2003.
- [31] J. Skaar, and K. M. Risvik, "A genetic algorithm for the inverse problem in synthesis of fiber gratings," *J. Lightwave Technol*, vol. 16,1928–32, 1998.
- [32] G. Cormier, R. Bourdreau, and S. Theriault, "Real-coded genetic algorithm for Bragg grating parameter synthesis," *JOSA B*, vol. 18, 1771-76, 2001.
- [33] J. Skaar, L. Wang and, T. Erdogan. "On the synthesis of fiber Bragg gratings by layer peeling," *J. Lightwave Technol*, vol. 37, 165–73, 2001.

- [34] J. Azana, and M. Muriel, "Fiber Bragg grating period reconstruction using time-frequency signal analysis and application to distributed sensing," *J. Lightwave Technol*, vol.16,1928-32, 2001.
- [35] D.B. Leviton, and B.J. Frey, "Temperature dependent absolute refractive index measurements of synthetic fused silica," *Proc. SPIE*, 6273, 2006.
- [36] R. Kashyap, "Fiber Bragg grating", Academic Press, 2009.
- [37] Y.J. Rao, D.J. Webb, D.A. Jackson, L. Zhang, and I. Bennion, "In-fibre Bragg grating temperature sensor system for medical applications," *J. Lightwave Technol*, vol.15, 779-85 ,1997.
- [38] S. Pal, "Non linear temperature dependence of Bragg gratings written in different fibers, optimised for sensor applications over a wide range of temperatures," *Sensor Actuat. A-Phy*,vol.112, 211-19, 2004.
- [39] P. Chapeleau, D. Casari, Y. Leduc, C. Scudeller, R. Lupi, L. Ny, and C. Boisrobert, "Determination of strain distribution and temperature gradient profiles from phase measurements of embedded fibre Bragg gratings," *J. Opt. A: Pure Appl. Opt.* vol.8, 775–81, 2006.
- [40] Y. J. Rao, "In-fibre Bragg grating sensors," *Meas. Sci. Technol*, vol. 8,355–75, 1997.
- [41] M. G. Xu, J. L. Archambault, L. Reekie, and J. P. Dakin, "Discrimination between strain and temperature effects using dual-wavelength fibre grating sensors," *Electron. Lett*, vol. 30,1085–7, 1994

- [42] J. Jones, "Review of fiber sensor techniques for temperature-strain discrimination," *Proceedings of the 12<sup>th</sup> International Conference on Optical Fiber Sensors (OFS-12)*, 36-39, 1997.
- [43] L. Ferreira, F. Araujo, J. Santos, and F. Farahi, "Simultaneous measurement of strain and temperature using interferometrically interrogated fiber Bragg grating sensors," *Opt. Eng.* vol. 39, 2226-34, 2000.
- [44] R. B. Wagreich, W.A. Atia, H. Singh, and J. S. Sirkis, "Effects of diametric load on fibre Bragg gratings fabricated in low birefringent fibre," *Electron. Lett.*, vol. 32, 1223– 1224, 1996.
- [45] R. Gafsi, and M. El-Sherif, "Analysis of Induced-Birefringence Effects on Fiber Bragg Gratings," *Opt. fiber technol.*, vol. 6, 299-323, 2000.
- [46] J. A. Guemes, and J. M. Menéndez, "Response of Bragg grating fiber-optic sensors when embedded in composite laminates," *Compos. Sci. Technol.*, vol. 62, 7-8, 2002.
- [47] C. Caucheteur, S. Bette, R. Garcia-Olcina, M. Wuilpart, S. Sales, J. Capmany, and P. Megret, "Transversal Strain Measurements Using the Birefringence Effect in Fiber Bragg Gratings," *IEEE Photonics Technol. Lett.*, 966 - 68, 2007.
- [48] M. Prabhugoud, and K. Peters, "Finite element model for embedded fiber Bragg grating sensor," *Smart Mater. Struct.* vol. 15, 550–62, 2006.
- [49] Y. Wang, B. Yun, W. Zhuyuan, L. Changgui, and C. Yiping, "Effects of distributed birefringence on fiber Bragg grating under non-uniform transversal load," *Opt. Lasers Eng.*, vol. 40, 1037-40, 2008.

- [50] E. Udd, W. S. Kreger, M. Kunzler, T. Taylor, and R. Lumsden, "Using Multi-Axis Fiber Grating Strain Sensors to Measure Transversal Strain and Transversal Strain Gradients in Composite Materials with Complex Weave Structures," *Proc. SPIE* 4694, p 162, 2002.
- [51] E. Udd, K. Black, W. Schulz, S. Kreger, and M. Kunzler, "In-Situ Evaluation of Composite Structural Performance in Presence of High Stress/Strain Gradients Using Multi-axis Fiber Grating Strain Sensors," Optical Fiber Sensors Conference Technical Digest, 2002.
- [52] R. M. Measures, "Structural Health Monitoring with Fiber", Optic Technology, Academic, 2001.
- [53] C. M. Lawrence D.V. Nelson, and E. Udd, "Measurement of transversal strains with fiber Bragg gratings," *Proc. SPIE* 042, 218, 1997.
- [54] C. M. Lawrence, D. V. Nelson, E. Udd, and T. Bennett, "A Fiber Optic Sensor for Transversal Strain Measurement," *Experimental Mechanics*, vol. 3, 1999.
- [55] E. Chehura, C .Ye, S. Staines, S. W. James and R. P. Tatam, "Characterization of the response of fibre Bragg gratings fabricated in stress and geometrically induced high birefringence fibres to temperature and transversal load," *Smart Mater. Struc*, vol. 4, 888–95, 2004.
- [56] J. F. Botero-Cadavid, J. D. Causado-Buelvas, and P. Torres, "Spectral Properties of Locally Pressed Fiber Bragg Gratings Written in Polarization Maintaining Fibers," *J. Lightwave Technol*, vol.28, 1291-97, 2010.
- [57] C. R. Dennison, and P. M. Wild, "Sensitivity of Bragg gratings in birefringent optical fiber to transversal compression between conforming materials," *Appl. Optics*, vol. 49, 2250-61, 2010.

- [58] M. Etezzad, M. Kahrizi, and K. Khorasani, "A novel multiplexed fiber Bragg grating sensor with application in structural health monitoring," *Phys. Status Solidi C*, 8, 2953-56, 2011.
- [59] Y. Wang, B. Yun, N. Chen, and Y. Cui, "Characterization of a high birefringence fibre Bragg grating sensor subjected tonon-homogeneous transversal strain fields," *Meas. Sci. Technol*, vol.17, 939–42, 2006.
- [60] C. A. Black, E. Udd, W. L. Schulz, S.T. Kreger, M. Kunzler, T. Taylor, R. W. Lumsden and D. Heider, "Using multi-axis fiber grating strain sensors to measure transversal strain and transversal strain gradients in composite materials with complex weave structures," *Proc. SPIE*, 4694: 162-167.
- [61] F. Bosia, P. Giaccari, J.Botsis, M.Facchini, H.G.Limberger, and R. Salathe, "Characterization of the response of fibre Bragg grating sensors subjected to a two-dimensional strain field," *Smart. Mater. Struct*, vol. 12, 925-34, 2003.
- [62] I. Abe, H. J. Kalinowski, O. Frazao, J. L. Santos, R. N. Nogueira, and J. L. Pinto, "Superimposed Bragg gratings in high-birefringence fibre optics: three-parameter simultaneous, Measurements," *Meas. Sci. Technol*, vol. 15, 1453–57,2004.
- [63] T. Mawatari, and D. A. Nelson, "multi-parameter Bragg grating fiber optic sensor and triaxial strain measurement," *Smart Mater. Struct*, vol.17, 035033, 2008.
- [64] G. Luyckx, W. Waele, J. Degrieck, and W. Paepegem, "Three dimensional strain and temperature monitoring of composite laminates," *Insight-Non-Destructive Testing and Condition Monitoring*, vol.49, 10-16, 2007.

- [65] M. Sudo, M. Nakai, S. Suzaki, A. Wada, and R. Yamauchi, "Simultaneous Measurement of Temperature and Strain using PANDA Fiber Grating," OSA Technical Digest Series, 1997.
- [66] G. Chen, L. Liu, H. Jia, J. Yu, L. Xu, and W. Wang, "Simultaneous pressure and temperature measurement using Hi-Bi fiber Bragg gratings," *Opt. Commun.*, 99–105, 2003.
- [67] S. T. Oh, W. T. Han, U. C. Paek, and Y. Chung, "Discrimination of temperature and strain with a single FBG based on the birefringence effect," *Opt. Express*, vol. 12, 724-29, 2004.
- [68] M. Frocht, "Photoelasticity", John Wiley and Sons, Inc, Volume 2.
- [69] F. Casagrande, P. Crespi, A. Grassi, A. Lulli, R. Kenny, and M. Whelan, "From the reflected spectrum to the properties of a fiber Bragg grating: A genetic algorithm approach with application to distributed strain sensing," *Appl. Opt.* vol. 41, 5238-44, 2002.
- [70] S. C. Rashleigh, "Origins and control of polarization effects in single-mode fibers," *J. Lightwave Technol.*, vol. 1, 312-31, 1983.
- [71] Y. Wang, B. Yun, W. Zhuyuan, L. Changgui, and C. Yiping, "Effects of distributed birefringence on fiber Bragg grating under non-uniform transversal load," *Opt. Lasers Eng.*, vol. 40, 1037-40, 2008.
- [72] J. Noda, K. Okamoto, and Y. Sasaki, "Polarization-maintaining fibers and their applications," *J. Lightwave Technol.*, vol. 4, 1071-89, 1986.

- [73] R. B. Dyott, J. R. Cozens, and D. G. Morris, "Preservation of polarisation in optical-fibre waveguides with elliptical cores," *Electron. Lett*, vol. 15, 380-82, 1979.
- [74] M. P. Varnham, A. J. Barlow, D. N. Payne, and K. Okamoto, "Polarimetric strain gauges using high birefringence fiber," *Electron. Lett*, vol. 19, 699-700, 1983.
- [75] K. S. Chiang, D. Wong, and P.L. Chu, "Strain-induced birefringence in a highly birefringent optical fiber," *Electron. Lett*, vol. 26, 1344-46, 2002.
- [76] O. H. Waagaard, and J. Skaar, "Synthesis of birefringent reflective gratings," *Opt. Soc. Am. A*, vol. 20, 1207-20, 2004.
- [77] Z. Michalewicz, "Genetic algorithms + Data Structures=Evolution Programs (Springer-Verlag)", 1996.
- [78] M. Etezzad, M. Kahrizi and K. Khorasani, "Damage Monitoring in Composite Structures by Embedded Fiber Bragg Grating Sensors," *Proc. Int. Conf. for Heterogeneous Materials Mechanics (China: Shanghai City/ DEStech Publications, Inc)* pp 953-56, 2011.
- [79] A. Gill, K. Peters, and M. Studer, "Genetic algorithm for the reconstruction of Bragg grating sensor strain profiles," *Meas. Sci. Technol.* vol. 15, 1877-84, 2004.
- [80] M. Etezzad, M. Kahrizi, K. Khorasani, "Analysis of temperature and strain changes profiles by using fiber Bragg grating sensors," *Fiber Optic Sensors and Applications VI conference, SPIE Symposium*, April 2010.



- [81] M. Etezzad, M. Kahrizi and K. Khorasani, "Monitoring of anomaly changes in composite structures by embedded high birefringence fiber Bragg grating sensors," IEEE Newfoundland Electrical and Computer Engineering Conference (NECEC), November 2011.
- [82] M. Etezzad, M. Kahrizi and K. Khorasani, "Two-dimensional strain field measurement using fiber Bragg grating sensor and genetic algorithm," submitted to *Measurement Science and Technology*, 2012.
- [83] M. Prabhugoud, and K. Peters, "Finite Element Analysis of Multi-axis Strain Sensitivities of Bragg Gratings in PM Fibers," *J. Intell. Mater. Syst. Struct.*, vol. 18, 861-73, 2007.
- [84] K. Okamoto, T. Hosaka, and T. Eda-hiro, "Stress analysis of optical fibers by a finite element method," *IEEE J. Quantum Electron.*, vol. 17, 1981.
- [85] C. Ye, S. Staines, S. W. James, and R. P. Tatam, "A polarization-maintaining fibre Bragg grating interrogation system for multi-axis strain sensing," *Meas. Sci. Technol.*, vol. 13, 1446-49, 2002.
- [86] K. S. Chiang, "Temperature sensitivity of coated stress-induced birefringent optical fibers", *Opt. Eng.*, vol. 36, 999-1007, 1997.
- [87] G. Luyckx, J. Degriek, W. Waele, W. Paepegem, J. Roosbroeck, K. Chah, J. Vlekken, and A. Obst, "Feasibility Study on Measuring Axial and Transversal Stress/Strain Components in Composite Materials using Bragg Sensors," Sixth International Conference on Space Optics, 2006.

- [88] K. Dossou, S. LaRochelle, and M. Fontaine, "Numerical analysis of the contribution of the transversal asymmetry in the photo-induced index change profile to the birefringence of optical fiber," *J. Lightwave Technol.* vol. 20, 1463-70, 2002.
- [89] A. J. Barlow and D. N. Payne, "The stress-optic effect in optical fibers," *IEEE J. Quantum Electron*, 1983.
- [90] E. Chmielewska, W. Urbanczyk, and W. Bock, "Measurement of pressure and temperature sensitivities of a Bragg grating imprinted in a highly birefringent side-hole fiber," *Appl. Opt.*, vol. 42, 6284-91, 2003.
- [91] Y. Zhou, K. Gao, R. Huang, R. Qu, and Z. Fang, "Temperature and stress tuning characteristics of long-period gratings imprinted in Panda fiber," *IEEE Photonics Technol. Lett.*, vol. 15, 1728-30, 2003.
- [92] Y. Dong, L. Chen, and X. Bao, "High-Spatial-Resolution Time-Domain Simultaneous Strain and Temperature Sensor Using Brillouin Scattering and Birefringence in a Polarization-Maintaining Fiber," *IEEE Photonics Technol. Lett.*, vol. 22, 1364 - 66, 2010.
- [93] S. T. Oh, W. T. Han, U. C. Paek, and Y. Chung, "Discrimination of temperature and strain with a single FBG based on the birefringence effect," *Opt. Express*, vol. 12, 2004.
- [94] K. Kim, L. Kollar, and G. Springer, "A model of embedded fiber optic fabry-perot temperature and strain sensors," *J. Compos. Mater.*, vol. 27, 1993.

- [95] D. Wada, H. Murayama, H. Igawa, K. Kageyama, K. Uzawa, and K. Omichi, "Simultaneous distributed measurement of strain and temperature by polarization maintaining fiber Bragg grating based on optical frequency domain reflectometry," *Smart Mater. Struct.*, vol. 20, 2011.
- [96] K. Han, Y. Lee, J. Kwon, S. Roh, J. Jung, B. Lee, "Simultaneous measurement of strain and temperature incorporating a long period fiber grating inscribed on a polarization-maintaining fiber," *IEEE Photonics Technol. Lett.*, vol. 16, 2114-16, 2004.
- [97] G. Chen, L. Liu, H. Jia, L. Xu, and W. Wang, "Simultaneous strain and temperature measurements with FBG written in novel Hi-Bi optical fiber," *IEEE Photonics Technol. Lett.*, vol. 16, 221-223, 2004.
- [98] C. Caucheteur, F. Lhommé, K. Chah, M. Blondel, and P. Mégret, "Novel technique for the simultaneous measurement of strain and temperature using polarization maintaining fiber Bragg gratings," International Conference on Optical Fiber Sensors, 2005.
- [99] T. Mizutani, Y. Okabe, and N. Takeda, "Quantitative evaluation of transverse cracks in carbon fiber reinforced plastic quasi-isotropic laminates with embedded small-diameter fiber Bragg grating sensors," *Smart Mater. Struct.*, vol. 12, 898-903, 2003.